UNIVERSITY OF NOVA GORICA
GRADUATE SCHOOL

SIMULATION OF HOT SHAPE ROLLING OF STEEL BY A MESHLESS METHOD

DISSERTATION

Umut Hanoglu

Mentor: Prof. Dr. Božidar Šarler

Nova Gorica, 2015

UNIVERZA V NOVI GORICI
FAKULTETA ZA PODIPLOMSKI ŠTUDIJ

SIMULACIJA VROČEGA VALJANJA JEKLA Z BREZMREŽNO METODO

DISERTACIJA

Umut Hanoglu

Mentor: Prof. Dr. Božidar Šarler

Nova Gorica, 2015

Acknowledgements

First of all I would like to thank my mentor Prof. Božidar Šarler, my parents and my brothers for their endless support.

I am also grateful to Štore Steel Company for providing useful data for my dissertation.

Finally, I would like thank Slovenian Research Agency for support in the framework of Young Researcher Programme 1000-08-310134 and Štore Steel company in the framework of the project L2-3651: Modelling of casing, rolling and heat treatment for competitive production of topmost steel.

Simulation of hot shape rolling of steel by a meshless method

Abstract

In the presented work, a simulation system for hot shape rolling of steel is developed for a continuous rolling mill. During the simulation, temperature, displacement, strain and stress fields are calculated. The problem is based on strong formulation. The solution procedure of a related thermo-mechanical problem is based on novel Local Radial Basis Function Collocation Method (LRBFCM). This local meshless method does not require integration and mesh generation (polygonisation). For the first time, a simulation of a whole rolling schedule is done by a meshless method. The calculations are made based on the travelling slice model assumption. The slices are aligned with the rolling direction. On each slice the deformation and temperature fields are calculated by assuming that there is no strain or heat flow in the rolling direction. By this approach large deformations can be calculated through a series of small deformation increments on each slice.

The governing equations and adjacent boundary conditions for thermal and mechanical models are in the travelling slice assumption reduced from three to two dimensions and adjusted for the application of LRBFCM. The governing equations for the mechanical model are separately defined for three types of material constitutional relations. These are: elastic, ideal plastic and slightly compressible ideal plastic. The governing equations for the thermal model are reduced from steady conductive-convective heat transport in three dimensions to transient conductive heat transport in two dimensions.

Through the simulation, every slice is being checked if there exists a contact with the roll or not. If the slice has a contact with the roll then first the mechanical model and later the thermal model is calculated. If there is no contact, only the thermal model is calculated on the slice. In case of a roll contact, internal heat generation due to deformation is taken into account. The material properties of the mechanical model can be temperature dependent. The mass flux through the continuous rolling mill is constant at all slices, therefore for each predefined slice position, its corresponding slice time can be calculated.

The corresponding two-dimensional groove geometry for contact under each roll is calculated as a function of position in the rolling direction and roll geometry parameters. The rolling parameters considered are: groove width, groove radius,

roll gap and roll radius. The first slice is set to 0.5 m away from the first rolling stand and the last slice is considered to be 0.3 m after the last rolling stand. The initial parameters of the first slice represent process parameters. These are: initial temperature distribution, initial shape, initial velocity, material type and properties and boundary conditions.

The computational domain, corresponding with the current slice shape is spatially discretized by nodes, positioned in the domain and on its boundary. The domain and boundary are arranged in overlapping local influence domains. Multiquadric (MQ) Radial Basis Functions (RBF) are used as shape functions on each of the influence domains. At least 7 nodes are positioned in every influence domain. Explicit time stepping is used for solving the thermal model and large deformation in the mechanical model is coped by successive small deformation steps.

A sparse matrix is created as a consequence of simultaneous solution of the displacement for all nodes. At each deformation step, small local matrices are created for the solution of the thermal model in each node for each time step. The non-linear system of equations for plastic deformation is solved by Newton-Raphson iteration method. The displacement field used for the initial iteration is taken from the elastic deformation results. However, during the calculation of large deformation cases, when ideal plastic material type is used, the results are not satisfactory converging. Therefore, a further research is needed on the simulation of a complete rolling schedule by a meshless method, considering ideal plastic material properties.

After a certain number of deformation steps, the collocation nodes at the boundary are equidistantly rearranged on the boundary curve and then the rest of the nodes in the domain are positioned according to the transfinite interpolation and elliptic node generation. The re-noding represents a mandatory step in solution procedure to analyze large deformation problems by LRBFCM. The calculated values of the thermal and mechanical fields are updated from the old node positions to the new node positions through inverse distance (Sheppard) interpolation. The final field values and node configuration on each of the slices become input values for the next slice, until the last slice in the simulation. The described simulation system was coded in C# from the scratch by the author in the framework of the research of this dissertation. A user interface for simple inclusion of the process parameters, geometry of rolling stands and material properties is developed as well. The graphical outputs are based on the ParaView software.

The thermal and mechanical models are thoroughly verified on spectra of various test cases. The thermal model is applied in a convective cooling test case and the LRBFCM results are compared with Finite Element Method (FEM). Moreover, an internal heat generation during an oval rolling is calculated by LRBFCM. The mechanical model is tested for seven different elastic deformation examples and LRBFCM results are compared with analytical or FEM solutions. These test cases are: tension with prescribed displacement, compression with prescribed pressure, tension with prescribed pressure, bending of a cantilever beam, expansion of a cylindrical tube, linear compression tension and bending of a beam by a uniform load. Furthermore, a flat rolling example without friction at the roll contact and considering a slightly compressible ideal plastic material (with a compressibility parameter $g = 0.001$), based on von Mises ideal plastic flow rule, is calculated by LRBFCM and compared with FEM. In addition to all previously mentioned test cases, flat and oval rolling examples are also calculated by LRBFCM in a stepwise solution procedure and compared with FEM when elastic material properties are used. At the roll contact, the sticking boundary conditions are applied. Comparisons of the results are made in terms of displacement and strain fields. Overall, the models have been tested for 11 predefined test cases before applying it to a whole rolling simulation.

In the simulation of hot shape rolling, a real rolling schedule as appears in Siderimpes constructed Štore Steel rolling mill is considered, which consists of five rolling stands with different groove geometries. 13 m long computational domain is defined in the rolling direction by considering 1455 slice positions. An initial rectangular cross section with dimensions 95 mm $\times$ 80 mm with 16MnCr5S steel is considered at uniform temperature 1100 °C and initial rolling speed 0.76 m/s. At the end of the rolling, bar with diameter of 60 mm is obtained. Temperature depended elastic material properties are considered. They are calculated from JmatPro data base for steel.

The results are calculated considering plane strain assumption and represented in terms of displacement, temperature, strain and stress fields for a slice that exits each of the five rolling stands. The sensitivity studies with increased roll's temperature, increased heat transfer coefficient to the roll and neglection of internal heat generation are performed to demonstrate expected behaviour of temperature on the slices. Moreover, constant elastic material properties at different temperatures have been considered. Their influence on slice velocities is shown. The simulation system is capable of calculating arbitrary rolling

schedule which is specified through user defined groove geometries and positions. Therefore it is especially useful when designing new rolling schedules for new steel grades.

Keywords

Computational thermo-mechanics, hot shape rolling, steel, elastic deformation, ideal plastic deformation, meshless methods, strong formulation, coupled systems, local radial basis function collocation method, simulation

Simulacija vročega oblikovnega valjanja z brezmrežno metodo

Povzetek

V predstavljenem delu je bil razvit simulacijski sistem za vroče oblikovno valjanje jekla na kontinuirni valjarni. Med simulacijo izračunavamo temperaturna, deformacijska, raztezna in napetostna polja. Problem temelji na močni formulaciji. Rešitveni postopek za tovrstni termo-mehanski problem temelji na novi Lokalni Kolokacijski Metodi z Radialnimi Baznimi Funkcijami (LRBFCM). Ta lokalna brezmrežna metoda ne potrebuje integracije in generacije mreže (poligonizacije). Prvič je narejena simulacija celotnega valjarskega razporeda z brezmrežno metodo. Izračuni so narejeni na podlagi predpostavk modela potujoče rezine. Rezine so poravnane v smeri valjanja. Na vsaki rezini je izračunano deformacijsko in temperaturno polje ob predpostavki, da ni raztezka in toplotnega toka v vzdolžni smeri. S to predpostavko lahko izračunavamo velike deformacije na podlagi vrste majhnih deformacijskih korakov na vsaki rezini.

Vodilne enačbe in pripadajoči robni pogoji za termični in mehanski model so v modelu potujoče rezine reducirani iz treh v dve dimenziji in prilagojeni za uporabo LRBFCM. Vodilne enačbe mehanskega modela so posebej definirane za tri različne tipe konstitucijskih relacij. Te so elastične, idealne plastične in rahlo stisljive idealne plastične. Vodilne enačbe termičnega modela so reducirane iz ustaljene kondukcijsko-konvekcijske transportne enačbe v treh dimenzijah na neustaljeno enačbo za prevod toplote v dveh dimenzijah.

Med simulacijo je za vsako rezino preverjano ali obstaja stik z valjčnico ali ne. Če ima rezina stik z valjčnico, potem je najprej izračunan mehanski model in nato termični. Če ni stika z valjčnico je na rezini izračunan samo termični model. V primeru kontakta z valjčnico, je upoštevana notranja generacija toplote zaradi deformacije. Snovne lastnosti mehanskega modela so lahko temperaturno odvisne. Masni tok skozi kontinuirno valjarno je konstanten za vse rezine, zato lahko za vsak vnaprej definiran položaj rezine izračunamo njen vnaprej definiran čas.

Ustrezna dvo-dimenzionalna gemeotrija vtika za stik pod vsako valjčnico je izračunana na podlagi položaja v smeri valjanja in geometrijskih parametrov valjčnice. Upoštevani geometrijski parametri vtika so: širina vtika, radij vtika, vmesna razdalja med valjčnicama in radij valjčnice. Prva rezina je postavljena 0,5 metra od prvega valjarskega orodja, zadnja pa 0,3 metra po zadnjem

valjarskem ogrodju. Začetni pogoji rezine predstavljajo procesne parametre. Ti so: začetna porazdelitev temperature, začetna oblika, začetna hitrost, tip materiala in snovne lastnosti ter robni pogoji.
Računska domena, ki sovpada s trenutno obliko rezine, je prostorsko diskretizirana z računskimi točkami, postavljenimi na območje in njegov rob. Območje in rob sta urejeni v prekrivajoče se lokalne vplivne domene. Multikvadrične radialne bazne funkcije so uporabljene kot oblikovne funkcije na vsaki izmed vplivnih domen. V vsaki vplivni domeni je najmanj 7 točk. Eksplicitno časovno korakanje je uporabljeno za rešitev termičnega modela in velike deformacije v mehanskem modelu so upoštevane s soslednimi majhnimi deformacijskimi koraki.
Redka matrika je postavljena kot posledica simultanega reševanja pomikov v vseh točkah. V vsakem deformacijskem koraku postavimo majhne lokalne matrike za reševanje termičnega modela v vsaki računski točki za vsak časovni korak. Nelinearni sistem enačb za plastično deformacijo je rešen z Newton-Raphsonovo iterativno metodo. Polje pomikov, uporabljeno za začetno iteracijo, je izračunano z elastičnim modelom. Vendar med izračunom velikih deformacij, ko uporabimo idealni plastični material, rezultati ne konvergirajo zadovoljivo. Zato so potrebne nadaljne raziskave za simulacijo celotne valjarske proge z brezmrežno metodo, z upoštevanjem idealnih plastičnih snovnih lastnosti.
Po določenem številu deformacijskih korakov so kolokacijske točke na robu ekvidistantno preporazdeljene na robni krivulji in nato je preostanek točk v notranjosti preporazdeljen na podlagi transfinitne interpolacije in eliptične generacije računskih točk. Preporazdelitev računskih točk predstavlja potreben korak za analizo velikih deformacij z LRBFCM. Izračunane vrednosti termičnega in mehanskega modela so posodobljene na novi položaj računskih točk iz starega položaja računskih točk na podlagi (Sheppard-ove) interpolacije z inverzno razdaljo. Končne vrednosti polj in konfiguracija računskih točk na vsaki izmed rezin predstavljajo vhodne podatke za naslednjo rezino do zadnje rezine simulacije. Opisani simulacijski sistem je bil programiran od začetka v programskem jeziku C# v okviru raziskav te disertacije. Razvit je bil tudi uporabniški vmesnik za preprosto vključitev procesnih parametrov, geometrije valjanja in snovni lastnosti. Grafični izhodi so bili narejeni na podlagi programske opreme ParaView.
Termični in mehanski model sta skrbno preverjena na spektru različnih testnih primerov. Termični model je uporabljen v konvekcijskem hlajenju in rezultati na podlagi LRBFCM so primerjani z rezultati metode končnih elementov (FEM).

Na podlagi LRBFCM je izračunana tudi generacija toplote na primeru ovalnega valjanja. Mehanski model je preverjen na sedmih različnih elastičnih deformacijskih primerih in rezultati na podlagi LRBFCM so primerjani z analitičnimi in FEM rešitvami. Ti testni primeri so: natezanje s predpisanim odmikom, stiskanje s predpisanim tlakom, zvijanje vzvodnega nosilca, ekspanzija cilindrične cevi, linearno stiskanje/natezanje in zvijanje nosilca na podlagi enakomerno porazdeljene obremenitve. Nadalje so bili primerjani izračuni ravnega valjanja, brez trenja na valjčnicah in z upoštevanjem malo stisljivega plastičnega materiala (s parametrom stisljivosti $g = 0.001$) ter von Misesovega idealnega plastičnega pravila tečenja, narejeni z LRBFCM, z rezultati FEM. Dodatno k vsem predhodno navedenim testnim prmerom so izračunani tudi ploski in ovalni primeri valjanja, izračunani na podlagi postopne deformacije za plastični material z LRBFCM in primerjani s FEM. Na stiku z valjčnico so upoštevani robni pogoji lepljenja. Primerjave rezultatov so narejene na podlagi polj striga in deformacije. Skupaj so bili modeli testirani na podlagi 11 predhodno definiranih testnih primerov, preden so bili uporabljeni na celotni valjarski progi.

Pri simulaciji vročega oblikovnega valjanja smo uporabili realistične parametre vtika, kot nastopajo na valjarski progi Siderimpes v podjetju Štore Steel, ki jo stestavlja pet orodij z različnimi geometrijami vtika. 13 m dolga računska domena je definirana v smeri valjanja ob upoštevanju 1455 pozicij rezin. Upoštevan je začetni profil dimenzije 95 mm × 80 mm iz jekla 16MnCr5S na začetni temperaturi 1100 °C, valjan z začetno hitrostjo 0,76 m/s. Na koncu valjanja dobimo okroglo palico s premerom 60 mm. Predpostavljene so temperaturno odvisne snovne lastnosti. Izračunane so iz podatkovne baze JmatPro za jekla.

Rezultati so izračunani na podlagi predpostavke ravninske deformacije in predstavljeni s polji deformacije, temperature, raztezka in napetosti za vsako rezino, ki izstopa iz petih orodij. Izdelane so bile občutljivostne študije s povišano temperaturo valjčnic, povišanim koeficientom prestopa toplote na valjčnice in z zanemarjeno notranjo generacijo toplote, s ciljem pokazati pričakovano obnašanje temperature na rezinah. Dodatno so upoštevane konstantne elastične snovne lastnosti pri različnih temperaturah. Prikazan je njihov vpliv na hitrosti rezin. Simulacijski sistem je zmožen izračuna poljubnega razporeda valjanja, ki ga uporabnik specificira z definiranimi geometrijami in pozicijami vtikov. Zato je uporaben posebej, ko projektiramo nove plane vtikov za nove vrste jekel.

Ključne besede

Računalniška termomehanka, vroče oblikovno valjanje, jeklo, elastična deformacija, idealna plastična deformacija, brezmrežna metoda, močna formulacija, sklopljeni sistem, lokalna kolokacijska metoda z radialnimi baznimi funkcijami, simulacija

Contents

List of Figures

List of Tables

List of Symbols

Latin symbols

A	area of slice
$\mathbf{A}$	solution matrix
$\mathbf{b}$	adjacent vector
c	shape parameter
c_p	specific heat
$\mathbf{C}^e$	elastic stiffness matrix
$\mathbf{C}^p$	plastic stiffness matrix
$\mathbf{d}$	body force vector
E	Young's modulus
e_{ij}	components of deviatoric strain
f	yield or loading function
g	slightly compressible material parameter
G	shear modulus
GH	groove height
GPR	groove point radius
GR	groove radius
GW	groove width
h_{air}	heat transfer coefficient to air
h_{roll}	heat transfer coefficient to the roll
H_p	plastic modulus
$\mathbf{i}_x, \mathbf{i}_y, \mathbf{i}_z$	base vectors of Cartesian x, y, z coordinate system
$\mathbf{I}$	identity matrix
I_i	invariants of the stress tensor
J_i	invariants of the stress deviator tensor
$\mathbf{J}$	Jacobian matrix
k	thermal conductivity
K	yield shear stress in pure shear
$\mathbf{L}$	derivative operator matrix
$\mathbf{n}$	unit normal
N	number of nodes
P	pressure

$\mathbf{p}$	position vector
$\dot{Q}$	internal heat generation rate per unit volume
r	rate of reduction
R_{gap}	roll gap
RR	roll radius
$\mathbf{s}$	stress deviator tensor
t	time
$\mathbf{T}$	stress tensor
T	temperature
T_{air}	air temperature
T_{fur}	initial temperature for hot rolling
T_{ref}	reference temperature
T_{roll}	roll temperature
$\mathbf{u}$	displacement vector
$\bar{\mathbf{u}}$	prescribed displacement vector
u_x	displacement in x direction
u_y	displacement in y direction
u_z	displacement in z direction
U	strain energy per unit volume
$\mathbf{U}$	column matrix of displacement
v_{entry}	entry velocity of the bloom
$\mathbf{v}$	velocity vector
z	position towards the rolling direction

Greek symbols

α	collocation coefficient
γ	shear strain
ρ	density
γ	shear strain
$\boldsymbol{\sigma}$	stress vector
σ_{ij}	components of stress vector
σ_m	hydrostatic stress
σ_p	yield stress
$\bar{\sigma}$	effective stress

$\boldsymbol{\varepsilon}$	strain vector
ε_{ij}	components of strain vector
ε_a	axial strain
ε_v	volumetric strain
$\bar{\varepsilon}$	effective strain
τ	shear stress
$\bar{\tau}$	prescribed shear stress
τ_{oct}	octahedral shear stress
ψ	shape function
$\boldsymbol{\Psi}$	interpolation matrix
$\boldsymbol{\delta}$	Kronecker's delta matrix
$\boldsymbol{\theta}$	local interpolation matrix
$\boldsymbol{\Phi}$	local solution matrix
ν	Poisson's ratio
η	Taylor-Quinney coefficient
Ω	domain
Γ	boundary

Subscripts

x, y, z	Coordinates of the x-y-z coordinate system
max	maximum value

Superscripts

D	Dirichlet boundary condition
N	Neumann boundary conditions
R	Robin boundary conditions
T	Transpose

Acronyms

2D	Two-Dimensional
3D	Three-Dimensional
EFGM	Element Free Galerkin Method
ENG	Elliptic Node Generation
FEM	Finite Element Method

FPM	Finite Points Method
LRBFCM	Local Radial Basis Function Collocation Method
LPIM	Local Point Interpolation Method
LRPIM	Local Radial Point Interpolation Method
LS-RPCM	Least-squares Radial Point Collocation Method
MLPGM	Meshless Local Petrov-Galerkin Method
MLS	Moving Least Squares
MQ	Multiquadrics
PCM	Point Collocation Method
PDE	Partial Differential Equation
PIM	Point Interpolation Method
RBF	Radial Basis Function
RKPM	Reproduction Kernel Particle Method
RPICM	Radial Point Interpolation Collocation Method
RPIM	Radial Point Interpolation Method
TFI	Transfinite Interpolation

1 Introduction

In this introductory chapter, first of all, goals and contents of the dissertation are elaborated. A brief history and basic principles of rolling are given afterwards. Moreover, a discussion on literature overview on simulation of rolling and meshless numerical methods is done. Finally, the objectives of this dissertation are postulated.

1.1 Goals of the dissertation and overview of contents

Numerical modelling and simulation of real-life thermo-mechanical systems is gaining its importance in the last few decades due to the fast development of computer hardware and software. Metal forming applications certainly belong to this class of systems. They can be found from the craftsman who is forging metals in his shop to contemporary large production range steel mills. However, the physical background behind it has always been the same. A deep understanding and simulation of the process gives us a possibility to create better and more effective designs in the future. At the present, simulations play a crucial role, since they can predict essential issues of today's mechanical system design tasks. That is why many publications are published each year in the field of computational thermo-mechanics [Lenard, 2007] and [Lenard, Pietrzyk and Cser, 1999].

The present dissertation is focused on development of a computational model and subsequent simulation of hot shape rolling of steel and it has two major objectives. The first objective stems from the importance of a variety of steel products in today's industrial world, each of them requiring a specific thermo-mechanical treatment that needs to be determined by simulation, and the second objective aims at the development of a novel meshless numerical approach used in the related simulations.

Steel has been and remains one of the most significant materials in the world since the industrial revolution. After having enough power to have mass production lines, steel was always in the scene either as the material used in the

production or the material being produced itself. Therefore, there is a mutual relation between the industry and the steel production. The increase in the total amount of annual steel production in the world can be seen in Figure 1.1.

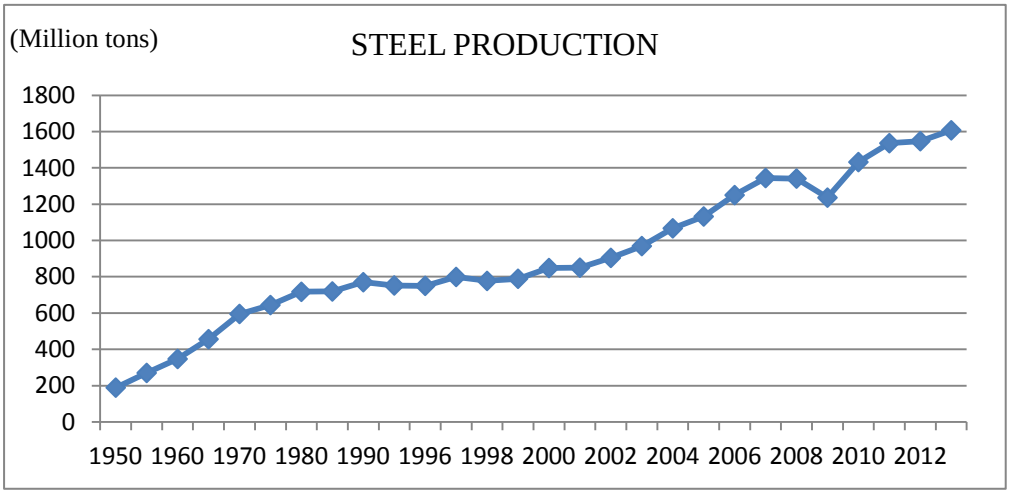

Figure 1.1: Anual total steel production around the world in million metric tons. [World Steel Association, 2014].

As steel gained importance, its applications varied enormously. Therefore, different usages of steel in different areas were introduced. New designs are needed for new applications. However, different applications of steel require specific shapes and dimensions of steel which are achieved through the process of casting, rolling, extrusion, etc. Therefore, the simulations of the rolling process become very important in order to successfully and effectively sustain the new demands of the today's world. The importance of steel is discussed in [Roberts, 1983].

Numerical methods in computational solid mechanics date back to 1960s where first applications of Finite Element Method (FEM) have been used [Zienkiewicz and Taylor, 2000]. Since then, thousands of publications and many user friendly commercial programs have been introduced based on FEM. This method still dominates the area of computational solid mechanics. However, FEM has several shortcomings like difficulty in meshing and re-meshing, low accuracy especially for computing stresses, simulation of the dynamic crack growth with arbitrary paths that does not coincide with the original mesh lines of the elements, handing large deformation cases that lead to an extremely distorted mesh, simulating the failure of structures or components with large number of fragments, solving dynamic contacts with moving boundaries and solving multi-physics problems. In the last decades, meshless methods became more and more

popular due to their simplicity, stability and straight forward application. Meshless methods can save significant amount of time because mesh generation is not required. They can easily solve large deformation and strong nonlinear problems because the connectivity among the nodes is generated as a part of the computation and can be modified over time, high accuracy can be achieved easily for example; in the areas where more node refinement is required. Nodes can be added easily, they can easily handle the damage of the components such as fracture which is very useful to simulate the material failures. They can easily solve the problems with requirement of multi domains and multi physics [Li and Mulay, 2013]. In this dissertation, development of suitable algorithms for simulation of a complete rolling schedule is done for the first time by a fully meshless method.

The contents of the dissertation are as follows: In the first chapter a brief history of rolling and basic principles are introduced such as first application of rolling to understand the need. Afterwards, a detailed literature overview is given on the subject of computational modelling of deformation and rolling. As expected, most of them are based on FEM. 3 commercial programs, which can be used for simulation of hot shape rolling, are also briefly described.

In the second chapter, governing equations are derived separately for thermal and mechanical models. The coupling of thermal and mechanical models is discussed. An overview of the equations can be seen at the end of the chapter.

In the third chapter the physical model used in the rolling simulation is described with corresponding boundary conditions, involving the slice model assumptions, definition and geometry of the grooves, material behaviour and rolling schedule as well. A set of parameters needed for rolling simulation is given as well as the flowchart of the simulation.

In the fourth chapter, a meshless numerical approach is developed and specified in details. Collocation points and influence domains are introduced, discretization is applied for thermal and mechanical models. Subsequently, a sparse system of equations is defined as a consequence of the mechanical solver as well as the explicit time stepping for the thermal model.

In chapter five, some tests are done to prove that the model is performing as expected. In elastic cases the results are compared with the analytical solution or FEM based commercial code DEFORM [DEFORM, 2009] and in plastic case only with FEM.

In the sixth chapter, the simulation is put to the rolling test and compared with FEM in many aspects of deformation.

In chapter seven, all the input parameters for a complete rolling schedule are given and a simulation of hot shape rolling of steel is done. The results are given in terms of temperature field, displacement field, strain field, and stress field.

Chapter eight includes concluding remarks and future developments followed by a list of references.

1.2 History and basic principles of rolling process

The first record of any type of true rolling mills was drawn by Leonardo da Vinci in 1480, however there is no evidence that his design has ever been built and used. The first elements processed by hand driven rolls were mostly gold, silver and lead since they are much softer than the other metals and this type of rolls dates back as late as 14th century. As discussed by W. L. Roberts [Roberts, 1978], the rolling of metals was not of big interest for people until the middle of 16th century. People at that time found many ways of using metal applications especially for lead which needed to be rolled into thin sheets. Such examples of usage of lead would be roof claddings and organ pipes at that time.
The first developments of rolling of iron are thought to be taken place in Germany, Belgium and Great Britain around 16th century, nevertheless there is no clear evidence where and how it started first. During the 17th century the exponential growth of rolling of iron was observed. Also in the same century, the hot rolling of iron was in operation and until then the rolled product was always at ambient temperature. Thin plate rolling of iron was not possible at that time with using cold rolling process. Germans were the first ones dominating the European market by using hot rolling of iron with the help of water power which led them to produce thin sheets of iron which served as a raw material for many applications at that time. It took British until the beginning of 18th century to take over the tinplate iron production from Germans. According to many observers from that time, Great Britain was then leading the way [Roberts, 1978].
In 1728, John Payne took the patent of various rolling mill configurations to produce different shapes and forms shown in Figure 1.2. This process is now called shape rolling. The difference between shape and flat rolling can be seen in Figure 1.3.

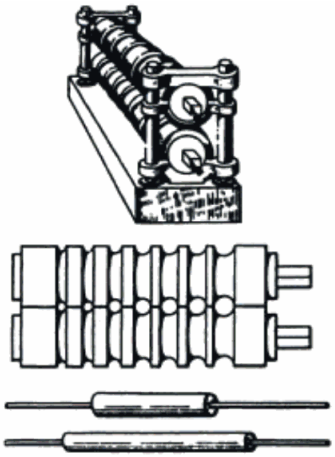

Figure 1.2: First rolling mill to produce various cross sections, patented by John Payne in 1728.

The first continuous hot rolling mills were patented by Sir Henry Bessemer in 1857 and by Dr. R. V. Leach in 1859 [Roberts, 1978].

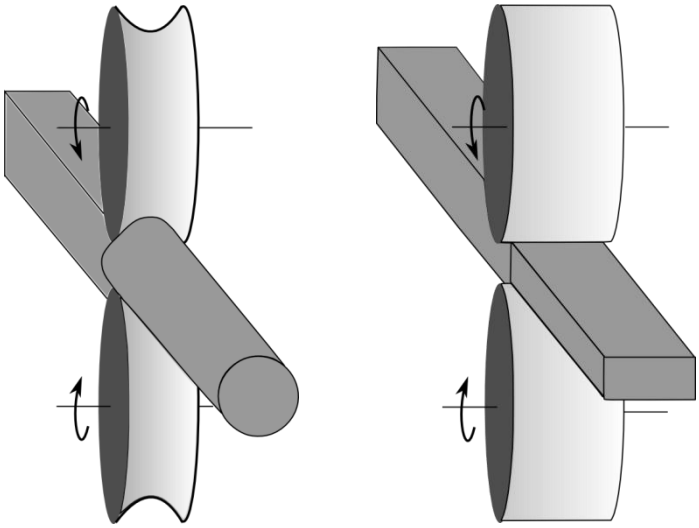

Figure 1.3: Example of an oval shape rolling on left and flat rolling on right.

1.3 Literature overview on simulation of rolling and discussion of models used

The rolling process can take place in two major modes; hot or cold rolling. Cold rolling does not require the energy to heat the metal in reheating furnaces, but it requires much more power to shape it. Due to high forces, lubricants are more

often used in cold rolling then in the hot rolling. In the hot rolling, water sprays are used for the roll not to exceed a certain temperature.
The physical explanation of the rolling process has been shown in many books [Lenard 2007], [Roberts 1983], [Lenard, Pietrzyk and Cser 1999], [Ginzburg 1993] and proceedings [Proceedings of the 4th international steel rolling conference, 1987], [Proceedings of the 9th international / 4th European steel rolling conference, 2006].
The first mechanical model was developed by Orowan which is also referred as 1D rolling model [Orowan, 1943]. He basically applied the equilibrium of forces in the rolling direction excluding any sideway impacts. Even before, Hitchcock derived a formula for reduction of roll radius during flat rolling [Hitchcock, 1935].
Sims additionally made a mechanical model to calculate the roll separating force [Sims, 1954]. It serves as one of the simplest models in use because the roll separating force can be directly calculated with Sims's formula. It has been widely used in the industry since it gives comparable results to observations and also it is quite simple to calculate.
Schey [Schey, 2000] introduced in his book "Introduction to Manufacturing Processes" a simple formula as well to calculate the roll separating force. He described the case when the sticking condition occurs and on a graph he related the pressure intensification factor, which is needed in his formula, in a system with different coefficients of friction.
Mechanical behaviour of steel can be analyzed at least in three regimes: elastic, plastic and elasto-plastic. The concepts with plasticity are the most complex, since the material behaviour is non-linear in this concept. The material scientists wanted to physically analyze and calculate the plastic deformation phenomena. The pioneer of this approach was von Mises who studied the plastic flow of a material and made a very useful assumption that connects the plastic flow function with the yielding function [von Mises, 1913]. This approach has been used by many researchers until now. The practical advantage is that von Mises flow rule can not only be used in uniaxial deformation, but also in the multiaxial cases. In the present dissertation, the von Mises flow rule assumption is applied to the cases with plastic deformation. The actual meaning of this assumption is, that the effective stress that causes plastic deformation is always equal to the yield stress. This can also be referred to ideal plastic behaviour or linearized plasticity. The implementation of deformation concepts is mainly associated with the implementation of the stress-strain relations. In the general formulation, the stresses are used, however in the simulation, displacements have to be calculated as a result. Therefore, writing the stresses in terms of displacements in

the framework of meshless discretization is one of the key elements of this dissertation.

When analyzing hot rolling of steel, one cannot cover the subject without introducing shape rolling. The steel factories, which have continuous casting stations, produce a constant cross sectioned steel. This initial cross sectional size is almost never used in any real world applications. Therefore, the rolling stations in the industry are positioned right after the continuous casting to reduce the cross sectional size to various demanded shapes. Many rolling stations use grooves to change the shape of the bloom. The types of these grooves can vary excessively. The design of grooves and stands can be very diverse in order to be able to produce specific structural shapes such as H or I beams. Many models in computational mechanics have been developed for the metal deformation problems since 1980s. The first numerical models of rolling were calculated for a 3D physical domain. The bloom to be rolled is a 3D object and deformation takes place in all three axes. Due to geometrical complexities the calculations took several days to complete. Later on some different methodologies have been applied to reduce the calculation effort and simplify the problem. These methods reduce 3D to a 2D problem by using discontinuous cross sections as physical computational domains. The models that are based on a 2D cross sectional model, also known as travelling slice model, calculate the new shapes of those slices which all together give the final 3D shape. There are two cases of commonly used slice models, the plane stress and the plane strain cases. A crucial part of this dissertation is the slice model assumption. A slice model was used by Glowacki and his co-workers in a plane strain rolling case to analyze a multi-pass bar rolling process in small steps [Glowacki, Kedzierski, Kusiak, Madej and Pietrzyk, 1992].

There have been some more advanced mechanical models developed to analyze the metal deformation process and also applied to the rolling process. One of the first complex models was based on the upper bound theorem, which was first described by Avitsur [Avitsur, 1968]. The idea is the balance of powers acting over the material during the deformation. The power balance equation can be separated into three parts. The first part is the power used for the material deformation, the second part is the power used for the surface tractions which take place at the contact surface and the third part is the power supplied due to the gravitational body forces.

Around the same time, the first FEM models were developed by [Marcel and King, 1967] and [Lee and Kobayashi, 1973]. Accurate results were gained for small plastic strains. Many more accurate results have been achieved by using FEM as presented by [Glowacki 1996], [Lenard, Pietrzyk and Cser 1999].

FEMs have been used many times to simulate the rolling process. They usually use the weak formulation of the power balance equation per unit width which requires to be integrated through volume and the contact surface. In order to do that the FEM requires integration over the polygons of the domain. However, this approach is not suitable in meshless methods because the background integration requires, even in a meshless method, a background meshing, similar to FEM, as discussed by [Liu, 2003]. Good examples of FEM application in rolling are presented by [Glowacki, Dyja and Lesik, 1995], [Hsiang and Lin, 2000], [Lenard, Pietrzyk and Cser, 1999], [Jiang, Tieu, Zhang, Lu and Sun, 2003] and [Glowacki, 2005]. FEM is also used for simulating shape rolling process for compensation of dies as in a PhD thesis by [Belinski, 1999] and for sensitivity studies of hot rolling by [Picque, 2004].

First slightly compressible material concept in solid mechanics is applied by [Osakada, Nakano and Mori, 1982]. The main advantage of using slightly compressible material is that, the governing equations derived from it are functioning to be more accurate than the extension of the simple infinitesimal deformation theory when dealing with non steady deformation problems.

After countless FEM applications in solid mechanics have been made, more and more deformation problems started to be solved by meshless methods. One of the first attempts is made by Chen et al. [Chen, Roque, Pan and Button, 1998] by using the reproduction kernel particle method (RKPM) [Liu, Jun and Zhang, 1995]. Since 1990s, several publications can be found on deformation problems by using meshless methods, particularly in terms of Point Interpolation Method (PIM). A two-dimensional deformed incompressible bubble in potential flow is calculated by Method of Fundamental Solutions (MFS) by [Šarler, 2006]. A Nodal Integration Radial Point Interpolation Method (NI-RPIM) has been applied to solve deformation problems by [Liu, Zhang, Wang, Zhong, Li and Han, 2007] and Radial point Interpolation Method (RPIM) by [Liu and Gu, 2005]. Local Radial Point Interpolation Method (LRPIM) has also been studied by [Liu and Gu, 2001a] and Local Point Interpolation Method (LPIM) by [Gu and Liu, 2001] and [Liu, and Gu, 2001b]. PIM method has also been studied in details in many publications by [Liu and Gu, 2001c], [Oñate, Idelsohn, Zienkiewicz and Taylor, 1996] and [Pozo, Perrazzo and Angulo, 2009]. The method includes collocation with using radial, polynomial or both of them as basis functions. The discussion of using different radial basis functions and adding polynomial functions has been done by [Liu and Gu, 2002] and by [Hu and Hua, 2006]. They all used the general definition of the deformation theory, however their solution procedure always relies on the weak formulation. Many application and test cases have been presented by them. A comparison between weak and strong formulation is also made by Batra and Zhang [Batra and Zhang,

2007] with using PIM. In their test cases weak formulation was shown to be more accurate than the strong formulation. Weak formulation requires integration, whereas the strong formulation does not need any integration and is thus completely meshless.

Several strong form meshless publications in the field of solid mechanics appeared recently. Most of them are based on Point Collocation Method (PCM) [Guo, Nakanishi and Yokouchi, 2005], Finite Points Method (FPM) [Oñate, Perazzo and Miquel, 2001], Radial Point Interpolation Collocation Method (RPICM) [Liu, Liu, Tai and Lam, 2005], Radial Point Collocation Method (RPCM) [Kee, Liu and Lu, 2008], Least-square Radial Point Collocation Method (LS-RPCM) [Kee, Liu and Lu, 2007]. In some publications, the use of strong form with RBFs is shown as a successful method [Kee, Liu, Zhang and Lu, 2008] as well as using RBF with polynomial functions [Liu, Kee, Zhong, Li and Han, 2007]. A rigid-plastic deformation case with strong formulation has also been calculated by [Guo, Nakanishi, 2003] with using MLS. The strong and weak formulation of mechanical deformation problem, such as in the case of rolling, is explained by [Liu, 2003]. The application of the weak form was made by [Atluri, 2004] and solved by Meshless Local Petrov Galerkin Method (MLPGM) for a 3D elastic material.

A 3D rolling analysis with FEM was also simulated by Hsiang and Lin [Hsiang and Lin, 2000]. However, in order to overcome the immense amount of computational power needed for a 3D FEM shape rolling, slice model is used. The computational framework can be chosen either Eulerian or Lagrangian in rolling. Eulerian analysis looks at the same frame and assumes a continuous flow at the inlet and the outlet of the mill. In such framework the calculation belongs to the specific position, not to the material, since the material is always changing at the same point. On the other hand, in a Lagrangian frame, the domain directly belongs to the same material throughout the deformation. Therefore all the slice models, regardless of the numerical method used, are based on Lagrangian frame. The examples of FEM based rolling simulations in Lagrangian description are discussed by [Lenard, Pietrzyk and Cser, 1999]. Moreover, also a mixed Lagrangian-Eulerian coordinate system could be used for rolling. In the rolling direction Eulerian coordinate system can be chosen, since the material has inflow and outflow in the longitudinal direction. For the vertical and lateral direction, Lagrangian coordinate system can be used, since temperature and deformation are calculated for a slice representing billet or bloom. The travelling slice always describes the same portion of the material at each step. The details of this system are explained and applied by [Synka and Kainz, 2003] and also by [Glowacki, 1996]. Within the content of the present dissertation, a mixed Lagrangian-Eulerian description will be used.

Commercial codes for rolling are also available in the market and some of them are also used as a reference in the present research. The program called Wicon [Wicon, 2004] is used to create and test the whole rolling schedule of shape rolling, including the creation of the custom rolling sequence and pass design. The grooves can be specifically designed for each pass. The main advantage of the program is that it calculates and shows the cross sectional appearance of the bloom after each pass. The snapshot of the program interface can be seen in Figure 1.5. Hot Strip Mill Modeling (HSMM) [HSMM, 2008] is another commercial program to analyze the hot rolling just, limited to flat rolling mills. It also calculates the width spread and analyzes the temperature changes, with being able to include the effects of the water sprays to cool down the rolls. The snapshot of the program interface can be seen in Figure 1.6.
Computational methods created a step forward in terms of various applications of thermo-mechanics. A user can define his own specific problem and get solution by using a computational method such as shown in this dissertation.

BIG_DIM Rolling schedule: RD38-103 Material: 7. Low Alloyed Steel 0.61C 1.6Si 1.0Mn (*1.00)

File Help Flow Stress Properties Rearrangements on/off Change data on/off Graphs on/off Picture on/off

PASS / SEQUENCE	no	1/1	2/1	3/1	4/2	5/2	6/3	7/3	8	9	10/4	11/4	12/4	13/5	14/5	15/6	16/6
STAND	no	1-0	1-0	1-0	1-0	1-0	1-0	1-0	1-0	1-0	2-0	2-0	2-0	2-0	2-0	2-0	2-0
GROOVE	no	BX	TBX	BX	TBX	BX	TBX	□BX	By-Pass	By-Pass	DI	DI	DI	DI	SQ	DI	SQ
Billet:SO183.2		3/B	3/B	5	3/B	7	3/B	7			1	2	3	4	1	5	2
ROLL GAP(empty)	mm																
ROLL GAP(active)	mm	57.00	33.00	30.00	8.00	27.00	14.00	16.00			6.00	6.00	6.00	6.00	6.00	6.00	4.00
PRIOR Gap -"-	mm																
Gap DIFF. -"-	mm																
Bar HEIGHT Hb	HOT	139.0	115.0	142.0	90.00	112.0	96.00	101.00			110.0	97.40	87.00	74.80	77.50	64.00	67.00
Bar WIDTH Wb	HOT	197.9	205.8	136.2	157.6	107.3	113.1	100.84			137.1	119.5	106.5	96.28	79.95	83.83	67.85
Inscr. circle Si	HOT										88.11	77.92	69.32	60.54	61.01	52.77	52.38
Reduction	%	18.67	14.60	20.15	24.60	17.01	7.65	6.69			15.77	21.43	21.04	22.18	10.25	18.79	9.40
ROLL DIAMETER	mm	800.0	800.0	800.0	800.0	800.0	800.0	800.0			650.0	650.0	650.0	650.0	650.0	650.0	650.0
EFFECTIVE dia.	mm	762.89	760.9	761.64	770.52	770.9	732.43	736.84			641.45	654.21	658.37	666.24	634.06	665.86	637.76
MOTOR revolution	rpm	175	175	175	175	175	175	175			600	600	700	700	700	800	961
SPEED	m/sec	6.99	6.97	6.98	7.06	7.06	6.71	6.75			2.91	2.97	3.48	3.53	3.35	4.03	4.63
Loop/Pull MIN	m or %																
Loop/Pull CAL.	m or %																
Loop/Pull MAX	m or %																
ENTRY temperature	°C	1150	1149	1141	1140	1133	1130	1117			1106	1095	1085	1073	1058	1040	1020
LOAD	kN	2793	2061	2265	2693	1655	824	671			997	1222	1103	1055	654	806	475
TORQUE	kNm	322	176	299	318	189	53.0	40.0			58.8	89.1	75.9	70.6	42.7	42.3	22.5
POWER	kW	5892	3220	5480	5825	3461	971	733			533	808	803	746	451	511	326
Power MAX	kW	======>	======>	======>	======>	======>	======>	======>	======>	! 6107	======>	======>	======>	======>	======>	======>	======>
Power MEAN	kW	======>	======>	======>	======>	======>	======>	======>	======>	1753	======>	======>	======>	======>	======>	======>	======>
Power AVAILABL	kW	======>	======>	======>	======>	======>	======>	======>	======>	2150	======>	======>	======>	======>	======>	======>	======>
Angle of Bite	°	20.2	14.8	24.3	21.0	20.2	11.1	10.3			16.2	21.7	19.5	19.0	14.6	13.3	13.8
Bar Area HOT	mm²	27225	23251	18567	13999	11618	10729	10011			8432	6625	5231	4071	3654	2967	2688
Bar length HOT	m	2.49	2.91	3.65	4.84	5.83	6.31	6.76			8.03	10.22	12.94	16.62	18.51	22.79	25.14
Spread Coefficient	:	1.10	1.10	1.10	1.10	1.10	1.10	1.10			1.00	1.00	1.00	1.00	1.00	1.00	1.00
! OBSERVATIONS !								1-F									
Flow stress	N/mm²	123	117	130	137	135	115	114			121	137	145	154	148	165	158
H.T.C.(Roll)	W/m²°C	3000	3000	3000	3000	3000	3000	3000			3000	3000	3000	3000	3000	3000	3000
H.T.C.(Air)	W/m²°C	30	30	30	30	30	30	30			30	30	30	30	30	30	30

Figure 1.4: Screenshot of the commercial program Wicon.

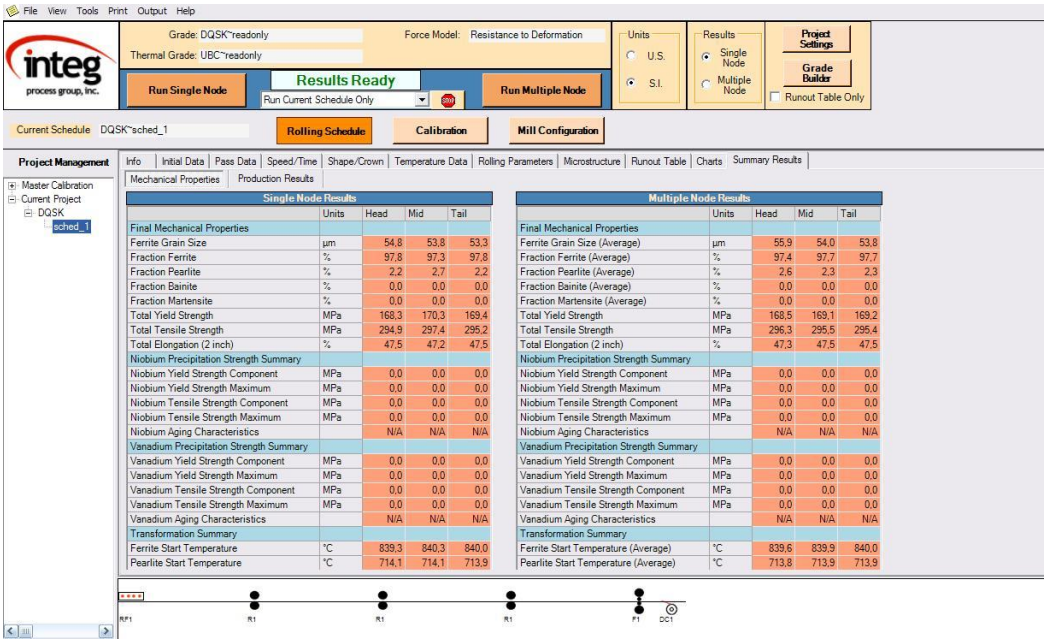

Single Node Results	Units	Head	Mid	Tail
Final Mechanical Properties				
Ferrite Grain Size	µm	54,8	53,8	53,3
Fraction Ferrite	%	97,8	97,3	97,8
Fraction Pearlite	%	2,2	2,7	2,2
Fraction Bainite	%	0,0	0,0	0,0
Fraction Martensite	%	0,0	0,0	0,0
Total Yield Strength	MPa	168,3	170,3	169,4
Total Tensile Strength	MPa	294,9	297,4	295,2
Total Elongation (2 inch)	%	47,5	47,2	47,5
Niobium Precipitation Strength Summary				
Niobium Yield Strength Component	MPa	0,0	0,0	0,0
Niobium Yield Strength Maximum	MPa	0,0	0,0	0,0
Niobium Tensile Strength Component	MPa	0,0	0,0	0,0
Niobium Tensile Strength Maximum	MPa	0,0	0,0	0,0
Niobium Aging Characteristics		N/A	N/A	N/A
Vanadium Precipitation Strength Summary				
Vanadium Yield Strength Component	MPa	0,0	0,0	0,0
Vanadium Yield Strength Maximum	MPa	0,0	0,0	0,0
Vanadium Tensile Strength Component	MPa	0,0	0,0	0,0
Vanadium Tensile Strength Maximum	MPa	0,0	0,0	0,0
Vanadium Aging Characteristics		N/A	N/A	N/A
Transformation Summary				
Ferrite Start Temperature	°C	839,3	840,3	840,0
Pearlite Start Temperature	°C	714,1	714,1	713,9

Multiple Node Results	Units	Head	Mid	Tail
Final Mechanical Properties				
Ferrite Grain Size (Average)	µm	55,9	54,0	53,8
Fraction Ferrite (Average)	%	97,4	97,7	97,7
Fraction Pearlite (Average)	%	2,6	2,3	2,3
Fraction Bainite (Average)	%	0,0	0,0	0,0
Fraction Martensite (Average)	%	0,0	0,0	0,0
Total Yield Strength	MPa	168,5	169,1	169,2
Total Tensile Strength	MPa	296,3	295,5	295,4
Total Elongation (2 inch)	%	47,3	47,5	47,5
Niobium Precipitation Strength Summary				
Niobium Yield Strength Component	MPa	0,0	0,0	0,0
Niobium Yield Strength Maximum	MPa	0,0	0,0	0,0
Niobium Tensile Strength Component	MPa	0,0	0,0	0,0
Niobium Tensile Strength Maximum	MPa	0,0	0,0	0,0
Niobium Aging Characteristics		N/A	N/A	N/A
Vanadium Precipitation Strength Summary				
Vanadium Yield Strength Component	MPa	0,0	0,0	0,0
Vanadium Yield Strength Maximum	MPa	0,0	0,0	0,0
Vanadium Tensile Strength Component	MPa	0,0	0,0	0,0
Vanadium Tensile Strength Maximum	MPa	0,0	0,0	0,0
Vanadium Aging Characteristics		N/A	N/A	N/A
Transformation Summary				
Ferrite Start Temperature (Average)	°C	839,6	839,9	840,0
Pearlite Start Temperature (Average)	°C	713,8	713,9	713,9

Figure 1.5: Screenshot of the commercial program HSMM

In some cases of flat rolling, the deformation of the bloom at the edges may be neglected. However, for the shape rolling, the edge deformation usually represents a major part of the solution. In order to know the final shape of the bloom after shape rolling, the spread of the width has to be calculated as well. There are many formulas developed by the researchers to calculate the width spread. These formulas were created by using many experimental data. Depending on the configuration, one may work better than the other. The spread calculation formulas were given by [Beese, 1980], [El-Kalay and Sparling, 1968], [Helmi and Alexander, 1968], [McCrum 1956], [Wusatovski, 1955] and [Shibahara, 1981]. Wusatowski's spread calculation formula was used by the commercial program Wicon with some further adjustments. Some of the researchers who analyzed the hot rolling have also made their own simulators which are mostly based on FEM. There exist also some rare models developed to analyze rolling by using meshless methods in the solution procedure. These attempts are explained in the next subchapter.

1.4 Meshless numerical methods for thermo-mechanics

There is a growing interest in developing new numerical methods in order to calculate and analyze complex mechanical systems such as rolling. The class of the numerical methods that are rising in its importance in the last decades are the

meshless methods. The literature survey of shape rolling analysis with meshless methods is described below.

Various applications of meshless methods on solid mechanics can be found in the books by [Atluri, Shen, 2002], [Li and Mulay, 2013], [Chen, Lee and Eskandarian, 2006] and [Li and Liu, 2004].

The Point Interpolation Method (PIM) was first proposed by [Liu and Gu, 2001] and later on used by [Hu, Yao and Hua, 2006]. Hu, Yao and Hua used PIM with the polynomial and radial basis functions (RBF) together and concluded that adding polynomial terms increases the stability. The results have been shown on the case of back extrusion process. The numerical applications of RBF interpolation are detailed in books by [Fasshauer, 2007], [Buhmann, 2003], [Chen, Fu and Chen, 2013] and [Wendland, 2010].

Smoothed Particle Hydrodynamics (SPH) is a meshfree solution procedure which was originally proposed by [Lucy, 1977] and applied to astrophysical problems. This method was first applied to solid mechanics by [Libersky and Petschek, 1991]. A further testing is done by [Batra and Zhang, 2007] for solid mechanics and also a comparison between strong and weak formulations has been made. Batra and Zhang have concluded that as the deformation increases the error of the strong formulation becomes larger than the error of the weak formulation. The stiffness matrix needed to solve the deformation problem is also clearly expressed here. A least squares meshfree method for rigid-plastic is also applied by [Kwon and Youn, 2006] using weak form, and an Element Free Galerkin Method (EFGM) for elasto-plastic deformation problems is applied by [Ullah and Augarde, 2013].

Oñate, Idelsohn, Zienkiewicz and Taylor first proposed and applied Finite Point Method (FPM) in computational mechanics [Oñate, Idelsohn, Zienkiewicz and Taylor, 1996]. Pozo, Perrazzo and Angulo have also used FPM to solve the nonlinear material behavior in the deformation theory [Pozo, Perrazzo and Angulo, 2009]. They have expressed their own effective Young's modulus to approximate the nonlinear plastic behavior. There are also many more meshless methods that can be applied as well, such as Meshless Local Petrov-Galerkin (MLPG) and Element Free Galerkin method (EFG).

Eventhough some meshless methods have been used to analyze the rolling process, the main approach to the solution in these cases are usually based on (weak formulation along with the integration polygons of the elements) as PIM used by [Hu, Yao and Hua, 2007] and EFG is applied by [Xiong, Rodrigues and Martins, 2004] and by [Gan, Zhao, Wu and Lu, 2007]. However, the meshless methods have been widely increasing its range of application. These lead many people to try different formulation of meshless methods in order to solve partial differential equations (PDEs) arising from the physical applications. Although

FEM is a very widely known procedure, it might run into difficulties on metal deformation analysis due to generation of meshes on complex geometries and the distortion of those generated meshes during deformation. This might substantially alter the accuracy and reliability of the simulation. Because of the truly meshless character, the local radial basis function collocation method (LRBFCM) offers a good alternative to FEM in simulations of large deformations. LRBFCM has been recently used in highly sophisticated simulations like multi-scale solidification modelling [Šarler, Kosec, Lorbiecka and Vertnik, 2010], convection driven melting of anisotropic metals [Kosec and Šarler, 2009], macrosegregation [Kosec and Šarler, 2014], continuous casting of steel [Vertnik and Šarler, 2009], [Vertnik and Šarler, 2014] and laminar flow under magnetic field [Mramor, Vertnik and Šarler, 2014]. Therefore LRBFCM is developed and shown in this dissertation to be capable of solving thermo-mechanical model of hot shape rolling without the need of any kind of meshing.

1.5 Objectives

The main aim of this dissertation is to develop LRBFCM for large deformation problems and to solve the hot shape rolling process by using this meshless numerical method. It is important to mention that the solution embraces coupled results from the thermal and the mechanical models which are strongly coupled.
The purpose of related simulations is for pre-testing different roll pass designs as well as the rolling stands with different grove geometries as a function of the material and shape of the strand rolled. Eventhough forward and backward slip based on friction are very important aspects of shape rolling, only sticking boundary condition is considered between steel and roll. The first aim of this research is to achieve numerical stability and to demonstrate successful results by LRBFCM for large deformation problems. Coupling of the mechanical and thermal models are achieved through temperature depended elastic material properties of steel. However, a realistic yiled function based on strain, strain rate and temperature will be included in the continuation of this work.The results on macro scale will be coupled with the microstructure models in order to have a complete micro-macro analysis of the deformation.

2 Governing Equations

In Chapter 2 first the mechanical and then the thermal models, employed in the dissertation, are explained in details. In the first part, theory of deformation and its applications to different material types is elaborated. The discussion considers three material types; elastic, ideal plastic and slightly compressible ideal plastic. In the second part, equations used in the thermal model are explained. They involve steady conductive-convective heat transport and transient conductive heat transport. The coupling of the mechanical and the thermal models is discussed at the end of this chapter.

2.1 Deformation theory

A solid material, such as steel at rest, resists the forces acting on it up to a certain limit. If these forces are over certain value, the material starts to change its shape. The surface that faces the pressure, moves in a positive way with respect to the direction of the force. This process of changing shape of a material is called and analysed in physics as a deformation problem.
The magnitude of the deformation in the material science is measured with strains. Strain is the ratio between the change of the length and the initial length across an axis due to deformation.
When a material is compressed in one direction, just like in flat rolling, this effect will be seen in other directions as an elongation and creates strains as well. The ratio, that relates those strain values to specific material, is the Poisson's ratio ν for a specific material and

$$\nu = -\frac{\varepsilon_t}{\varepsilon_a}, \tag{2.1}$$

where ε_t is the transversal strain and ε_a is the axial strain. The negative sign in Equation (2.1) shows that the material elongates in one direction (axial direction) with a positive axial strain, in the other two directions the material shrinks; therefore it gets a negative transversal strain as shown in Figure 2.1. A

typical value of Poisson's ratio used in simulations for a hot rolled steel is 0.49 [Glowacki, 2005].

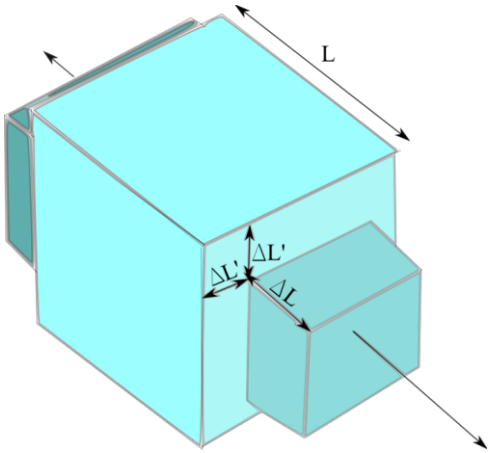

Figure 2.1: Definition of the Poisson's ratio for an isotropic cubic material with side L when one side is elongated for ΔL and due to this effect the other two sides are shrunk by $\Delta L'$. The strains are $\varepsilon_a = \Delta L / L$ and $\varepsilon_t = \Delta L' / L$.

The ultimate stress point is the highest stress value during the uniaxial tension test that material achieves, because beyond this point less stress is necessary to cause more strain due to reduction in cross sectional area which appears as necking. Between necking and yielding, stress still increases as the strain increases as in Figure 2.6.
Brittle materials such as glass do not have any yield stress, strain hardening and plastic region. The fracture occurs in the elastic region and the stress strain graph has a very steep linear shape as seen in Figure 2.2.

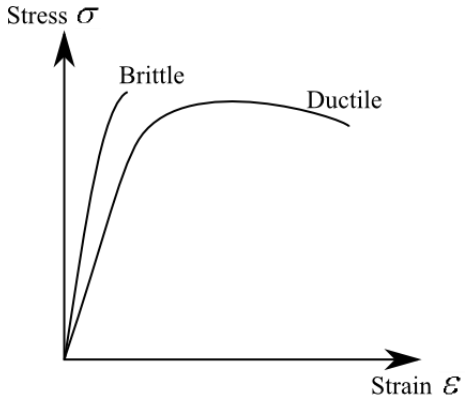

Figure 2.2: Stress-strain graphs of brittle and ductile materials.

The forces acting on material's surface to deform the sample also create shear forces or stresses that act tangential or parallel to the surface. Shearing can be imagined as sliding of an imaginary internal plane relative to its original position. The forces acting perpendicular to the surface are called the normal forces.
The relationship between the shear stress τ and the shear strain γ is described as

$$G = \frac{\tau}{\gamma}, \tag{2.2}$$

where G is the shear modulus.
When analyzing the deformation of a realistic, three dimensional object, the stresses σ_{ij} are used in calculations. In a Cartesian coordinate system, where the axes x, y, z are used, the components of a stress tensor can be seen in Figure 2.3. The stresses σ_{xx}, σ_{yy}, σ_{zz} are in the direction of axes x, y, z respectively. The other stress components, σ_{ij} where $i \neq j$ are in the direction perpendicular to the axes and represent shearing.

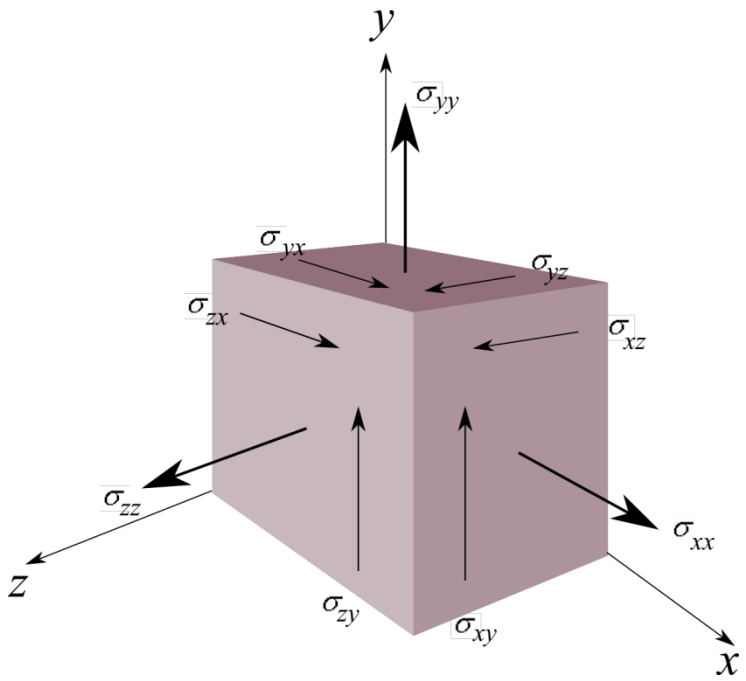

Figure 2.3: Normal and shear stresses are shown on a cube.

Stress tensor $\mathbf{T}$ can be written in a matrix form as

$$\mathbf{T} = \begin{bmatrix} \sigma_{xx} & \sigma_{xy} & \sigma_{xz} \\ \sigma_{yx} & \sigma_{yy} & \sigma_{yz} \\ \sigma_{zx} & \sigma_{zy} & \sigma_{zz} \end{bmatrix}. \tag{2.3}$$

The same stress tensor can, by rotational transformation, be written in terms of principle stresses σ_i, which are chosen in such a way that no shearing occurs. After the rotation, the new axes obtained, are called principle directions and

$$\mathbf{T} = \begin{bmatrix} \sigma_x & 0 & 0 \\ 0 & \sigma_y & 0 \\ 0 & 0 & \sigma_z \end{bmatrix}. \tag{2.4}$$

Hydrostatic stress σ_m is defined in terms of principle stresses as

$$\sigma_m = \frac{\sigma_x + \sigma_y + \sigma_z}{3}. \tag{2.5}$$

Hydrostatic stress tensor is

$$\sigma_m \boldsymbol{\delta} = \begin{bmatrix} \sigma_m & 0 & 0 \\ 0 & \sigma_m & 0 \\ 0 & 0 & \sigma_m \end{bmatrix}, \tag{2.6}$$

where $\boldsymbol{\delta}$ is 3x3 identity matrix

$$\boldsymbol{\delta} = \begin{bmatrix} 1 & 0 & 0 \\ 0 & 1 & 0 \\ 0 & 0 & 1 \end{bmatrix}. \tag{2.7}$$

Stress deviator tensor $\mathbf{s}$ is defined as

$$\mathbf{s} = \begin{bmatrix} \sigma_{xx} - \sigma_m & \sigma_{xy} & \sigma_{xz} \\ \sigma_{yx} & \sigma_{xx} - \sigma_m & \sigma_{yz} \\ \sigma_{zx} & \sigma_{zy} & \sigma_{zz} - \sigma_m \end{bmatrix} = \begin{bmatrix} s_{xx} & s_{xy} & s_{xz} \\ s_{yx} & s_{yy} & s_{yz} \\ s_{zx} & s_{zy} & s_{zz} \end{bmatrix}, \tag{2.8}$$

or in component from, s_{ij} is equals to

$$s_{ij} = \sigma_{ij} - \sigma_m \delta_{ij} . \tag{2.9}$$

In the deformation theory, Cauchy's stress formulation is one of the fundamental theorems, which states that the forces acting at a point over the surface of a material can be defined through a stress vector

$$\mathbf{t} = \mathbf{T} \cdot \mathbf{n} , \tag{2.10}$$

where $\mathbf{t}$ is the stress vector which has three components in 3D coordinate system, $\mathbf{T}$ is the stress tensor and $\mathbf{n}$ is the unit normal vector. The stress vector on an arbitrary plane defined by its unit normal $\mathbf{n}$ can be calculated in terms of components of stress and unit normal as

$$t_i = \sigma_{ij} n_j . \tag{2.11}$$

Cauchy's theorem in (2.10) can now be written in a form of the following three equations

$$\begin{aligned} \sigma_{xx} n_x + \sigma_{xy} n_y + \sigma_{xz} n_z &= \sigma n_x , \\ \sigma_{yx} n_x + \sigma_{yy} n_y + \sigma_{yz} n_z &= \sigma n_y , \\ \sigma_{zx} n_x + \sigma_{zy} n_y + \sigma_{zz} n_z &= \sigma n_z , \end{aligned} \tag{2.12}$$

where σ is a magnitude of stress in direction of unit normal vector $\mathbf{n}$.

A trivial solution can be determined if the following condition is met,

$$\begin{vmatrix} \sigma_{xx} - \sigma & \sigma_{xy} & \sigma_{xz} \\ \sigma_{yx} & \sigma_{yy} - \sigma & \sigma_{yz} \\ \sigma_{zx} & \sigma_{zy} & \sigma_{zz} - \sigma \end{vmatrix} = 0 . \tag{2.13}$$

From this condition we get the following characteristic equation to solve,

$$\sigma^3 - I_1 \sigma^2 + I_2 \sigma - I_3 = 0 , \tag{2.14}$$

where I_1, I_2 and I_3 are the invariants of the stress tensor. They are defined as

$$\begin{aligned} I_1 &= \sigma_{xx} + \sigma_{yy} + \sigma_{zz} , \\ I_2 &= \sigma_{xx}\sigma_{yy} + \sigma_{yy}\sigma_{zz} + \sigma_{xx}\sigma_{zz} - \sigma_{xy}^2 - \sigma_{yz}^2 - \sigma_{xz}^2 , \\ I_3 &= \sigma_{xx}\sigma_{yy}\sigma_{zz} + 2\sigma_{xy}\sigma_{yz}\sigma_{zx} - \sigma_{xy}^2\sigma_{zz} - \sigma_{yz}^2\sigma_{xx} - \sigma_{xz}^2\sigma_{yy} . \end{aligned} \tag{2.15}$$

Similarly, for the stress deviator tensor $\mathbf{s}$, its invariants (J_i) can be defined as

$$\begin{aligned} J_1 &= s_{xx} + s_{yy} + s_{zz} = 0, \\ J_2 &= \frac{1}{6}\left[\left(\sigma_{xx} - \sigma_{yy}\right)^2 + \left(\sigma_{yy} - \sigma_{zz}\right)^2 + \left(\sigma_{zz} - \sigma_{xx}\right)^2 \right] + \sigma_{xy}^2 + \sigma_{yz}^2 + \sigma_{zx}^2, \\ J_3 &= \det\left(\mathbf{s}\right) = \frac{2}{27} I_1^3 - \frac{1}{3} I_1 I_2 + I_3 \ . \end{aligned} \tag{2.16}$$

The advantage of using stress deviator tensor can be directly seen, since its first invariant always gets a zero value.
In case of a unit normal, which makes equal angles with all three axes in a Cartesian coordinate system, written as $\mathbf{n} = \left(1/\sqrt{3}\right)\mathbf{i}_x + \left(1/\sqrt{3}\right)\mathbf{i}_y + \left(1/\sqrt{3}\right)\mathbf{i}_z$ where $\mathbf{i}_x, \mathbf{i}_y, \mathbf{i}_z$ are the base vectors and *x, y, z* are the coordinates, the plane that this unit normal is perpendicular to, creates an octahedral plane shown in Figure 2.11. The normal stress on the face of this octahedral plane is called octahedral stress, and defined as

$$\tau_{oct} = \sqrt{\frac{2}{3} J_2} \ . \tag{2.17}$$

2.2 Mechanical model

This sub-chapter discusses the formulation of the mechanical model within strong formulation. The model with its boundary conditions is explained for elastic materials, ideal plastic materials and ideal slightly compressible plastic materials.

2.2.1 Formulation of mechanical model

The mechanical model used in rolling is based on the deformation theory. There are two types of formulation; weak and strong. A comparison of these two formulations is made by [Liu, 2003] in the context of meshless methods. In the weak form the governing equation is written in terms of volume or area integrals, however in strong form the governing equation is defined by forces per unit volume and does not include any integration. A strong form is chosen in present analysis due to its compatibility with strong form heat and fluid flow simulations with meshless methods, previously developed in our group. The background theory of the mechanical equations used in this subchapter can be

found in [Lai, Krempl and Ruben, 2010], [Fung and Tong, 2001] and [Kleiber, 1998].

The static deformation problems is defined as

$$\mathbf{L}^T\boldsymbol{\sigma}+\mathbf{d}=\mathbf{0}, \tag{2.18}$$

where $\mathbf{L}$ is a derivative operator and represented by a 3×6 matrix as,

$$\mathbf{L}=\begin{bmatrix} \frac{\partial}{\partial p_x} & 0 & 0 & 0 & \frac{\partial}{\partial p_z} & \frac{\partial}{\partial p_y} \\ 0 & \frac{\partial}{\partial p_y} & 0 & \frac{\partial}{\partial p_z} & 0 & \frac{\partial}{\partial p_x} \\ 0 & 0 & \frac{\partial}{\partial p_z} & \frac{\partial}{\partial p_y} & \frac{\partial}{\partial p_x} & 0 \end{bmatrix}^{\mathrm{T}}, \tag{2.19}$$

where the position vector is defined as $\mathbf{p}=p_x\mathbf{i}_x+p_y\mathbf{i}_y+p_y\mathbf{i}_y$ and T denotes the transpose of a matrix.

The stress vector $\boldsymbol{\sigma}$ is described in terms of its six components in a Cartesian coordinate system with axes x, y, z as

$$\boldsymbol{\sigma}=\begin{bmatrix}\sigma_{xx} & \sigma_{yy} & \sigma_{zz} & \sigma_{yz} & \sigma_{xz} & \sigma_{xy}\end{bmatrix}^{\mathrm{T}}. \tag{2.20}$$

The last term in Equation (2.18) is the body force vector $\mathbf{d}$. It is the contribution of body forces due to weight of the material during the deformation. In 3 dimensional Cartesian coordinates it has the following components,

$$\mathbf{d}=\begin{bmatrix} d_x \\ d_y \\ d_z \end{bmatrix}. \tag{2.21}$$

The strong formulation of deformation constitutes three individual balance equations in each three principle directions which are in the discussed 3D coordinate system

$$\frac{\partial\sigma_{xx}}{\partial p_x}+\frac{\partial\sigma_{xy}}{\partial p_y}+\frac{\partial\sigma_{xz}}{\partial p_z}+d_x=0, \tag{2.22}$$

$$\frac{\partial \sigma_{xy}}{\partial p_x} + \frac{\partial \sigma_{yy}}{\partial p_y} + \frac{\partial \sigma_{yz}}{\partial p_z} + d_y = 0\,, \tag{2.23}$$

$$\frac{\partial \sigma_{xz}}{\partial p_x} + \frac{\partial \sigma_{yz}}{\partial p_y} + \frac{\partial \sigma_{zz}}{\partial p_z} + d_z = 0\,. \tag{2.24}$$

The components of the stress vector can be related to the components of the strain vector with 6×6 stiffness matrix $\mathbf{C}$. The corresponding values depend on the material behaviour and will be given later for considered three types of materials.

$$\boldsymbol{\sigma} = \mathbf{C}\boldsymbol{\varepsilon}\,, \tag{2.25}$$

where the strain vector is

$$\boldsymbol{\varepsilon} = \left[\varepsilon_{xx} \;\; \varepsilon_{yy} \;\; \varepsilon_{zz} \;\; \varepsilon_{yz} \;\; \varepsilon_{xz} \;\; \varepsilon_{xy} \right]^{\mathrm{T}}. \tag{2.26}$$

The strain vector can be related to the displacement vector $\mathbf{u} = \left[u_x \;\; u_y \;\; u_z \right]^{\mathrm{T}}$

$$\boldsymbol{\varepsilon} = \mathbf{L}\mathbf{u}\,. \tag{2.27}$$

The volumetric strain ε_v in Cartesian coordinate system is

$$\varepsilon_v = \varepsilon_{xx} + \varepsilon_{yy} + \varepsilon_{yy}\,. \tag{2.28}$$

The displacement vector between two positions can be seen in Figure 2.4.

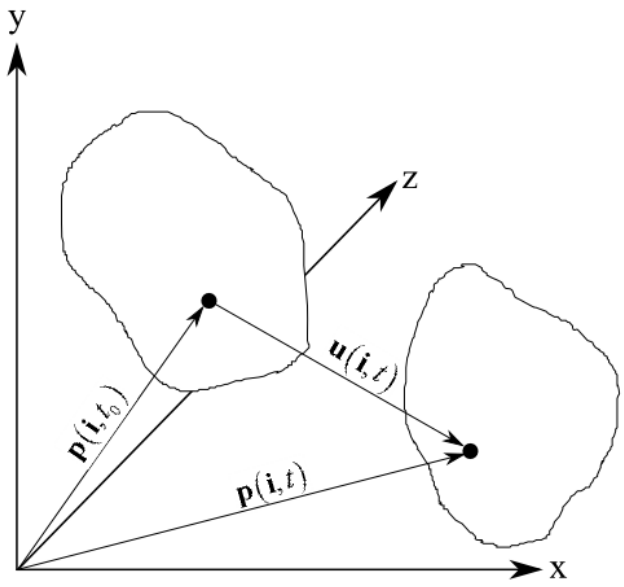

Figure 2.4: Displacement and position vectors are shown for a corresponding time t.

Hence the governing equation can be written in terms of displacement as

$$\mathbf{L}^{\mathrm{T}}\mathbf{CLu} + \mathbf{d} = \mathbf{0}. \tag{2.29}$$

Same equation can also be written more explicitly

$$
\begin{aligned}
&\frac{\partial}{\partial x}\left[C_{11}\frac{\partial u_x}{\partial p_x}\right]+\frac{\partial}{\partial x}\left[C_{12}\frac{\partial u_y}{\partial p_y}\right]+\frac{\partial}{\partial x}\left[C_{13}\frac{\partial u_z}{\partial p_z}\right]+\frac{\partial}{\partial x}\left[C_{14}\left(\frac{\partial u_y}{\partial p_z}+\frac{\partial u_z}{\partial p_y}\right)\right]\\
&+\frac{\partial}{\partial x}\left[C_{15}\left(\frac{\partial u_x}{\partial p_z}+\frac{\partial u_z}{\partial p_x}\right)\right]+\frac{\partial}{\partial x}\left[C_{16}\left(\frac{\partial u_x}{\partial p_y}+\frac{\partial u_y}{\partial p_x}\right)\right]\\
&+\frac{\partial}{\partial y}\left[C_{61}\frac{\partial u_x}{\partial p_x}\right]+\frac{\partial}{\partial y}\left[C_{62}\frac{\partial u_y}{\partial p_y}\right]+\frac{\partial}{\partial y}\left[C_{63}\frac{\partial u_z}{\partial p_z}\right]+\frac{\partial}{\partial y}\left[C_{64}\left(\frac{\partial u_y}{\partial p_z}+\frac{\partial u_z}{\partial p_y}\right)\right]\\
&+\frac{\partial}{\partial y}\left[C_{65}\left(\frac{\partial u_x}{\partial p_z}+\frac{\partial u_z}{\partial p_x}\right)\right]+\frac{\partial}{\partial y}\left[C_{66}\left(\frac{\partial u_x}{\partial p_y}+\frac{\partial u_y}{\partial p_x}\right)\right]\\
&+\frac{\partial}{\partial z}\left[C_{51}\frac{\partial u_x}{\partial p_x}\right]+\frac{\partial}{\partial z}\left[C_{52}\frac{\partial u_y}{\partial p_y}\right]+\frac{\partial}{\partial z}\left[C_{53}\frac{\partial u_z}{\partial p_z}\right]+\frac{\partial}{\partial z}\left[C_{54}\left(\frac{\partial u_y}{\partial p_z}+\frac{\partial u_z}{\partial p_y}\right)\right]\\
&+\frac{\partial}{\partial z}\left[C_{55}\left(\frac{\partial u_x}{\partial p_z}+\frac{\partial u_z}{\partial p_x}\right)\right]+\frac{\partial}{\partial z}\left[C_{56}\left(\frac{\partial u_x}{\partial p_y}+\frac{\partial u_y}{\partial p_x}\right)\right]+d_x=0,
\end{aligned}
\tag{2.30}
$$

$$
\begin{aligned}
&\frac{\partial}{\partial x}\left[C_{61}\frac{\partial u_x}{\partial p_x}\right]+\frac{\partial}{\partial x}\left[C_{62}\frac{\partial u_y}{\partial p_y}\right]+\frac{\partial}{\partial x}\left[C_{63}\frac{\partial u_z}{\partial p_z}\right]+\frac{\partial}{\partial x}\left[C_{64}\left(\frac{\partial u_y}{\partial p_z}+\frac{\partial u_z}{\partial p_y}\right)\right]\\
&+\frac{\partial}{\partial x}\left[C_{65}\left(\frac{\partial u_x}{\partial p_z}+\frac{\partial u_z}{\partial p_x}\right)\right]+\frac{\partial}{\partial x}\left[C_{66}\left(\frac{\partial u_x}{\partial p_y}+\frac{\partial u_y}{\partial p_x}\right)\right]\\
&+\frac{\partial}{\partial y}\left[C_{21}\frac{\partial u_x}{\partial p_x}\right]+\frac{\partial}{\partial y}\left[C_{22}\frac{\partial u_y}{\partial p_y}\right]+\frac{\partial}{\partial y}\left[C_{23}\frac{\partial u_z}{\partial p_z}\right]+\frac{\partial}{\partial y}\left[C_{24}\left(\frac{\partial u_y}{\partial p_z}+\frac{\partial u_z}{\partial p_y}\right)\right]\\
&+\frac{\partial}{\partial y}\left[C_{25}\left(\frac{\partial u_x}{\partial p_z}+\frac{\partial u_z}{\partial p_x}\right)\right]+\frac{\partial}{\partial y}\left[C_{26}\left(\frac{\partial u_x}{\partial p_y}+\frac{\partial u_y}{\partial p_x}\right)\right]\\
&+\frac{\partial}{\partial z}\left[C_{41}\frac{\partial u_x}{\partial p_x}\right]+\frac{\partial}{\partial z}\left[C_{42}\frac{\partial u_y}{\partial p_y}\right]+\frac{\partial}{\partial z}\left[C_{43}\frac{\partial u_z}{\partial p_z}\right]+\frac{\partial}{\partial z}\left[C_{44}\left(\frac{\partial u_y}{\partial p_z}+\frac{\partial u_z}{\partial p_y}\right)\right]\\
&+\frac{\partial}{\partial z}\left[C_{45}\left(\frac{\partial u_x}{\partial p_z}+\frac{\partial u_z}{\partial p_x}\right)\right]+\frac{\partial}{\partial z}\left[C_{46}\left(\frac{\partial u_x}{\partial p_y}+\frac{\partial u_y}{\partial p_x}\right)\right]+d_y=0,
\end{aligned}
\tag{2.31}
$$

$$\begin{aligned}
&\frac{\partial}{\partial x}\left[C_{51}\frac{\partial u_x}{\partial p_x}\right]+\frac{\partial}{\partial x}\left[C_{52}\frac{\partial u_y}{\partial p_y}\right]+\frac{\partial}{\partial x}\left[C_{53}\frac{\partial u_z}{\partial p_z}\right]+\frac{\partial}{\partial x}\left[C_{54}\left(\frac{\partial u_y}{\partial p_z}+\frac{\partial u_z}{\partial p_y}\right)\right]\\
&+\frac{\partial}{\partial x}\left[C_{55}\left(\frac{\partial u_x}{\partial p_z}+\frac{\partial u_z}{\partial p_x}\right)\right]+\frac{\partial}{\partial x}\left[C_{56}\left(\frac{\partial u_x}{\partial p_y}+\frac{\partial u_y}{\partial p_x}\right)\right]\\
&+\frac{\partial}{\partial y}\left[C_{41}\frac{\partial u_x}{\partial p_x}\right]+\frac{\partial}{\partial y}\left[C_{42}\frac{\partial u_y}{\partial p_y}\right]+\frac{\partial}{\partial y}\left[C_{43}\frac{\partial u_z}{\partial p_z}\right]+\frac{\partial}{\partial y}\left[C_{44}\left(\frac{\partial u_y}{\partial p_z}+\frac{\partial u_z}{\partial p_y}\right)\right]\\
&+\frac{\partial}{\partial y}\left[C_{45}\left(\frac{\partial u_x}{\partial p_z}+\frac{\partial u_z}{\partial p_x}\right)\right]+\frac{\partial}{\partial y}\left[C_{46}\left(\frac{\partial u_x}{\partial p_y}+\frac{\partial u_y}{\partial p_x}\right)\right]\\
&+\frac{\partial}{\partial z}\left[C_{31}\frac{\partial u_x}{\partial p_x}\right]+\frac{\partial}{\partial z}\left[C_{32}\frac{\partial u_y}{\partial p_y}\right]+\frac{\partial}{\partial z}\left[C_{33}\frac{\partial u_z}{\partial p_z}\right]+\frac{\partial}{\partial z}\left[C_{34}\left(\frac{\partial u_y}{\partial p_z}+\frac{\partial u_z}{\partial p_y}\right)\right]\\
&+\frac{\partial}{\partial z}\left[C_{35}\left(\frac{\partial u_x}{\partial p_z}+\frac{\partial u_z}{\partial p_x}\right)\right]+\frac{\partial}{\partial z}\left[C_{36}\left(\frac{\partial u_x}{\partial p_y}+\frac{\partial u_y}{\partial p_x}\right)\right]+d_z=0.
\end{aligned} \tag{2.32}$$

In a 2D system, the stress, strain and displacement vectors are reduced to

$$\boldsymbol{\sigma}=\begin{bmatrix}\sigma_{xx} & \sigma_{yy} & \sigma_{xy}\end{bmatrix}^{\mathrm{T}},\ \boldsymbol{\varepsilon}=\begin{bmatrix}\varepsilon_{xx} & \varepsilon_{yy} & \varepsilon_{xy}\end{bmatrix}^{\mathrm{T}},\ \mathbf{u}=\begin{bmatrix}u_x & u_y\end{bmatrix}^{\mathrm{T}}. \tag{2.33}$$

Therefore the governing equation (2.29) becomes

$$\frac{\partial\sigma_{xx}}{\partial p_x}+\frac{\partial\sigma_{xy}}{\partial p_y}+d_x=0, \tag{2.34}$$

$$\frac{\partial\sigma_{xy}}{\partial p_x}+\frac{\partial\sigma_{yy}}{\partial p_y}+d_y=0. \tag{2.35}$$

In terms of displacement

$$\begin{aligned}
&\frac{\partial}{\partial x}\left[C_{11}\frac{\partial u_x}{\partial p_x}\right]+\frac{\partial}{\partial x}\left[C_{12}\frac{\partial u_y}{\partial p_y}\right]+\frac{\partial}{\partial x}\left[C_{13}\left(\frac{\partial u_x}{\partial p_y}+\frac{\partial u_y}{\partial p_x}\right)\right]\\
&+\frac{\partial}{\partial y}\left[C_{31}\frac{\partial u_x}{\partial p_x}\right]+\frac{\partial}{\partial y}\left[C_{32}\frac{\partial u_y}{\partial p_y}\right]+\frac{\partial}{\partial y}\left[C_{33}\left(\frac{\partial u_x}{\partial p_y}+\frac{\partial u_y}{\partial p_x}\right)\right]+d_x=0,
\end{aligned} \tag{2.36}$$

$$\begin{aligned}&\frac{\partial}{\partial x}\left[C_{31}\frac{\partial u_x}{\partial p_x}\right]+\frac{\partial}{\partial x}\left[C_{32}\frac{\partial u_y}{\partial p_y}\right]+\frac{\partial}{\partial x}\left[C_{33}\left(\frac{\partial u_x}{\partial p_y}+\frac{\partial u_y}{\partial p_x}\right)\right]\\&+\frac{\partial}{\partial y}\left[C_{21}\frac{\partial u_x}{\partial p_x}\right]+\frac{\partial}{\partial y}\left[C_{22}\frac{\partial u_y}{\partial p_y}\right]+\frac{\partial}{\partial y}\left[C_{23}\left(\frac{\partial u_x}{\partial p_y}+\frac{\partial u_y}{\partial p_x}\right)\right]+d_y=0.\end{aligned} \tag{2.37}$$

It is important to note that in 2D the stiffness matrix is reduced to 3×3.

2.2.2 Boundary conditions

Consider a domain Ω with boundary Γ, where the boundary consists of two types of boundary conditions: the natural (displacement) Γ^u or Dirichlet and essential (traction) Γ^τ or Neumann boundaries $\Gamma=\Gamma^u\cup\Gamma^\tau$. In the natural boundary condition a prescribed displacement $\bar{u}$ is known and in the essential boundary condition the prescribed traction is known $\bar{\tau}$.

The main equation for natural boundary condition is written as

$$\mathbf{N}^{\mathrm{T}}\boldsymbol{\sigma}=\bar{\boldsymbol{\tau}}, \tag{2.38}$$

where in a 3D model, $\mathbf{N}$ becomes a 6×3 matrix consisting of unit normals coordinates

$$\mathbf{N}^{\mathrm{T}}=\begin{bmatrix}n_x & 0 & 0 & 0 & n_z & n_y\\ 0 & n_y & 0 & n_z & 0 & n_x\\ 0 & 0 & n_z & n_y & n_x & 0\end{bmatrix}. \tag{2.39}$$

Also $\bar{\boldsymbol{\tau}}$ represents the prescribed shear stress at the surface where stress is applied. The components in Cartesian coordinate system are shown below

$$\bar{\boldsymbol{\tau}}=\begin{bmatrix}\bar{\tau}_x\\ \bar{\tau}_y\\ \bar{\tau}_z\end{bmatrix}. \tag{2.40}$$

The set of equations for natural boundary condition becomes

$$n_x\sigma_{xx}+n_y\sigma_{xy}+n_z\sigma_{xz}=\bar{\tau}_x;\mathbf{p}\in\Gamma^{\tau x}, \tag{2.41}$$

$$n_x\sigma_{xy}+n_y\sigma_{yy}+n_z\sigma_{yz}=\bar{\tau}_y;\mathbf{p}\in\Gamma^{\tau y}, \tag{2.42}$$

$$n_x\sigma_{xz} + n_y\sigma_{yz} + n_z\sigma_{zz} = \bar{\tau}_z; \mathbf{p} \in \Gamma^{\tau z}. \tag{2.43}$$

Each row above is indicated with different boundary notation $\Gamma^{\tau x}$, $\Gamma^{\tau y}$ and $\Gamma^{\tau z}$ respectively where $\Gamma^{\tau} = \Gamma^{\tau x} \cup \Gamma^{\tau y} \cup \Gamma^{\tau z}$. In terms of displacement

$$\begin{aligned}
&n_x\left(\begin{array}{l} C_{11}\dfrac{\partial u_x}{\partial p_x} + C_{12}\dfrac{\partial u_y}{\partial p_y} + C_{13}\dfrac{\partial u_z}{\partial p_z} + C_{14}\left(\dfrac{\partial u_y}{\partial p_z} + \dfrac{\partial u_z}{\partial p_y}\right) \\ +C_{15}\left(\dfrac{\partial u_x}{\partial p_z} + \dfrac{\partial u_z}{\partial p_x}\right) + C_{16}\left(\dfrac{\partial u_x}{\partial p_y} + \dfrac{\partial u_y}{\partial p_x}\right) \end{array}\right) \\
&+n_y\left(\begin{array}{l} C_{61}\dfrac{\partial u_x}{\partial p_x} + C_{62}\dfrac{\partial u_y}{\partial p_y} + C_{63}\dfrac{\partial u_z}{\partial p_z} + C_{64}\left(\dfrac{\partial u_y}{\partial p_z} + \dfrac{\partial u_z}{\partial p_y}\right) \\ +C_{65}\left(\dfrac{\partial u_x}{\partial p_z} + \dfrac{\partial u_z}{\partial p_x}\right) + C_{66}\left(\dfrac{\partial u_x}{\partial p_y} + \dfrac{\partial u_y}{\partial p_x}\right) \end{array}\right) \\
&+n_z\left(\begin{array}{l} C_{51}\dfrac{\partial u_x}{\partial p_x} + C_{52}\dfrac{\partial u_y}{\partial p_y} + C_{52}\dfrac{\partial u_z}{\partial p_z} + C_{54}\left(\dfrac{\partial u_y}{\partial p_z} + \dfrac{\partial u_z}{\partial p_y}\right) \\ +C_{55}\left(\dfrac{\partial u_x}{\partial p_z} + \dfrac{\partial u_z}{\partial p_x}\right) + C_{56}\left(\dfrac{\partial u_x}{\partial p_y} + \dfrac{\partial u_y}{\partial p_x}\right) \end{array}\right) = \bar{\tau}_x,
\end{aligned} \tag{2.44}$$

$$
\begin{aligned}
&n_x\left(\begin{array}{l} C_{61}\dfrac{\partial u_x}{\partial p_x}+C_{62}\dfrac{\partial u_y}{\partial p_y}+C_{63}\dfrac{\partial u_z}{\partial p_z}+C_{64}\left(\dfrac{\partial u_y}{\partial p_z}+\dfrac{\partial u_z}{\partial p_y}\right) \\ +C_{65}\left(\dfrac{\partial u_x}{\partial p_z}+\dfrac{\partial u_z}{\partial p_x}\right)+C_{66}\left(\dfrac{\partial u_x}{\partial p_y}+\dfrac{\partial u_y}{\partial p_x}\right) \end{array}\right) \\
&+n_y\left(\begin{array}{l} C_{21}\dfrac{\partial u_x}{\partial p_x}+C_{22}\dfrac{\partial u_y}{\partial p_y}+C_{23}\dfrac{\partial u_z}{\partial p_z}+C_{24}\left(\dfrac{\partial u_y}{\partial p_z}+\dfrac{\partial u_z}{\partial p_y}\right) \\ +C_{25}\left(\dfrac{\partial u_x}{\partial p_z}+\dfrac{\partial u_z}{\partial p_x}\right)+C_{26}\left(\dfrac{\partial u_x}{\partial p_y}+\dfrac{\partial u_y}{\partial p_x}\right) \end{array}\right) \\
&+n_z\left(\begin{array}{l} C_{41}\dfrac{\partial u_x}{\partial p_x}+C_{42}\dfrac{\partial u_y}{\partial p_y}+C_{42}\dfrac{\partial u_z}{\partial p_z}+C_{44}\left(\dfrac{\partial u_y}{\partial p_z}+\dfrac{\partial u_z}{\partial p_y}\right) \\ +C_{45}\left(\dfrac{\partial u_x}{\partial p_z}+\dfrac{\partial u_z}{\partial p_x}\right)+C_{46}\left(\dfrac{\partial u_x}{\partial p_y}+\dfrac{\partial u_y}{\partial p_x}\right) \end{array}\right)=\overline{\tau}_y,
\end{aligned}
\tag{2.45}
$$

$$
\begin{aligned}
&n_x\left(\begin{array}{l} C_{51}\dfrac{\partial u_x}{\partial p_x}+C_{52}\dfrac{\partial u_y}{\partial p_y}+C_{53}\dfrac{\partial u_z}{\partial p_z}+C_{54}\left(\dfrac{\partial u_y}{\partial p_z}+\dfrac{\partial u_z}{\partial p_y}\right) \\ +C_{55}\left(\dfrac{\partial u_x}{\partial p_z}+\dfrac{\partial u_z}{\partial p_x}\right)+C_{56}\left(\dfrac{\partial u_x}{\partial p_y}+\dfrac{\partial u_y}{\partial p_x}\right) \end{array}\right) \\
&+n_y\left(\begin{array}{l} C_{41}\dfrac{\partial u_x}{\partial p_x}+C_{42}\dfrac{\partial u_y}{\partial p_y}+C_{43}\dfrac{\partial u_z}{\partial p_z}+C_{44}\left(\dfrac{\partial u_y}{\partial p_z}+\dfrac{\partial u_z}{\partial p_y}\right) \\ +C_{45}\left(\dfrac{\partial u_x}{\partial p_z}+\dfrac{\partial u_z}{\partial p_x}\right)+C_{46}\left(\dfrac{\partial u_x}{\partial p_y}+\dfrac{\partial u_y}{\partial p_x}\right) \end{array}\right) \\
&+n_z\left(\begin{array}{l} C_{31}\dfrac{\partial u_x}{\partial p_x}+C_{32}\dfrac{\partial u_y}{\partial p_y}+C_{33}\dfrac{\partial u_z}{\partial p_z}+C_{34}\left(\dfrac{\partial u_y}{\partial p_z}+\dfrac{\partial u_z}{\partial p_y}\right) \\ +C_{35}\left(\dfrac{\partial u_x}{\partial p_z}+\dfrac{\partial u_z}{\partial p_x}\right)+C_{36}\left(\dfrac{\partial u_x}{\partial p_y}+\dfrac{\partial u_y}{\partial p_x}\right) \end{array}\right)=\overline{\tau}_z.
\end{aligned}
\tag{2.46}
$$

In a 2D system the Equation (2.38) is reduced to

$$
n_x\sigma_x+n_y\sigma_{xy}=\overline{\tau}_x, \tag{2.47}
$$

$$n_y \sigma_y + n_x \sigma_{xy} = \bar{\tau}_y , \tag{2.48}$$

where $\Gamma^{\tau} = \Gamma^{\tau x} \cup \Gamma^{\tau y}$. The Equations (2.47) and (2.48) can be written in terms of displacement as

$$\begin{aligned} & n_x \left(C_{11} \frac{\partial u_x}{\partial p_x} + C_{12} \frac{\partial u_y}{\partial p_y} + C_{13} \left(\frac{\partial u_x}{\partial p_y} + \frac{\partial u_y}{\partial p_x} \right) \right) \\ & + n_y \left(C_{31} \frac{\partial u_x}{\partial p_x} + C_{32} \frac{\partial u_y}{\partial p_y} + C_{33} \left(\frac{\partial u_x}{\partial p_y} + \frac{\partial u_y}{\partial p_x} \right) \right) = \bar{\tau}_x , \end{aligned} \tag{2.49}$$

$$\begin{aligned} & n_y \left(C_{21} \frac{\partial u_x}{\partial p_x} + C_{22} \frac{\partial u_y}{\partial p_y} + C_{23} \left(\frac{\partial u_x}{\partial p_y} + \frac{\partial u_y}{\partial p_x} \right) \right) \\ & + n_x \left(C_{31} \frac{\partial u_x}{\partial p_x} + C_{32} \frac{\partial u_y}{\partial p_y} + C_{33} \left(\frac{\partial u_x}{\partial p_y} + \frac{\partial u_y}{\partial p_x} \right) \right) = \bar{\tau}_y . \end{aligned} \tag{2.50}$$

The equation used for the essential boundary condition is in terms of prescribed displacement $\bar{\mathbf{u}}$ on the boundary,

$$\mathbf{u} = \bar{\mathbf{u}} . \tag{2.51}$$

In component form

$$\begin{aligned} u_x &= \bar{u}_x ; \mathbf{p} \in \Gamma^{ux} , \\ u_y &= \bar{u}_y ; \mathbf{p} \in \Gamma^{uy} , \\ u_z &= \bar{u}_z ; \mathbf{p} \in \Gamma^{uz} , \end{aligned} \tag{2.52}$$

where each row has specific boundary indicator Γ^{ux}, Γ^{uy} and Γ^{uz} respectively where $\Gamma^{u} = \Gamma^{ux} \cup \Gamma^{uy} \cup \Gamma^{uz}$. In component form in 2D

$$\begin{bmatrix} u_x \\ u_y \end{bmatrix} = \begin{bmatrix} \bar{u}_x \\ \bar{u}_y \end{bmatrix} . \tag{2.53}$$

where u_i is the component of the displacement vector and $\bar{u}_i$ is the component of the prescribed displacement vector in $\Gamma^{u} = \Gamma^{ux} \cup \Gamma^{uy}$. This boundary

condition is applied when the displacement on the boundary is known or can be calculated. It is important to note that a boundary in one direction can have an essential boundary condition while in the other direction the natural boundary condition. The displacement vectors between different position vectors are drawn in Figure 2.5.

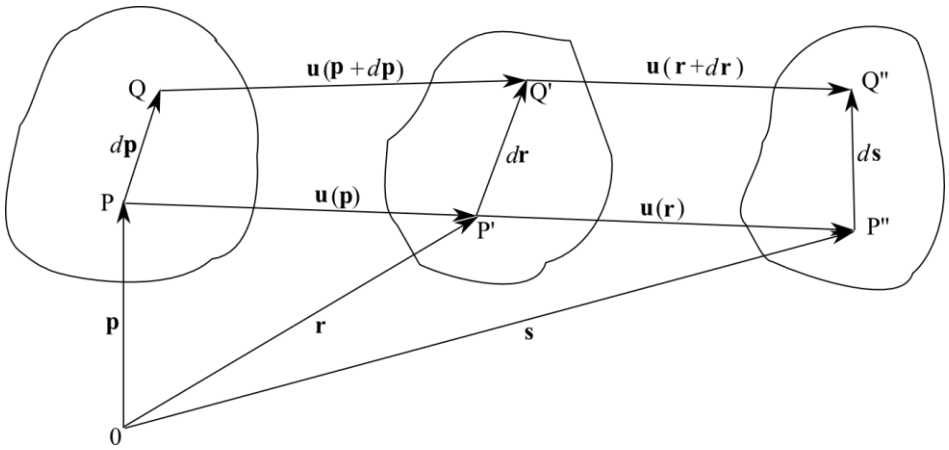

Figure 2.5: Evolution of displacement vector $\mathbf{u}$ between different position vectors $\mathbf{p}, \mathbf{r}, \mathbf{s}$ through the deformation.

2.2.3 Elastic deformation

The material behaviour is elastic up to the yield stress. Any deformation not exceeding the yield stress creates an elastic deformation. Under the elastic limit of deformation, the stress strain relation is approximately linear up to the point of proportional limit. When stresses up to the yield stress are applied and then they are released, the final strain becomes zero, which means the material goes back to its original shape. This is called elastic recovery. Up to the elastic limit the steel will not face any permanent deformation due to elastic recovery. However, elastic recovery can occur after higher amounts of stress exceeding yield stress as seen in Figure 2.6. The ratio of stress over strain up to the elastic limit is called Young's modulus or modulus of elasticity E.

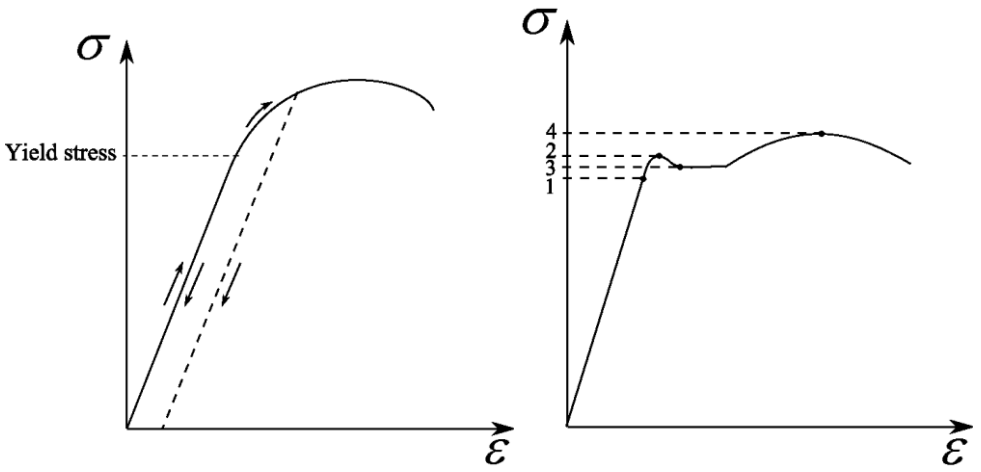

Figure 2.6: Scheme of uniaxial stress strain relations. Demonstration of elastic recovery (on left). Details of stress values of mild steel. 1- proportional limit, 2- elastic limit, 3- yield point, 4- ultimate stress (on right).

According to Hooke's law, the uniaxial stress strain relation can be expressed in the following way

$$\sigma = E\varepsilon \,. \tag{2.54}$$

In a 3D case, the stiffness matrix $\mathbf{C}^e$ relates the vector of stresses with the vector of strains. It is given by

$$\mathbf{C}^e = \frac{E}{(1+\nu)(1-2\nu)} \begin{bmatrix} (1-\nu) & \nu & \nu & 0 & 0 & 0 \\ \nu & (1-\nu) & \nu & 0 & 0 & 0 \\ \nu & \nu & (1-\nu) & 0 & 0 & 0 \\ 0 & 0 & 0 & \dfrac{(1-2\nu)}{2} & 0 & 0 \\ 0 & 0 & 0 & 0 & \dfrac{(1-2\nu)}{2} & 0 \\ 0 & 0 & 0 & 0 & 0 & \dfrac{(1-2\nu)}{2} \end{bmatrix}. \tag{2.55}$$

The matrix above requires the knowledge of Young's modulus E and Poisson's ratio ν.

2.2.3.1 Plane stress case

In continuum mechanics, a material is said to be under plane stress if the stress vector is zero across a particular surface. When that situation occurs over an entire element of a structure, as is often the case for thin plates, the stress analysis is considerably simplified, as the stress state can be represented by a tensor of dimension 2 (representable as a 2 × 2 matrix rather than 3 × 3). An example of an object obeying plane stress assumption is shown in Figure 2.7 below.

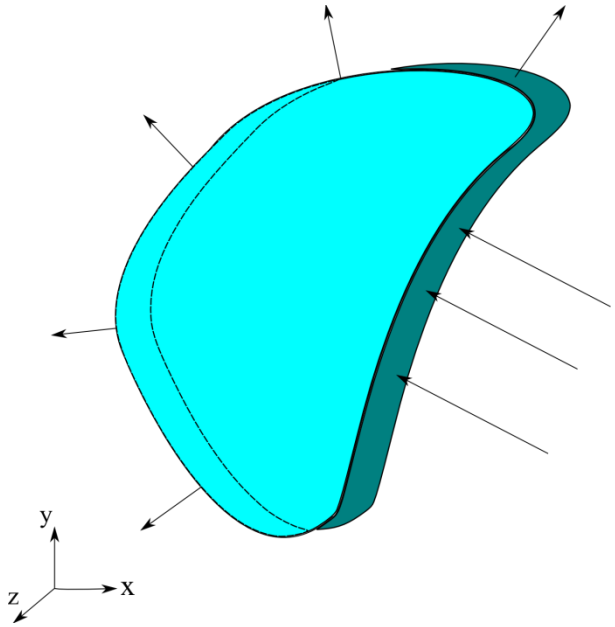

Figure 2.7: Scheme of plane stress situation. Demonstration of application when the force is being applied and material elongates.

Plane stress case is defined when $\sigma_{zz} = \sigma_{yz} = \sigma_{xz} = 0$ but $\varepsilon_{zz} \neq 0$.

The plane stress elastic stiffness matrix $\mathbf{C}^e$ is defined as

$$\mathbf{C}^e = \begin{bmatrix} \frac{E}{1-\nu^2} & \frac{E\nu}{1-\nu^2} & 0 \\ \frac{E\nu}{1-\nu^2} & \frac{E}{1-\nu^2} & 0 \\ 0 & 0 & \frac{E}{2(1+\nu)} \end{bmatrix}. \tag{2.56}$$

2.2.3.2 Plane strain case

In real engineering components, stresses and strains are 3D tensors but in prismatic structures such as long metal billet, the length of the structure is much larger than the other two dimensions. The strains associated with length, i.e. ε_{zz} and the shear strains ε_{zx} and ε_{zy} are determined by nearby material and are small compared to the cross-sectional strains. Plane strain then becomes an acceptable approximation, as shown in Figure 2.8.

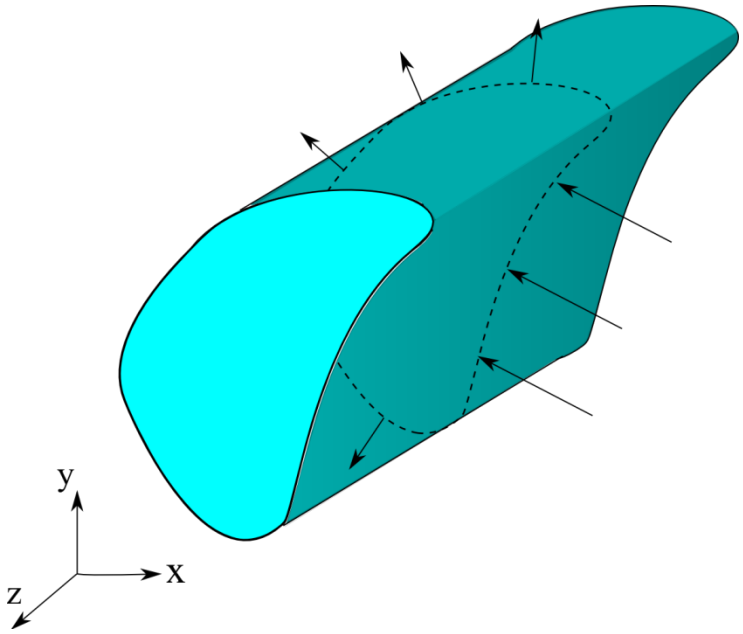

Figure 2.8: Scheme of a plane strain situation over a long body and when a 2D plane is chosen for a 3D approximation of the object.

The plane strain case is defined where $\varepsilon_{zz} = \varepsilon_{xz} = \varepsilon_{yz} = 0$ but $\sigma_{zz} \neq 0$. The strain components, related with the z direction are limited to 0 which means the material is bounded to have no deformation in the third direction. The plane strain elastic stiffness matrix is shown to be [Chen and Han, 1988]

$$\mathbf{C}^e = \begin{bmatrix} \frac{E(1-\nu)}{(1+\nu)(1-2\nu)} & \frac{E\nu}{(1+\nu)(1-2\nu)} & 0 \\ \frac{E\nu}{(1+\nu)(1-2\nu)} & \frac{E(1-\nu)}{(1+\nu)(1-2\nu)} & 0 \\ 0 & 0 & \frac{E}{2(1+\nu)} \end{bmatrix}. \tag{2.57}$$

This plane strain assumption is consistent with the homogeneous compression situation in rolling, when planes remain planes, as discussed in Chapter 3.

2.2.4 Plastic deformation

Plastic deformation, beyond the elastic region, observed beyond the yield stress in Figure 2.6. In the plastic region, the elastic recovery is not enough to change the material back to its original shape, so there is a residual strain after the applied stress is released. This permanent deformation is also called plastic strain or plastic deformation.

The yielding of a material is important in the present work, because it is also the point where the plastic deformation starts. Another important material characteristic is that the yield stress σ_p of a metal is sensitive to strain, strain rate and temperature. Some metals, such as carbon steel experience approximately constant stress after the yielding point [Chen and Han, 1988]. This region is called the plastic flow. This becomes quite useful for some material behaviour assumptions discussed further in this dissertation.

In isotropic hardening, the yield surface is assumed to expand uniformly with respect to the origin. In kinematic hardening however, the yielding surface is not deformed, but shifted as shown in Figure 2.9. The experiments show that there is anisotropy during plastic deformation [Chen and Han, 1988], called Bauschinger effect.

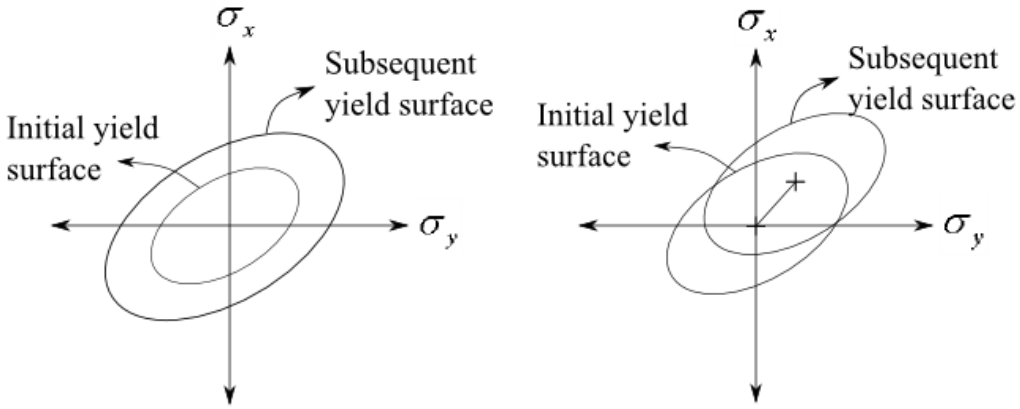

Figure 2.9: Isotropic hardening (on the left) and kinematic hardening (on the right) are shown in terms of change in yield surface.

2.2.4.1 Ideal plastic deformation

Ideal plastic deformation takes place when it is assumed that the stress is always at yield surface. In other words, there is no work hardening. In this case the elastic region is neglected, and hence no elastic recovery takes place. Such material can be referred as rigid plastic. As a result, the total strain is equal to the plastic strain.

There are different models to express the ideal plastic deformation, such as Tresca or von Mises. In this dissertation the assumptions from von Mises model are used. Von Mises defines the yield function of a material as

$$f(\mathbf{T},K)=\sqrt{J_2}-K=0 \text{ or } f(\mathbf{T},K)=J_2-K^2=0, \tag{2.58}$$

where K is maximum shear that a material can take and $f\left(\mathbf{T},K\right)$ is the yielding function. The yielding functions of von Mises assumption in 1D and 2D are drawn in figure 2.10 and for 3D in Figure 2.12. Equation (2.58) can be written in terms of principle stresses as

$$\left(\sigma_x-\sigma_y\right)^2+\left(\sigma_y-\sigma_z\right)^2+\left(\sigma_x-\sigma_z\right)^2=6K^2, \tag{2.59}$$

or in general

$$\left(\sigma_{xx}-\sigma_{yy}\right)^2+\left(\sigma_{yy}-\sigma_{zz}\right)^2+\left(\sigma_{zz}-\sigma_{xx}\right)^2+6\left(\sigma_{xy}^2+\sigma_{yz}^2+\sigma_{zx}^2\right)=6K^2. \tag{2.60}$$

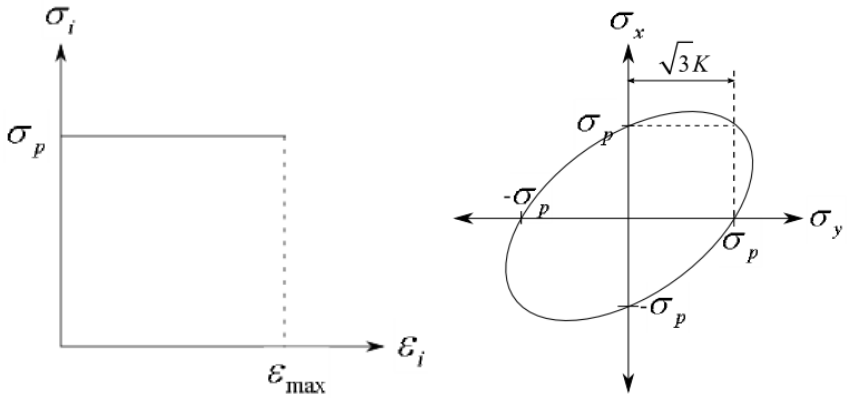

Figure 2.10: Stress-strain curve of an ideal plastic material under uniaxial stress (left). Dual axial stress (right).

In case when the stresses are applied in multiple directions, it is more complicated to determine exactly when the yielding starts. Von Mises stated that yielding starts when the octahedral shear τ_{oct} reaches a K value, where K means maximum shear stress, a material can take in pure shear [von Mises, 1913]. The octahedral shear stress is shown in Figure 2.11. From Equation (2.17) and Equation (2.22),

$$\tau_{oct} = \sqrt{\frac{2}{3} J_2} = \sqrt{\frac{2}{3}} K \,. \tag{2.61}$$

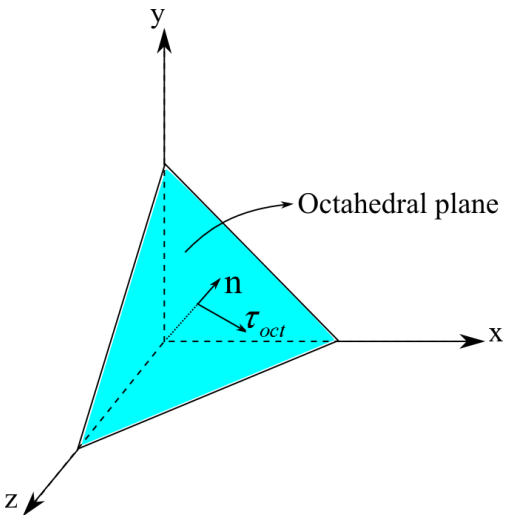

Figure 2.11: Scheme of shear stress τ_{oct} acting on octahedral plane with unit normal $\mathbf{n}$.

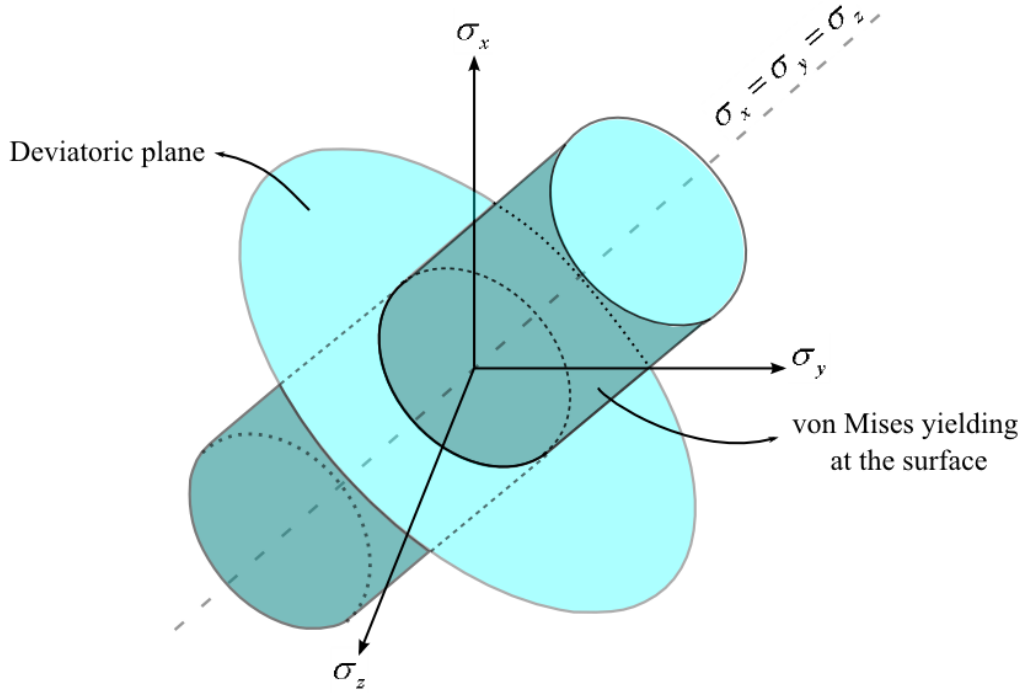

Figure 2.12: Cylinder surface showing the von Mises yielding criterion in terms of principle stresses and deviatoric plane where $\sigma_x + \sigma_y + \sigma_z = 0$.

The equation (2.58) also gives the relation for uniaxial case ($\sigma_y = \sigma_z = 0$) when yielding occurs,

$$\sigma_x = \sigma_p = \sqrt{3}K = \sqrt{3J_2}\,, \tag{2.62}$$

or in plane stress case when $(\sigma_z = 0)$,

$$\sigma_x^2 + \sigma_y^2 - \sigma_x\sigma_y = \sigma_p^2\,. \tag{2.63}$$

The effective stress $\bar{\sigma}$ can be defined from von Mises equation (2.57), where

$$\bar{\sigma} = \sigma_p = \sqrt{3J_2}\,. \tag{2.64}$$

Effective stress can be defined in terms of components of stress tensor [Zhou, Qin, Huang and Wang, 2004]. In terms of principle stresses,

$$\bar{\sigma} = \sqrt{\frac{1}{2}\left[\left(\sigma_x - \sigma_y\right)^2 + \left(\sigma_y - \sigma_z\right)^2 + \left(\sigma_x - \sigma_z\right)^2\right]}. \tag{2.65}$$

In general it can be written as

$$\bar{\sigma} = \sqrt{\frac{1}{2}\left[\left(\sigma_{xx} - \sigma_{yy}\right)^2 + \left(\sigma_{yy} - \sigma_{zz}\right)^2 + \left(\sigma_{zz} - \sigma_{xx}\right)^2 + 6\left(\sigma_{xy}^2 + \sigma_{yz}^2 + \sigma_{zx}^2\right)\right]}. \tag{2.66}$$

It can be also be written in terms of components of stress deviator tensor $\mathbf{s}$

$$\bar{\sigma} = \sqrt{\frac{3}{2} s_{ij} s_{ij}}\ . \tag{2.67}$$

Von Mises flow rule can be simply rewritten as a stress strain relationship

$$s_{ij} = \frac{2}{3}\frac{\bar{\sigma}}{\bar{\varepsilon}}\varepsilon_{ij}\,. \tag{2.68}$$

The relation can be explicitly written as

$$\varepsilon_{xx} = \frac{\bar{\varepsilon}}{\bar{\sigma}}\left[\sigma_{xx} - \frac{1}{2}\left(\sigma_{yy} + \sigma_{zz}\right)\right], \tag{2.69}$$

$$\varepsilon_{yy} = \frac{\bar{\varepsilon}}{\bar{\sigma}}\left[\sigma_{yy} - \frac{1}{2}\left(\sigma_{xx} + \sigma_{zz}\right)\right], \tag{2.70}$$

$$\varepsilon_{zz} = \frac{\bar{\varepsilon}}{\bar{\sigma}}\left[\sigma_{zz} - \frac{1}{2}\left(\sigma_{xx} + \sigma_{yy}\right)\right], \tag{2.71}$$

$$\varepsilon_{xy} = 3\frac{\bar{\varepsilon}}{\bar{\sigma}}\sigma_{xy}\,, \tag{2.72}$$

$$\varepsilon_{yz} = 3\frac{\bar{\varepsilon}}{\bar{\sigma}}\sigma_{yz}\,, \tag{2.73}$$

$$\varepsilon_{zx} = 3\frac{\bar{\varepsilon}}{\bar{\sigma}}\sigma_{zx}\,. \tag{2.74}$$

Where $\bar{\sigma}/\bar{\varepsilon}$ is referred as plastic modulus H_p. The effective strain $\bar{\varepsilon}$ can be defined as

$$\bar{\varepsilon} = \sqrt{\frac{2}{3} e_{ij} e_{ij}}\,, \tag{2.75}$$

where e is the deviatoric strain defined as $e_{ij} = \varepsilon_{ij} - \frac{1}{3}\varepsilon_v \delta_{ij}$. Therefore, effective strain

$$\bar{\varepsilon} = \sqrt{\frac{2}{9}\left[\left(\varepsilon_{xx}-\varepsilon_{yy}\right)^2 + \left(\varepsilon_{yy}-\varepsilon_{zz}\right)^2 + \left(\varepsilon_{zz}-\varepsilon_{xx}\right)^2 + 6\left(\varepsilon_{xy}^2 + \varepsilon_{yz}^2 + \varepsilon_{zx}^2\right)\right]}\,. \tag{2.76}$$

The stiffness matrix $\mathbf{C}^p$ in a 3D Cartesian coordinate system is defined for ideal plastic deformation as follows

$$\mathbf{C}^p = \frac{\bar{\sigma}}{\bar{\varepsilon}} \begin{bmatrix} \frac{2}{3} & 0 & 0 & 0 & 0 & 0 \\ 0 & \frac{2}{3} & 0 & 0 & 0 & 0 \\ 0 & 0 & \frac{2}{3} & 0 & 0 & 0 \\ 0 & 0 & 0 & \frac{1}{3} & 0 & 0 \\ 0 & 0 & 0 & 0 & \frac{1}{3} & 0 \\ 0 & 0 & 0 & 0 & 0 & \frac{1}{3} \end{bmatrix}. \tag{2.77}$$

The governing equations (2.30), (2.31) and (2.32) become

$$\begin{aligned} &\frac{2}{3}\left[\left(\frac{\partial\bar{\sigma}}{\partial p_x}\frac{1}{\bar{\varepsilon}} - \frac{\partial\bar{\varepsilon}}{\partial p_x}\frac{\bar{\sigma}}{\bar{\varepsilon}^2}\right)\frac{\partial u_x}{\partial p_x} + \frac{\partial^2 u_x}{\partial p_x^2}\frac{\bar{\sigma}}{\bar{\varepsilon}}\right] \\ &+\frac{1}{3}\left[\left(\frac{\partial\bar{\sigma}}{\partial p_y}\frac{1}{\bar{\varepsilon}} - \frac{\partial\bar{\varepsilon}}{\partial p_y}\frac{\bar{\sigma}}{\bar{\varepsilon}^2}\right)\left(\frac{\partial u_x}{\partial p_y} + \frac{\partial u_y}{\partial p_x}\right) + \left(\frac{\partial^2 u_x}{\partial p_y^2} + \frac{\partial^2 u_y}{\partial p_x \partial p_y}\right)\frac{\bar{\sigma}}{\bar{\varepsilon}}\right] \\ &+\frac{1}{3}\left[\left(\frac{\partial\bar{\sigma}}{\partial p_z}\frac{1}{\bar{\varepsilon}} - \frac{\partial\bar{\varepsilon}}{\partial p_z}\frac{\bar{\sigma}}{\bar{\varepsilon}^2}\right)\left(\frac{\partial u_x}{\partial p_z} + \frac{\partial u_z}{\partial p_x}\right) + \left(\frac{\partial^2 u_x}{\partial p_z^2} + \frac{\partial^2 u_z}{\partial p_x \partial p_z}\right)\frac{\bar{\sigma}}{\bar{\varepsilon}}\right] + b_x = 0, \end{aligned} \tag{2.78}$$

$$\begin{aligned}
&\frac{1}{3}\left[\left(\frac{\partial\bar{\sigma}}{\partial p_x}\frac{1}{\bar{\varepsilon}}-\frac{\partial\bar{\varepsilon}}{\partial p_x}\frac{\bar{\sigma}}{\bar{\varepsilon}^2}\right)\left(\frac{\partial u_x}{\partial p_y}+\frac{\partial u_y}{\partial p_x}\right)+\left(\frac{\partial^2 u_x}{\partial p_x\partial p_y}+\frac{\partial^2 u_y}{\partial p_x^2}\right)\frac{\bar{\sigma}}{\bar{\varepsilon}}\right]\\
&+\frac{2}{3}\left[\left(\frac{\partial\bar{\sigma}}{\partial p_y}\frac{1}{\bar{\varepsilon}}-\frac{\partial\bar{\varepsilon}}{\partial p_y}\frac{\bar{\sigma}}{\bar{\varepsilon}^2}\right)\frac{\partial u_y}{\partial p_y}+\frac{\partial^2 u_y}{\partial p_y^2}\frac{\bar{\sigma}}{\bar{\varepsilon}}\right]\\
&+\frac{1}{3}\left[\left(\frac{\partial\bar{\sigma}}{\partial p_z}\frac{1}{\bar{\varepsilon}}-\frac{\partial\bar{\varepsilon}}{\partial p_z}\frac{\bar{\sigma}}{\bar{\varepsilon}^2}\right)\left(\frac{\partial u_y}{\partial p_z}+\frac{\partial u_z}{\partial p_y}\right)+\left(\frac{\partial^2 u_y}{\partial p_z^2}+\frac{\partial^2 u_z}{\partial p_y\partial p_z}\right)\frac{\bar{\sigma}}{\bar{\varepsilon}}\right]+d_y=0,
\end{aligned}\tag{2.79}$$

$$\begin{aligned}
&\frac{1}{3}\left[\left(\frac{\partial\bar{\sigma}}{\partial p_x}\frac{1}{\bar{\varepsilon}}-\frac{\partial\bar{\varepsilon}}{\partial p_x}\frac{\bar{\sigma}}{\bar{\varepsilon}^2}\right)\left(\frac{\partial u_x}{\partial p_z}+\frac{\partial u_z}{\partial p_x}\right)+\left(\frac{\partial u_x}{\partial p_x\partial p_z}+\frac{\partial u_z}{\partial p_x^2}\right)\frac{\bar{\sigma}}{\bar{\varepsilon}}\right]\\
&+\frac{1}{3}\left[\left(\frac{\partial\bar{\sigma}}{\partial p_y}\frac{1}{\bar{\varepsilon}}-\frac{\partial\bar{\varepsilon}}{\partial p_y}\frac{\bar{\sigma}}{\bar{\varepsilon}^2}\right)\left(\frac{\partial u_y}{\partial p_z}+\frac{\partial u_z}{\partial p_y}\right)+\left(\frac{\partial u_y}{\partial p_y\partial p_z}+\frac{\partial u_z}{\partial p_y^2}\right)\frac{\bar{\sigma}}{\bar{\varepsilon}}\right]\\
&+\frac{2}{3}\left[\left(\frac{\partial\bar{\sigma}}{\partial p_z}\frac{1}{\bar{\varepsilon}}-\frac{\partial\bar{\varepsilon}}{\partial p_z}\frac{\bar{\sigma}}{\bar{\varepsilon}^2}\right)\frac{\partial u_z}{\partial p_z}+\frac{\partial^2 u_z}{\partial p_z^2}\frac{\bar{\sigma}}{\bar{\varepsilon}}\right]+d_z=0.
\end{aligned}\tag{2.80}$$

The set of equations (2.78), (2.79) and (2.70) can be simplified by considering Laplace of the displacements

$$\begin{aligned}
\nabla^2 u_x=&-\left(\frac{\partial^2 u_x}{\partial p_x^2}+\frac{\partial^2 u_y}{\partial p_x\partial p_y}+\frac{\partial^2 u_z}{\partial p_x\partial p_z}\right)-2\left(\frac{1}{\bar{\sigma}}\frac{\partial\bar{\sigma}}{\partial p_x}-\frac{1}{\bar{\varepsilon}}\frac{\partial\bar{\varepsilon}}{\partial p_x}\right)\frac{\partial u_x}{\partial p_x}\\
&-\left(\frac{1}{\bar{\sigma}}\frac{\partial\bar{\sigma}}{\partial p_y}-\frac{1}{\bar{\varepsilon}}\frac{\partial\bar{\varepsilon}}{\partial p_y}\right)\left(\frac{\partial u_x}{\partial p_y}+\frac{\partial u_y}{\partial p_x}\right)-\left(\frac{1}{\bar{\sigma}}\frac{\partial\bar{\sigma}}{\partial p_z}-\frac{1}{\bar{\varepsilon}}\frac{\partial\bar{\varepsilon}}{\partial p_z}\right)\left(\frac{\partial u_x}{\partial p_z}\frac{\partial u_z}{\partial p_x}\right)+d_x,
\end{aligned}\tag{2.81}$$

$$\begin{aligned}
\nabla^2 u_y=&-\left(\frac{\partial^2 u_x}{\partial p_x\partial p_y}+\frac{\partial^2 u_y}{\partial p_y^2}+\frac{\partial^2 u_z}{\partial p_y\partial p_z}\right)-\left(\frac{1}{\bar{\sigma}}\frac{\partial\bar{\sigma}}{\partial p_x}-\frac{1}{\bar{\varepsilon}}\frac{\partial\bar{\varepsilon}}{\partial p_x}\right)\left(\frac{\partial u_x}{\partial p_y}\frac{\partial u_y}{\partial p_x}\right)\\
&-2\left(\frac{1}{\bar{\sigma}}\frac{\partial\bar{\sigma}}{\partial p_y}-\frac{1}{\bar{\varepsilon}}\frac{\partial\bar{\varepsilon}}{\partial p_y}\right)\frac{\partial u_y}{\partial p_y}-\left(\frac{1}{\bar{\sigma}}\frac{\partial\bar{\sigma}}{\partial p_z}-\frac{1}{\bar{\varepsilon}}\frac{\partial\bar{\varepsilon}}{\partial p_z}\right)\frac{\partial u_y}{\partial p_z}\frac{\partial u_z}{\partial p_y}+d_y,
\end{aligned}\tag{2.82}$$

$$\nabla^2 u_z = -\left(\frac{\partial^2 u_x}{\partial p_x \partial p_z} + \frac{\partial^2 u_y}{\partial p_y \partial p_z} + \frac{\partial^2 u_z}{\partial p_z^2}\right) - \left(\frac{1}{\bar{\sigma}}\frac{\partial \bar{\sigma}}{\partial p_x} - \frac{1}{\bar{\varepsilon}}\frac{\partial \bar{\varepsilon}}{\partial p_x}\right)\left(\frac{\partial u_x}{\partial p_z}\frac{\partial u_z}{\partial p_x}\right)$$
$$-\left(\frac{1}{\bar{\sigma}}\frac{\partial \bar{\sigma}}{\partial p_y} - \frac{1}{\bar{\varepsilon}}\frac{\partial \bar{\varepsilon}}{\partial p_y}\right)\frac{\partial u_y}{\partial p_z}\frac{\partial u_z}{\partial p_y} - 2\left(\frac{1}{\bar{\sigma}}\frac{\partial \bar{\sigma}}{\partial p_z} - \frac{1}{\bar{\varepsilon}}\frac{\partial \bar{\varepsilon}}{\partial p_z}\right)\frac{\partial u_z}{\partial p_z} + d_z. \tag{2.83}$$

The traction boundary conditions can also be written in terms of displacement for an ideal plastic material.

$$n_x\left(\frac{1}{3}\frac{\bar{\sigma}}{\bar{\varepsilon}}\left(\frac{\partial u_x}{\partial y} + \frac{\partial u_y}{\partial x}\right)\right) + n_y\left(\frac{2}{3}\frac{\bar{\sigma}}{\bar{\varepsilon}}\frac{\partial u_y}{\partial y}\right) + n_z\left(\frac{1}{3}\frac{\bar{\sigma}}{\bar{\varepsilon}}\left(\frac{\partial u_y}{\partial z} + \frac{\partial u_z}{\partial y}\right)\right) = \bar{\tau}_y, \tag{2.84}$$

$$n_x\left(\frac{2}{3}\frac{\bar{\sigma}}{\bar{\varepsilon}}\frac{\partial u_x}{\partial x}\right) + n_y\left(\frac{1}{3}\frac{\bar{\sigma}}{\bar{\varepsilon}}\left(\frac{\partial u_x}{\partial y} + \frac{\partial u_y}{\partial x}\right)\right) + n_z\left(\frac{1}{3}\frac{\bar{\sigma}}{\bar{\varepsilon}}\left(\frac{\partial u_x}{\partial z} + \frac{\partial u_z}{\partial x}\right)\right) = \bar{\tau}_x, \tag{2.85}$$

$$n_x\left(\frac{1}{3}\frac{\bar{\sigma}}{\bar{\varepsilon}}\left(\frac{\partial u_x}{\partial z} + \frac{\partial u_z}{\partial x}\right)\right) + n_y\left(\frac{1}{3}\frac{\bar{\sigma}}{\bar{\varepsilon}}\left(\frac{\partial u_y}{\partial z} + \frac{\partial u_z}{\partial y}\right)\right) + n_z\left(\frac{2}{3}\frac{\bar{\sigma}}{\bar{\varepsilon}}\frac{\partial u_z}{\partial z}\right) = \bar{\tau}_z. \tag{2.86}$$

The stiffness matrix $\mathbf{C}^p$ in 2D is

$$\mathbf{C}^p = \frac{\bar{\sigma}}{\bar{\varepsilon}}\begin{bmatrix} \frac{2}{3} & 0 & 0 \\ 0 & \frac{2}{3} & 0 \\ 0 & 0 & \frac{1}{3} \end{bmatrix}. \tag{2.87}$$

The governing equations in 2D are

$$\nabla^2 u_x = -\left(\frac{\partial^2 u_x}{\partial p_x^2} + \frac{\partial^2 u_y}{\partial p_x \partial p_y}\right) - 2\left(\frac{1}{\bar{\sigma}}\frac{\partial \bar{\sigma}}{\partial p_x} - \frac{1}{\bar{\varepsilon}}\frac{\partial \bar{\varepsilon}}{\partial p_x}\right)\frac{\partial u_x}{\partial p_x}$$
$$-\left(\frac{1}{\bar{\sigma}}\frac{\partial \bar{\sigma}}{\partial p_y} - \frac{1}{\bar{\varepsilon}}\frac{\partial \bar{\varepsilon}}{\partial p_y}\right)\left(\frac{\partial u_x}{\partial p_y} + \frac{\partial u_y}{\partial p_x}\right) + d_x, \tag{2.88}$$

$$\nabla^2 u_y = -\left(\frac{\partial^2 u_x}{\partial p_x \partial p_y} + \frac{\partial^2 u_y}{\partial p_y^2}\right) - 2\left(\frac{1}{\bar{\sigma}}\frac{\partial \bar{\sigma}}{\partial p_y} - \frac{1}{\bar{\varepsilon}}\frac{\partial \bar{\varepsilon}}{\partial p_y}\right)\frac{\partial^2 u_y}{\partial p_y^2}$$
$$-\left(\frac{1}{\bar{\sigma}}\frac{\partial \bar{\sigma}}{\partial p_x} - \frac{1}{\bar{\varepsilon}}\frac{\partial \bar{\varepsilon}}{\partial p_x}\right)\left(\frac{\partial u_x}{\partial p_y} + \frac{\partial u_y}{\partial p_x}\right) + d_y. \tag{2.89}$$

The traction boundary conditions in 2D are

$$n_x\left(\frac{2}{3}\frac{\bar{\sigma}}{\bar{\varepsilon}}\frac{\partial u_x}{\partial x}\right) + n_y\left(\frac{1}{3}\frac{\bar{\sigma}}{\bar{\varepsilon}}\left(\frac{\partial u_x}{\partial y} + \frac{\partial u_y}{\partial x}\right)\right) = \bar{\tau}_x, \tag{2.90}$$

$$n_y\left(\frac{2}{3}\frac{\bar{\sigma}}{\bar{\varepsilon}}\frac{\partial u_y}{\partial y}\right) + n_x\left(\frac{1}{3}\frac{\bar{\sigma}}{\bar{\varepsilon}}\left(\frac{\partial u_x}{\partial y} + \frac{\partial u_y}{\partial x}\right)\right) = \bar{\tau}_y. \tag{2.91}$$

The partial derivatives of the effective strain are

$$\frac{\partial \bar{\varepsilon}}{\partial p_x} = \frac{1}{3}\frac{\left(2\varepsilon_{xx} - \varepsilon_{yy}\right)\frac{\partial \varepsilon_{xx}}{\partial p_x} + \left(2\varepsilon_{yy} - \varepsilon_{xx}\right)\frac{\partial \varepsilon_{yy}}{\partial p_x} + 6\varepsilon_{xy}\frac{\partial \varepsilon_{xy}}{\partial p_x}}{\sqrt{\varepsilon_{xx}^2 - \varepsilon_{xx}\varepsilon_{yy} + \varepsilon_{yy}^2 + 3\varepsilon_{xy}^2}}, \tag{2.92}$$

$$\frac{\partial \bar{\varepsilon}}{\partial p_y} = \frac{1}{3}\frac{\left(2\varepsilon_{xx} - \varepsilon_{yy}\right)\frac{\partial \varepsilon_{xx}}{\partial p_y} + \left(2\varepsilon_{yy} - \varepsilon_{xx}\right)\frac{\partial \varepsilon_{yy}}{\partial p_y} + 6\varepsilon_{xy}\frac{\partial \varepsilon_{xy}}{\partial p_y}}{\sqrt{\varepsilon_{xx}^2 - \varepsilon_{xx}\varepsilon_{yy} + \varepsilon_{yy}^2 + 3\gamma_{xy}^2}}. \tag{2.93}$$

The partial derivatives of the effective stress are defined as

$$\frac{\partial \bar{\sigma}}{\partial p_i} = \frac{\partial \bar{\sigma}}{\partial \bar{\varepsilon}}\frac{\partial \bar{\varepsilon}}{\partial p_i};\ i = x, y, z, \tag{2.94}$$

where $\partial\bar{\sigma}/\partial\bar{\varepsilon}$ is taken from the effective stress- effective strain relation for a specific material used.

2.2.4.2 Slightly compressible deformation

A slightly compressible material first used for deformation problems in [Osakada, Nakano, and Mori, 1982] and also applied to rolling in [Mori and Osakada, 1984] by FEM. The mechanical results with using slightly compressible plastic material should not differ much from the ideal plastic incompressible material, since this method is applied to increase the stability and accuracy. The stiffness matrix for slightly compressible material has additional components regarding the ideal plastic stiffness matrix written in Equation (2.77). A small positive free parameter g is introduced and added to the non shear stress related components of the matrix. The stiffness matrix for a slightly compressible material is

$$C^p = \frac{\bar{\sigma}}{\bar{\varepsilon}}\left[\begin{bmatrix} \frac{2}{3} & 0 & 0 & 0 & 0 & 0 \\ 0 & \frac{2}{3} & 0 & 0 & 0 & 0 \\ 0 & 0 & \frac{2}{3} & 0 & 0 & 0 \\ 0 & 0 & 0 & \frac{1}{3} & 0 & 0 \\ 0 & 0 & 0 & 0 & \frac{1}{3} & 0 \\ 0 & 0 & 0 & 0 & 0 & \frac{1}{3} \end{bmatrix} + \left(\frac{1}{g} - \frac{2}{9}\right)\begin{bmatrix} 1 & 1 & 1 & 0 & 0 & 0 \\ 1 & 1 & 1 & 0 & 0 & 0 \\ 1 & 1 & 1 & 0 & 0 & 0 \\ 0 & 0 & 0 & 0 & 0 & 0 \\ 0 & 0 & 0 & 0 & 0 & 0 \\ 0 & 0 & 0 & 0 & 0 & 0 \end{bmatrix}\right]. \tag{2.95}$$

The effective stress is

$$\bar{\sigma} = \sqrt{\frac{1}{2}\begin{bmatrix} \left(\sigma_{xx} - \sigma_{yy}\right)^2 + \left(\sigma_{yy} - \sigma_{zz}\right)^2 + \left(\sigma_{zz} - \sigma_{xx}\right)^2 \\ +6\left(\sigma_{xy}^2 + \sigma_{yz}^2 + \sigma_{zx}^2\right) \end{bmatrix} + g\sigma_m^2}\,, \tag{2.96}$$

where g is a small positive constant suggested by Mori and Osakada [Mori and Osakada, 1984], to be between 0.01 and 0.0001.

The effective strain is

$$\bar{\varepsilon} = \sqrt{\frac{2}{9}\left[\left(\varepsilon_{xx}-\varepsilon_{yy}\right)^2+\left(\varepsilon_{yy}-\varepsilon_{zz}\right)^2+\left(\varepsilon_{zz}-\varepsilon_{xx}\right)^2+6\left(\varepsilon_{xy}^2+\varepsilon_{yz}^2+\varepsilon_{zx}^2\right)\right]+\frac{\varepsilon_v^2}{g}}\,. \tag{2.97}$$

The following relation can be written between the hydrostatic stress and the volumetric strain for a slightly compressible material

$$\frac{\varepsilon_v}{\bar{\varepsilon}} = g\,\frac{\sigma_m}{\bar{\sigma}}\,. \tag{2.98}$$

In a 2D Cartesian coordinate system, the stiffness matrix for a slightly compressible material is

$$C^p = \frac{\bar{\sigma}}{\bar{\varepsilon}}\left[\begin{bmatrix}\frac{2}{3} & 0 & 0\\ 0 & \frac{2}{3} & 0\\ 0 & 0 & \frac{1}{3}\end{bmatrix}+\left(\frac{1}{g}-\frac{2}{9}\right)\begin{bmatrix}1 & 1 & 0\\ 1 & 1 & 0\\ 0 & 0 & 0\end{bmatrix}\right]. \tag{2.99}$$

Hence the governing equation (2.28) becomes

$$\begin{aligned}\nabla^2 u_x = &-\left(\frac{3}{g}+\frac{1}{3}\right)\left(\frac{\partial^2 u_x}{\partial p_x^2}+\frac{\partial^2 u_y}{\partial p_x \partial p_y}\right)\\ &-\left(\frac{1}{\bar{\sigma}}\frac{\partial \bar{\sigma}}{\partial p_x}-\frac{1}{\bar{\varepsilon}}\frac{\partial \bar{\varepsilon}}{\partial p_x}\right)\left[2\frac{\partial u_x}{\partial p_x}+\left(\frac{3}{g}-\frac{2}{3}\right)\left(\frac{\partial u_x}{\partial p_x}+\frac{\partial u_y}{\partial p_y}\right)\right]\\ &-2\left(\frac{1}{\bar{\sigma}}\frac{\partial \bar{\sigma}}{\partial p_y}-\frac{1}{\bar{\varepsilon}}\frac{\partial \bar{\varepsilon}}{\partial p_y}\right)\left(\frac{\partial u_x}{\partial p_y}+\frac{\partial u_y}{\partial p_x}\right)-d_x,\end{aligned} \tag{2.100}$$

$$\nabla^2 u_y = -\left(\frac{3}{g}+\frac{1}{3}\right)\left(\frac{\partial^2 u_x}{\partial p_x \partial p_y}+\frac{\partial^2 u_y}{\partial p_y^2}\right)$$
$$-\left(\frac{1}{\bar{\sigma}}\frac{\partial \bar{\sigma}}{\partial p_y}-\frac{1}{\bar{\varepsilon}}\frac{\partial \bar{\varepsilon}}{\partial p_y}\right)\left[2\frac{\partial u_y}{\partial p_y}+\left(\frac{3}{g}-\frac{2}{3}\right)\left(\frac{\partial u_x}{\partial p_x}+\frac{\partial u_y}{\partial p_y}\right)\right] \tag{2.101}$$
$$-2\left(\frac{1}{\bar{\sigma}}\frac{\partial \bar{\sigma}}{\partial p_x}-\frac{1}{\bar{\varepsilon}}\frac{\partial \bar{\varepsilon}}{\partial p_x}\right)\left(\frac{\partial u_x}{\partial p_y}+\frac{\partial u_y}{\partial p_x}\right)-d_y.$$

The traction boundary conditions for a slightly compressible plastic material are

$$n_y\left[\left(\frac{1}{g}-\frac{2}{9}\right)\frac{\bar{\sigma}}{\bar{\varepsilon}}\frac{\partial u_x}{\partial p_x}+\left(\frac{1}{g}+\frac{4}{9}\right)\frac{\bar{\sigma}}{\bar{\varepsilon}}\frac{\partial u_y}{\partial p_y}\right]+n_x\frac{1}{3}\frac{\bar{\sigma}}{\bar{\varepsilon}}\left(\frac{\partial u_x}{\partial p_y}+\frac{\partial u_y}{\partial p_x}\right)=\bar{\tau}_y, \tag{2.102}$$

$$n_x\left[\left(\frac{1}{g}+\frac{4}{9}\right)\frac{\bar{\sigma}}{\bar{\varepsilon}}\frac{\partial u_x}{\partial p_x}+\left(\frac{1}{g}-\frac{2}{9}\right)\frac{\bar{\sigma}}{\bar{\varepsilon}}\frac{\partial u_y}{\partial p_y}\right]+n_y\frac{1}{3}\frac{\bar{\sigma}}{\bar{\varepsilon}}\left(\frac{\partial u_x}{\partial p_y}+\frac{\partial u_y}{\partial p_x}\right)=\bar{\tau}_x. \tag{2.103}$$

2.3 Thermal model

In this section, the governing equations for a steady convective diffusion equation in 3D that is in the context of a slice model converted to a 2D transient heat diffusion equation are given. The internal heat generation equations are written for elastic and plastic materials. Neumann, Robin and Dirichlet boundary conditions are defined.

2.3.1 Formulation of thermal model

A 3D steady convective-diffusive heat transfer equation is

$$\nabla\cdot\left(\rho c_p \mathbf{v} T\right)=\nabla\cdot\left(k\nabla T\right)+\dot{Q}, \tag{2.104}$$

where ρ is the density, c_p is the specific heat, $\mathbf{v}$ is the velocity vector**,** T is temperature, k is the thermal conductivity, and $\dot{Q}$ is the internal heat generation rate due to deformation.

If we assume a constant velocity and density over a cross section, which is the same assumption as in the slice model discussed in Chapter 3, then the governing equation can be rewritten for a 2D model in transient diffusive form

$$\rho c_p \frac{\partial T(\mathbf{p},t)}{\partial t} = \nabla \cdot \left(k \nabla T(\mathbf{p},t) \right) + \dot{Q}\,;\ \mathbf{p} \in \Omega^{2\mathrm{D}}. \tag{2.105}$$

The governing equation (2.105) in 2D is

$$\rho c_p \frac{\partial T}{\partial t} = \left(\frac{\partial k}{\partial p_x}\frac{\partial T}{\partial p_x} + k\frac{\partial^2 T}{\partial p_x^2} + \frac{\partial k}{\partial p_y}\frac{\partial T}{\partial p_y} + k\frac{\partial^2 T}{\partial p_y^2} \right) + \dot{Q}\,. \tag{2.106}$$

2.3.2 Boundary conditions

There are three types of boundary conditions which are used in the thermal model over the boundary Γ. These are Robin, Neumann and Dirichlet boundary conditions acting on the parts of boundaries Γ^R, Γ^N, Γ^D, where $\Gamma = \Gamma^R \cup \Gamma^N \cup \Gamma^D$.

$$-k\frac{\partial T(\mathbf{p},t)}{\partial \mathbf{n}_\Gamma} = h\left[T(\mathbf{p},t) - T_\Gamma^{ref}(\mathbf{p},t) \right];\ \mathbf{p} \in \Gamma^R, \tag{2.107}$$

$$-k\frac{\partial T(\mathbf{p},t)}{\partial \mathbf{n}_\Gamma} = q;\ \mathbf{p} \in \Gamma^N, \tag{2.108}$$

$$T_\Gamma(\mathbf{p},t) = T;\ \mathbf{p} \in \Gamma^D. \tag{2.109}$$

Thermal conductivity k, heat transfer coefficient h, heat flux q, unit normal vector $\mathbf{n}$ and the reference temperature T^{ref} have to be known in order to calculate the temperature at the corresponding boundary.

Coupling of the thermal and mechanical models is possible through properly applied material model properties. During the plastic deformation, if effective stress definition includes temperature as a parameter, then the coupling exists. Similarly for the elastic deformation if the material properties $E(T)$, $\nu(T)$ are temperature depended, coupling can be done. The deformation is first calculated by mechanical model and the material properties are obtained by using initial

temperature field. After the deformation, a new computational domain is obtained and thermal model is run for exactly the same time as the mechanical model has been run. The calculated new temperature field over the domain influences new material properties for the mechanical model, used in further deformation steps.

2.3.3 Internal heat generation

The area under the stress strain curve represents the strain energy per unit volume U, in the uniaxial case, it represents the integration of the stress over the strain of the deformation as

$$U = \int_{\varepsilon} \sigma d\varepsilon . \tag{2.110}$$

In the multiaxial case, the sum of integrations over the strain components is considered

$$U\left(\varepsilon_{ij}\right) = \int_{\varepsilon_{ij}} \sigma_{ij} d\varepsilon_{ij} . \tag{2.111}$$

The internal heat generation rate $\dot{Q}$ can be expressed as,

$$\dot{Q} = \eta \frac{\partial U}{\partial t}, \tag{2.112}$$

where η is the Taylor-Quinney parameter, which indicates the rate of mechanical energy turning into heat. A detailed study on this subject is given in [Rusinek and Klepaczko, 2009]. Internal heat generation rate can be defined for an ideal plastic material in the same way over the effective strain $\bar{\varepsilon}$ as

$$\dot{Q} = \eta \frac{\partial}{\partial t} U = \eta \frac{\partial}{\partial t} \int_{\bar{\varepsilon}} \bar{\sigma} d\bar{\varepsilon} . \tag{2.113}$$

In a discrete way, internal heat generation rate defined in (2.113) for a small deformation step between ε_0 and ε can be written as

$$\dot{Q} = \frac{\partial}{\partial t} \eta \int_{\bar{\varepsilon}_0}^{\bar{\varepsilon}} \bar{\sigma} d\bar{\varepsilon} \simeq \eta \bar{\sigma} \frac{\Delta \bar{\varepsilon}}{\Delta t} . \tag{2.114}$$

This method is applicable to slice model where the whole deformation (strain) is analyzed in a sequence of smaller reductions.
From the previous equation, an increase in the temperature during a small deformation step can also be expressed

$$\Delta T_{gain} = \eta \frac{\bar{\sigma}\left(\bar{\varepsilon}, \dot{\bar{\varepsilon}}, T\right)}{\rho c_p} \Delta \bar{\varepsilon} \,. \tag{2.115}$$

For isotropic elastic materials, the amount of energy in volume V is

$$\int_V U dV = \frac{1}{2} \int_V \left(\sigma_{xx}\varepsilon_{xx} + \sigma_{yy}\varepsilon_{yy} + \sigma_{zz}\varepsilon_{zz} + 2\sigma_{yz}\varepsilon_{yz} + 2\sigma_{xz}\varepsilon_{xz} + 2\sigma_{xy}\varepsilon_{xy} \right) dV \,. \tag{2.116}$$

The amount of energy per unit volume is

$$U = \frac{1}{2} \boldsymbol{\sigma}^{\mathrm{T}} \boldsymbol{\varepsilon} \,. \tag{2.117}$$

In component form

$$U = \frac{1}{2} \left(\sigma_{xx}\varepsilon_{xx} + \sigma_{yy}\varepsilon_{yy} + \sigma_{zz}\varepsilon_{zz} + 2\sigma_{yz}\varepsilon_{yz} + 2\sigma_{xz}\varepsilon_{xz} + 2\sigma_{xy}\varepsilon_{xy} \right) . \tag{2.118}$$

In a 2D system

$$U = \frac{1}{2} \left(\sigma_{xx}\varepsilon_{xx} + \sigma_{yy}\varepsilon_{yy} + 2\sigma_{xy}\varepsilon_{xy} \right) . \tag{2.119}$$

The major governing equations used in this dissertation are written in Table 2.1, Table 2.2 and Table 2.3 for isotropic elastic material, ideal plastic material and ideal plastic slightly compressible material respectively.

Mechanical governing equation in *x* direction for elastic material	$C_{11}\frac{\partial^2 u_x}{\partial p_x^2}+C_{12}\frac{\partial^2 u_y}{\partial p_x \partial p_y}+C_{13}\left(\frac{\partial^2 u_x}{\partial p_x \partial p_y}+\frac{\partial^2 u_y}{\partial p_x^2}\right)$ $+C_{31}\frac{\partial^2 u_x}{\partial p_x \partial p_y}+C_{32}\frac{\partial^2 u_y}{\partial p_y^2}+C_{33}\left(\frac{\partial^2 u_x}{\partial p_y^2}+\frac{\partial^2 u_y}{\partial p_x \partial p_y}\right)+d_x=0$
Mechanical governing equation in *y* direction for elastic material	$C_{21}\frac{\partial^2 u_x}{\partial p_x \partial p_y}+C_{22}\frac{\partial^2 u_y}{\partial p_y^2}+C_{23}\left(\frac{\partial^2 u_x}{\partial p_y^2}+\frac{\partial^2 u_y}{\partial p_x \partial p_y}\right)$ $+C_{31}\frac{\partial^2 u_x}{\partial p_x^2}+C_{32}\frac{\partial^2 u_y}{\partial p_x \partial p_y}+C_{33}\left(\frac{\partial^2 u_x}{\partial p_x \partial p_y}+\frac{\partial^2 u_y}{\partial p_x^2}\right)+d_y=0$
Heat transfer equation	$\rho c_p \frac{\partial T}{\partial t}=\left(\frac{\partial k}{\partial p_x}\frac{\partial T}{\partial p_x}+k\frac{\partial^2 T}{\partial p_x^2}+\frac{\partial k}{\partial p_y}\frac{\partial T}{\partial p_y}+k\frac{\partial^2 T}{\partial p_y^2}\right)+\dot{Q}$
Internal heat generation rate	$\dot{Q}=\frac{\eta}{2}\frac{\partial}{\partial t}\left(\sigma_{xx}\varepsilon_{xx}+\sigma_{yy}\varepsilon_{yy}+2\sigma_{xy}\varepsilon_{xy}\right)$

Table 2.1: Governing equations used for isotropic elastic material in 2D.

Mechanical governing equation in *x* direction for ideal plastic material	$\nabla^2 u_x=-\left(\frac{\partial^2 u_x}{\partial p_x^2}+\frac{\partial^2 u_y}{\partial p_x \partial p_y}\right)-2\left(\frac{1}{\bar{\sigma}}\frac{\partial \bar{\sigma}}{\partial p_x}-\frac{1}{\bar{\varepsilon}}\frac{\partial \bar{\varepsilon}}{\partial p_x}\right)\frac{\partial u_x}{\partial p_x}$ $-\left(\frac{1}{\bar{\sigma}}\frac{\partial \bar{\sigma}}{\partial p_y}-\frac{1}{\bar{\varepsilon}}\frac{\partial \bar{\varepsilon}}{\partial p_y}\right)\left(\frac{\partial u_x}{\partial p_y}+\frac{\partial u_y}{\partial p_x}\right)+d_x$
Mechanical governing equation in *y* direction for ideal plastic material	$\nabla^2 u_y=-\left(\frac{\partial^2 u_x}{\partial p_x \partial p_y}+\frac{\partial^2 u_y}{\partial p_y^2}\right)-2\left(\frac{1}{\bar{\sigma}}\frac{\partial \bar{\sigma}}{\partial p_y}-\frac{1}{\bar{\varepsilon}}\frac{\partial \bar{\varepsilon}}{\partial p_y}\right)\frac{\partial^2 u_y}{\partial p_y^2}$ $-\left(\frac{1}{\bar{\sigma}}\frac{\partial \bar{\sigma}}{\partial p_x}-\frac{1}{\bar{\varepsilon}}\frac{\partial \bar{\varepsilon}}{\partial p_x}\right)\left(\frac{\partial u_x}{\partial p_y}+\frac{\partial u_y}{\partial p_x}\right)+d_y$
Heat transfer equation	$\rho c_p \frac{\partial T}{\partial t}=\left(\frac{\partial k}{\partial p_x}\frac{\partial T}{\partial p_x}+k\frac{\partial^2 T}{\partial p_x^2}+\frac{\partial k}{\partial p_y}\frac{\partial T}{\partial p_y}+k\frac{\partial^2 T}{\partial p_y^2}\right)+\dot{Q}$
Internal heat generation rate	$\dot{Q}=\eta\frac{\partial}{\partial t}\int_{\bar{\varepsilon}}\bar{\sigma}d\bar{\varepsilon}$

Table 2.2: Governing equations used for ideal plastic material in 2D.

Mechanical governing equation in *x* direction for slightly compressible plastic material	$\nabla^2 u_x = -\left(\frac{3}{g}+\frac{1}{3}\right)\left(\frac{\partial^2 u_x}{\partial p_x^2}+\frac{\partial^2 u_y}{\partial p_x \partial p_y}\right)$ $-\left(\frac{1}{\bar{\sigma}}\frac{\partial \bar{\sigma}}{\partial p_x}-\frac{1}{\bar{\varepsilon}}\frac{\partial \bar{\varepsilon}}{\partial p_x}\right)\left[2\frac{\partial u_x}{\partial p_x}+\left(\frac{3}{g}-\frac{2}{3}\right)\left(\frac{\partial u_x}{\partial p_x}+\frac{\partial u_y}{\partial p_y}\right)\right]$ $-2\left(\frac{1}{\bar{\sigma}}\frac{\partial \bar{\sigma}}{\partial p_y}-\frac{1}{\bar{\varepsilon}}\frac{\partial \bar{\varepsilon}}{\partial p_y}\right)\left(\frac{\partial u_x}{\partial p_y}+\frac{\partial u_y}{\partial p_x}\right)-d_x$
Mechanical governing equation in *y* direction for slightly compressible plastic material	$\nabla^2 u_y = -\left(\frac{3}{g}+\frac{1}{3}\right)\left(\frac{\partial^2 u_x}{\partial p_x \partial p_y}+\frac{\partial^2 u_y}{\partial p_y^2}\right)$ $-\left(\frac{1}{\bar{\sigma}}\frac{\partial \bar{\sigma}}{\partial p_y}-\frac{1}{\bar{\varepsilon}}\frac{\partial \bar{\varepsilon}}{\partial p_y}\right)\left[2\frac{\partial u_y}{\partial p_y}+\left(\frac{3}{g}-\frac{2}{3}\right)\left(\frac{\partial u_x}{\partial p_x}+\frac{\partial u_y}{\partial p_y}\right)\right]$ $-2\left(\frac{1}{\bar{\sigma}}\frac{\partial \bar{\sigma}}{\partial p_x}-\frac{1}{\bar{\varepsilon}}\frac{\partial \bar{\varepsilon}}{\partial p_x}\right)\left(\frac{\partial u_x}{\partial p_y}+\frac{\partial u_y}{\partial p_x}\right)-d_y$
Heat transfer equation	$\rho c_p \frac{\partial T}{\partial t}=\left(\frac{\partial k}{\partial p_x}\frac{\partial T}{\partial p_x}+k\frac{\partial^2 T}{\partial p_x^2}+\frac{\partial k}{\partial p_y}\frac{\partial T}{\partial p_y}+k\frac{\partial^2 T}{\partial p_y^2}\right)+\dot{Q}$
Internal heat generation rate	$\dot{Q}=\eta\frac{\partial}{\partial t}\int_{\bar{\varepsilon}}\bar{\sigma}d\bar{\varepsilon}$

Table 2.3: Governing equations used for slightly compressible plastic material in 2D.

3 Physical Model of Hot Rolling

In Chapter 3 the modelling assumptions of the hot rolling process are given. Slice model assumptions and their application to rolling are explained. Specific boundary conditions and symmetry assumptions for a slice model are determined. The mathematical description of grooves, rolls and a rolling schedule are discussed in detail. A complete set of the parameters, needed for a rolling simulation are given. A flowchart of the solution procedure strategy is shown as well.

3.1 Slice model

Rolling is a very complex 3D problem however, several assumptions can be made for its reasonably simplified description. The calculations can be done on 2D cross sections which are parallel and aligned with the rolling direction with base vector $\mathbf{i}_z$. This solution concept is referred as the travelling slice method in which plane strain approach is used. The overall 3D process is analyzed by discrete 2D slices under compression by neglecting the thermal and mechanical interactions in the rolling direction. This is considered as a mixed Eulerian-Lagrangian model. The details can be seen in Figure 3.1 and [Hanoglu and Šarler, 2013].

The position of a slice z is a time depended function which is needed for calculating the cooling intensity in the thermal model and deformation in the mechanical model. The relation between the slice position and time in Eulerian system is defined as

$$z(t) = \int_t v(t)dt; v(t) = \mathbf{v}(t) \cdot \mathbf{i}_z, \; v(t) = A(t_0)v_{entry} / A(t). \tag{3.1}$$

where $A(t_0)$ is the area of initial slice and initial slice velocity $v_{entry} = v(t_0)$. $A(t)$ and $v(t)$ represent the area of a slice and its velocity in the rolling direction at time t, when conservation of volume is considered.

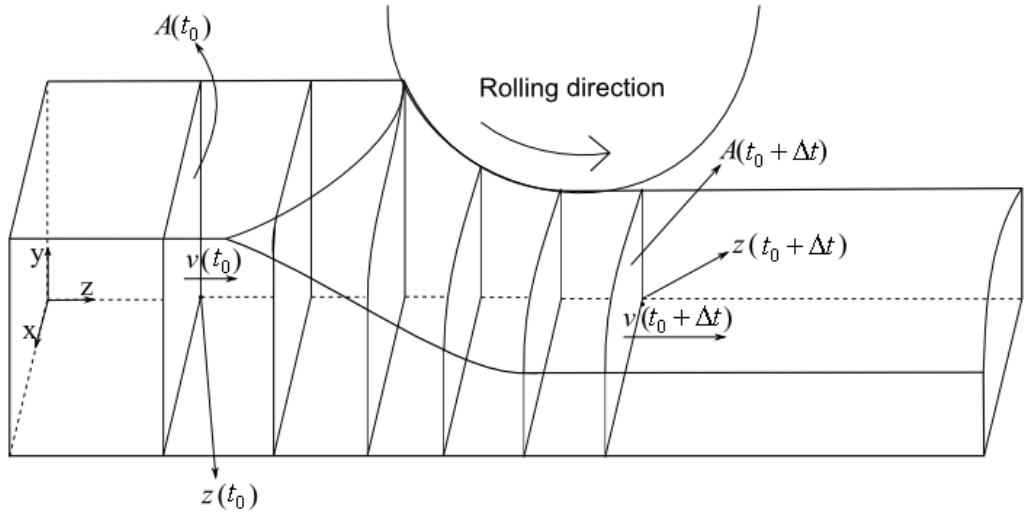

Figure 3.1: Scheme of slices used as computational domains through a rolling stand only when quadrant of a billet is considered.

This slice model is based on the assumption of homogenous compression where planes remain planes as seen on Figure 3.2.

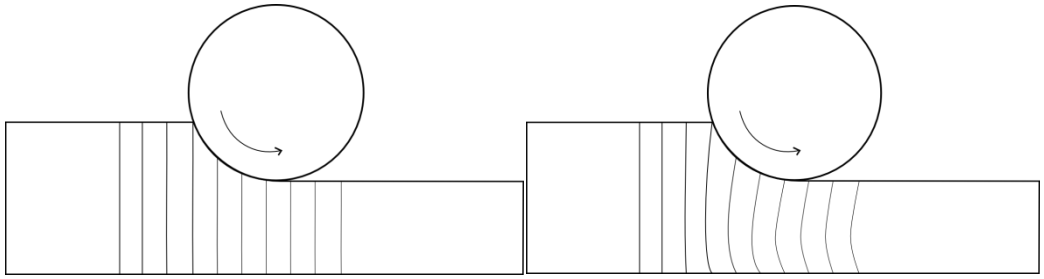

Figure 3.2: Homogeous (on left) and non-homogenous compression (on right).

Due to the geometry of a slice, there are usually 4 boundaries that have to be defined individually for each side of the slice. However, due to symmetry, and by neglecting the non symmetrical effect of body forces, a quarter of the slice can be analyzed as presented in Figure 3.3.

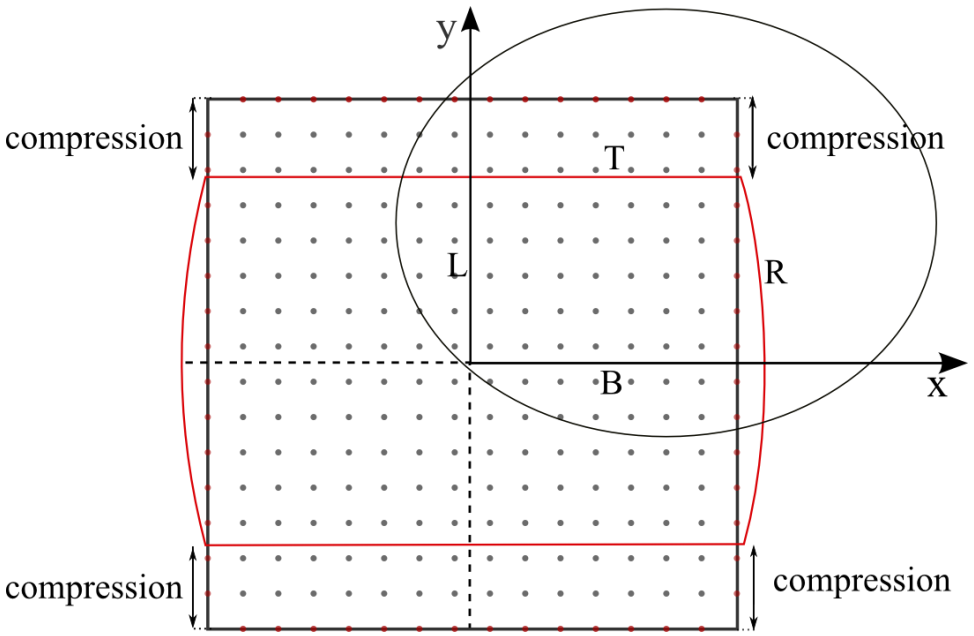

Figure 3.3: Symmetry on a rolled slice.

Left (L) and Bottom (B) boundaries are on the symmetry lines which require appropriate symmetry boundary conditions. For the mechanical model, the L boundary experiences

$$\bar{u}_x = 0, \ \bar{\tau}_y = 0. \tag{3.2}$$

Similarly, the B boundary experiences

$$\bar{\tau}_x = 0, \ \bar{u}_y = 0. \tag{3.3}$$

For the thermal model B and L boundaries experience insulating Neumann boundary conditions where the prescribed heat flux q equals 0.

For Top (T) and Right (R) boundaries, it is important to define first if there exists a contact with the roll or not. This can be predicted by considering the groove geometry and current geometry of the slice, which is discussed later in this chapter. In short, a cross section of a groove for a belonging slice position is drawn over the same slice. If there is no contact, the following boundary condition is applied for sides T and R in the mechanical model

$$\bar{\tau}_x = 0, \ \bar{\tau}_y = 0. \tag{3.4}$$

For the thermal model, Robin boundary conditions are used

$$-k\frac{\partial T}{\partial \mathbf{n}_\Gamma} = h_{air}\left[T - T_{air}\right]. \tag{3.5}$$

In case of a contact, there are two possibilities to be used in the mechanical model. First is to use traction between the slice and the groove surface as determined by coefficient of friction. Traction boundary conditions at the contact will be numerically implemented in the future. Second is to use the sticking boundary condition. For the rolling simulation in this dissertation, the sticking boundary condition is applied

$$u_x = \bar{u}_x,\ u_y = \bar{u}_y. \tag{3.6}$$

In this case it is important to define the contact length. For the thermal model over the region with the contact, again Robin type is used

$$-k\frac{\partial T}{\partial \mathbf{n}_\Gamma} = h_{roll}\left[T - T_{roll}\right], \tag{3.7}$$

however with different reference temperature and heat transfer coefficient. Examples of boundary conditions for mechanical and thermal models are shown in Figure 3.5.

The simulation is a sequence of calculations in a predefined order. The details can be seen in Figure 3.6. Initial conditions have to be known in order to start the simulation. These initial conditions are: Initial temperature field when $t = t_0$, initial size of the slice which is actually top right quarter of the whole slice, initial or entry velocity of the slice v_{entry} together with the initial area $A(t_0)$ which are needed to calculate the velocity of any calculated slice during the simulation due to conservation of volume $A(t_0)v(t_0) = A(t)v(t)$, material type or properties such as effective stress-effective strain relation for a rigid plastic material or Young's modulus and Poisson's ratio based on various temperature values for elastic model. Also some other parameters are needed to define the boundary conditions such as the ambient temperature T_{air} or roll temperature T_{roll} and the heat transfer coefficients to air h_{air} and roll h_{roll}. The area of a slice is calculated as sum of area of triangles as shown in Figure 3.4, where one point

is always at the origin and two points are on the side boundary. The total number of nodes on the side boundary is N_{side} and area is calculated through positions of these two nodes on the side boundary as

$$A = \sum_{i=1}^{N_{side}-1} \frac{\left| p_{xi} p_{yi+1} - p_{xi+1} p_{yi} \right|}{2}, \tag{3.8}$$

where p_x and p_y are the components of the position vector **p** in Cartesian coordinate system.

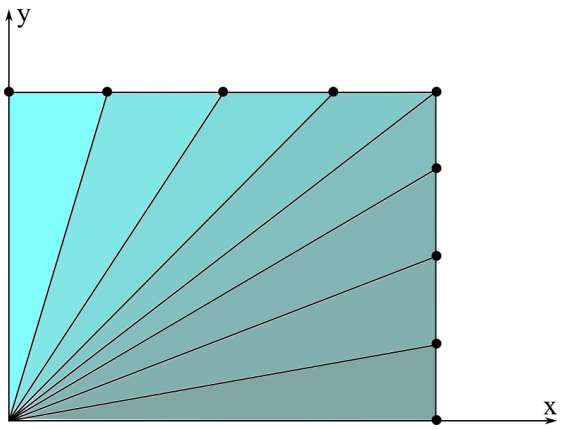

Figure 3.4: Scheme of triangles used in the calculation of a slice area. Side boundary nodes are shown by black dots.

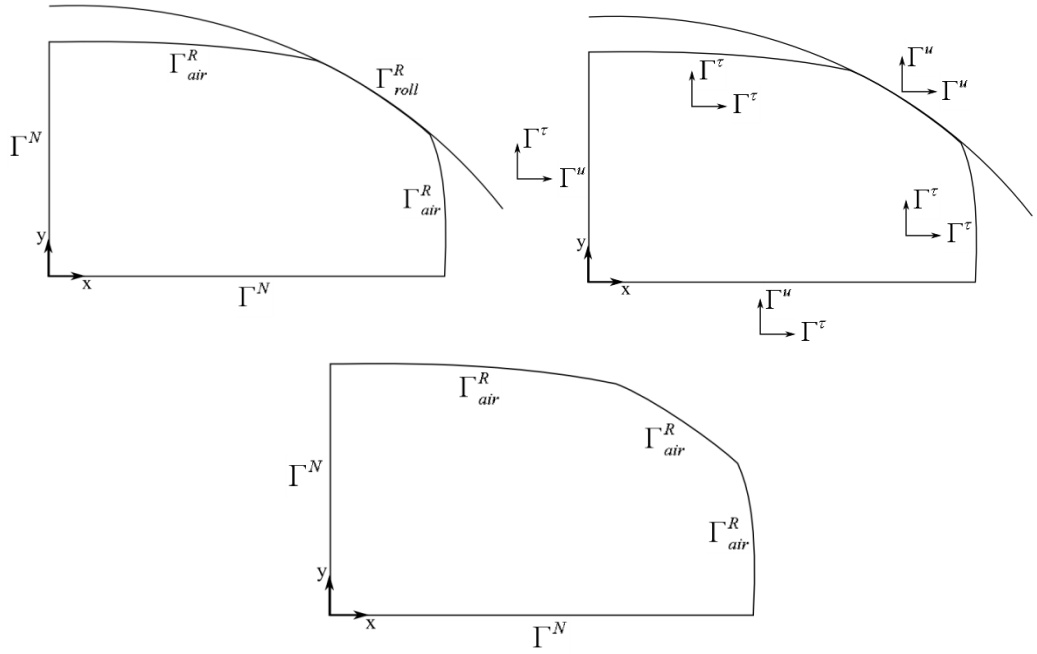

Figure 3.5: A scheme of boundaries with different boundary conditions for the thermal model (on top left) and for the mechanical model (on top right), when there is a contact with a roll. The boundary conditions for the thermal model are also shown (on bottom) when there is no contact.

The rolling simulation is done through calculation over aligned slices towards the rolling direction. There is a sequence of calculation steps for each slice and these steps are repeated for every slice until the end of the rolling process. The details can be seen in the flowchart of the rolling simulation in Figure 3.6.

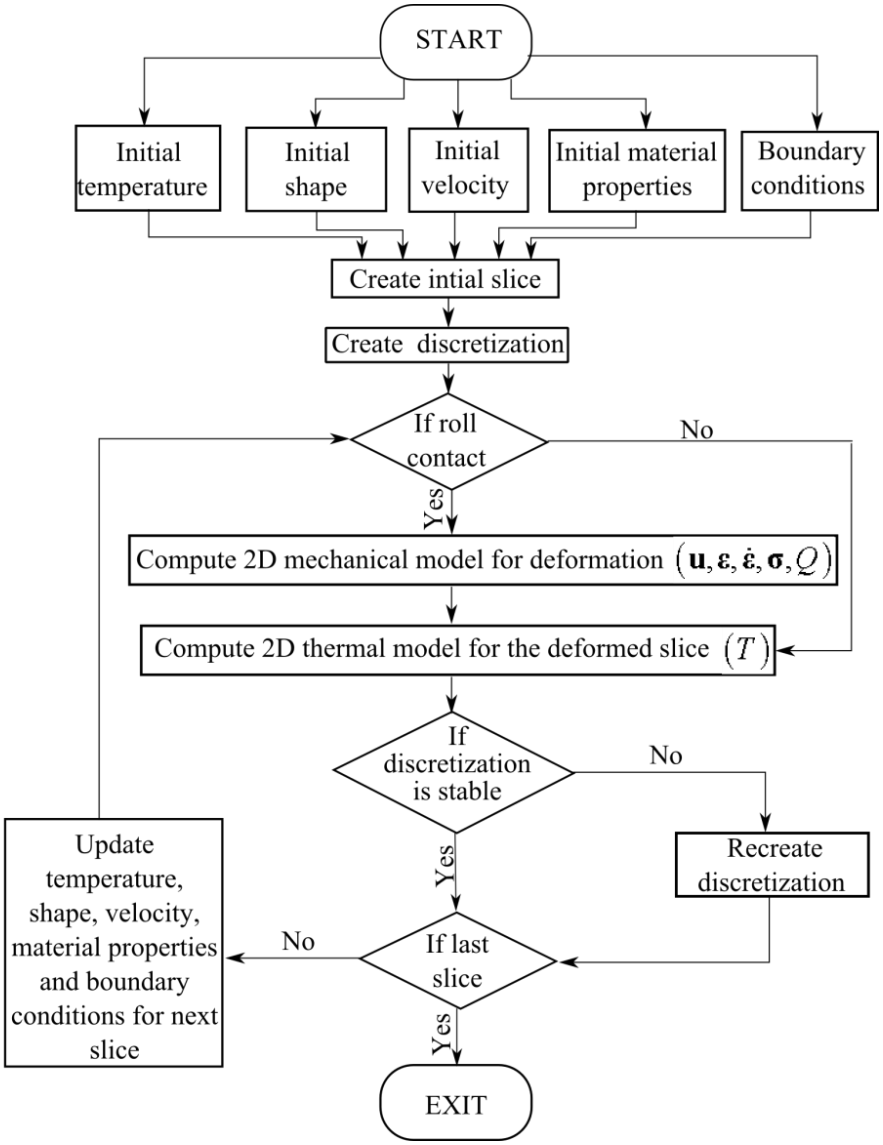

Figure 3.6: Flowchart of the simulation.

3.2 Modelling of hot rolling

The set of parameters, which define the rolling simulation are: heat transfer coefficient to air h_{air}, heat transfer coefficient to roll h_{roll}, specific heat, thermal conductivity and density of steel c_p, k, ρ. Initial slice shape, initial slice rolling temperature T_{fur}, initial slice rolling speed v_{entry}, ambient temperature T_{ref}, roll

temperature T_{roll}, Taylor-Quenny parameter η, effective stress definition $\bar{\sigma}\left(\bar{\varepsilon},\dot{\bar{\varepsilon}},T\right)$ or in elastic case Young's modulus $E\left(T\right)$ and Poisson ratio $\nu\left(T\right)$.

In the simulation initial slice is positioned with a certain distance from the centre of the first rolling stand, and that position is assumed as $z\left(t_0\right)=0$ at $t=t_0$. The simulation is based on incremental solutions. These incremental steps can be defined in terms of time or position. In this dissertation a position depended incremental steps are chosen with two different slice position steps. If the slice is not influenced by the roll then an incremental step of $\Delta z=10\,\text{mm}$ is used, otherwise an incremental step $\Delta z=5$ mm is used. Therefore, the positions of the slices through the simulation are predefined, however the corresponding time between the slices is calculated during the simulation as

$$\Delta t=\frac{A\left(t\right)\Delta z}{A\left(t_0\right)v\left(t_0\right)}. \tag{3.9}$$

If the simulation had been based on predefined time increments then the corresponding time values of slices would have been previously set and positions and velocities in the rolling direction would have been calculated during the simulation.

3.3 Rolling schedule

A rolling schedule consists of a sequence of rolling stands. Each rolling stand might have different orientation, such as vertical or horizontal. For large shape changes, the rolling schedule usually consists of varying orientation of the rolling stands in a sequence. The roll in the rolling stand has specific groove geometry. It can be flat or have some other shape. Grooves are used for shape rolling. Therefore, a further description is needed for grooves in a geometrical sense. An example of a rolling schedule can be seen in Figure 3.7.

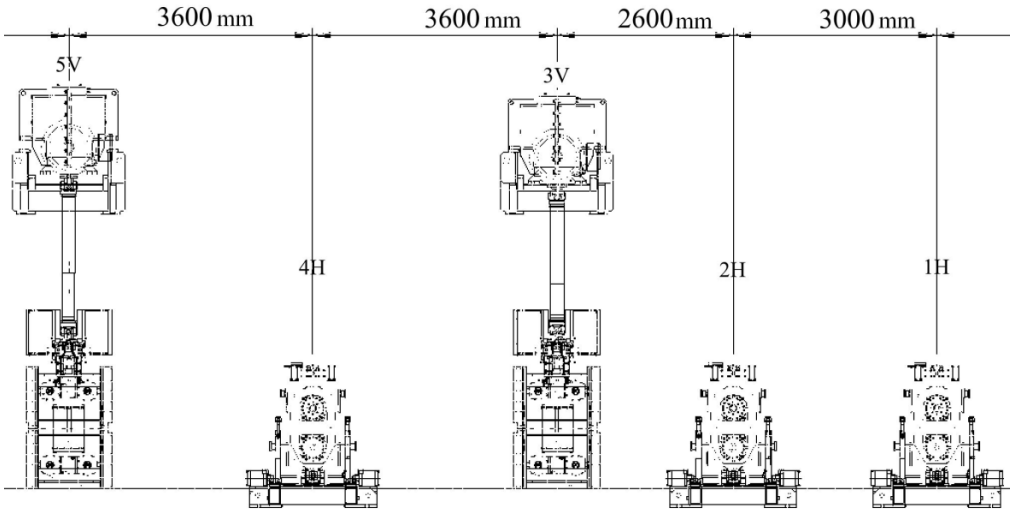

Figure 3.7: An exmple of rolling schedule consisting of horizontal (H) and vertical (V) rolling stands.

3.3.1 Groove dimensions

A groove is a particular shape which can be of oval, diamond, box, round or of the some other type. A cross section of the groove should be calculated for each position of the slice towards the rolling direction. Thus, all the geometrical parameters should be known for each groove. In the present dissertation, grooves, such as schematically plotted in Figure 3.8, are assumed.

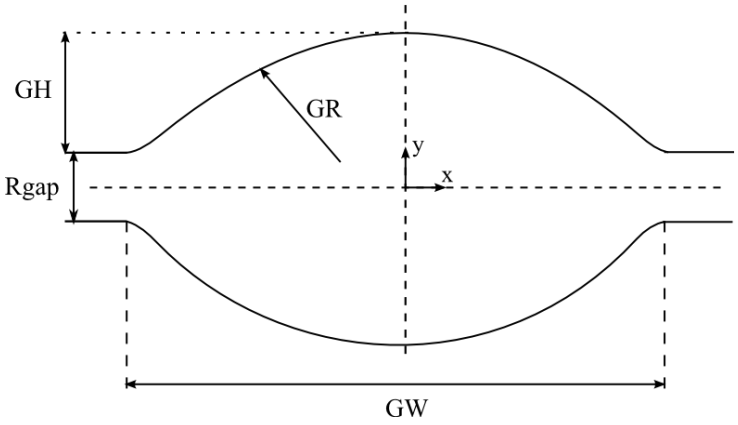

Figure 3.8: A horizontal oval groove dimensions. GH is the groove height, GR is the groove radius, GW is the groove width and Rgap is the roll gap.

In the simulation, 15 imaginary groove nodes are created on the groove, each with different radial distance, groove point radius (GPR), from the centre of the roll which can be seen on Figure 3.9. All these points are positioned for a given slice position p_{zS} and then the vertical groove can be redrawn with discrete groove lines between groove points $GPR_i\left(p_{xi}, p_{yi}\right)$ as seen on Figures 3.9 and 3.10. These groove points, for a slice position p_{zS}, under the groove, which has roll centre positioned at p_{zG} can be created in this way

$$p_{xi} = \frac{GW}{2\left(N_G - 1\right)}\left(i-1\right); i = 1, 2, .. N_G, \tag{3.10}$$

$$p_{yi} = RR - \sqrt{\left(p_{zG} - p_{zS}\right)^2 + \left(GPR_i\right)^2} + \frac{R_{gap}}{2}; i = 1, 2, .., N_G, \tag{3.11}$$

where N_G is the total number of groove nodes and GPR_i is the groove point radius for each groove node as shown in Figure 3.9. In case of horizontal groove orientation, definitions of p_{xi} and p_{yi} are swapped.

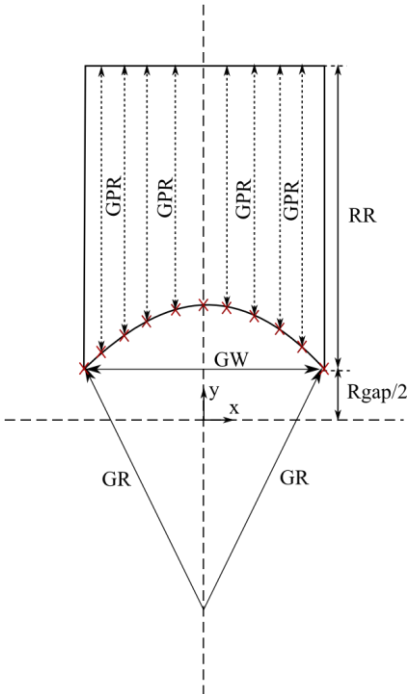

Figure 3.9: Groove point radii GPR are defined for each point on the groove. Only the top roll is shown in the Figure.

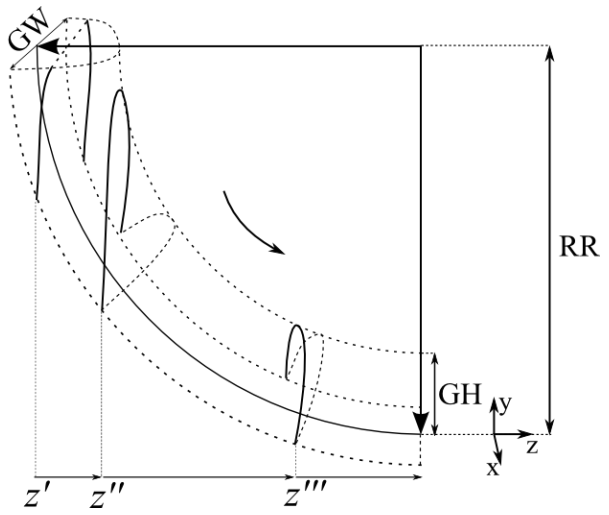

Figure 3.10: Corresponding groove lines used in the simulation for slices along the rolling direction with positions z', z'' and z'''. RR is the roll radius, GH is the groove height, GW is the groove width and z is the position of the groove line towards the rolling direction. Only the top roll is shown.

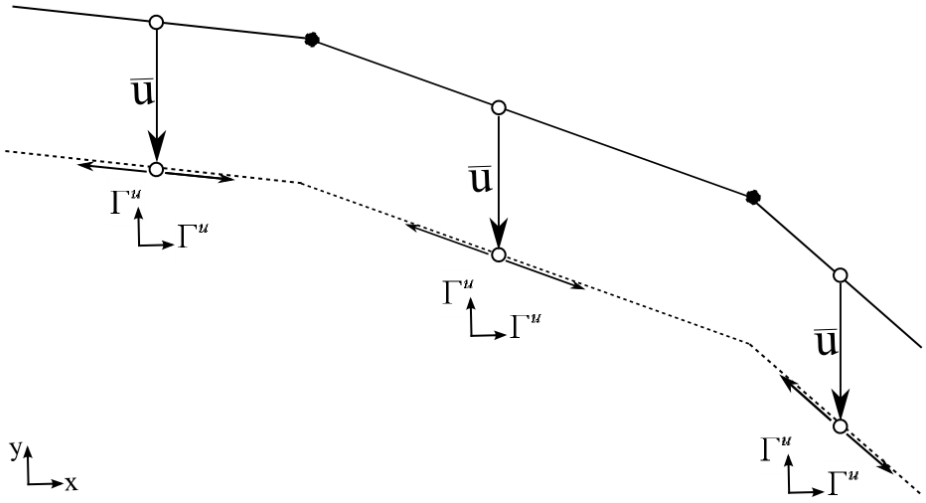

Figure 3.11: Discrete groove lines with contacted points and reduction $\bar{\mathbf{u}}$. New position of the groove is drawn with a dashed line.

A groove slice is created by connecting groove nodes as shown in Figure 3.11. All the groove slices through the simulation can be previously created for every incrementally increasing slice position which is under the groove. An example of groove slices can be seen in Figure 3.12 over the predefined slice until the position of the centre of the rolling stand. A groove slice can be drawn as soon

as the slice enters below the roll regardless of a contact. Groove slices before the contact are drawn for every 5 mm towards the rolling direction which are aligned from top to bottom until the contact. The groove slices are also needed for determination of contact between groove and slice. If there is a contact, also the amount of prescribed displacement is obtained as shown in Figure 3.13 due to sticking boundary condition. All of these physical assumptions presented in this chapter have to be defined in the pre-process of the simulation. This is mandatory step for the rolling simulation to start. An example of all the groove slices of a roll is shown in Figure 3.14.

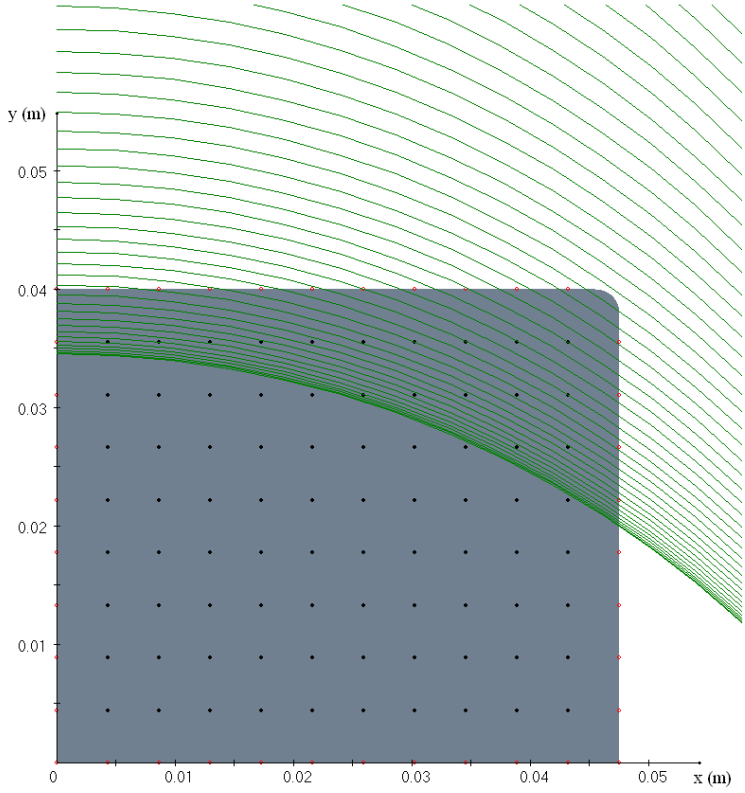

Figure 3.12: Groove slices for an oval groove through a horizontal rolling stand drawn for every 5 mm towards the rolling direction until the centre of the roll. Roll radius is 450 mm, groove radius is 85 mm and roll gap is 17 mm.

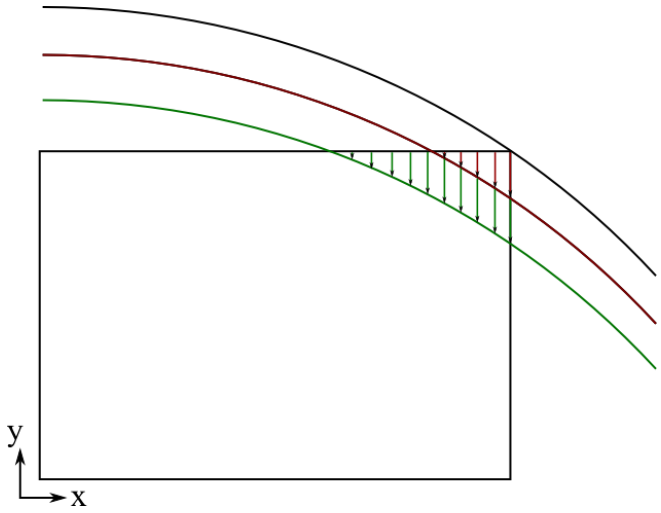

Figure 3.13: Scheme of groove lines and contact on the boundary with sticking boundary conditions. Red and green arrows show the amount of movement at the boundary for a corresponding slice of the red groove. The same assumption is done for the slice of the green groove.

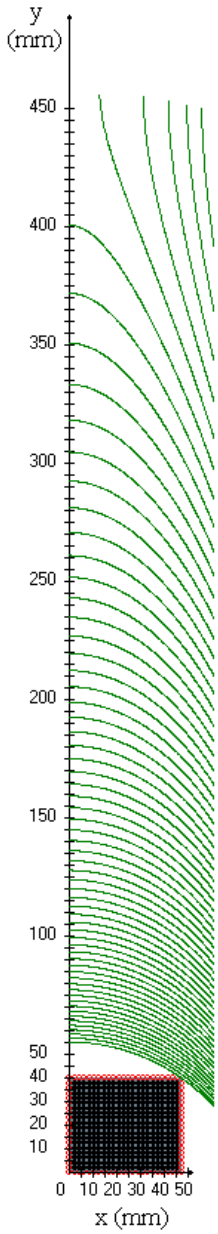

Figure 3.14: Corresponding groove lines depending on the slice position are drawn starting from the 450 mm away from the roll centre until the contact location at 125 mm away from the roll centre where the radius of the roll is 450 mm and groove radius is 85 mm.

4 Meshless Solution Procedure

In Chapter 4 the LRBFCM solution procedure for mechanical and thermal models are given. In both models a local strong form solution procedure is used. This leads in the mechanical model to formation and solution of a global sparse matrix for each deformation step and in the thermal model to formation and solution by a set of local matrices for each time step. The solution of the non-linear plastic material behaviour is achieved by Newton-Raphson iteration method. The details of numerical implementation of specific boundary conditions are given. The positioning and repositioning of the nodes relies on application of Elliptic Node Generation (ENG) with Transfinite Interpolation (TFI). A summary of the numerical implementation is given.

4.1 Local radial basis function collocation method for mechanical model

The meshless solution is in the present work based on discretization of the solution with RBF shape functions augmented with polynomial functions over the collocation nodes. The details are discussed and explained in [Šarler and Vertnik, 2006] and [Šarler, 2007]. The solution is based on discretization of the unknowns which is obtained from overlapping local influence domains created for each central node as shown in Figure 4.1. The performance of described LRBFCM has been assessed for large deformations by comparison [Hanoglu, Islam and Šarler, 2011] with FEM.

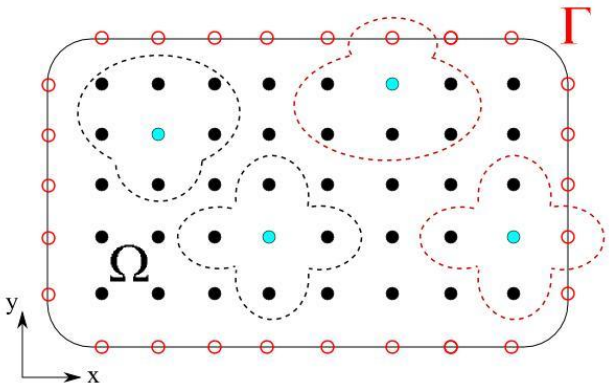

Figure 4.1: A scheme of a computational domain with collocation nodes on the boundary Γ and domain Ω. Examples of typical influence domains for calculated nodes are shown as blue dots in the centre. The influence domain that involves only domain points is given by a dashed black line and the influence domain that involves a boundary point is described by a dashed red line.

7 nodes are used in an influence domain in the mechanical model and 5 nodes for the thermal model. This is sufficient to calculate the required derivatives in the mechanical and thermal models, respectively. The 4 neighbouring nodes for each internal node are chosen from the 2 closest nodes on vertical and horizontal node order. In case of 7 nodded influence domains, additionally 2 closest nodes are chosen regarding the central node, however these nodes cannot be on the boundary. Examples of these two types of influence domains can be seen in Figure 4.1. In the mechanical model, 5 nodded influence domain is not enough to get accurate results, therefore at least one more additional node needs to be used, which has different position on *x* and *y* regarding the central node.

During the solution procedure a slice is taken as a computational domain. A meshless numerical approach, described in the continuation, is used here for the solution of displacements and temperatures. All the other unknowns of the mechanical model can be obtained through known displacement values. The discretization of the displacement vector is done locally by using the nodes in the respective influence domain. The local displacement discretization is used to create a global system of equations for solving the displacement in each of the nodes.

The slice is discretized by a total number of the nodes

$$N = N_\Omega + N_\Gamma , \tag{4.1}$$

where N_Ω is the number of the nodes in the domain as well as the number of overlapping influence domains, and N_Γ is the number of the nodes on the boundary.

The governing equations in Tables 2.1, 2.2 and 2.3 require the displacement vector $\mathbf{u}$ to be determined, where its components in 2D can be discretized as

$$u_x(\mathbf{p}) = \sum_{n=1}^{{}_l N_\omega + N_p} {}_l\psi_n(\mathbf{p})\, {}_l\alpha_{xn} \,, \tag{4.2}$$

$$u_y(\mathbf{p}) = \sum_{n=1}^{{}_l N_\omega + N_p} {}_l\psi_n(\mathbf{p})\, {}_l\alpha_{yn} \,. \tag{4.3}$$

where ${}_l\psi_n$ are RBF interpolation functions together with the first order polynomial functions, l is the influence domain index, ${}_l\alpha_{xn}, {}_l\alpha_{yn}$ are the collocation coefficients to be determined, ${}_l N_\omega$ is the number of nodes in the influence domain and in mechanical model considered as 7, N_p is the number of polynomial functions and $\mathbf{p}$ is the position vector in a 2D Cartesian coordinate system

$$\mathbf{p} = p_x \mathbf{i}_x + p_y \mathbf{i}_y \,, \tag{4.4}$$

and $\mathbf{i}_x, \mathbf{i}_y$ are the Cartesian base vectors. Radial basis functions used in the calculations are multiquadric (MQ) by [Franke, 1982] and defined as

$$\psi_n(\mathbf{p}) = \sqrt{\left(p_x - p_{xn}\right)^2 / x_{\max}^2 + \left(p_y - p_{yn}\right)^2 / y_{\max}^2 + c^2} \,, \tag{4.5}$$

where $\left(p_{xn}, p_{yn}\right)$ is the position of the n$^{\text{th}}$ neighbouring point and c is a free parameter chosen as 32 in the present work which is consistent with the research done by [Vertnik, 2010] and [Mramor, 2014]. A detailed study on optimal shape parameters is made by [Wang and Liu, 2002]. $x_{\max}$ and $y_{\max}$ are scaling parameters, chosen as maximum axial distances in between considered nodes.

Same function can also be defined for each node in an influence domain

$$ {}_l\psi_n\left(\mathbf{p}_{k(l,m)}\right)=\sqrt{\left(p_{xk(l,m)}-p_{xk(l,n)}\right)^2/{}_l x_{\max}^2+\left(p_{yk(l,m)}-p_{yk(l,n)}\right)^2/{}_l y_{\max}^2+c^2}; \quad \text{n=1,2,..,} N_\omega;\ m=1,2,..,N_\omega, k=1,2,..,N \tag{4.6} $$

We choose 3 polynomial augmentation functions, i.e. $N_p=3$, defined as

$$ {}_l\psi_{N_\omega+1}\left(\mathbf{p}_{k(l,m)}\right)=1, \tag{4.7} $$

$$ {}_l\psi_{N_\omega+2}\left(\mathbf{p}_{k(l,m)}\right)=p_{xk(l,m)}-p_{xk(l,1)}, \tag{4.8} $$

$$ {}_l\psi_{N_\omega+3}\left(\mathbf{p}_{k(l,m)}\right)=p_{yk(l,m)}-p_{yk(l,1)}, \tag{4.9} $$

where k is the function returning global node index, m is the node index in influence domain l, l is the influence domain index, $k(l,1)$ is the global index of central node in influence domain l, ${}_l x_{\max}$ and ${}_l y_{\max}$ are the maximum distances between the nodes in an influence domain in *x* and *y* directions.

The involved first and second derivatives of the RBF and polynomial functions are

$$ \frac{\partial\,{}_l\psi_n}{\partial p_\phi}=\frac{\left(\dfrac{p_\phi-{}_l p_{\phi n}}{{}_l\phi_{\max}^2}\right)}{\sqrt{\left(\dfrac{p_x-{}_l p_{xn}}{{}_l x_{\max}}\right)^2+\left(\dfrac{p_y-{}_l p_{yn}}{{}_l y_{\max}}\right)^2+c^2}}; \phi=x,y; n=1,2,..,{}_l N_\omega, \tag{4.10} $$

$$ \frac{\partial^2\,{}_l\psi_n}{\partial p_x^2}=\frac{\dfrac{1}{{}_l x_{\max}^2}\left(\left(\dfrac{p_y-{}_l p_{yn}}{{}_l y_{\max}}\right)^2+c^2\right)}{\left(\left(\dfrac{p_x-{}_l p_{xn}}{{}_l x_{\max}}\right)^2+\left(\dfrac{p_y-{}_l p_{yn}}{{}_l y_{\max}}\right)^2+c^2\right)^{3/2}}; n=1,2,...,{}_l N_\omega, \tag{4.11} $$

$$\frac{\partial^2 {}_l\psi_n}{\partial p_y^2} = \frac{\frac{1}{{}_l y_{\max}^2}\left(\left(\frac{p_x - {}_l p_{xn}}{{}_l x_{\max}}\right)^2 + c^2\right)}{\left(\left(\frac{p_x - {}_l p_{xn}}{x_{\max}}\right)^2 + \left(\frac{p_y - {}_l p_{yn}}{y_{\max}}\right)^2 + c^2\right)^{3/2}}; n = 1, 2, ..., {}_l N_\omega, \tag{4.12}$$

$$\frac{\partial^2 {}_l\psi_n}{\partial p_x \partial p_y} = -\frac{\left(\frac{p_y - {}_l p_{yn}}{{}_l y_{\max}^2}\right)\left(\frac{p_x - {}_l p_{xn}}{{}_l x_{\max}^2}\right)}{\left(\left(\frac{p_x - {}_l p_{xn}}{x_{\max}}\right)^2 + \left(\frac{p_y - {}_l p_{yn}}{y_{\max}}\right)^2 + c^2\right)^{3/2}}; n = 1, 2, ..., {}_l N_\omega \cdot \tag{4.13}$$

$$\frac{\partial {}_l\psi_{N_\omega+1}}{\partial p_i} = 0; i = x, y. \tag{4.14}$$

$$\frac{\partial {}_l\psi_{N_\omega+2}}{\partial p_x} = 1, \frac{\partial {}_l\psi_{N_\omega+2}}{\partial p_y} = 0, \frac{\partial {}_l\psi_{N_\omega+3}}{\partial p_x} = 0, \frac{\partial {}_l\psi_{N_\omega+3}}{\partial p_y} = 1. \tag{4.15}$$

All the second derivatives of the first order polynomial functions in Equations (4.7), (4.8) and (4.9) vanish.

The application of displacement discretization in (4.2) and (4.3) in the governing equations for elastic material in (2.35) and (2.36) gives the following expression

$$\begin{aligned} &C_{11} \sum_{n=1}^{{}_l N_\omega + N_p} \frac{\partial^2 {}_l\psi_n(\mathbf{p})}{\partial p_x^2} {}_l\alpha_{xn} + (C_{12} + C_{33}) \sum_{n=1}^{{}_l N_\omega + N_p} \frac{\partial^2 {}_l\psi_n(\mathbf{p})}{\partial p_y \partial p_x} {}_l\alpha_{yn} \\ &+ (C_{13} + C_{31}) \sum_{n=1}^{{}_l N_\omega + N_p} \frac{\partial^2 {}_l\psi_n(\mathbf{p})}{\partial p_y \partial p_x} {}_l\alpha_{xn} + C_{13} \sum_{n=1}^{{}_l N_\omega + N_p} \frac{\partial^2 {}_l\psi_n(\mathbf{p})}{\partial p_x^2} {}_l\alpha_{yn} \\ &+ C_{32} \sum_{n=1}^{{}_l N_\omega + N_p} \frac{\partial^2 {}_l\psi_n(\mathbf{p})}{\partial p_y^2} {}_l\alpha_{yn} + C_{33} \sum_{n=1}^{{}_l N_\omega + N_p} \frac{\partial^2 {}_l\psi_n(\mathbf{p})}{\partial p_y^2} {}_l\alpha_{xn} + d_x(\mathbf{p}) = 0, \end{aligned} \tag{4.16}$$

$$\begin{aligned}
&\left(C_{21}+C_{33}\right)\sum_{n=1}^{{}_{l}N_{\omega}+N_{p}}\frac{\partial^{2}{}_{l}\psi_{n}\left(\mathbf{p}\right)}{\partial p_{y}\partial p_{x}}{}_{l}\alpha_{xn}+C_{22}\sum_{n=1}^{{}_{l}N_{\omega}+N_{p}}\frac{\partial^{2}{}_{l}\psi_{n}\left(\mathbf{p}\right)}{\partial p_{y}^{2}}{}_{l}\alpha_{yn}\\
&+C_{23}\sum_{n=1}^{{}_{l}N_{\omega}+N_{p}}\frac{\partial^{2}{}_{l}\psi_{n}\left(\mathbf{p}\right)}{\partial p_{y}^{2}}{}_{l}\alpha_{xn}+\left(C_{23}+C_{32}\right)\sum_{n=1}^{{}_{l}N_{\omega}+N_{p}}\frac{\partial^{2}{}_{l}\psi_{n}\left(\mathbf{p}\right)}{\partial p_{y}\partial p_{x}}{}_{l}\alpha_{yn}\\
&+C_{31}\sum_{n=1}^{{}_{l}N_{\omega}+N_{p}}\frac{\partial^{2}{}_{l}\psi_{n}\left(\mathbf{p}\right)}{\partial p_{x}^{2}}{}_{l}\alpha_{xn}+\mathrm{C}_{33}\sum_{n=1}^{{}_{l}N_{\omega}+N_{p}}\frac{\partial^{2}{}_{l}\psi_{n}\left(\mathbf{p}\right)}{\partial p_{x}^{2}}{}_{l}\alpha_{yn}+d_{y}\left(\mathbf{p}\right)=0.
\end{aligned}\tag{4.17}$$

It is important to note that the stiffness matrix components might also be different in each of the nodes, depending on the material type used. The equations (4.9) and (4.10) are simplified to

$$\begin{aligned}
&\sum_{n=1}^{{}_{l}N_{\omega}+N_{p}}{}_{l}\alpha_{xn}\left[\begin{array}{l}C_{11}\dfrac{\partial^{2}{}_{l}\psi_{n}\left(\mathbf{p}\right)}{\partial p_{x}^{2}}+C_{33}\dfrac{\partial^{2}{}_{l}\psi_{n}\left(\mathbf{p}\right)}{\partial p_{y}^{2}}\\ +\left(C_{13}+C_{31}\right)\dfrac{\partial^{2}{}_{l}\psi_{n}\left(\mathbf{p}\right)}{\partial p_{y}\partial p_{x}}\end{array}\right]\\
&+\sum_{n=1}^{{}_{l}N_{\omega}+N_{p}}{}_{l}\alpha_{yn}\left[\begin{array}{l}\left(C_{12}+C_{33}\right)\dfrac{\partial^{2}{}_{l}\psi_{n}\left(\mathbf{p}\right)}{\partial p_{y}\partial p_{x}}\\ +C_{13}\dfrac{\partial^{2}{}_{l}\psi_{n}\left(\mathbf{p}\right)}{\partial p_{x}^{2}}+C_{32}\dfrac{\partial^{2}{}_{l}\psi_{n}\left(\mathbf{p}\right)}{\partial p_{y}^{2}}\end{array}\right]+d_{x}\left(\mathbf{p}\right)=0,
\end{aligned}\tag{4.18}$$

$$\begin{aligned}
&\sum_{n=1}^{{}_{l}N_{\omega}+N_{p}}{}_{l}\alpha_{xn}\left[\begin{array}{l}C_{31}\dfrac{\partial^{2}{}_{l}\psi_{n}\left(\mathbf{p}\right)}{\partial p_{x}^{2}}+C_{23}\dfrac{\partial^{2}{}_{l}\psi_{n}\left(\mathbf{p}\right)}{\partial p_{y}^{2}}\\ +\left(C_{21}+C_{33}\right)\dfrac{\partial^{2}{}_{l}\psi_{n}\left(\mathbf{p}\right)}{\partial p_{y}\partial p_{x}}\end{array}\right]\\
&+\sum_{n=1}^{{}_{l}N_{\omega}+N_{p}}{}_{l}\alpha_{yn}\left[\begin{array}{l}C_{22}\dfrac{\partial^{2}{}_{l}\psi_{n}\left(\mathbf{p}\right)}{\partial p_{y}^{2}}+\mathrm{C}_{33}\dfrac{\partial^{2}{}_{l}\psi_{n}\left(\mathbf{p}\right)}{\partial p_{x}^{2}}\\ +\left(C_{23}+C_{32}\right)\dfrac{\partial^{2}{}_{l}\psi_{n}\left(\mathbf{p}\right)}{\partial p_{y}\partial p_{x}}\end{array}\right]+d_{y}\left(\mathbf{p}\right)=0.
\end{aligned}\tag{4.19}$$

For each node in an influence domain, except for the boundary nodes, displacement discretization can be written as in equations (4.2) and (4.3). For a boundary node, the displacement discretization is implemented in the corresponding boundary equation for that node. Therefore, a local system of

equations can be written in a matrix form for each influence domain to obtain $2\left({}_{l}N_{\omega}+N_{p}\right)$ collocation constants from the equation

$$ {}_{l}\boldsymbol{\Psi}\,{}_{l}\boldsymbol{\alpha}={}_{l}\mathbf{b}, \tag{4.20}$$

where ${}_{l}\boldsymbol{\alpha}=\left[{}_{l}\alpha_{x1},{}_{l}\alpha_{y1},....,{}_{l}\alpha_{x\left({}_{l}N_{\omega}+N_{p}\right)},{}_{l}\alpha_{y\left({}_{l}N_{\omega}+N_{p}\right)}\right]^{\mathrm{T}}$ and ${}_{l}\boldsymbol{\Psi}$ is the local interpolation matrix with a size of $2\left({}_{l}N_{\omega}+N_{p}\right)\times 2\left({}_{l}N_{\omega}+N_{p}\right)$. Its components are defined as

$$ {}_{l}\Psi_{2m-1,2n-1}=\left\{\begin{array}{l}{}_{l}\psi_{n}\left(\mathbf{p}_{k(l,m)}\right);\mathbf{p}\notin\Gamma^{\tau x}\\ \left[\begin{array}{l}n_{xk(l,m)}\left(C_{11}\dfrac{\partial\,{}_{l}\psi_{n}\left(\mathbf{p}_{k(l,m)}\right)}{\partial p_{x}}\right)\\ +n_{yk(l,m)}\left(C_{33}\dfrac{\partial\,{}_{l}\psi_{n}\left(\mathbf{p}_{k(l,m)}\right)}{\partial p_{y}}\right)\end{array}\right];\mathbf{p}\in\Gamma^{\tau x}\end{array}\right\};m=1,2,..,2\,{}_{l}N_{\omega}\ , \tag{4.21}$$

$$ {}_{l}\Psi_{2m-1,2n}=\left\{\begin{array}{l}0;\mathbf{p}\notin\Gamma^{\tau y}\\ \left[\begin{array}{l}n_{xk(l,m)}\left(C_{12}\dfrac{\partial\,{}_{l}\psi_{n}\left(\mathbf{p}_{k(l,m)}\right)}{\partial p_{y}}\right)\\ +n_{yk(l,m)}\left(C_{33}\dfrac{\partial\,{}_{l}\psi_{n}\left(\mathbf{p}_{k(l,m)}\right)}{\partial p_{x}}\right)\end{array}\right];\mathbf{p}\in\Gamma^{\tau x}\end{array}\right\};m=1,2,..,2\,{}_{l}N_{\omega}\,, \tag{4.22}$$

$$ {}_{l}\Psi_{2m,2n-1}=\left\{\begin{array}{l}0;\mathbf{p}\notin\Gamma^{\tau y}\\ \left[\begin{array}{l}n_{xk(l,m)}\left(C_{33}\dfrac{\partial\,{}_{l}\psi_{n}\left(\mathbf{p}_{k(l,m)}\right)}{\partial p_{y}}\right)\\ +n_{yk(l,m)}\left(C_{21}\dfrac{\partial\,{}_{l}\psi_{n}\left(\mathbf{p}_{k(l,m)}\right)}{\partial p_{x}}\right)\end{array}\right];\mathbf{p}\in\Gamma^{\tau y}\end{array}\right\};m=1,2,..,2\,{}_{l}N_{\omega}\,, \tag{4.23}$$

$$ {}_{l}\Psi_{2m,2n} = \left\{ \begin{array}{l} {}_{l}\psi_{n}\left(\mathbf{p}_{k(l,m)}\right); \mathbf{p} \notin \Gamma^{\tau y} \\ \left[\begin{array}{l} n_{xk(l,m)} \left(C_{33} \dfrac{\partial\, {}_{l}\psi_{n}\left(\mathbf{p}_{k(l,m)}\right)}{\partial p_{x}} \right) \\ +n_{yk(l,m)} \left(+C_{22} \dfrac{\partial\, {}_{l}\psi_{n}\left(\mathbf{p}_{k(l,m)}\right)}{\partial p_{y}} \right) \end{array} \right]; \mathbf{p} \in \Gamma^{\tau y} \end{array} \right\}; m = 1,2,..,2\,{}_{l}N_{\omega}. \tag{4.24} $$

$$ {}_{l}\Psi_{m,n} = {}_{l}\Psi_{n,m}; m = 2\,{}_{l}N_{\omega}+1, 2\,{}_{l}N_{\omega}+2,..,2\left({}_{l}N_{\omega}+N_{p}\right); n = 1,2,..,2\,{}_{l}N_{\omega}. \tag{4.25} $$

$$ {}_{l}\Psi_{m,n} = 0; m = 2\,{}_{l}N_{\omega}+1, 2\,{}_{l}N_{\omega}+2,..,2\left({}_{l}N_{\omega}+N_{p}\right); n > 2\,{}_{l}N_{\omega}. \tag{4.26} $$

The adjacent vector ${}_{l}\mathbf{b}$ is defined as

$$ {}_{l}b_{2m-1} \begin{cases} u_{xk(l,m)}; \mathbf{p} \in \Omega \\ \bar{u}_{xk(l,m)}; \mathbf{p} \in \Gamma^{ux} \\ \bar{\tau}_{xk(l,m)}; \mathbf{p} \in \Gamma^{\tau x} \end{cases}, {}_{l}b_{2m} \begin{cases} u_{yk(l,m)}; \mathbf{p} \in \Omega \\ \bar{u}_{yk(l,m)}; \mathbf{p} \in \Gamma^{uy} \\ \bar{\tau}_{yk(l,m)}; \mathbf{p} \in \Gamma^{\tau y} \end{cases}; m = 1,2,..,{}_{l}N_{\omega}, \tag{4.27} $$

$$ {}_{l}b_{m} = 0; m > 2\,{}_{l}N_{\omega}. \tag{4.28} $$

The coefficients are obtained from the following condition

$$ {}_{l}\boldsymbol{\alpha} = {}_{l}\boldsymbol{\Psi}^{-1}\,{}_{l}\mathbf{b}. \tag{4.29} $$

The coefficients ${}_{l}\alpha_{xn}$, ${}_{l}\alpha_{yn}$ can be rewritten as

$$ {}_{l}\alpha_{xn} = \sum_{r=1}^{{}_{l}N_{\omega}} {}_{l}\Psi^{-1}_{(2n-1)r}\,{}_{l}b_{2r-1}, \; {}_{l}\alpha_{yn} = \sum_{r=1}^{{}_{l}N_{\omega}} {}_{l}\Psi^{-1}_{(2n)r}\,{}_{l}b_{2r}. \tag{4.30} $$

The collocation coefficients in local system of equations (as in Equation (4.30)) are subsequently used to replace all coefficients in the governing equation (4.16) and (4.17). Therefore the governing equation can now be written with collocation coefficients replaced by the displacement values and/or boundary conditions

$$
\begin{aligned}
&\sum_{n=1}^{{}_{l}N_{\omega}+N_{p}} \sum_{r=1}^{2\,{}_{l}N_{\omega}} {}_{l}\Psi^{-1}_{(2n-1)r}\, {}_{l}b_{r} \begin{bmatrix} C_{11}\dfrac{\partial^{2}\,{}_{l}\psi_{n}(\mathbf{p})}{\partial p_{x}^{2}} + C_{33}\dfrac{\partial^{2}\,{}_{l}\psi_{n}(\mathbf{p})}{\partial p_{y}^{2}} \\ +\left(C_{13}+C_{31}\right)\dfrac{\partial^{2}\,{}_{l}\psi_{n}(\mathbf{p})}{\partial p_{y}\partial p_{x}} \end{bmatrix} \\
&+\sum_{n=1}^{{}_{l}N_{\omega}+N_{p}} \sum_{r=1}^{2\,{}_{l}N_{\omega}} {}_{l}\Psi^{-1}_{(2n)r}\, {}_{l}b_{r} \begin{bmatrix} C_{13}\dfrac{\partial^{2}\,{}_{l}\psi_{n}(\mathbf{p})}{\partial p_{x}^{2}} + C_{32}\dfrac{\partial^{2}\,{}_{l}\psi_{n}(\mathbf{p})}{\partial p_{y}^{2}} \\ +\left(C_{12}+C_{33}\right)\dfrac{\partial^{2}\,{}_{l}\psi_{n}(\mathbf{p})}{\partial p_{y}\partial p_{x}} \end{bmatrix} \\
&+d_{x}(\mathbf{p})=0,
\end{aligned}
\tag{4.31}
$$

$$
\begin{aligned}
&\sum_{n=1}^{{}_{l}N_{\omega}+N_{p}} \sum_{r=1}^{2\,{}_{l}N_{\omega}} {}_{l}\Psi^{-1}_{(2n-1)r}\, {}_{l}b_{r} \begin{bmatrix} C_{31}\dfrac{\partial^{2}\,{}_{l}\psi_{n}(\mathbf{p})}{\partial p_{x}^{2}} + C_{23}\dfrac{\partial^{2}\,{}_{l}\psi_{n}(\mathbf{p})}{\partial p_{y}^{2}} \\ +\left(C_{21}+C_{33}\right)\dfrac{\partial^{2}\,{}_{l}\psi_{n}\left(\mathbf{p}_{k(l,m)}\right)}{\partial p_{y}\partial p_{x}} \end{bmatrix} \\
&+\sum_{n=1}^{{}_{l}N_{\omega}+N_{p}} \sum_{r=1}^{2\,{}_{l}N_{\omega}} {}_{l}\Psi^{-1}_{(2n)r}\, {}_{l}b_{r} \begin{bmatrix} C_{22}\dfrac{\partial^{2}\,{}_{l}\psi_{n}(\mathbf{p})}{\partial p_{y}^{2}} + \mathrm{C}_{33}\dfrac{\partial^{2}\,{}_{l}\psi_{n}(\mathbf{p})}{\partial p_{x}^{2}} \\ +\left(C_{23}+C_{32}\right)\dfrac{\partial^{2}\,{}_{l}\psi_{n}(\mathbf{p})}{\partial p_{y}\partial p_{x}} \end{bmatrix} \\
&+d_{y}(\mathbf{p})=0.
\end{aligned}
\tag{4.32}
$$

The equations above are written considering only local influence domains. However, these two set of equations for each node on the domain can also be written in a global way, by considering the neighbours in an influence domain that the node is in. In this way, the displacement vectors for all the collocation nodes on a domain can be solved at once. A sparse matrix $\mathbf{A}$ is created for the solution of displacements in which two rows are occupied for each node in the domain and the number of non-zero elements on the rows is two times the number of neighbouring nodes in the domain inside the influence domain of the same node. Hence we would end up with a matrix $\mathbf{A}$ with a size of $2N_{\Omega}\times 2N_{\Omega}$ and the following equation can be written for all the nodes $\mathbf{p}\in\Omega$

$$\mathbf{AU}=\mathbf{B}. \tag{4.33}$$

Where the components of matrix A_{ij} are

$$A_{2k(l,m)-1,2k(l,r)-1} = \sum_{n=1}^{{}^{l}N_{\omega}+N_p} \begin{bmatrix} C_{11}\dfrac{\partial^2 {}_l\psi_n\left(\mathbf{p}_{k(l,m)}\right)}{\partial p_x^2} \\ +C_{33}\dfrac{\partial^2 {}_l\psi_n\left(\mathbf{p}_{k(l,m)}\right)}{\partial p_y^2} \\ +\left(C_{13}+C_{31}\right)\dfrac{\partial^2 {}_l\psi_n\left(\mathbf{p}_{k(l,m)}\right)}{\partial p_y \partial p_x} \end{bmatrix} \Psi^{-1}_{2n-1,2r-1}$$

$$+ \sum_{n=1}^{{}^{l}N_{\omega}+N_p} \begin{bmatrix} C_{13}\dfrac{\partial^2 {}_l\psi_n\left(\mathbf{p}_{k(l,m)}\right)}{\partial p_x^2} \\ +C_{32}\dfrac{\partial^2 {}_l\psi_n\left(\mathbf{p}_{k(l,m)}\right)}{\partial p_y^2} \\ +\left(C_{12}+C_{33}\right)\dfrac{\partial^2 {}_l\psi_n\left(\mathbf{p}_{k(l,m)}\right)}{\partial p_y \partial p_x} \end{bmatrix} \Psi^{-1}_{2n,2r-1}; \mathbf{p}_{k(l,m)} \in \Omega, \mathbf{p}_{k(l,r)} \in \Omega, \tag{4.34}$$

$$A_{2k(l,m)-1,2k(l,r)} = \sum_{n=1}^{{}^{l}N_{\omega}+N_p} \begin{bmatrix} C_{11}\dfrac{\partial^2 {}_l\psi_n\left(\mathbf{p}_{k(l,m)}\right)}{\partial p_x^2} \\ +C_{33}\dfrac{\partial^2 {}_l\psi_n\left(\mathbf{p}_{k(l,m)}\right)}{\partial p_y^2} \\ +\left(C_{13}+C_{31}\right)\dfrac{\partial^2 {}_l\psi_n\left(\mathbf{p}_{k(l,m)}\right)}{\partial p_y \partial p_x} \end{bmatrix} \Psi^{-1}_{2n-1,2r}$$

$$+ \sum_{n=1}^{{}^{l}N_{\omega}+N_p} \begin{bmatrix} C_{13}\dfrac{\partial^2 {}_l\psi_n\left(\mathbf{p}_{k(l,m)}\right)}{\partial p_x^2} \\ +C_{32}\dfrac{\partial^2 {}_l\psi_n\left(\mathbf{p}_{k(l,m)}\right)}{\partial p_y^2} \\ +\left(C_{12}+C_{33}\right)\dfrac{\partial^2 {}_l\psi_n\left(\mathbf{p}_{k(l,m)}\right)}{\partial p_y \partial p_x} \end{bmatrix} \Psi^{-1}_{2n,2r}; \mathbf{p}_{k(l,m)} \in \Omega, \mathbf{p}_{k(l,r)} \in \Omega, \tag{4.35}$$

$$A_{2k(l,m),2k(l,r)-1} = \sum_{n=1}^{{}_{l}N_{\omega}+N_{p}} \left[\begin{array}{l} C_{31} \dfrac{\partial^2 {}_{l}\psi_n\left(\mathbf{p}_{k(l,m)}\right)}{\partial p_x^2} \\ +C_{23} \dfrac{\partial^2 {}_{l}\psi_n\left(\mathbf{p}_{k(l,m)}\right)}{\partial p_y^2} \\ +\left(C_{21}+C_{33}\right) \dfrac{\partial^2 {}_{l}\psi_n\left(\mathbf{p}_{k(l,m)}\right)}{\partial p_y \partial p_x} \end{array} \right] \Psi^{-1}_{2n-1,2r-1}$$

$$+ \sum_{n=1}^{{}_{l}N_{\omega}+N_{p}} \left[\begin{array}{l} C_{22} \dfrac{\partial^2 {}_{l}\psi_n\left(\mathbf{p}_{k(l,m)}\right)}{\partial p_y^2} \\ +\mathrm{C}_{33} \dfrac{\partial^2 {}_{l}\psi_n\left(\mathbf{p}_{k(l,m)}\right)}{\partial p_x^2} \\ +\left(C_{23}+C_{32}\right) \dfrac{\partial^2 {}_{l}\psi_n\left(\mathbf{p}_{k(l,m)}\right)}{\partial p_y \partial p_x} \end{array} \right] \Psi^{-1}_{2n,2r-1}; \mathbf{p}_{k(l,m)} \in \Omega, \mathbf{p}_{k(l,r)} \in \Omega, \tag{4.36}$$

$$A_{2k(l,m),2k(l,r)} = \sum_{n=1}^{{}_{l}N_{\omega}+N_{p}} \left[\begin{array}{l} C_{31} \dfrac{\partial^2 {}_{l}\psi_n\left(\mathbf{p}_{k(l,m)}\right)}{\partial p_x^2} \\ +C_{23} \dfrac{\partial^2 {}_{l}\psi_n\left(\mathbf{p}_{k(l,m)}\right)}{\partial p_y^2} \\ +\left(C_{21}+C_{33}\right) \dfrac{\partial^2 {}_{l}\psi_n\left(\mathbf{p}_{k(l,m)}\right)}{\partial p_y \partial p_x} \end{array} \right] \Psi^{-1}_{2n-1,2r}$$

$$+ \sum_{n=1}^{{}_{l}N_{\omega}+N_{p}} \left[\begin{array}{l} C_{22} \dfrac{\partial^2 {}_{l}\psi_n\left(\mathbf{p}_{k(l,m)}\right)}{\partial p_y^2} \\ +\mathrm{C}_{33} \dfrac{\partial^2 {}_{l}\psi_n\left(\mathbf{p}_{k(l,m)}\right)}{\partial p_x^2} \\ +\left(C_{23}+C_{32}\right) \dfrac{\partial^2 {}_{l}\psi_n\left(\mathbf{p}_{k(l,m)}\right)}{\partial p_y \partial p_x} \end{array} \right] \Psi^{-1}_{2n,2r}; \mathbf{p}_{k(l,m)} \in \Omega, \mathbf{p}_{k(l,r)} \in \Omega. \tag{4.37}$$

and $\mathbf{U}=\left[u_{x1},u_{y1},u_{x2},u_{y2},...,u_{xN_\Omega},u_{yN_\Omega}\right]^{\mathrm{T}}$,

$$B_{2m}=-\sum_{r=1}^{{}^{l}N_\omega}A_{2k(l,m)-1,2k(l,r)-1}\Upsilon^{x}_{k(l,r)}-\sum_{r=1}^{{}^{l}N_\omega}A_{2k(l,m)-1,2k(l,r)}\Upsilon^{y}_{k(l,r)}\,, \tag{4.38}$$

$$B_{2m-1}=-\sum_{r=1}^{{}^{l}N_\omega}A_{2k(l,m),2k(l,r)-1}\Upsilon^{x}_{k(l,r)}-\sum_{r=1}^{{}^{l}N_\omega}A_{2k(l,m),2k(l,r)}\Upsilon^{y}_{k(l,r)}\,. \tag{4.39}$$

Where the introduced boundary indicators are defined as

$$\Upsilon^{x}\left(\mathbf{p}\right)=\begin{cases}0;\mathbf{p}\in\Omega\\ \overline{u}_x\left(\mathbf{p}\right);\mathbf{p}\in\Gamma^{ux}\\ \overline{\tau}_x\left(\mathbf{p}\right);\mathbf{p}\in\Gamma^{\tau x}\end{cases},\ \Upsilon^{y}\left(\mathbf{p}\right)=\begin{cases}0;\mathbf{p}\in\Omega\\ \overline{u}_y\left(\mathbf{p}\right);\mathbf{p}\in\Gamma^{uy}\\ \overline{\tau}_y\left(\mathbf{p}\right);\mathbf{p}\in\Gamma^{\tau y}\end{cases}. \tag{4.40}$$

For ideal plastic or slightly compressible ideal plastic material in 2D, the displacements in the governing equations (2.87, 2.88) or (2.99, 2.100) can be discretized as

$$\sum_{n=1}^{{}^{l}N_\omega+N_p}\sum_{r=1}^{2\,{}^{l}N_\omega}{}^{l}\Psi^{-1}_{(2n-1)r}\,{}^{l}b_r\left[\frac{\partial^2\,{}^{l}\psi_n\left(\mathbf{p}_{k(l,m)}\right)}{\partial p_x^2}+\frac{\partial^2\,{}^{l}\psi_n\left(\mathbf{p}_{k(l,m)}\right)}{\partial p_y^2}\right]=f_x\left(\mathbf{u}_{k(l,m)}\right), \tag{4.41}$$

$$\sum_{n=1}^{{}^{l}N_\omega+N_p}\sum_{r=1}^{2\,{}^{l}N_\omega}{}^{l}\Psi^{-1}_{(2r)n}\,{}^{l}b_r\left[\frac{\partial^2\,{}^{l}\psi_n\left(\mathbf{p}_{k(l,m)}\right)}{\partial p_x^2}+\frac{\partial^2\,{}^{l}\psi_n\left(\mathbf{p}_{k(l,m)}\right)}{\partial p_y^2}\right]=f_y\left(\mathbf{u}_{k(l,m)}\right). \tag{4.42}$$

where f_x and f_y are the right hand side of the governing equations (2.87, 2.88) or (2.99, 2.100) and defined for a global point $k(l,m)$ and calculated from the displacement vector at that point. These functions are also displacement depended equations, however discretization cannot be applied due to their non-linear behaviour. Therefore the right hand side of the equation is satisfied with previous values of displacement and an initial guess is used at the beginning. This method is called Newton-Raphson and explained in Subchapter 4.3.

If the material parameter g used in slightly compressible material model, is set to $9/2$, than the same stiffness matrix is obtained as in the ideal plastic

deformation. Again, a system of sparse equations can be written, with its elements

$$A_{2k(l,m)-1,2k(l,r)-1} = \sum_{n=1}^{N_\omega+N_p} \left[\frac{\partial^2 {}_l\psi_n\left(\mathbf{p}_{k(l,m)}\right)}{\partial p_x^2} + \frac{\partial^2 {}_l\psi_n\left(\mathbf{p}_{k(l,m)}\right)}{\partial p_y^2} \right] \Psi^{-1}_{2n-1,2r-1}\,, \tag{4.43}$$

$$A_{2k(l,m)-1,2k(l,r)} = 0\,, \tag{4.44}$$

$$A_{2k(l,m),2k(l,r)-1} = 0\,, \tag{4.45}$$

$$A_{2k(l,m),2k(l,r)} = \sum_{n=1}^{N_\omega+N_p} \left[\frac{\partial^2 {}_l\psi_n\left(\mathbf{p}_{k(l,m)}\right)}{\partial p_x^2} + \frac{\partial^2 {}_l\psi_n\left(\mathbf{p}_{k(l,m)}\right)}{\partial p_y^2} \right] \Psi^{-1}_{2n,2r}\,. \tag{4.46}$$

where $\mathbf{p}_{k(l,m)} \in \Omega$, $\mathbf{p}_{k(l,r)} \in \Omega$ and $k(l,m) = 1,2,..,N_i$, $k(l,r) = 1,2,..,N_i$.

The definition of the right hand side of the sparse system of equations for both plastic cases is

$$B_{2m} = -\sum_{r=1}^{{}_lN_\omega} A_{2k(l,m)-1,2k(l,r)-1}\Upsilon^x_{k(l,r)} - \sum_{r=1}^{{}_lN_\omega} A_{2k(l,m)-1,2k(l,r)}\Upsilon^y_{k(l,r)} + f_{xk(l,m)}\,, \tag{4.47}$$

$$B_{2m-1} = -\sum_{r=1}^{{}_lN_\omega} A_{2k(l,m),2k(l,r)-1}\Upsilon^x_{k(l,r)} - \sum_{r=1}^{{}_lN_\omega} A_{2k(l,m),2k(l,r)}\Upsilon^y_{k(l,r)} + f_{yk(l,m)}\,. \tag{4.48}$$

The boundary indicators are the same as in (4.34).

4.2.2 Newton-Raphson iteration method

The ideal plastic solution requires partial derivatives of effective stress and effective strain. The governing equation can be separated into two parts, discretized and non-discretized parts. Non-discretized part can be calculated by using previous displacement values and recalculated in an iterative method called Newton-Raphson until a satisfactory convergence has been achieved. The details of this approach are discussed in the books by [Chen and Han, 1988] and [Press, Teukolsky, Vetterling and Flannery, 1992]. The governing equation is in

the form of Laplace equation. The equation of mechanical equilibrium can be expressed as

$$\nabla^2 \mathbf{U} = \mathbf{f} \,. \tag{4.49}$$

The equation has both sides depended on the unknown displacements and their partial derivatives. Therefore the solution can be obtained by iterative Newton-Raphson method as described below.

General theory of Newton-Raphson Method for a scalar U with iteration index j is

$$AU^{j+1} = f\left(U^{j+1}\right), \quad f\left(U^{j+1}\right) = \frac{\partial f\left(U^{j}\right)}{\partial U}\left(U^{j+1} - U^{j}\right) + f\left(U^{j}\right), \tag{4.50}$$

where A is a known scalar and $f(U)$ is a known function. U^0 is the initial guess for the iteration to start. For a 2D vector of displacement $\mathbf{u} = \begin{bmatrix} u_x & u_y \end{bmatrix}^{\mathrm{T}}$ the solution is in the following form

$$\mathbf{A}\mathbf{u} = \mathbf{f}\left(\mathbf{u}\right). \tag{4.51}$$

In component form

$$\begin{aligned} A_x u_x &= f_x\left(u_x, u_y\right), \\ A_y u_y &= f_y\left(u_x, u_y\right). \end{aligned} \tag{4.52}$$

The right hand side of the equations above can be approximated with Newton-Raphson method for a 2D system

$$f_i\left(\mathbf{u}^{j+1}\right) \simeq \sum_{i=x,y} \frac{\partial f_i\left(\mathbf{u}^{j}\right)}{\partial p_i}\left(u_i^{j+1} - u_i^{j}\right) + f_i\left(\mathbf{u}^{j}\right). \tag{4.53}$$

The solution equation (4.49) for displacements can be written in terms of global node index $k(l,m)$ and components of sparse matrix A_{ij} as in (4.30)

$$\sum_{m=1}^{l^{N_\omega}} A_{2k(l,1)-1,2k(l,m)-1} u_{xk(l,m)} = f_x\left(\mathbf{u}_{k(l,1)}\right), \tag{4.54}$$

$$\sum_{m=1}^{N_\omega} A_{2k(l,1),2k(l,m)} u_{yk(l,m)} = f_y\left(\mathbf{u}_{k(l,1)}\right). \tag{4.55}$$

Application of Newton-Raphson method with an iteration index j

$$\begin{aligned}\sum_{m=1}^{N_\omega} A_{2k(l,m)-1} u^{j+1}_{xk(l,m)} &= \frac{\partial f_x\left(\mathbf{u}^j_{k(l,1)}\right)}{\partial u_x}\left(u^{j+1}_{xk(l,1)} - u^j_{xk(l,1)}\right) \\ &+ \frac{\partial f_x\left(\mathbf{u}^j_{k(l,1)}\right)}{\partial u_y}\left(u^{j+1}_{yk(l,1)} - u^j_{yk(l,1)}\right) + f_x\left(u^j_{k(l,1)}\right),\end{aligned} \tag{4.56}$$

$$\begin{aligned}\sum_{m=1}^{N_\omega} A_{2k(l,m)} u^{j+1}_{yk(l,m)} &= \frac{\partial f_y\left(\mathbf{u}^j_{k(l,1)}\right)}{\partial u_x}\left(u^{j+1}_{xk(l,1)} - u^j_{xk(l,1)}\right) \\ &+ \frac{\partial f_y\left(\mathbf{u}^j_{k(l,1)}\right)}{\partial u_y}\left(u^{j+1}_{yk(l,1)} - u^j_{yk(l,1)}\right) + f_y\left(u^j_{k(l,1)}\right).\end{aligned} \tag{4.57}$$

The system of equations can now be written in a matrix form by introducing a Jacobian matrix $\mathbf{J}\left(\mathbf{U}^j\right)$ for N_Ω internal nodes on a computational domain

$$\underbrace{\begin{pmatrix} A_{1,1} & \cdots & A_{1,N_\Omega} \\ \vdots & \ddots & \vdots \\ A_{N_\Omega,1} & \cdots & A_{N_\Omega,N_\Omega} \end{pmatrix}}_{\mathbf{A}} \underbrace{\begin{pmatrix} u_{x1}^{j+1} \\ u_{y1}^{j+1} \\ . \\ . \\ . \\ u_{xN_\Omega}^{j+1} \\ u_{yN_\Omega}^{j+1} \end{pmatrix}}_{\mathbf{U}^{j+1}} = \underbrace{\begin{pmatrix} \frac{\partial f_{x1}^j}{\partial u_x} & \frac{\partial f_{x1}^j}{\partial u_y} & \cdots & 0 \\ \frac{\partial f_{y1}^j}{\partial u_x} & \frac{\partial f_{y1}^j}{\partial u_y} & \cdots & 0 \\ 0 & \frac{\partial f_{x2}^j}{\partial u_x} & \frac{\partial f_{x2}^j}{\partial u_y} & \cdots & 0 \\ 0 & \frac{\partial f_{y2}^j}{\partial u_x} & \frac{\partial f_{y2}^j}{\partial u_y} & \cdots & 0 \\ \vdots & & & \ddots & \vdots \\ 0 & \cdots & & \frac{\partial f_{xN_\Omega}^j}{\partial u_x} & \frac{\partial f_{xN_\Omega}^j}{\partial u_y} \\ 0 & \cdots & & \frac{\partial f_{yN_\Omega}^j}{\partial u_x} & \frac{\partial f_{yN_\Omega}^j}{\partial u_y} \end{pmatrix}}_{\mathbf{J}(\mathbf{U}^j)} \underbrace{\begin{pmatrix} \Delta u_{x1}^{j+1} \\ \Delta u_{y1}^{j+1} \\ . \\ . \\ . \\ \Delta u_{xN_\Omega}^{j+1} \\ \Delta u_{yN_\Omega}^{j+1} \end{pmatrix}}_{\Delta\mathbf{U}^{j+1}} + \underbrace{\begin{pmatrix} f_{x1}^j \\ f_{y1}^j \\ . \\ . \\ . \\ f_{xN_\Omega}^j \\ f_{yN_\Omega}^j \end{pmatrix}}_{\mathbf{f}(\mathbf{U}^j)}. \tag{4.58}$$

The matrix representation is

$$\mathbf{A}\mathbf{U}^{j+1} = \mathbf{J}\left(\mathbf{U}^j\right)\Delta\mathbf{U}^{j+1} + \mathbf{f}\left(\mathbf{U}^j\right). \tag{4.59}$$

The derivatives in the Jacobian matrix are too complex to be solved analytically. Therefore they are replaced by their numerical approximation

$$\frac{\partial f_x\left(u_x,u_y\right)}{\partial u_x} = \frac{f_x\left(u_x+\Delta u_x,u_y\right) - f_x\left(u_x,u_y\right)}{\Delta u_x}, \tag{4.60}$$

$$\frac{\partial f_x\left(u_x,u_y\right)}{\partial u_y} = \frac{f_x\left(u_x,u_y+\Delta u_y\right) - f_x\left(u_x,u_y\right)}{\Delta u_y}, \tag{4.61}$$

$$\frac{\partial f_y\left(u_x,u_y\right)}{\partial u_x} = \frac{f_y\left(u_x+\Delta u_x,u_y\right) - f_y\left(u_x,u_y\right)}{\Delta u_x}, \tag{4.62}$$

$$\frac{\partial f_y\left(u_x,u_y\right)}{\partial u_y}=\frac{f_y\left(u_x,u_y+\Delta u_y\right)-f_y\left(u_x,u_y\right)}{\Delta u_y}. \tag{4.63}$$

where the additional displacements $\Delta u_x,\Delta u_y$ are usually taken between 1 % and 10 % of the displacement u_x,u_y. In the present work, 5 % is chosen.

Finally, the system of equations (4.56) and (4.57) can be rewritten as

$$\begin{aligned}
&\sum_{m=1}^{N_\omega} A_{2k(l,m)-1}u_{xk(l,m)}^{j+1}-\frac{f_x\left(u_{xk(l,1)}^{j}+\Delta u_x,u_{yN(l,1)}^{j}\right)-f_x\left(u_{xk(l,1)}^{j},u_{yk(l,1)}^{j}\right)}{\Delta u_x}u_{xk(l,1)}^{j+1}\\
&-\frac{f_x\left(u_{xk(l,1)}^{j},u_{yk(l,1)}^{j}+\Delta u_y\right)-f_x\left(u_{xk(l,1)}^{j},u_{yk(l,1)}^{j}\right)}{\Delta u_y}u_{yk(l,1)}^{j+1}\\
&=-\frac{f_x\left(u_{xk(l,1)}^{j}+\Delta u_x,u_{yk(l,1)}^{j}\right)-f_x\left(u_{xk(l,1)}^{j},u_{yk(l,1)}^{j}\right)}{\Delta u_x}u_{xk(l,1)}^{j}\\
&-\frac{f_x\left(u_{xk(l,1)}^{j},u_{yk(l,1)}^{j}+\Delta u_y\right)-f_x\left(u_{xk(l,1)}^{j},u_{yk(l,1)}^{j}\right)}{\Delta u_y}u_{yk(l,1)}^{j}+f_x\left(\mathbf{u}_{k(l,1)}^{j}\right),
\end{aligned} \tag{4.64}$$

$$\begin{aligned}
&\sum_{m=1}^{N_\omega} A_{2k(l,m)}u_{yN(l,m)}^{j+1}-\frac{f_y\left(u_{xk(l,1)}^{j}+\Delta u_x,u_{yk(l,1)}^{j}\right)-f_y\left(u_{xk(l,1)}^{j},u_{yk(l,1)}^{j}\right)}{\Delta u_x}u_{xk(l,1)}^{j+1}\\
&-\frac{f_y\left(u_{xk(l,1)}^{j},u_{yk(l,1)}^{j}+\Delta u_y\right)-f_y\left(u_{xk(l,1)}^{j},u_{yN(l,1)}^{j}\right)}{\Delta u_y}u_{yN(l,1)}^{j+1}\\
&=-\frac{f_y\left(u_{xk(l,1)}^{j}+\Delta u_x,u_{yk(l,1)}^{j}\right)-f_y\left(u_{xk(l,1)}^{j},u_{yk(l,1)}^{j}\right)}{\Delta u_x}u_{yk(l,1)}^{j}\\
&-\frac{f_y\left(u_{xk(l,1)}^{j},u_{yk(l,1)}^{j}+\Delta u_y\right)-f_y\left(u_{xk(l,1)}^{j},u_{yk(l,1)}^{j}\right)}{\Delta u_y}u_{xk(l,1)}^{j}+f_y\left(\mathbf{u}_{k(l,1)}^{j}\right).
\end{aligned} \tag{4.65}$$

The solution above, after a number of iterations, gives us the two linearly independent displacements for each node in a column matrix for total number of N_Ω nodes, which is

$$\mathbf{U} = \left[u_{x1}\ u_{y1}\ u_{x2}\ u_{y2}\ \ldots\ u_{xN_\Omega}\ u_{yN_\Omega} \right]^{\mathrm{T}}. \tag{4.66}$$

In a matrix form new displacements can be obtained by using previous displacement values as shown below until a convergence has been achieved

$$\left(\mathbf{A} - \mathbf{J}^j\right)\mathbf{U}^{j+1} = \mathbf{J}^j\mathbf{U}^j + \mathbf{f}^j. \tag{4.67}$$

This method also requires an initial guess to start with the iterations. In the current model, displacement field from the elastic solutions are used as initial guess and derivatives for Jacobian matrix are obtained. This is required only at the beginning of the iteration. Once the iterations start the iterations continue until convergence has been achieved. The vector of displacements obtained from the iteration number $j+1$ is used during the next iteration $j+2$. The convergence criteria for the calculated displacement values is defined by [Lenard, Pietrzyk, and Cser, 1999]

$$\frac{\sum_{i=1}^{2N_\Omega}\left(U_i^{j+1} - U_i^j\right)^2}{\sum_{i=1}^{2N_\Omega}\left(U_i^{j+1}\right)^2} \le 0.001. \tag{4.68}$$

For the boundary nodes, displacements can be solved afterwards by using local collocation expansion coefficients in (4.29) and then applying the same coefficients to discretization of displacements in (4.2) and (4.3).

4.2 Local radial basis function collocation method for thermal model

The governing equation of the thermal model for a 2D slice is written in Table 2.1. When a time discretization is applied the equation becomes

$$\rho c_p \frac{\Delta T}{\Delta t} = \nabla \cdot \left(k \nabla T\right) + \dot{Q}. \tag{4.69}$$

When the internal heat generation rate is discretized for a slice

$$\dot{Q} = \eta \frac{\Delta U_{slice}}{\Delta t_{slice}}, \tag{4.70}$$

where ΔU_{slice} is the difference in strain energy, Δt_{slice} is the time difference between the previous and current slices. Therefore the Equation (4.69) can be written in explicit time stepping as

$$T_i = T_{i0} + \frac{\Delta t}{\rho c_p}\left(\nabla k_{0i} \cdot \nabla T_{0i} + k_{0i} \cdot \nabla^2 T_{0i}\right) + \Delta t \frac{\eta \Delta U_{slice}}{\Delta t_{slice} \rho c_p} \tag{4.71}$$

The discretization takes place in the thermal model in terms of temperature T and thermal conductivity k as shown below,

$$T(\mathbf{p}) = \sum_{n=1}^{{}_l N_\omega + N_p} {}_l\psi_n(\mathbf{p})\, {}_l\alpha_{Tn}\,, \tag{4.72}$$

$$k(\mathbf{p}) = \sum_{n=1}^{{}_l N_\omega + N_p} {}_l\psi_n(\mathbf{p})\, {}_l\alpha_{kn}\,. \tag{4.73}$$

In thermal model it is enough to use ${}_l N_\omega = 5$. If we assume constant thermal conductivity in a 2D system then the explicit equation written above becomes

$$\begin{aligned} T_\xi(\mathbf{p}) &= T_{\xi-1}(\mathbf{p}) + \frac{\Delta t}{\rho c_p} k \left[\sum_{m=1}^{{}_l N_\omega + N_p} \left(\frac{\partial^2}{\partial p_x^2} {}_l\psi_m(\mathbf{p}) + \frac{\partial^2}{\partial p_y^2} {}_l\psi_m(\mathbf{p}) \right) {}_l\alpha_{Tm} \right] \\ &+ \Delta t \frac{\eta \Delta U_{slice}}{\Delta t_{slice} \rho c_p}, \end{aligned} \tag{4.74}$$

where ξ is the index of explicit time stepping. Robin Γ^R and Neumann Γ^N boundary conditions given in (2.106) and (2.107) can also be written in terms of collocation as

$$\begin{aligned} &-k \sum_{m=1}^{{}_l N_\omega + N_p} \begin{pmatrix} n_x(\mathbf{p}) \dfrac{\partial}{\partial x} {}_l\psi_m(\mathbf{p}) + n_y(\mathbf{p}) \dfrac{\partial}{\partial y} {}_l\psi_m(\mathbf{p}) \\ -h\, {}_l\psi_m(\mathbf{p}) \end{pmatrix} {}_l\alpha_{Tm}, \\ &= h\left(T_\Gamma^{ref}\right);\ \mathbf{p} \in \Gamma^R \end{aligned} \tag{4.75}$$

$$-k \sum_{m=1}^{{}_l N_\omega + N_p} \left(n_x(\mathbf{p}) \frac{\partial}{\partial x} {}_l\psi_m(\mathbf{p}) + n_y(\mathbf{p}) \frac{\partial}{\partial y} {}_l\psi_m(\mathbf{p}) \right) {}_l\alpha_{Tm} = q(\mathbf{p});\ \mathbf{p} \in \Gamma^N. \tag{4.76}$$

The temperature interpolation in (4.67) can be written as set of equations for each node in an influence domain. Collocation constants for a local influence domain can be then obtained through local interpolation of the current temperatures as

$$ {}_{l}\boldsymbol{\alpha}_{T} = {}_{l}\boldsymbol{\theta}^{-1}\,{}_{l}\mathbf{T}\,, \tag{4.77} $$

where ${}_{l}\boldsymbol{\alpha} = \left[{}_{l}\alpha_{T1}, {}_{l}\alpha_{T2}, ..., {}_{l}\alpha_{T({}_{l}N_{\omega}+N_{p})} \right]^{\mathrm{T}}$ and ${}_{l}\mathbf{T} = \left[T_{k(l,1)}, ..., T_{k(l,{}_{l}N_{\omega})}, 0, 0, 0 \right]^{\mathrm{T}}$. The size of the local interpolation matrix for thermal model is $\left({}_{l}N_{\omega} + N_{p} \right) \times \left({}_{l}N_{\omega} + N_{p} \right)$ and its components are

$$ {}_{l}\theta_{nm} = {}_{l}\psi_{n}\left(\mathbf{p}_{k(l,m)} \right); n = 1, 2, .., {}_{l}N_{\omega}\,, \tag{4.78} $$

$$ {}_{l}\theta_{nm} = {}_{l}\theta_{mn}; n = {}_{l}N_{\omega} + 1, {}_{l}N_{\omega} + 1, .., {}_{l}N_{\omega} + N_{p}; m = 1, 2, .., {}_{l}N_{\omega}\,, \tag{4.79} $$

$$ {}_{l}\theta_{nm} = 0; n, m = {}_{l}N_{\omega} + 1, {}_{l}N_{\omega} + 2, .., {}_{l}N_{\omega} + N_{p}\,. \tag{4.80} $$

These collocation constants calculated here are used in equation (4.72) to calculate new values of temperature. This is repeated until the total number of explicit time stepping ξ times the Δt becomes equal to Δt_{slice}.

$$ \xi\ \Delta t = \Delta t_{slice}\,, \tag{4.81} $$

For the boundary conditions another local system of solutions can be written for the influence domains which have a node on the boundary in a very similar way as in the mechanical model, however the size of the matrixes are half of the size used in the mechanical model. The matrix presentation is

$$ {}_{l}\boldsymbol{\Phi}_{l}\boldsymbol{\alpha}_{T} = {}_{l}\mathbf{b}\,, \tag{4.82} $$

where ${}_{l}\boldsymbol{\alpha} = \left[{}_{l}\alpha_{T1}, {}_{l}\alpha_{T2}, ..., {}_{l}\alpha_{T(N_{\omega}+N_{p})} \right]^{\mathrm{T}}$, components of local solution matrix for the thermal model ${}_{l}\Phi_{ij}$ and right hand side b_{i} are shown below

$$
{}_l\Phi_{mn} = \left\{ \begin{array}{l} \\ k\left(\begin{array}{l} n_x(\mathbf{p}_{k(l,m)}) \dfrac{\partial}{\partial x} {}_l\psi_m(\mathbf{p}_{k(l,m)}) \\ +n_y(\mathbf{p}_{k(l,m)}) \dfrac{\partial}{\partial y} {}_l\psi_m(\mathbf{p}_{k(l,m)}) \end{array} \right); \mathbf{p} \in \Gamma^R \\ {}_l\psi_m\left(\mathbf{p}_{k(l,m)}\right); \mathbf{p} \in \Omega \\ k\left(\begin{array}{l} n_x(\mathbf{p}_{k(l,m)}) \dfrac{\partial}{\partial x} {}_l\psi_m(\mathbf{p}_{k(l,m)}) \\ +n_y(\mathbf{p}_{k(l,m)}) \dfrac{\partial}{\partial y} {}_l\psi_m(\mathbf{p}_{k(l,m)}) \\ -h\, {}_l\psi_m(\mathbf{p}) \end{array} \right); \mathbf{p} \in \Gamma^N \end{array} \right\}; m = 1, 2, .., {}_lN_\omega \tag{4.83}
$$

$$
{}_l\Phi_{mn} = {}_l\Phi_{nm}; m = {}_lN_\omega + 1, {}_lN_\omega + 2, ..., {}_lN_\omega + N_p; n = 1, 2, .., {}_lN_\omega \tag{4.84}
$$

$$
{}_l\Phi_{mn} = 0; m, n = {}_lN_\omega + 1, {}_lN_\omega + 2, ..., {}_lN_\omega + N_p \tag{4.85}
$$

$$
{}_lb_m = \left\{ \begin{array}{l} T\left(\mathbf{p}_{k(l,m)}\right); \mathbf{p} \in \Omega \\ q\left(\mathbf{p}_{k(l,m)}\right); \mathbf{p} \in \Gamma^N \\ -h_{ref} T^{ref}; \mathbf{p} \in \Gamma^R \end{array} \right\}; m = 1, 2, .., {}_lN_\omega \tag{4.86}
$$

$$
{}_lb_m = 0; m = {}_lN_\omega + 1, {}_lN_\omega + 2, .., {}_lN_\omega + N_p \tag{4.87}
$$

The ($N_\omega + N_p$) number of expansion coefficients ${}_l\alpha_{Tm}$ for each of the influences domain l can be obtained through

$$
{}_l\boldsymbol{\alpha}_T = {}_l\boldsymbol{\Phi}^{-1}\, {}_l\mathbf{b}, \tag{4.88}
$$

The coefficients ${}_l\alpha_{Tm}$ above for a boundary node in an influence domain l should also satisfy the temperature interpolation in equation 4.70 for the same influence domain. Thus the temperature value on a boundary point can be obtained to complete the thermal calculation.

4.3 Generation and manipulation of the nodes

Even though the collocation nodes are uniformly distributed on the rectangular initial slice, deformation through many steps forces the collocation nodes to obtain completely irregular positions. Since the stability of the solution also depends on the position of the collocation nodes, eventually a repositioning of the collocation nodes is necessary for the system to stay stable for further deformation steps. Especially in between the rolling stands when the same roll orientation is repeated such as horizontal-horizontal or vertical-vertical. When it has been decided to reposition the collocation nodes, first the nodes on the boundary are equidistantly redistributed. After that, the internal nodes are distributed as orthogonally as possible with its neighbouring nodes. The new arrangement of the nodes is done in two steps. First, Trans Finite Interpolation (TFI) [Thompson and Han, 1999] is used for aligning of the nodes in accordance with the boundary nodes. This is followed by Elliptic Node Generation (ENG) [Thompson and Han, 1999] which repositions them in an iterative way to make them approximately orthogonal.

4.3.1 Trans finite interpolation

When the slice goes through a set of vertical and horizontal rolling stands, it is necessary to reposition the nodes in order to continue with the calculations. Node generation function first positions the nodes based on TFI. Boundary nodes are distributed on each side with equal distances. However, the number of the nodes on 4 sides needs to be determined. Facing sides such as top and bottom have to have the same number of the nodes. It is easy to define the bottom and the left side which overlay the symmetry axes. However it is important to separate top and right boundary lines. During the deformation steps an index called the last contact node, is taken into consideration. This is the node with highest latitudinal value in case of vertical rolling stand or highest longitudinal value in case of the horizontal rolling stand among all the nodes which are in contact with the roll. Details can be seen in Figure 4.2.

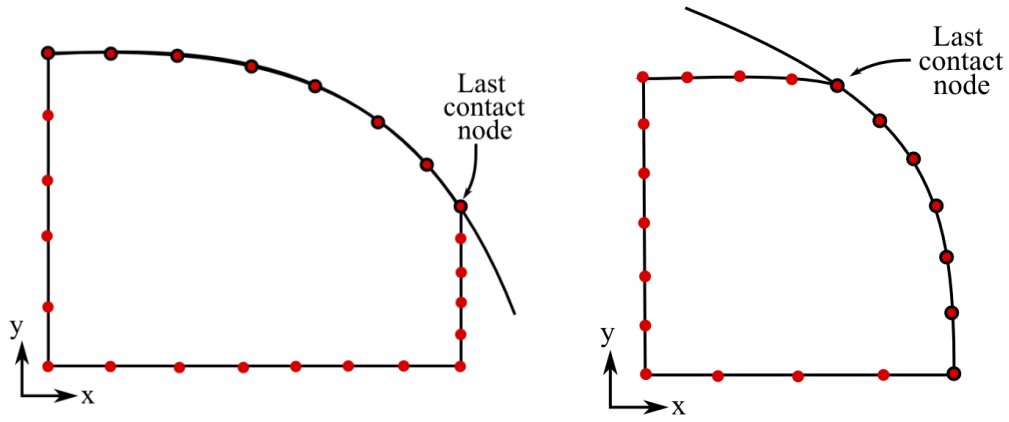

Figure 4.2: Scheme of the boundary node positions during horizontal (left) or vertical (right) approach of the roll. The nodes that have contact with the roll are denoted with black circles and the last contact node is shown for both cases.

This last contact node separates the top boundary from the right. Therefore, the boundary nodes on the top and the right sides can also be positioned with equal distance. All the nodes besides the boundary can now be positioned in a loop based on TFI.

$$\begin{aligned} p_{x,\vartheta(r,s)} &= (1-\beta_r)\, p_{x,\vartheta(1,s)} + \beta_r p_{x,\vartheta(r_{\max},s)} + (1-\beta_j)\, p_{x,\vartheta(r,1)} \\ &+\beta p_{x,\vartheta(r,s_{\max})} - (1-\beta_r)(1-\beta_s)\, p_{x,\vartheta(1,1)} - (1-\beta_r)\beta_s p_{x,\vartheta(1,s_{\max})} \\ &-\beta_r (1-\beta_2)\, p_{x,\vartheta(r_{\max},1)} - \beta_s\beta_s p_{x,\vartheta(r_{\max,},s_{\max})}; r = 2,3,..,r_{\max}-1, s = 2,3,..,s_{\max}-1, \end{aligned} \tag{4.89}$$

$$\begin{aligned} p_{y\gamma(r,s)} &= (1-\beta_r)\, p_{y,\vartheta(1,s)} + \beta_i p_{y,\vartheta(r_{\max},s)} + (1-\beta_s)\, p_{y,\vartheta(r,1)} \\ &+\beta p_{y,\vartheta(r,s_{\max})} - (1-\beta_r)(1-\beta_2)\, p_{y,\vartheta(1,1)} - (1-\beta_r)\beta_s p_{y,\vartheta(1,s_{\max})} \\ &-\beta_r (1-\beta_2)\, p_{y,\vartheta(r_{\max},1)} - \beta_s\beta_s p_{y,\vartheta(r_{\max,},s_{\max})}; r = 2,3,..,r_{\max}-1, s = 2,3,..,s_{\max}-1. \end{aligned} \tag{4.90}$$

$\vartheta(r,s)$ is the function that returns global node index when r is the index of the node on latitudinal direction and s is on longitudinal direction, $r_{\max}$ is the number of the boundary nodes on right or left boundaries, $s_{\max}$ is the number of the boundary nodes on top or bottom boundaries including the corner nodes and $\beta_r = r/r_{\max}$, $\beta_s = s/s_{\max}$.

4.3.2 Elliptic node generation

The TFI does not achieve the desired orthogonal node arrangement, therefore an iterative method called ENG is applied. Again the boundary nodes remain as they are. In the calculations Gauss-Seidel iteration is used and can be written for a node $\vartheta(r,s)$.

$$p_{x\vartheta(r,s)} = \frac{1}{2(g_{11}+g_{22})}\left[\begin{array}{l} g_{22}\left(p_{x\vartheta(r+1,s)} + p_{x\vartheta(r-1,s)}\right) \\ +\dfrac{g_{12}}{2}\left(\begin{array}{l} -p_{x\vartheta(r+1,s+1)} + p_{x\vartheta(r+1,s-1)} \\ -p_{x\vartheta(r-1,s-1)} + p_{x\vartheta(r-1,s+1)} \end{array}\right) \\ +g_{11}\left(p_{x\vartheta(r,s+1)} + p_{x\vartheta(r,s-1)}\right) \end{array}\right]; \tag{4.91}$$

$$r = 2,3,..,r_{\max}-1; s = 2,3,..,s_{\max}-1,$$

$$p_{y\vartheta(r,s)} = \frac{1}{2(g_{11}+g_{22})}\left[\begin{array}{l} g_{22}\left(p_{y\vartheta(r+1,s)} + p_{y\vartheta(r-1,s)}\right) \\ +\dfrac{g_{12}}{2}\left(\begin{array}{l} -p_{y\vartheta(r+1,s+1)} + p_{y\vartheta(r+1,s-1)} \\ -p_{y\vartheta(r-1,s-1)} + p_{y\vartheta(r-1,s+1)} \end{array}\right) \\ +g_{11}\left(p_{y\vartheta(r,s+1)} + p_{y\vartheta(r,s-1)}\right) \end{array}\right]. \tag{4.92}$$

$$r = 2,3,..,r_{\max}-1; s = 2,3,..,s_{\max}-1.$$

Where the parameters g_{11}, g_{12} and g_{22} are defined as

$$g_{11} = \frac{\left(p_{x\vartheta(r+1,s)} - p_{x\vartheta(r-1,s)}\right)^2 + \left(p_{y\vartheta(r+1,s)} - p_{y\vartheta(r-1,s)}\right)^2}{4}, \tag{4.93}$$

$$g_{12} = \frac{\left[\begin{array}{l} \left(p_{x\vartheta(r+1,s)} - p_{x\vartheta(r-1,s)}\right)\left(p_{x\vartheta(r,s+1)} - p_{x\vartheta(r,s-1)}\right) \\ +\left(p_{y\vartheta(r+1,s)} - p_{y\vartheta(r-1,s)}\right)\left(p_{y\vartheta(r,s+1)} - p_{y\vartheta(r,s-1)}\right) \end{array}\right]}{4}, \tag{4.94}$$

$$g_{22} = \frac{\left(p_{x\vartheta(r,s+1)} - p_{x\vartheta(r-1,s-1)}\right) + \left(p_{y\vartheta(r,s+1)} - p_{y\vartheta(r,s-1)}\right)}{4}. \tag{4.95}$$

ENG is an iterative method which means that for all the nodes the positions are recalculated until a satisfactory convergence has been achieved. However, the previously defined TFI is calculated only once for each node. In the rolling simulation, 100 iterations are used, which is always enough to satisfy a reasonably orthogonal node repositioning, and to continue with the simulation. An example of the repositioning of the nodes is shown in Figure 4.3.

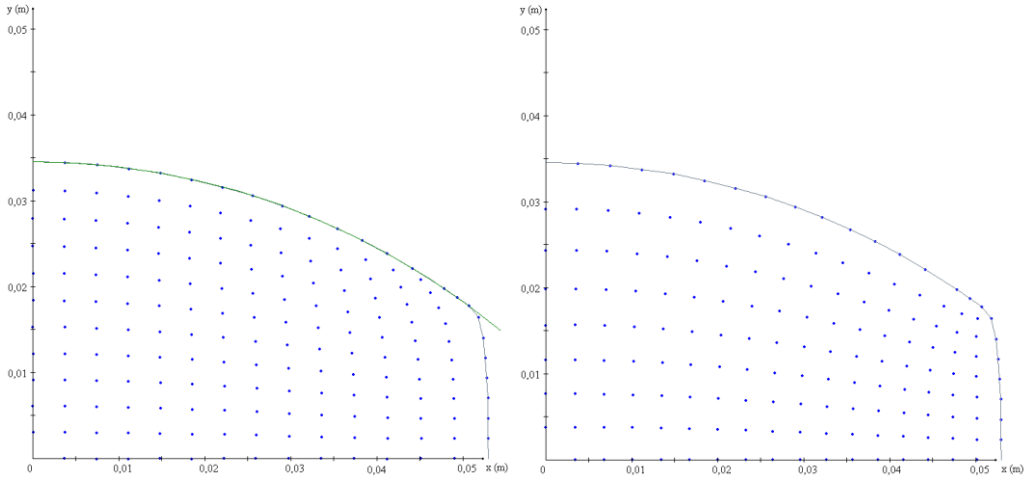

Figure 4.3: An example of generation of nodes with Elliptic Node Generation (ENG). Picture on the left is the deformation results after an oval rolling when a uniform node distribution is applied to an initial rectangle and picture on the right is the same deformed slice when nodes are redistributed with ENG.

After the application of ENG, newly positioned nodes obtain new values of temperature and displacement from the interpolation from TFI positioned nodes. For this purpose, a simple inverse distance interpolation [Shepard, 1968] is used for each new node over the overlapping old influence domain. This interpolation has to be applied, because of the very big gradients of the field. RBF interpolation would give too much over or undershoot as explained below. Shepard interpolation is given

$$f(\mathbf{p}) = \frac{\sum_{i=1}^{N_\omega} w(\mathbf{p},\mathbf{p}_i)\, f(\mathbf{p}_i)}{\sum_{i=1}^{N_\omega} w_i(\mathbf{p},\mathbf{p}_i)};\ w_i(\mathbf{p},\mathbf{p}_i) = \frac{1}{D_i(\mathbf{p},\mathbf{p}_i)^{\lambda}}, \tag{4.96}$$

where D is the Euclidean distance and λ is in the present work taken as 2. The function f can stand for temperature field or components of the displacement vector. A scheme of Shepard's interpolation for a newly positioned node over an influence domain, from the previous configuration, is shown in Figure 4.4.

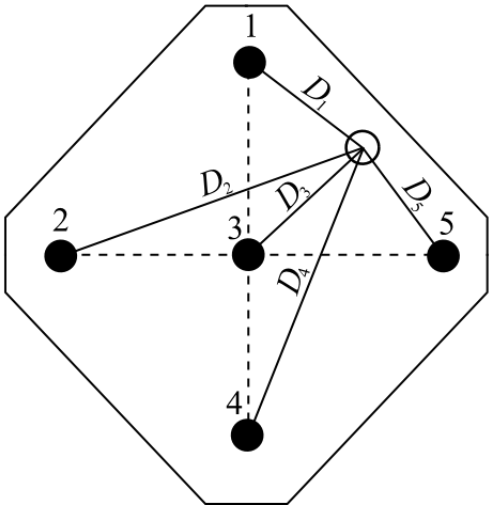

Figure 4.4: Scheme of obtaining a value for a new node position (hollow) with using old node configuration (black nodes) with their values and distances D_i in an influence domain.

The temperature and the displacement values for the newly positioned node could have been also calculated with RBF interpolation over the nearest previous influence domain. On the other hand, after the new node arrangement, node positions in an influence domain could be completely different or similar to the nodes positions from the old node arrangement. In case of the nodes from the new and the old configuration are very closely positioned, an overshoot can be observed through RBF interpolation for the new values to be recalculated, which is not acceptable for the simulation results. Therefore Shepard's interpolation is chosen here in which overshot is not observed.

4.4 Numerical implementation

The static solid material deformation problem is an elliptic problem which does not include time variation. A global system of equations are written based on Local Radial Basis Function Collocation Method (LRBFCM) which results in a sparse matrix where still a global approach is considered but instead of the

whole domain, local influence domains are considered. Solution of the sparse system of equations gives us the displacement results which are stored in the computer for further strain and stress calculations. An amount of $4N_{\omega}N_{\Omega}$ data are stored in the sparse matrix so if the number of the nodes increases, the calculation time increases nearly linear. In case of a full matrix, the computing time increases proportionally to the number of algebraic operations, which is $2\left(2N_{\Omega}\right)^{3}/3$. However, for the thermal model, only the local matrices are created at the beginning of the calculation, and if there is no deformation, then the previous ones are used. Even though thermal part requires time depended solution, it is much faster than the mechanical solution. An open source library Math.Net [Math.Net Iridium, 2008] is chosen for matrix calculations, LU decomposition is used for solving the system of equations.

A code has been written in C# [Microsoft Visual C#, 2007] with an interface where all the pre-process parameters are defined and also all the post process results can be seen as shown in Figure 4.5. The number of the slices is predefined though the positions in the rolling direction with a predefined incremental slice distance. Results can also be seen in a stepwise approach and for each slice. A similar approach as in the commercial codes is used. The results of temperature, displacement vectors, strain vector components and stress vector components can be seen on the interface of the program for a desired slice. For each slice also the position and corresponding time are also shown. Results can also be saved for a corresponding slice for further analysis by using various post process programs. In this dissertation ParaView [ParaView Parallel Visualization Application, 2012] post-processing program is used.

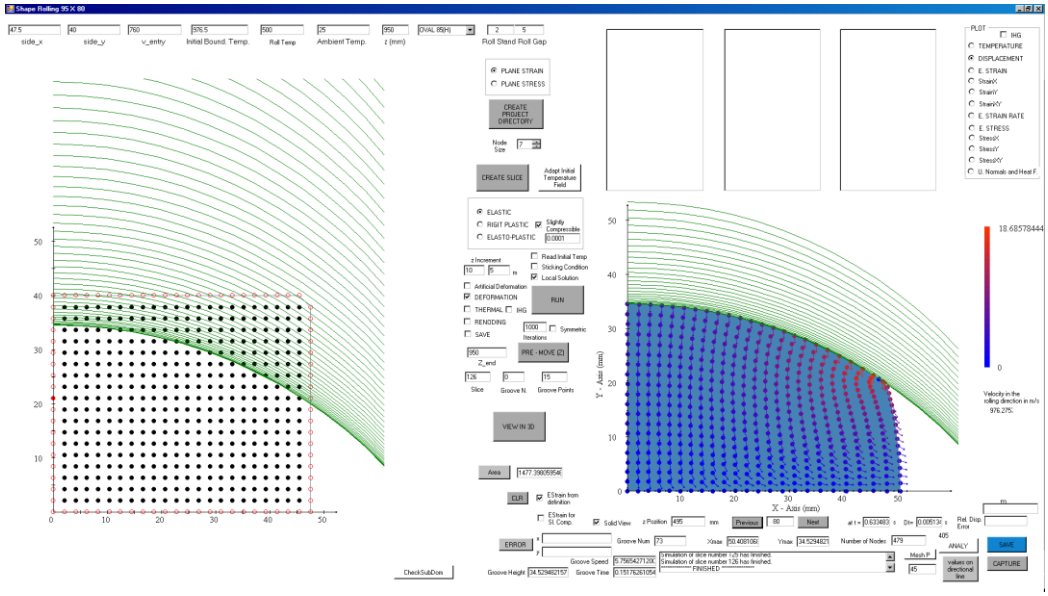

Figure 4.5: Snapshot of the software developed in C#.

Thermal field is always calculated in a continuous form from the beginning until the end, however results from the mechanical model are separately stored for each rolling stand. This means there is a continuous deformation through each rolling stand. Displacement, strain and stress values are cumulatively calculated for each rolling stand through the deformation steps.

The code can be easily modified for different rolling schedules. New groove geometries can be easily defined or added. Initial shape and velocity can be changed on the interface. The user can individually chose thermal and/or mechanical models to calculate. Material properties with material constants can be entered on the interface or can be read from a file where material properties are written in form of temperature depended table. A table which is used in this dissertation is included in the Appendix.

5 Verification of the Method

In Chapter 5, spectra of mechanical and thermal test cases are performed and compared with reference solutions to assess the accuracy and behaviour of the LRBFCM solution. Concerning the thermal model, a convective cooling test case is compared with FEM. Concerning the mechanical model, compression and tension examples are separately tested with prescribed displacement and traction by LRBFCM for an elastic material. The results from these cases are compared also with FEM and excellent agreement has been found. Moreover, bending of a cantilever beam, expansion of a cylindrical tube, linear compression-tension and bending of a beam by a uniform load are calculated and compared with analytical solutions. The tests are concluded by a flat rolling example with ideal plastic behaviour, compared with FEM.

5.1 Testing of the thermal model

Simulation of hot shape rolling is a very complicated process. The complicated geometry and large deformations might create numerical instabilities that are difficult to handle. Therefore, focusing on numerical issues such as proper solution of thermal and mechanical fields is of high priority. The results from the FEM based code DEFORM are used as reference solutions.

The solution of hot shape rolling is a coupled thermo-mechanical process. In order to get confidence in the results, the thermal and the mechanical models are first tested separately to check their accuracy. First, a convective cooling example is calculated, to see the accuracy of the thermal model. The Equation (4.69) is used as governing equation in this test.

5.1.1 Convective cooling

A square domain with 50 mm side is used for testing. The density is $\rho = 7450$ kg/m^3, specific heat is $c_p = 630$ J/kgK, thermal conductivity is $k = 29$ W/mK. Uniformly distributed 676 discretization points are used across the domain. 1076 elements are used in reference FEM. The time step in LRBFCM is set to 0.1 s and for FEM 1 s is used. The scheme of the problem can be seen in Figure 5.1.

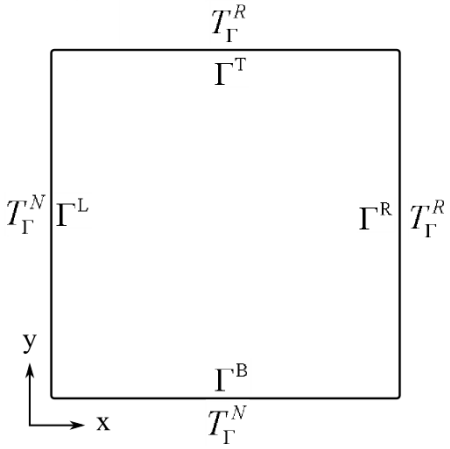

Figure 5.1: Scheme of the boundary conditions of the thermal test case.

Left and bottom boundaries are of the Neumann type where the prescribed heat flux is 0 W/m^2. For the top and right boundaries Robin type of boundary condition is applied.

$$T_\Gamma^N = n_x \frac{\partial T}{\partial p_x} = 0 \ \ \mathrm{W/m^2K} \qquad \mathbf{p} \in \Gamma^{\mathrm{L}},$$

$$T_\Gamma^R = n_x \frac{\partial T}{\partial p_x} = -\left(h_1/k\right)\left(T - T_{ref\,1}\right) \qquad \mathbf{p} \in \Gamma^{\mathrm{R}},$$

$$T_\Gamma^R = n_y \frac{\partial T}{\partial p_y} = -\left(h_2/k\right)\left(T - T_{ref\,2}\right) \qquad \mathbf{p} \in \Gamma^{\mathrm{T}},$$

$$T_\Gamma^N = n_y \frac{\partial T}{\partial p_y} = 0 \ \ \mathrm{W/m^2K} \qquad \mathbf{p} \in \Gamma^{\mathrm{B}}.$$

The initial temperature is set to 1000 °C, $h_1 = 20$ W/m^{2}K, $h_2 = 5000$ W/m^{2}K, $T_{ref\,1} = 25$ °C, $T_{ref\,2} = 500$ °C and $\dot{Q} = 0$ W/m^3. The heat transfer coefficient on the top side is chosen in such a way to be consistent with the contact with the roll and the heat transfer coefficient of the right side imitates the heat flow to the air. The simulation result as 10 s, 30 s and 60 s are compared with FEM in Figure 5.2, Figure 5.3 and Figure 5.4 respectively.

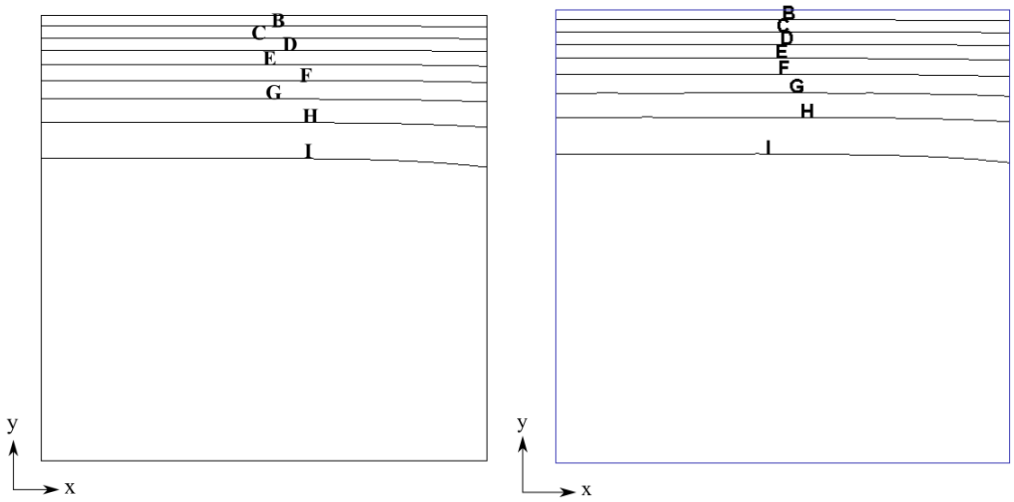

Figure 5.2: Thermal test case. Left: LRBFCM, Right: FEM at time 10 s. All of the sides have the length of 50 mm. Lines represent B = 709 °C, C = 745 °C, D = 782 °C, E = 818 °C, F = 854 °C, G = 891 °C, H = 927 °C and I = 964 °C.

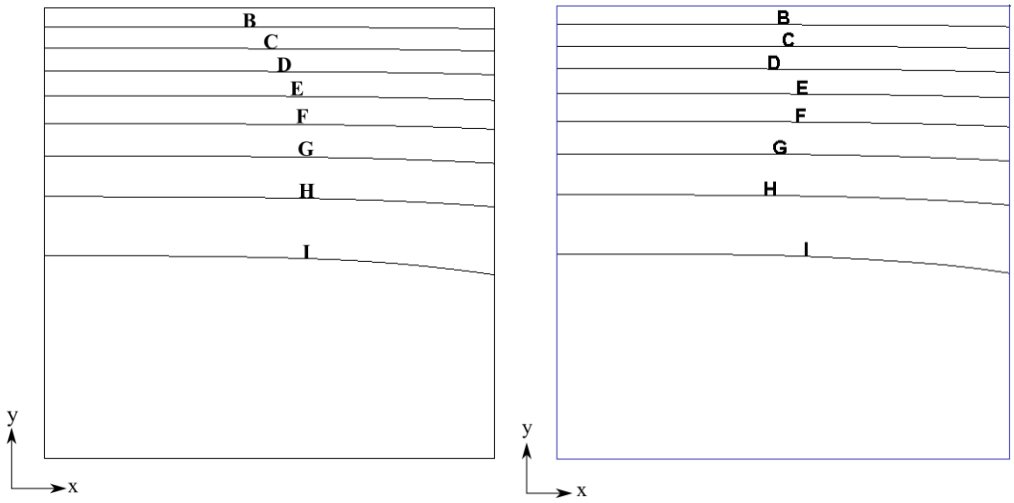

Figure 5.3: Thermal test case. Left: LRBFCM, Right: FEM at time 30 s. All of the sides have the length of 50 mm. Lines represent B = 651 °C, C = 694 °C, D = 737 °C, E = 780 °C, F = 823 °C, G = 866 °C, H = 909 °C and I = 952 °C.

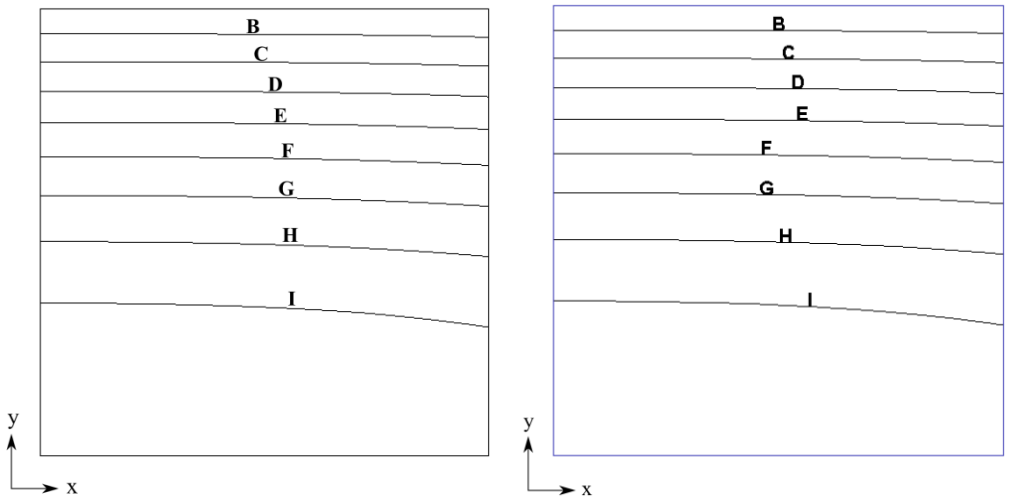

Figure 5.4: Thermal test case. Left: LRBFCM, Right: FEM at time 60 s. All of the sides have the length of 50 mm. The contour lines represents B = 620 °C, C = 662 °C, D = 703 °C, E = 745 °C, F = 787 °C, G = 829 °C, H = 871 °C and I = 913 °C.

The shaded graphs of the results in Figure 5.4 are shown in Figure 5.5 below.

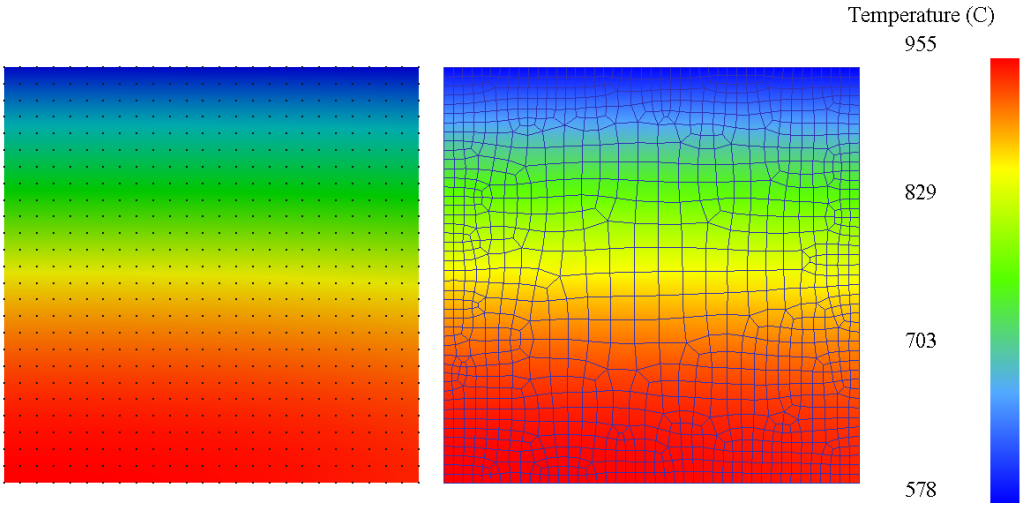

Figure 5.5: Thermal test case. All of the sides have the length of 50 mm. Left: LRBFCM, Right: FEM at time 60 s.

5.1.2 Internal heat generation during deformation

In this case a rectangular domain 47.5×40 mm is chosen and deformation is applied through oval groove like in Figure 6.9. An elastic plane strain model is used with $E = 100.404\,\text{GPa}$ and $\nu = 0.3535$. On the boundaries Neumann type is used $T_{\Gamma}^{N} = 0$ W/m^{2}K and uniform initial temperate of the slice is 1100 °C. An oval groove is used for rolling with GR = 85 mm, GW = 122 mm, RR = 540 mm and $R_{gap} = 17$ mm. The temperature increase due to internal heat generation calculated by LRBFCM is seen in Figure 5.6 below. 525 collocation nodes are used.

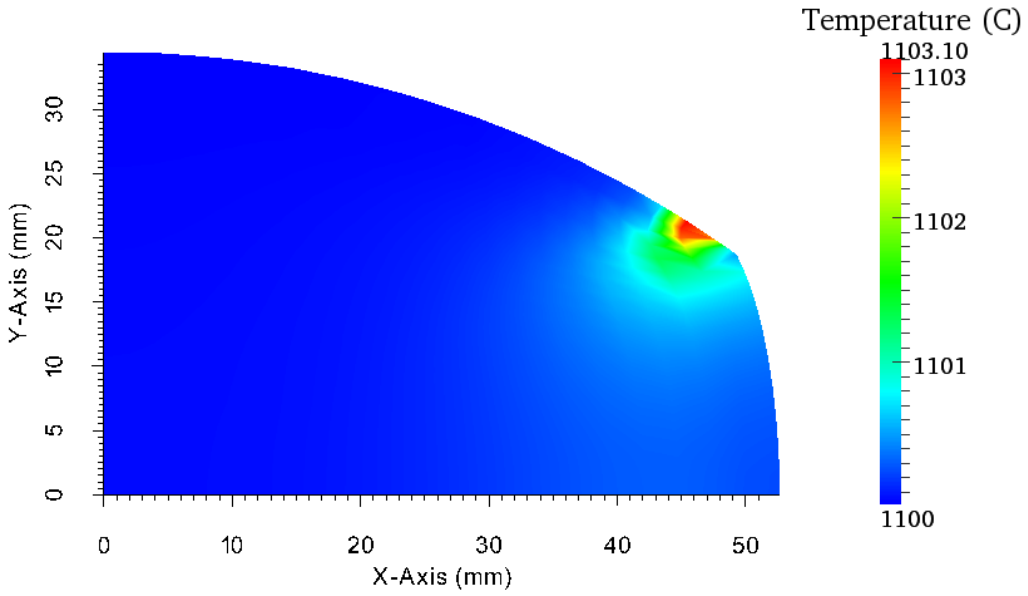

Figure 5.6: Temperature increase due to internal heat generation when no heat flux occurs at the boundaries and initial uniform temperature at 1100 °C and $\eta = 10^{-4}$.

5.2 Testing of the mechanical model

The computer code, developed for rolling, is tested on several quite simple deformation cases. These are: various compression or tension examples with prescribed displacements or traction, 4 different deformation cases with known analytical solutions and a flat rolling example. In all the tests with elastic material, governing equations in Table 2.1 are used.

5.2.1 Compression - tension examples

Compression and tension tests are the first examples used for testing LRBFCM solved mechanical model. Many combinations of the boundary conditions can be applied in terms of prescribed traction or prescribed displacement. During the following examples, an elastic 2 × 2 m material with Young's modulus $E = 1$ Pa and Poisson ratio $\nu = 0.3$ is chosen. Centre of the coordinate system is in the middle of the bottom line of the object. At the top, the prescribed displacement or pressure is applied towards the y direction, however the displacement in *x* direction is always fixed to 0. The results in this section are compared with FEM.

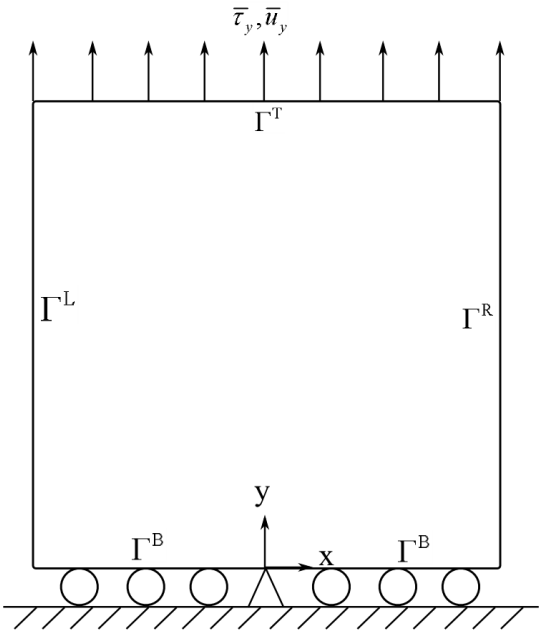

Figure 5.7: Testing of the mechanical model. Scheme of the geometry and boundary conditions for compression-tension examples. The size of the square is 2 × 2 m.

5.2.1.1 Compression with prescribed displacement

In this example, a compression is applied from the top, with a prescribed displacement. This is an elastic plane strain problem as shown in Figure 5.7. The boundary conditions are given below,

$$\bar{u}_x = 0 \text{ m}, \ \bar{u}_y = -0.5 \text{ m} \qquad \mathbf{p} \in \Gamma^T,$$

$$\bar{\tau}_x = 0 \text{ Pa}, \ \bar{\tau}_y = 0 \text{ Pa} \qquad \mathbf{p} \in \Gamma^{\mathrm{R}},$$

$$\begin{aligned} &\bar{u}_x = 0 \text{ m}, \bar{u}_y = 0 \text{ m} \\ &\bar{\tau}_x = 0 \text{ Pa}, \bar{u}_y = 0 \text{ m} \end{aligned} \qquad \begin{cases} \mathbf{p} \in \Gamma^{\mathrm{B}} \wedge \mathbf{p} \in (0,0) \\ \mathbf{p} \in \Gamma^{\mathrm{B}} \wedge \mathbf{p} \notin (0,0) \end{cases},$$

$$\bar{\tau}_x = 0 \text{ Pa}, \ \bar{\tau}_y = 0 \text{ Pa} \qquad \mathbf{p} \in \Gamma^{\mathrm{L}}.$$

The displacement vectors, calculated LRBFCM are shown in Figure 5.8 below.

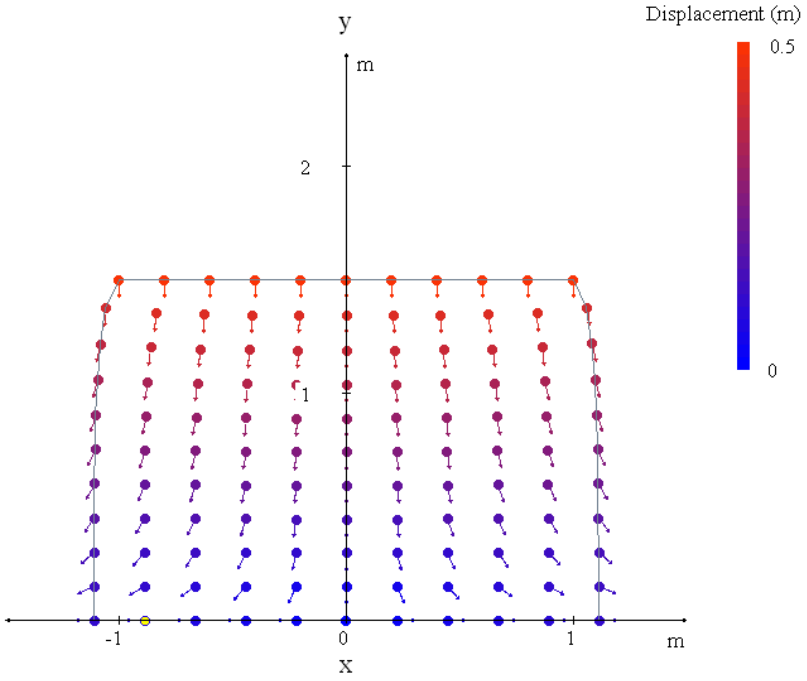

Figure 5.8: LRBFCM solution of the compression test. Displacement field after the compression. 121 collocation nodes are used in the calculation.

The same compression test is also calculated by FEM and the deformation, illustrated with displacement vectors is show in Figure 5.9.

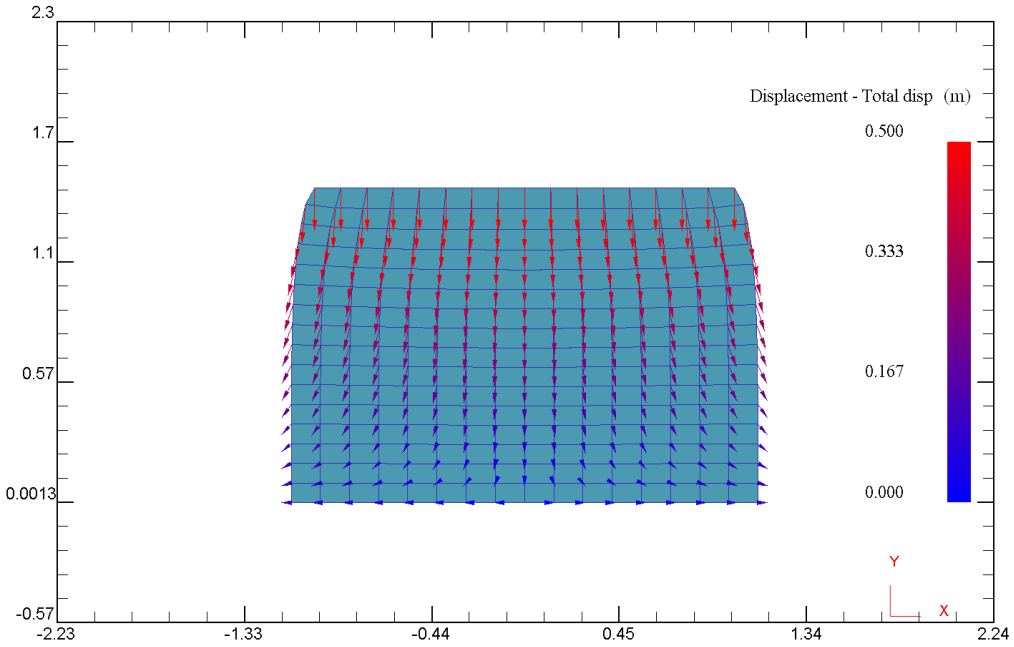

Figure 5.9: FEM solution of the compression test and displacement field after the compression.

Comparison between LRBFCM and FEM is made in terms of displacement field in Figure 5.10 and excellent agreement has been found.

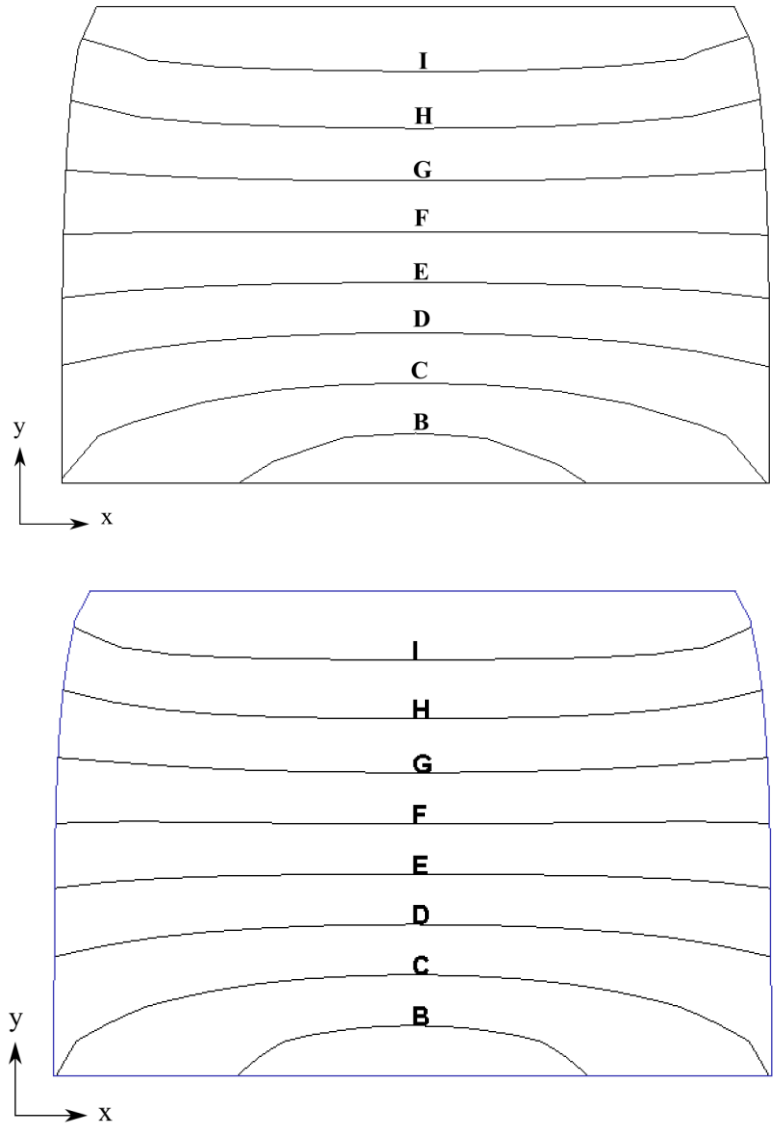

Figure 5.10: Contour graphs of displacement fields when a deformation of 0.5 m is imposed from the top with sticking boundary conditions. LRBFCM solution (on top) and FEM solution (at the bottom). The lines represent B = 0.0556 m, C = 0.111 m, D = 0.167 m, E = 0.222 m, F = 0.278 m, G = 0.333 m, H = 0.389 m, I = 0.444 m and J = 0.5 m.

Three different compression rates are applied and a very good match has been achieved between LRBFCM and FEM as in Table 5.1.

Compression rates	Width calculated by LRBFCM in m	Width calculated by FEM in m
10 %	2.0895	2.0894
25 %	2.2237	2.2236
50 %	2.4475	2.4472

Table 5.1: Comparison of expansion at the bottom of the square, calculated by LRBFCM and FEM.

5.2.1.2 Tension with prescribed displacement

In this example, tension is applied from the top with a prescribed displacement. This is an elastic plane strain problem as shown in Figure 5.7. The boundary conditions are given below,

$$\bar{u}_x = 0 \text{ m},\ \bar{u}_y = 0.2 \text{ m} \qquad \mathbf{p} \in \Gamma^{\mathrm{T}},$$

$$\bar{\tau}_x = 0 \text{ Pa},\ \bar{\tau}_y = 0 \text{ Pa} \qquad \mathbf{p} \in \Gamma^{\mathrm{R}},$$

$$\begin{matrix} \bar{u}_x = 0 \text{ m},\ \bar{u}_y = 0 \text{ m} \\ \bar{\tau}_x = 0 \text{ Pa},\ \bar{u}_y = 0 \text{ m} \end{matrix} \qquad \begin{cases} \mathbf{p} \in \Gamma^{\mathrm{B}} \wedge \mathbf{p} \in (0,0) \\ \mathbf{p} \in \Gamma^{\mathrm{B}} \wedge \mathbf{p} \notin (0,0) \end{cases},$$

$$\bar{\tau}_x = 0 \text{ Pa},\ \bar{\tau}_y = 0 \text{ Pa} \qquad \mathbf{p} \in \Gamma^{\mathrm{L}}.$$

Displacement fields calculated by LRBFCM and FEM, illustrated by displacement vectors and a comparison of contour graphs is made in Figures 5.11, 5.12 and 5.13 respectively.

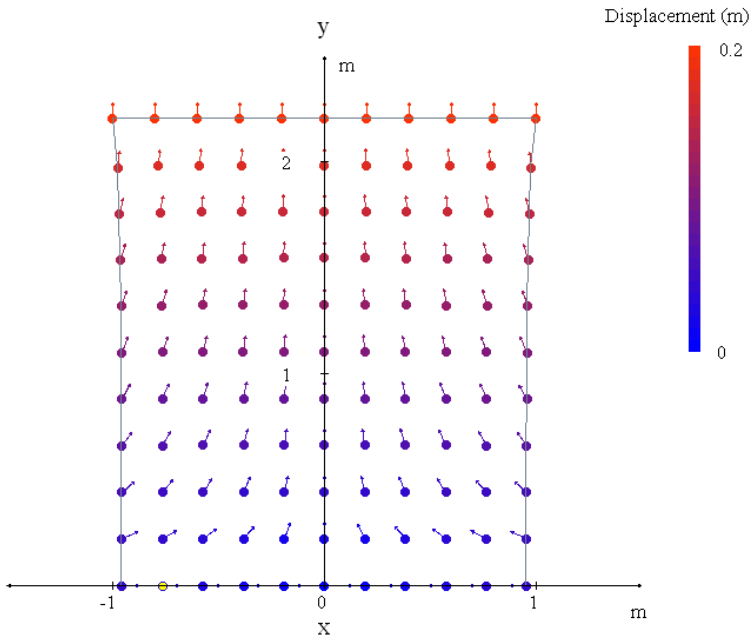

Figure 5.11: Displacement field calculated by LRBFCM when 0.2 mm tension is applied on the top with sticking boundary conditions. 121 nodes are used.

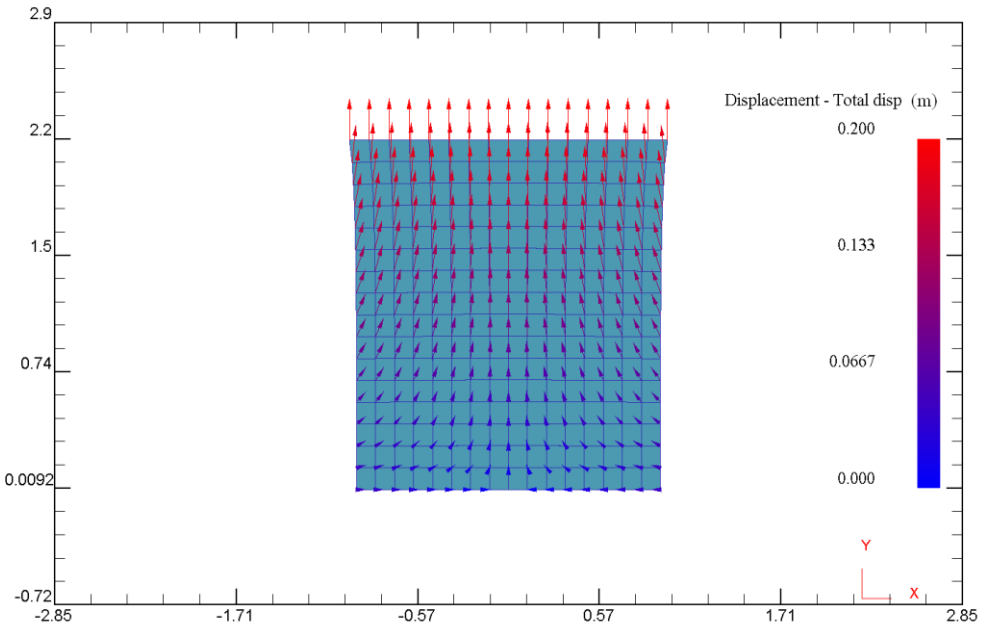

Figure 5.12: Displacement field calculated by FEM when 0.2 mm tension is applied on the top with sticking boundary conditions. 256 finite elements are used.

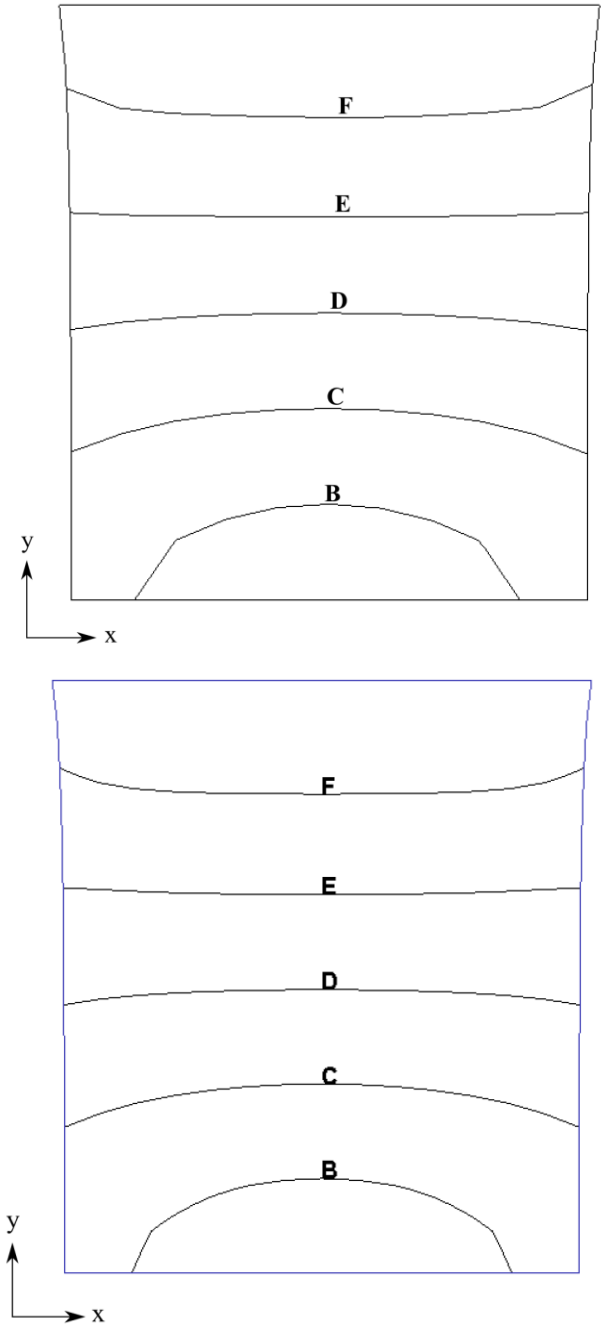

Figure 5.13: Contour lines of displacement fields compared, LRBFCM (on top) with FEM (at bottom). Lines represent A = 0.0 m, B = 0.033 m, C = 0.067 m, D = 0.1 m, E = 1.033 m and F = 1.067 m.

For this test case, three different compression rates are also applied and very good match has been achieved as in Table 5.2.

Tension rates	**Width calculated by LRBFCM (m)**	**Width calculated by FEM (m)**
10 %	1.9105	1.9106
25 %	1.7763	1.7764
50 %	1.5525	1.5528

Table 5.2: Comparison of expansion at the bottom of the square, calculated by LRBFCM and FEM.

5.2.1.3 Compression with prescribed pressure

In this example, a compression is applied from the top with a prescribed traction. This is an elastic plane strain problem as shown in Figure 5.7. The boundary conditions are given below,

$$\bar{u}_x = 0 \text{ m},\ \bar{\tau}_y = -0.5 \text{ Pa} \qquad \mathbf{p} \in \Gamma^{\mathrm{T}},$$

$$\bar{\tau}_x = 0 \text{ Pa},\ \bar{\tau}_y = 0 \text{ Pa} \qquad \mathbf{p} \in \Gamma^{\mathrm{R}},$$

$$\begin{aligned} &\bar{u}_x = 0 \text{ m}, \bar{u}_y = 0 \text{ m} \\ &\bar{\tau}_x = 0 \text{ Pa}, \bar{u}_y = 0 \text{ m} \end{aligned} \qquad \begin{cases} \mathbf{p} \in \Gamma^{\mathrm{B}} \wedge \mathbf{p} \in (0,0) \\ \mathbf{p} \in \Gamma^{\mathrm{B}} \wedge \mathbf{p} \notin (0,0) \end{cases},$$

$$\bar{\tau}_x = 0 \text{ Pa},\ \bar{\tau}_y = 0 \text{ Pa} \qquad \mathbf{p} \in \Gamma^{\mathrm{L}}.$$

The displacement fields in vector form calculated by LRBFCM and FEM and shown in Figures 5.14 and 5.15. Further comparisons of displacement fields and strain vector components $\varepsilon_{xx}, \varepsilon_{yy}, \varepsilon_{xy}$ are made in Figure 5.16, Figure 5.17, Figure 5.18 and Figure 5.19 respectively. 441 collocation nodes are used in LRBFCM solutions.

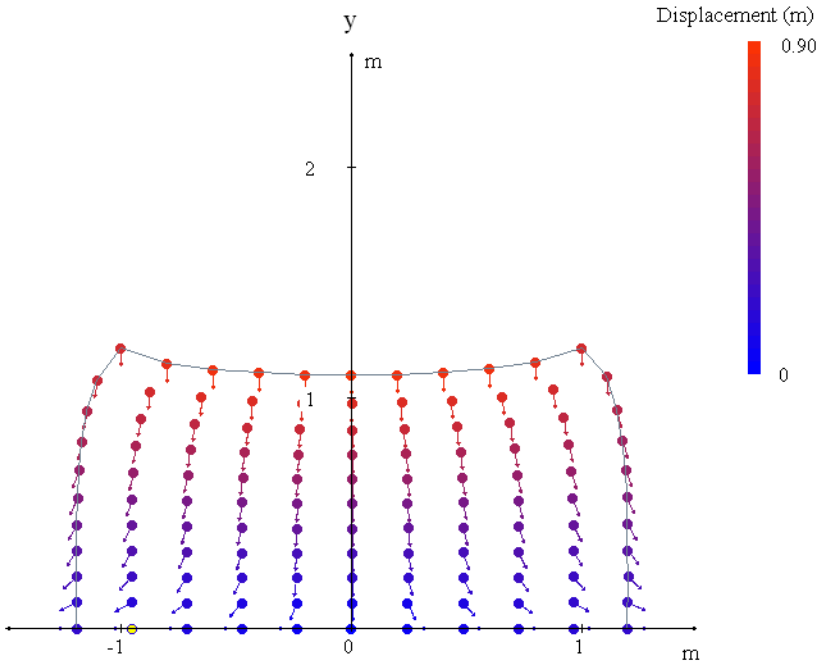

Figure 5.14: Displacement field calculated by LRBFCM FEM when-0.5 Pa pressure is applied at the top boundary. 121 collocation nodes are used.

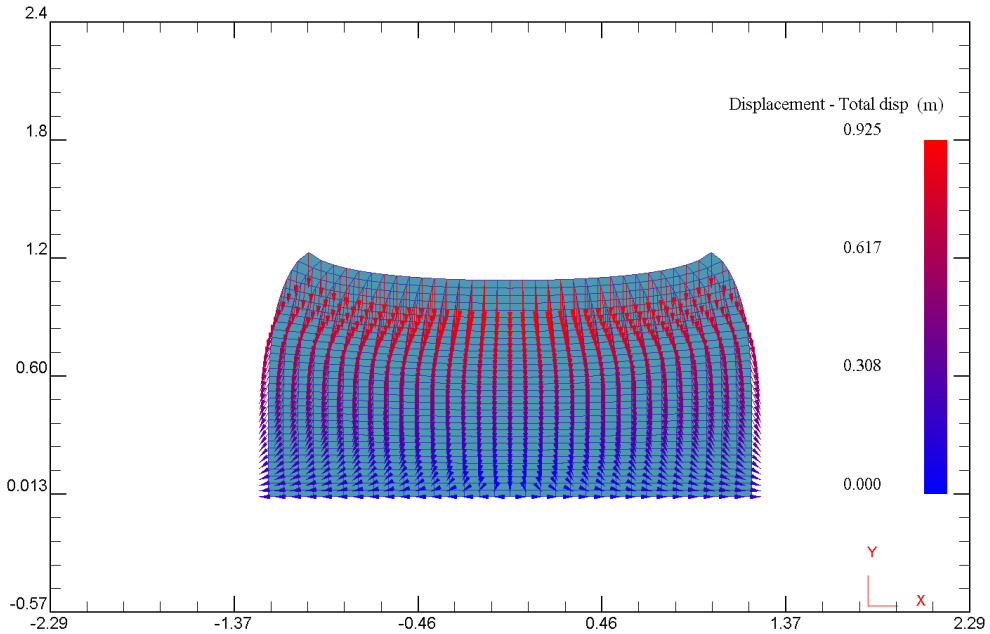

Figure 5.15: Displacement field calculated by FEM when-0.5 Pa pressure is applied at the top boundary. 1024 elements are used.

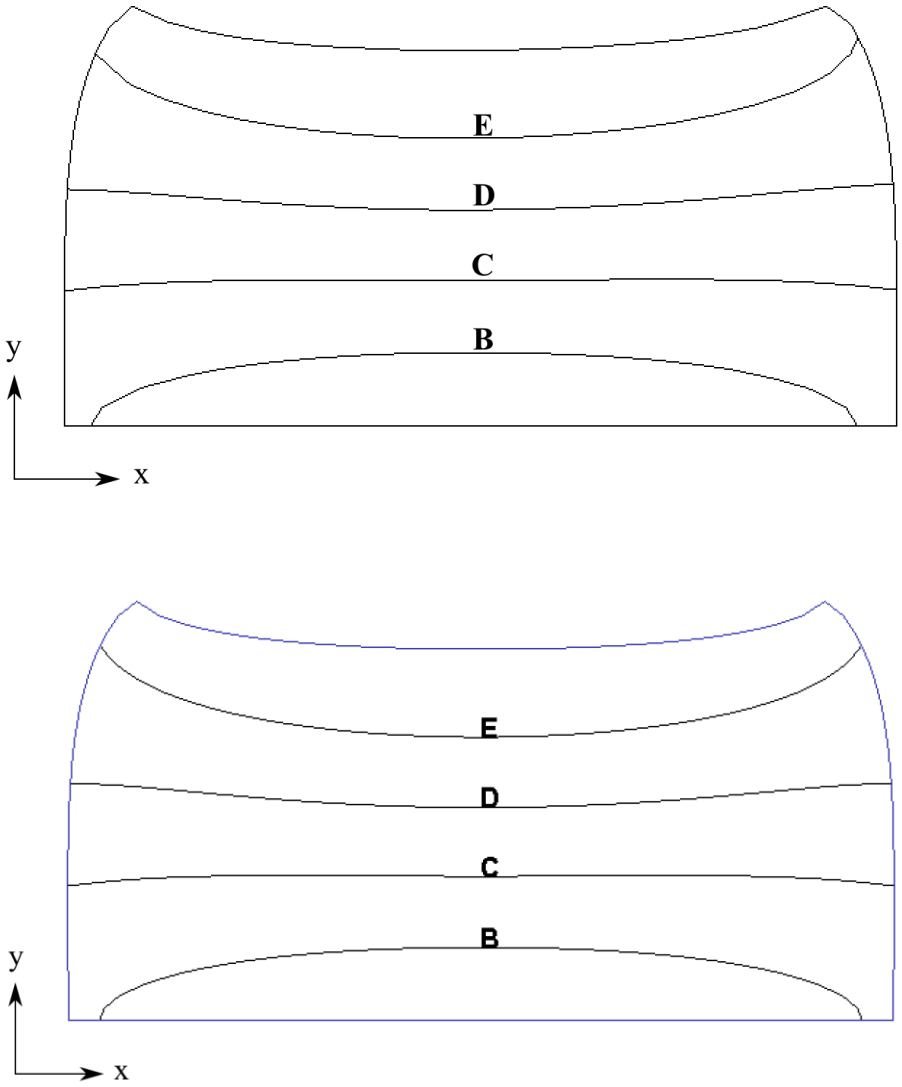

Figure 5.16: Comparison of displacement fields with LRBFCM (on top) and FEM (at the bottom). At top boundary -0.5 Pa pressure is applied when the movement along the *x* axis is fixed to 0. Lines represent B = 0.185 m, C = 0.37 m, D = 0.555 m and E = 0.74 m.

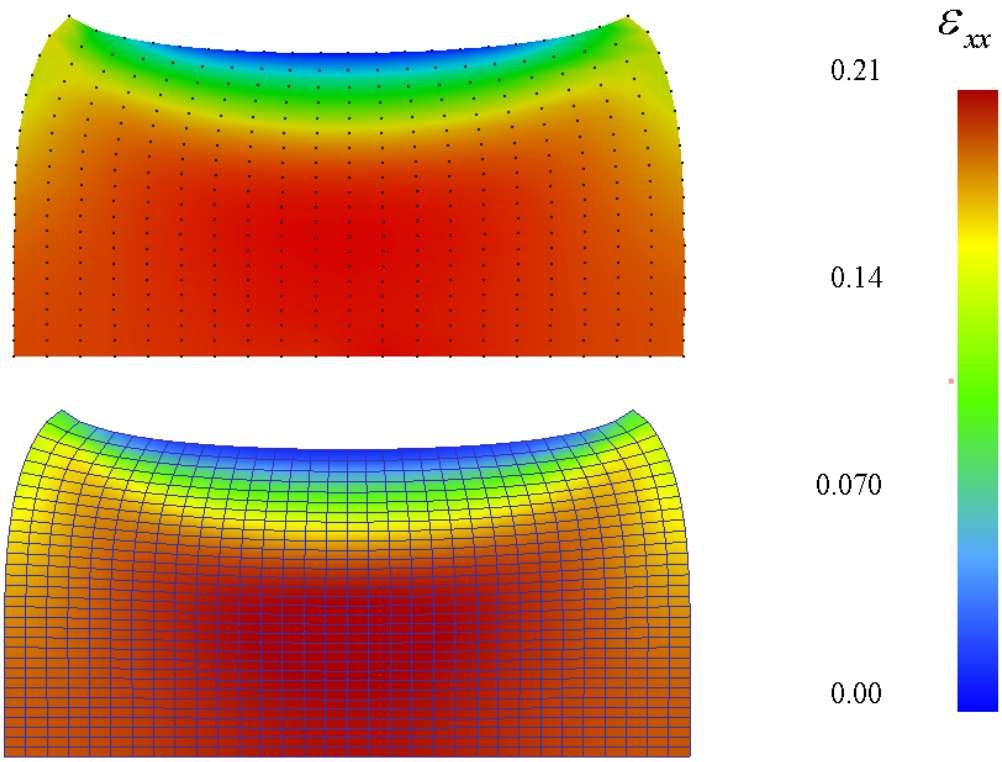

Figure 5.17: ε_{xx} contours calculated by LRBFCM on top and FEM at the bottom for compression with prescribed pressure example.

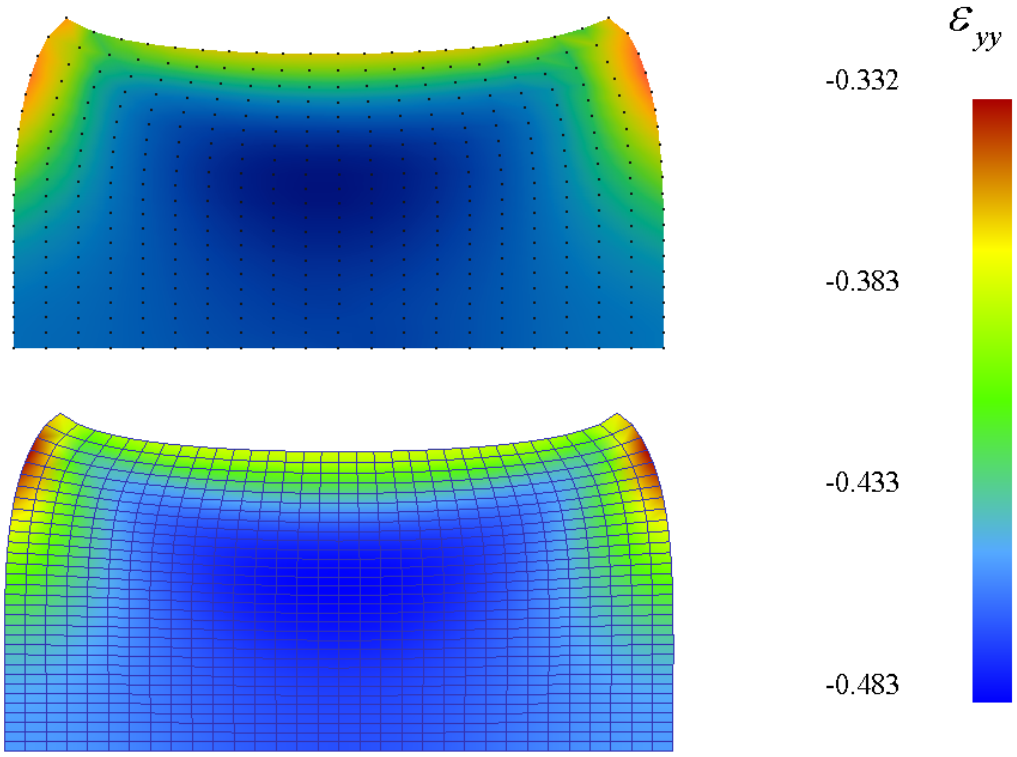

Figure 5.18: ε_{yy} contours calculated by LRBFCM on top and FEM at the bottom for compression with prescribed pressure example.

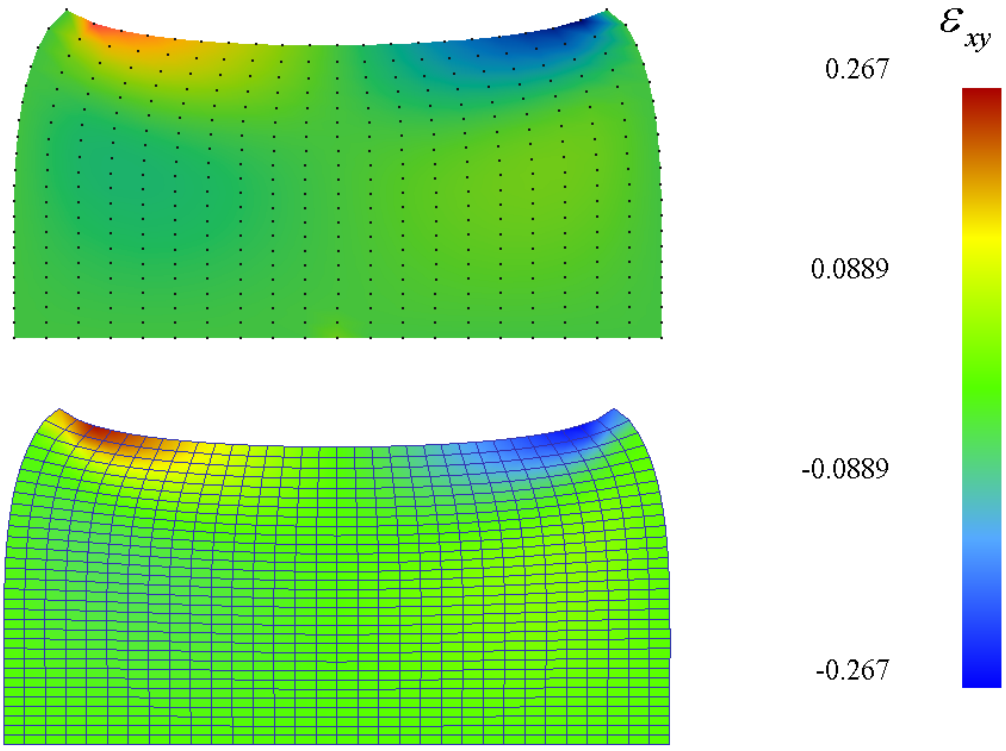

Figure 5.19: ε_{xy} contours calculated by LRBFCM on top and FEM at the bottom for compression with prescribed pressure example.

5.2.1.4 Tension with prescribed pressure

In this example, a compression is applied from the top with a prescribed traction. This is an elastic plane strain problem as shown in Figure 5.7. The boundary conditions are given below,

$$\bar{u}_x = 0 \text{ m}, \ \bar{\tau}_y = 0.2 \text{ Pa} \qquad \mathbf{p} \in \Gamma^{\mathrm{T}},$$

$$\bar{\tau}_x = 0 \text{ Pa}, \ \bar{\tau}_y = -0.5 \text{ Pa} \qquad \mathbf{p} \in \Gamma^{\mathrm{R}},$$

$$\begin{aligned} &\bar{u}_x = 0 \text{ m}, \bar{u}_y = 0 \text{ m} \\ &\bar{\tau}_x = 0 \text{ Pa}, \bar{u}_y = 0 \text{ m} \end{aligned} \qquad \begin{cases} \mathbf{p} \in \Gamma^{\mathrm{B}} \wedge \mathbf{p} \in (0,0) \\ \mathbf{p} \in \Gamma^{\mathrm{B}} \wedge \mathbf{p} \notin (0,0) \end{cases},$$

$$\bar{\tau}_x = 0 \text{ Pa}, \ \bar{\tau}_y = 0 \text{ Pa} \qquad \mathbf{p} \in \Gamma^{\mathrm{L}}.$$

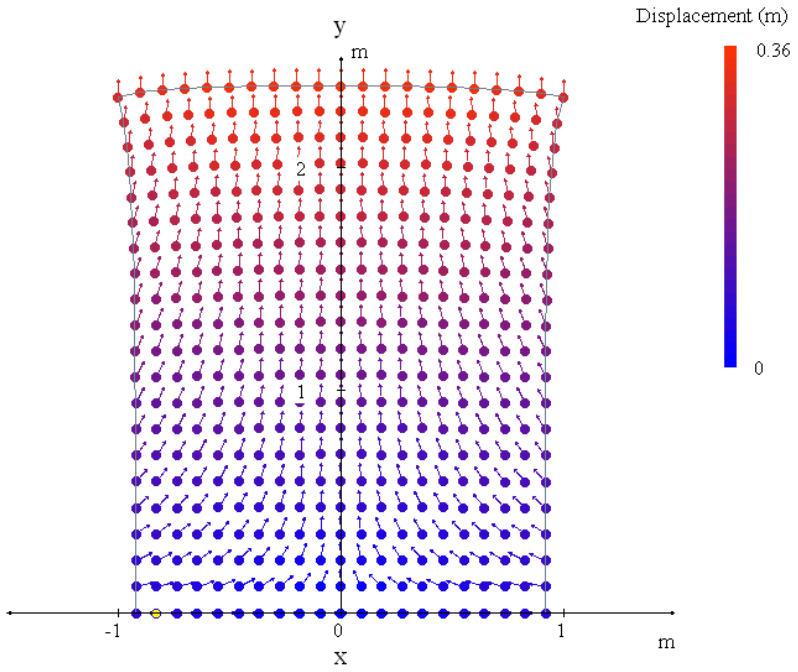

Figure 5.20: Displacement field calculated by LRBFCM when 0.2 Pa tension is applied at the top. 441 nodes are used.

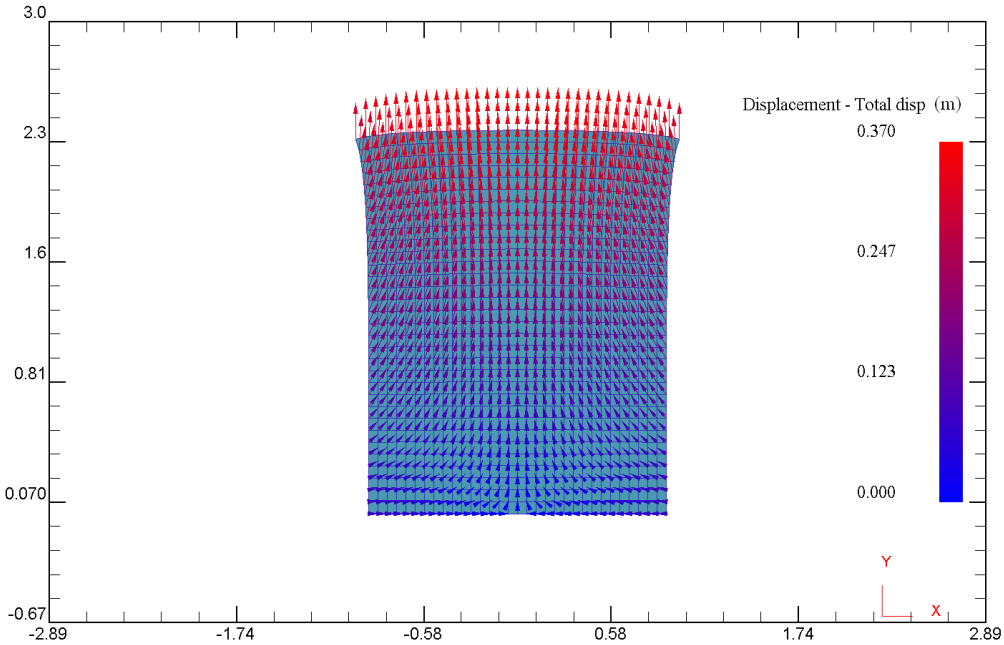

Figure 5.21: Displacement field calculated by FEM when 0.2 Pa tension is applied at the top. 1024 finite elements are used.

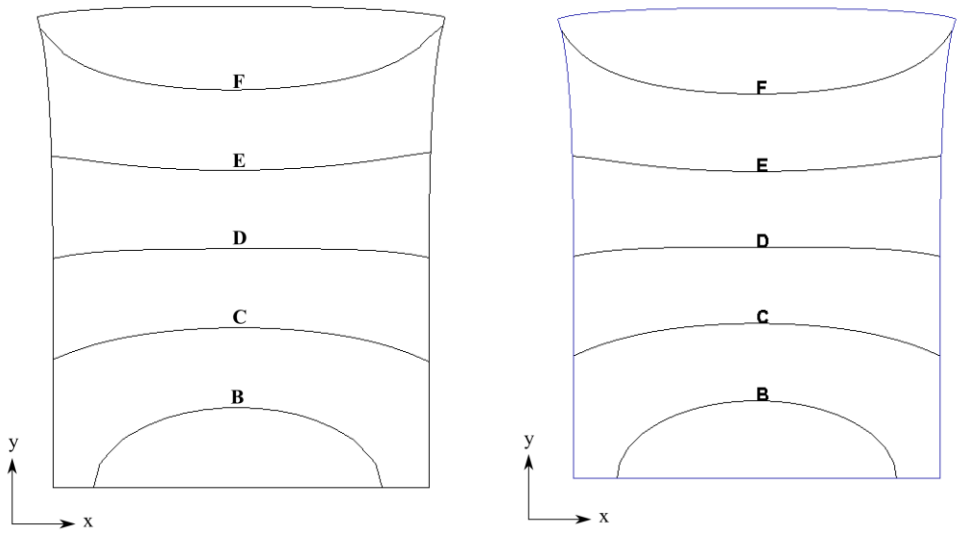

Figure 5.22: Comparison of displacement fields with LRBFCM (left) and by FEM (right). At top boundary 0.2 Pa pressure is applied towards the outside when the movement along the x axis is fixed to 0. Lines represent B = 0.0617 m, C = 0.123 m, D = 0.185 m, E = 0.247 m and F = 0.308 m.

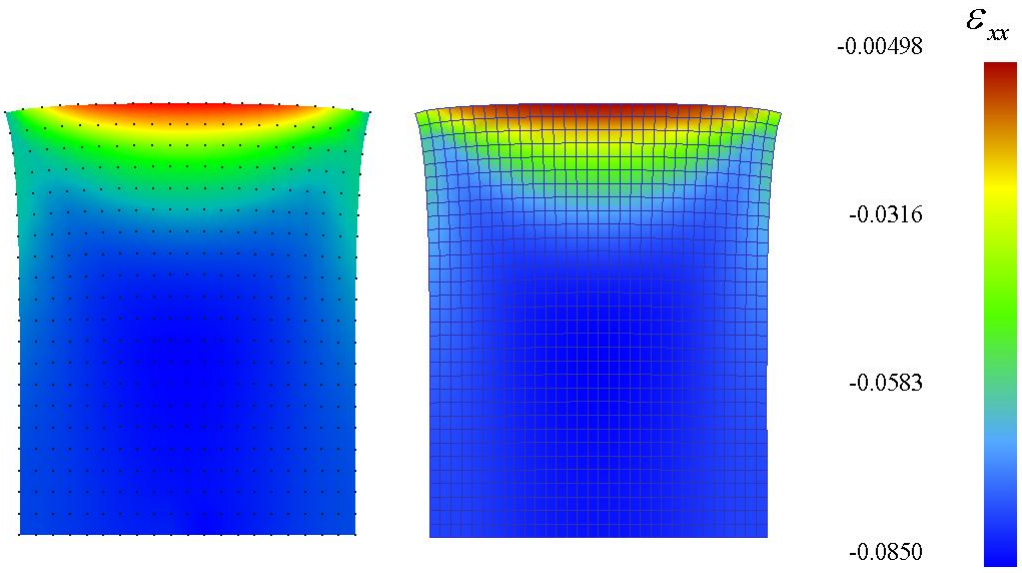

Figure 5.23: ε_{xx} contours calculated by LRBFCM on left and FEM on right for tension with prescribed pressure case.

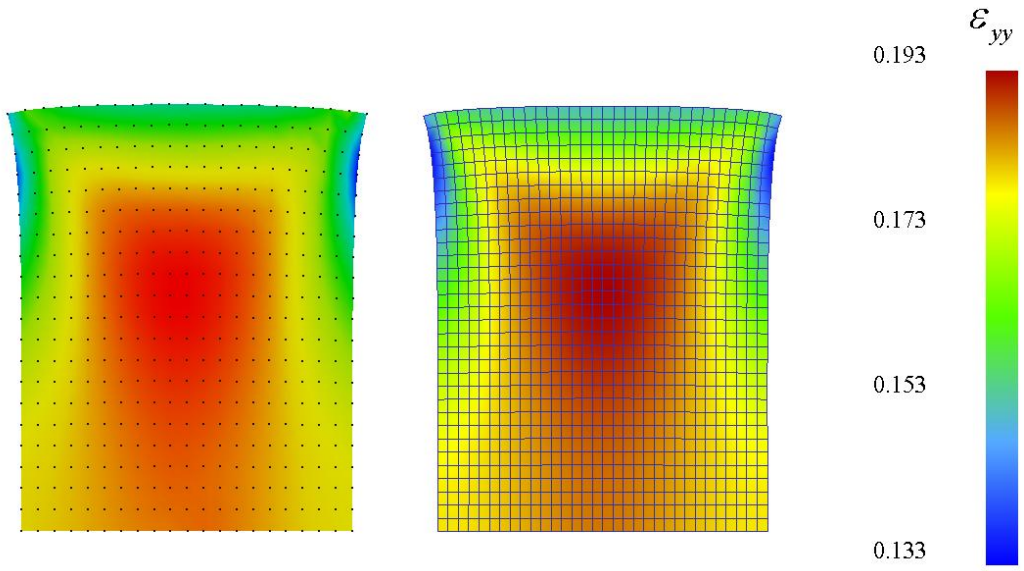

Figure 5.24: ε_{yy} contours calculated by LRBFCM on left and FEM on right for tension with prescribed pressure case.

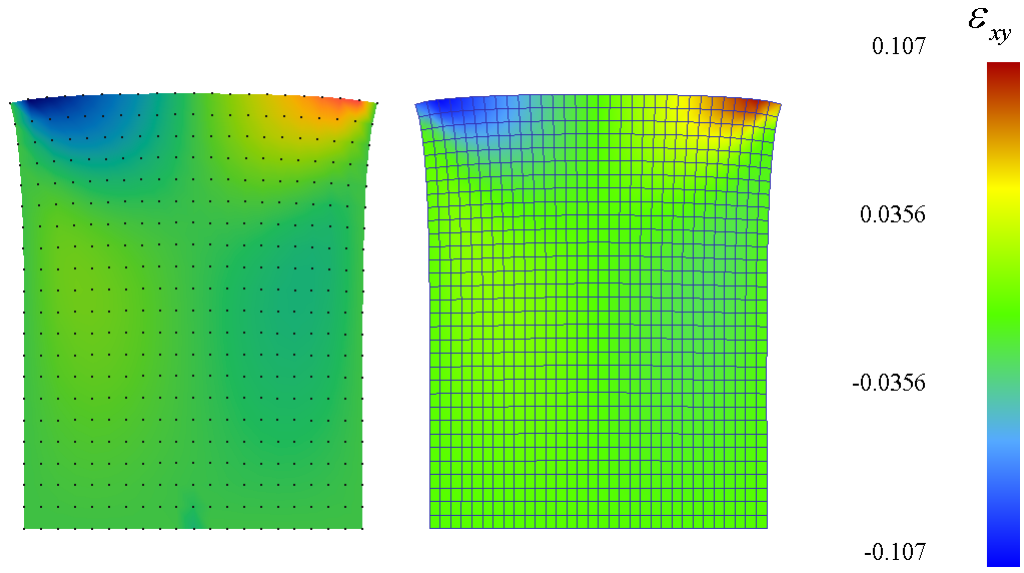

Figure 5.25: ε_{xy} contours calculated by LRBFCM on left and FEM on right for tension with prescribed pressure case.

Displacement vectors calculated by LRBFCM and FEM are shown in Figure 5.20 and Figure 5.21. Further comparisons of displacement fields and strain

vector components $\varepsilon_{xx}, \varepsilon_{yy}, \varepsilon_{xy}$ are made in Figure 5.22, 5.23, 5.24 and 5.25 respectively. 441 collocation nodes are used in LRBFCM solutions.

During the compression and tension examples with prescribed pressure, the computations with LRBFCM are much faster than with FEM. This is because number of nodes used in LRBFCM results is less than half of the number of finite elements used in FEM. It is also observed that with the same number of computational nodes in LRBFCM and FEM, LRBFCM would give results faster approximately up to a few hundred nodes/elements. When that number is exceeded, FEM code would be faster. It should also be noted, that the code, developed in the framework of this dissertation is of the laboratory type, whereas the used FEM code is commercial.

5.2.2 Bending of a cantilever beam

Another mechanical deformation example widely used for comparison is bending of a cantilever beam. This is an elastic plan stress problem. Side L is 48 m and height H is 12 m. The traction applied at the end $P = 30\,\text{Pa}$, Young's modulus of the beam $E = 1000$ Pa and $\nu = 0.3$. Boundary conditions are explained below.

$$\bar{\tau}_x = 0 \text{ Pa},\ \bar{\tau}_y = 0 \text{ Pa} \qquad \mathbf{p} \in \Gamma^{\mathrm{T}},$$

$$\bar{\tau}_x = 0 \text{ Pa},\ \bar{\tau}_y = P \qquad \mathbf{p} \in \Gamma^{\mathrm{R}},$$

$$\bar{\tau}_x = 0 \text{ Pa},\ \bar{\tau}_y = 0 \text{ Pa} \qquad \mathbf{p} \in \Gamma^{\mathrm{B}},$$

$$\bar{u}_x = u_x\ ,\ \bar{u}_y = u_y \qquad \mathbf{p} \in \Gamma^{\mathrm{L}}.$$

The boundary conditions on the left side are taken from the analytical solution. The definition of the problem can be seen in Figure 5.26 below.

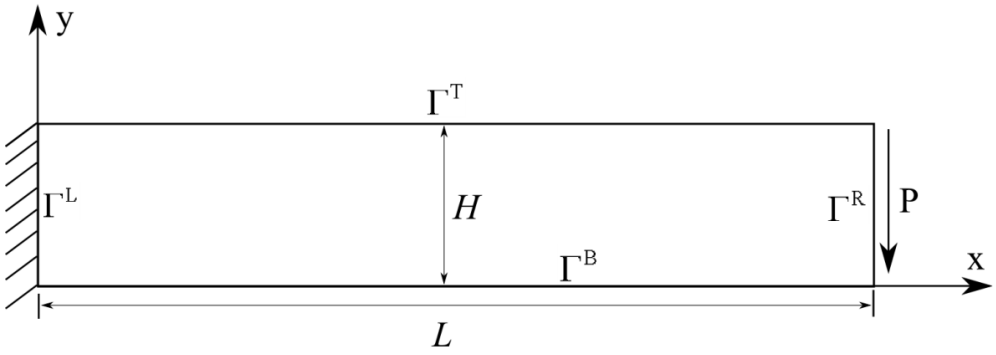

Figure 5.26: Scheme of the problem with bending of a cantilever beam.

The analytical solution is taken from [Liu, 2003].

$$u_x = -\frac{P}{6EI}\left(p_y - \frac{H}{2}\right)\left[\left(6L - 3p_x\right)p_x + \left(2+\nu\right)\left(\left(p_y - \frac{H}{2}\right)^2 - H^2\right)\right] \tag{5.1}$$

$$u_y = \frac{P}{6EI}\left[3\nu\left(p_y - \frac{H}{2}\right)\left(L - p_x\right) + \left(4+5\nu\right)\left(\frac{H^2 p_x}{4}\right) + \left(3L - p_x\right)p_x^2\right] \tag{5.2}$$

whit the moment of inertia $I = H^3/12$.

The LRBFCM solution for the bending of a cantilever beam problem is shown in Figure 5.27 with analytical solution. The displacement field with displacement vectors are also calculated by LRBFCM in Figure 5.28.

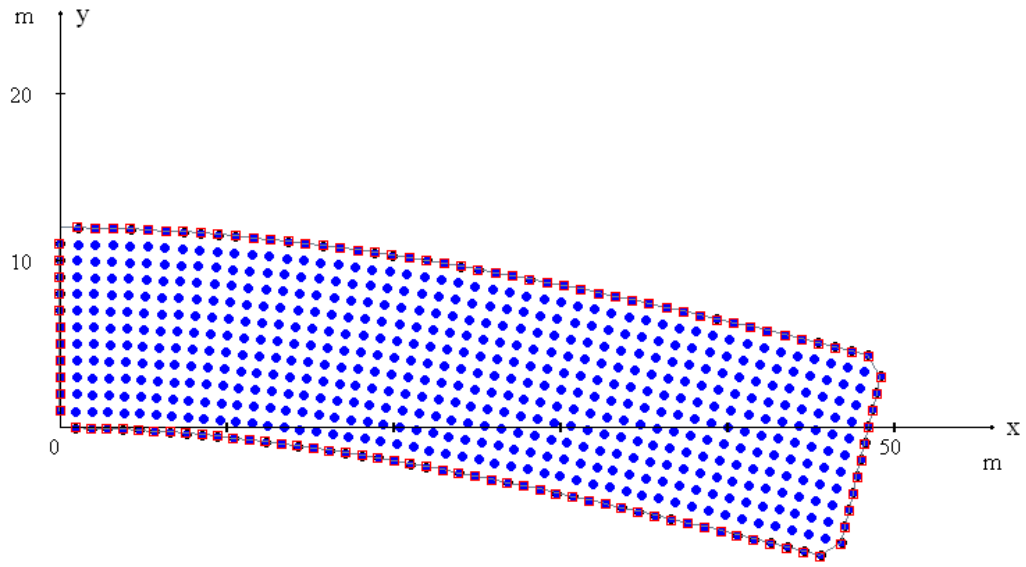

Figure 5.27: LRBFCM results of deformation (blue points) compared with the analytical solution (red squares) at the boundary points. 633 collocation nodes are used.

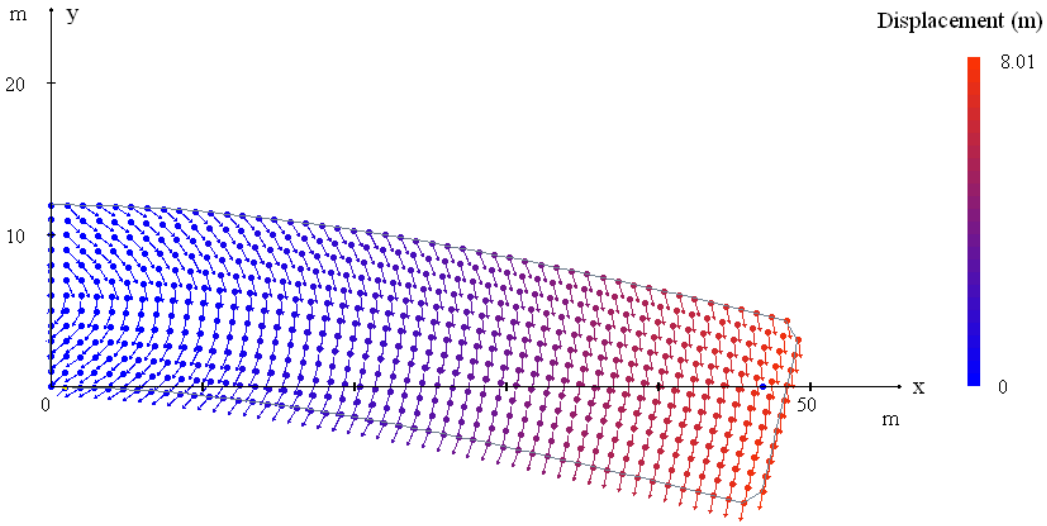

Figure 5.28: Displacement field of bending of a cantilever beam calculated by LRBFCM. 633 collocation nodes are used.

This solution of the test is achieved with different number of collocation nodes. The root mean square errors (RMSE) of the displacements are shown in Figure 5.29 as a function of the number of collocation nodes.

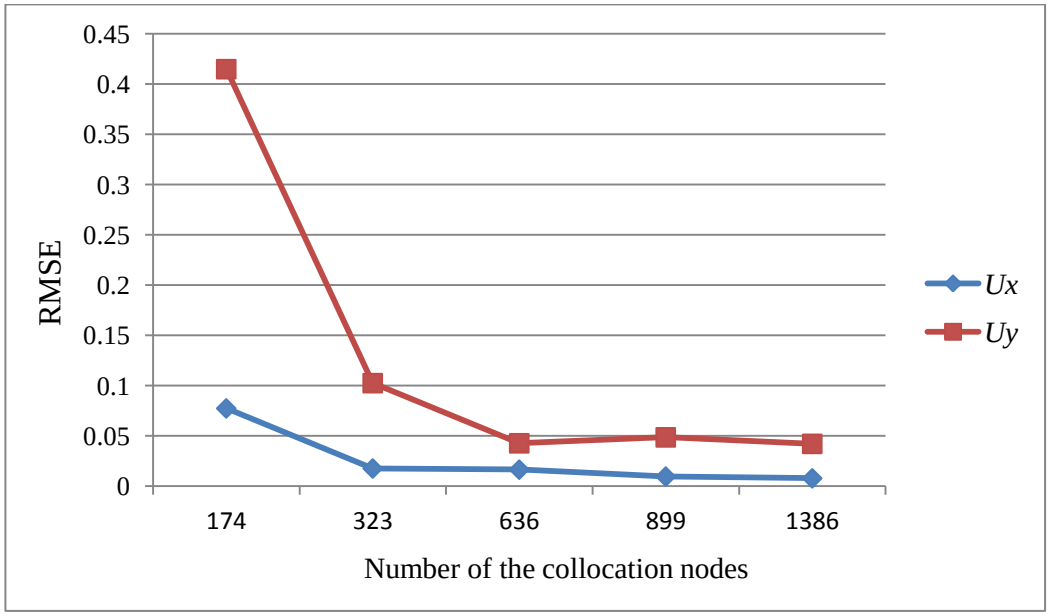

Figure 5.29: RMSE of displacements as a function of the node density.

The shear stress at the right side is also defined as

$$\tau_{xy} = \frac{P}{2I}\left[\frac{H^2}{4} - \left(p_y - \frac{H}{2}\right)^2\right] \tag{5.3}$$

For the same case, the shear stress at the end of the beam ($x = 48$ m) can be calculated with LRBFCM and compared with the Equation (5.3). The comparison is shown in Figure 5.30.

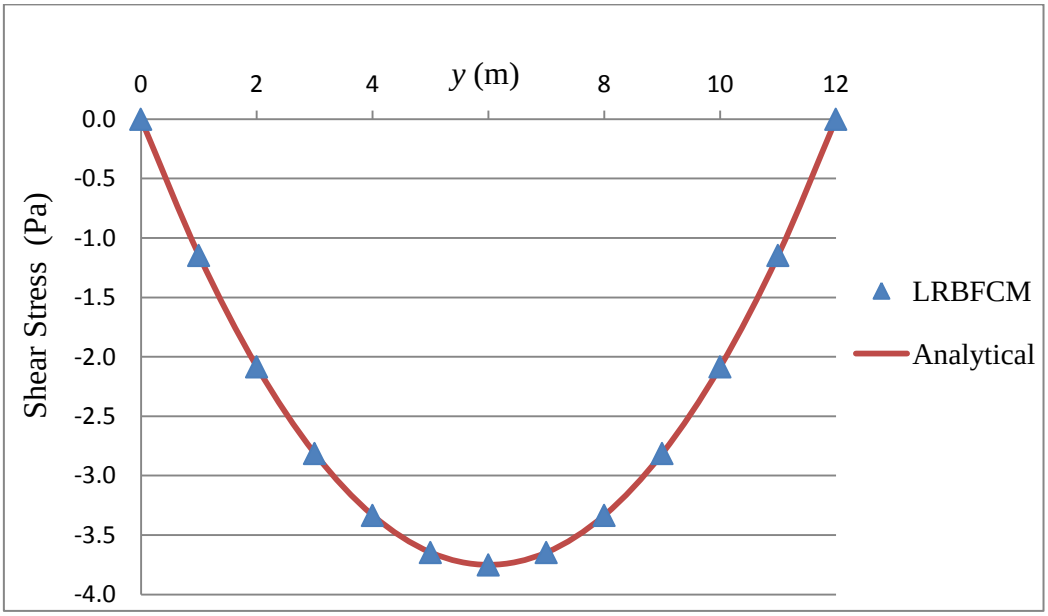

Figure 5.30: Shear stress at the end of the cantilever beam when $x = 48$ m compared with the analytical solution when 633 collocation nodes are used.

5.2.3 Expansion of a cylindrical tube

The following example is also solved by LRBFCM, denoted pressure in an infinite tube. The details are shown in Figure 5.31. This is an elastic plane strain problem with analytical solution [Liu, 2003]. Parameters used in the solution are; $E = 10000$ Pa, $\nu = 0.3$, $P = 1000$ Pa, $r_1 = 15$ m, $r_2 = 35.75$ m. The boundary conditions are given below.

$$\bar{\tau}_x = 0 \text{ Pa}, \ \bar{\tau}_y = 0 \text{ Pa} \qquad \mathbf{p} \in \Gamma^{\text{out}},$$

$$\bar{\tau}_x = -n_x P, \ \bar{\tau}_y = -n_y P \qquad \mathbf{p} \in \Gamma^{\text{in}}.$$

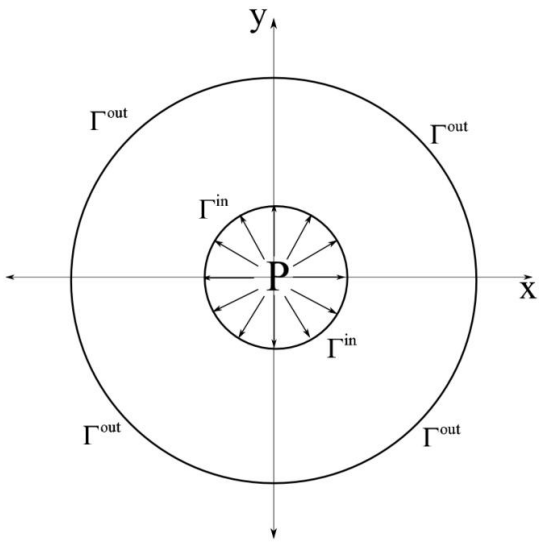

Figure 5.31: Scheme of expansion of a tube with an internal pressure in 2D.

The analytical solution is represented in terms of the radial displacement u_r, since the angular displacement (u_θ) is always 0 and given by [Liu, 2003] as

$$u_r(r) = \frac{Pr_1 r}{E\left(r_2^2 - r_1^2\right)}\left[(1-\nu)(1+\nu)\frac{r_2^2}{r^2}\right]. \tag{5.4}$$

Due to symmetry only the top right quarter of the domain is considered.

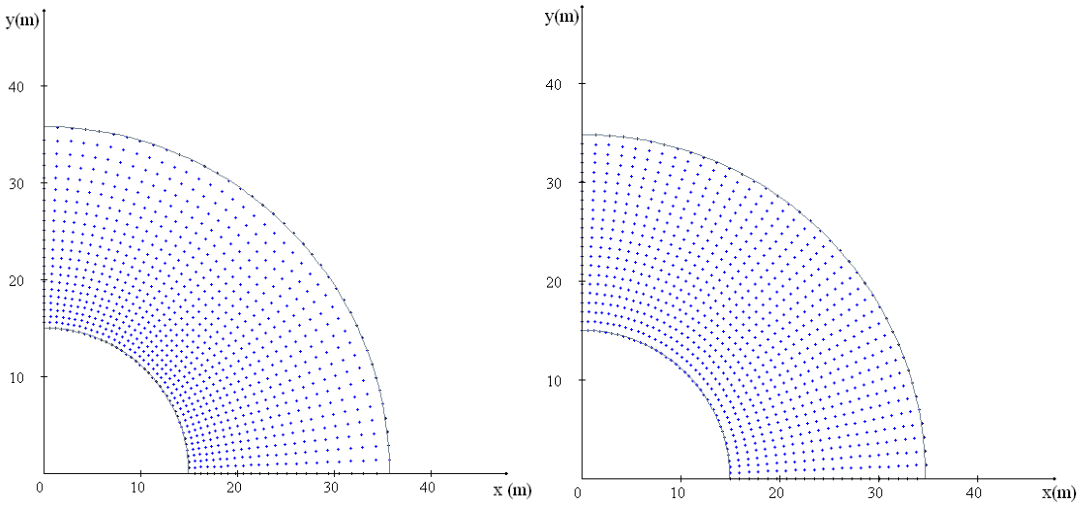

Figure 5.32: Uniform node arrangement with 919 nodes on the right and equal distance nodes arrangement also with 919 nodes on the left.

Due to better compatibility with the meshless method, an equal distance node arrangement is used for the interpolation of the computational domain, as seen in Figure 5.32. The LRBFCM and analytical solutions can be seen in Figure 5.33 below.

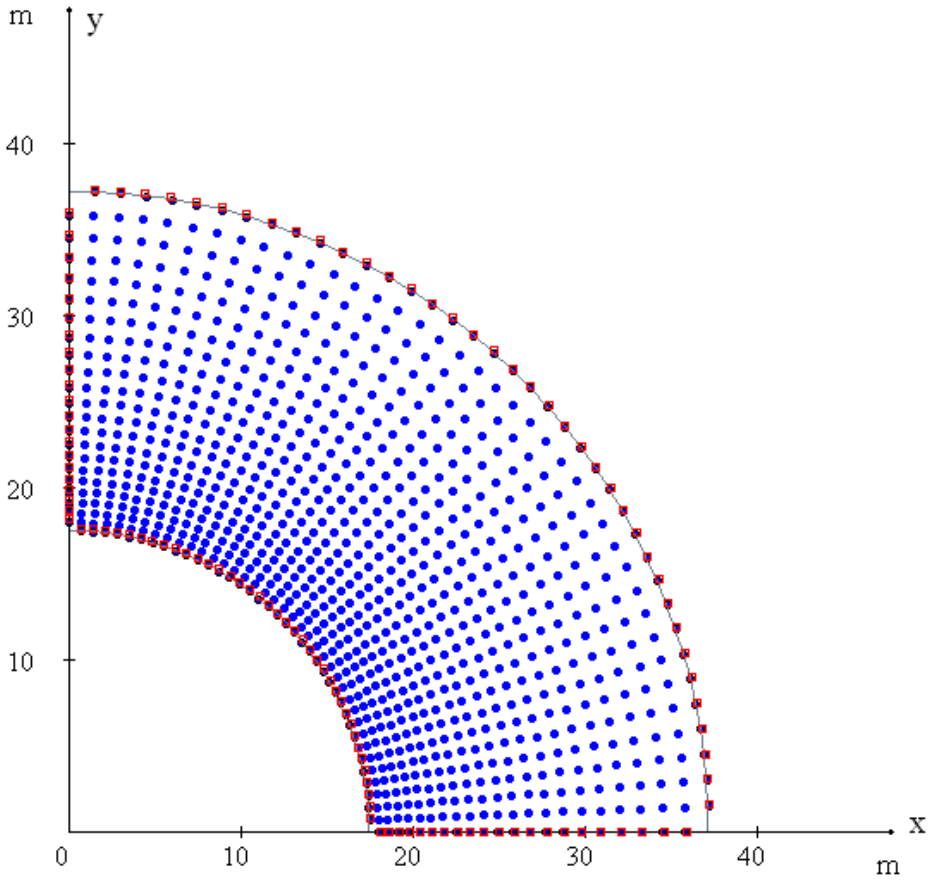

Figure 5.33: Comparison of LBFCM solution (blue points) with analytical solution at the boundary points (red squares) when $E = 10000$ Pa, $\nu = 0.3$ and P= 1000 Pa with 919 collocation nodes.

The RMSE of the LRBFCM solution of the pressure in an infinite tube case with increasing number nodes is presented in Figure 5.34. The displacement vectors of the solution are shown in Figure 5.35.

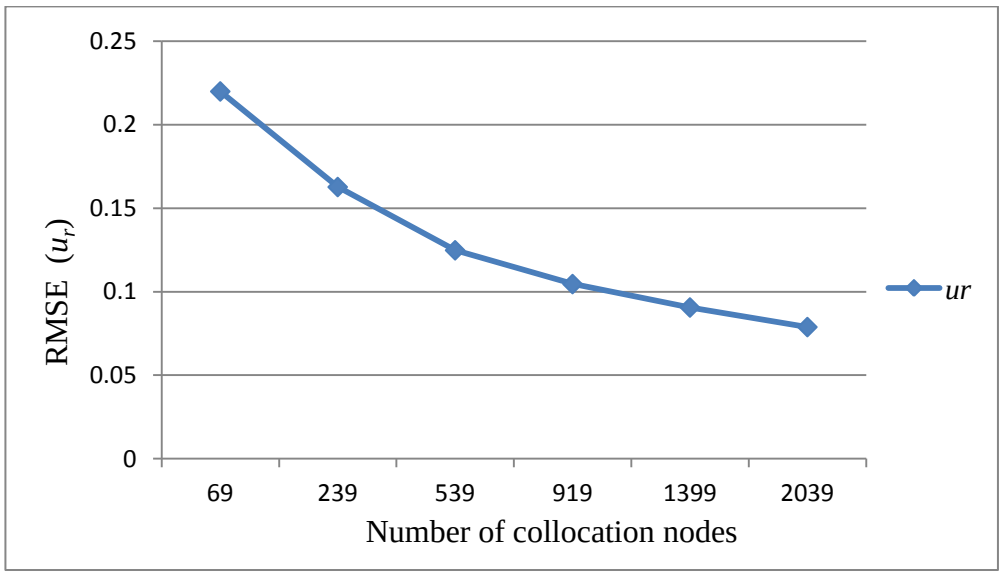

Figure 5.34: RMSE of radial displacements as a function of the node density.

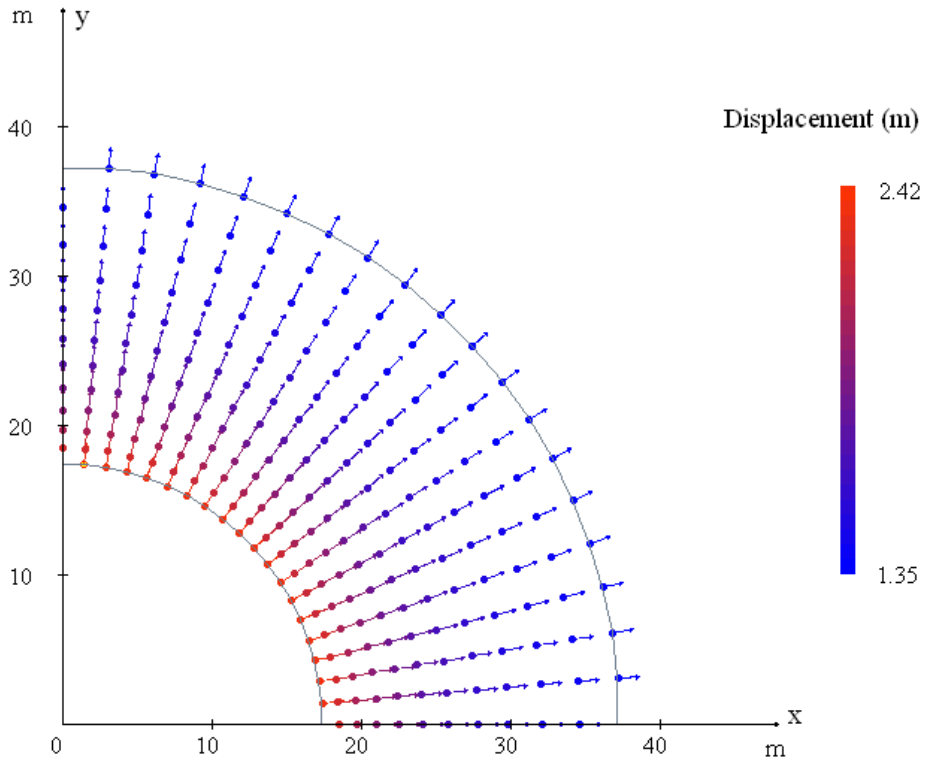

Figure 5.35: Displacement field with 239 collocation nodes.

5.2.4 Linear compression-tension

In this example a $2\text{m}\times 2\text{m}$ square material is used with Young's modulus $E=1$ Pa and Poisson's ratio $\nu=0.3$. The details of the problem can be seen in Figure 5.36 Maximum pressure is equal to the Young's modulus $P=E$. Solution is based on LRBFCM for this plane strain problem. The boundary conditions are given as

$$\bar{\tau}_x = 0 \text{ Pa},\ \bar{\tau}_y = 0 \text{ Pa} \qquad \mathbf{p}\in\Gamma^L,$$

$$\bar{\tau}_x = 0 \text{ Pa},\ \bar{\tau}_y = 0 \text{ Pa} \qquad \mathbf{p}\in\Gamma^{\mathrm{R}},$$

$$\begin{aligned} &\bar{u}_x = 0 \text{ m},\ \bar{u}_y = 0 \text{ m} && \begin{cases} \mathbf{p}\in\Gamma^{\mathrm{B}} \wedge \mathbf{p}\in(1,0) \\ \mathbf{p}\in\Gamma^{\mathrm{B}} \wedge \mathbf{p}\notin(1,0) \end{cases} \\ &\bar{\tau}_x = 0 \text{ Pa},\ \bar{u}_y = 0 \text{ m} && \end{aligned},$$

$$\bar{\tau}_x = 0 \text{ Pa},\ \bar{\tau}_y = P\times\left(p_x - 1\right) \text{ Pa} \qquad \mathbf{p}\in\Gamma^{\mathrm{R}}.$$

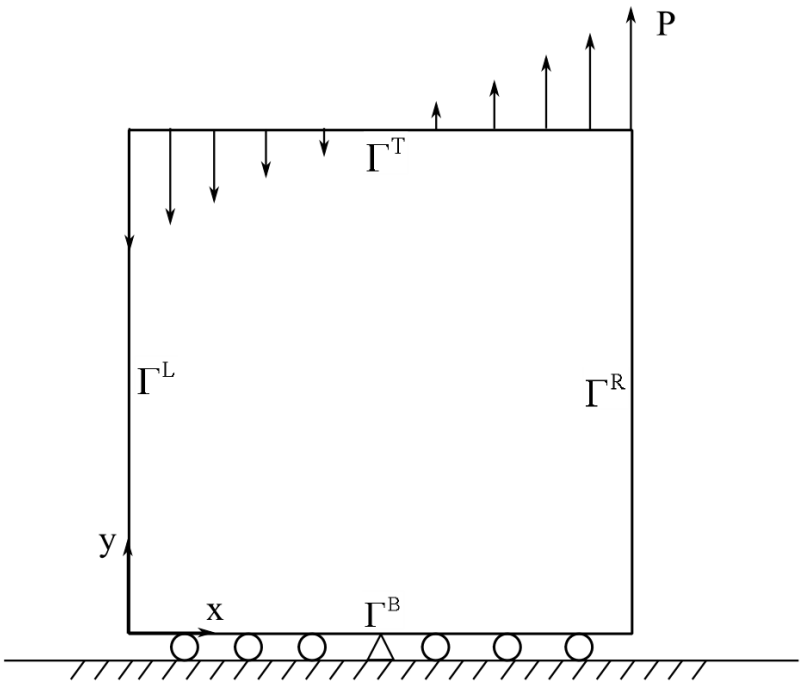

Figure 5.36: Example of linearly distributed decreasing pressure from the top.

Analytical solution for this case is given by [Huang and Cruse, 1994]

$$u_x = -0.195\left(p_x - 1\right)^2 - 0.445\left(p_y^2\right), \tag{5.5}$$

$$u_y = 0.91\left(p_x - 1\right) p_y \ . \tag{5.6}$$

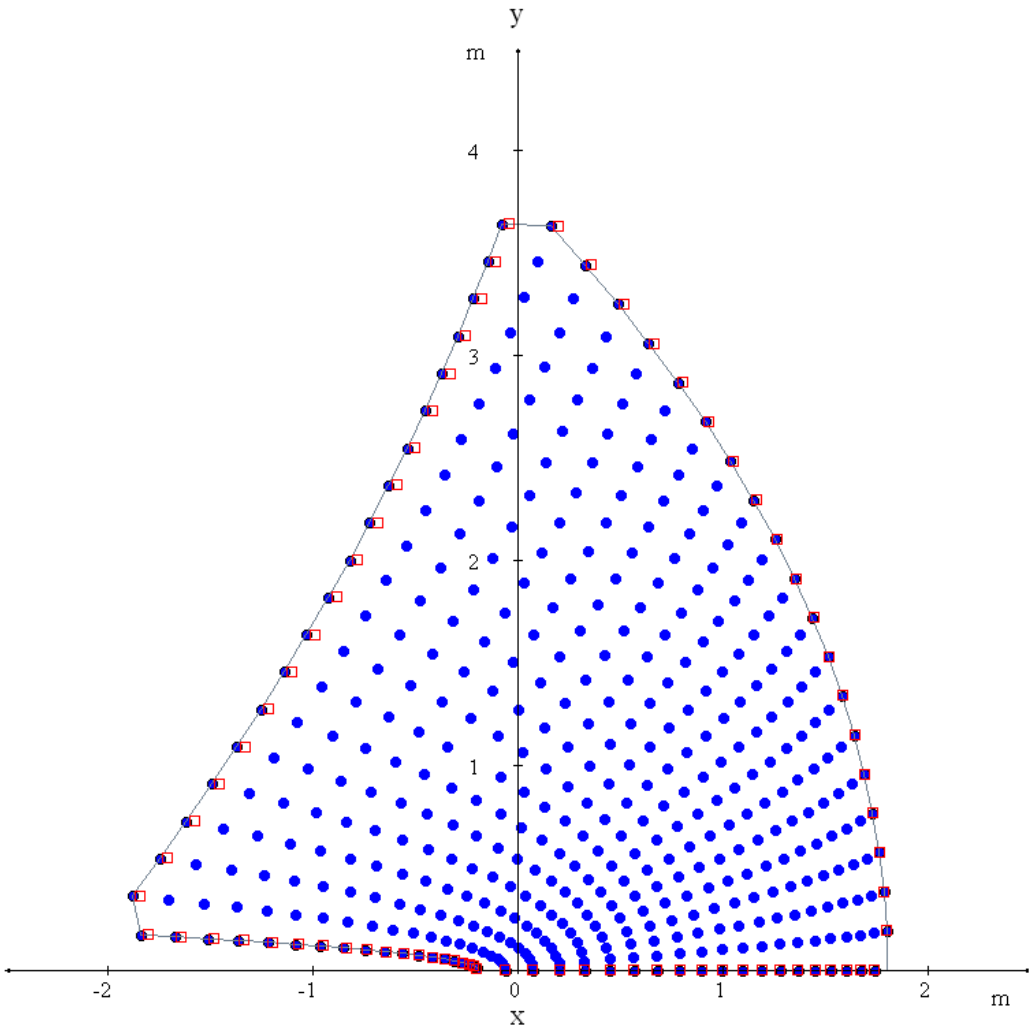

Figure 5.37: Blue points are the positions of the collocation nodes after the deformation, and compared with the analytical solution at the boundaries, represented by red squares. 437 collocation nodes are used.

The solution of linear compression-tension example calculated by LRBFCM is shown in Figure 5.37 and the displacement vectors can be seen in Figure 5.38.

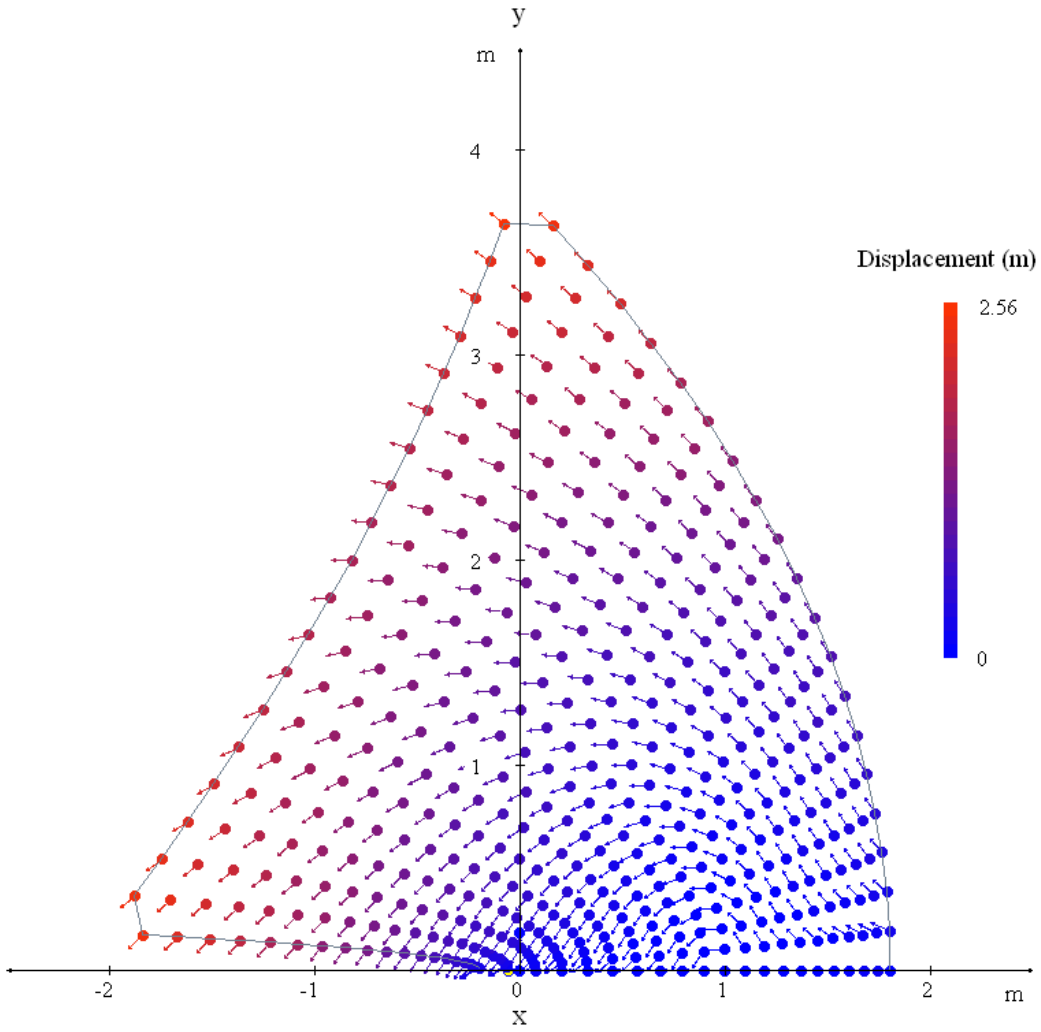

Figure 5.38: Displacement field calculated by LRBFCM for each node after the deformation. 437 collocation nodes are used.

RMSEs of the displacements are calculated with increasing number of the nodes and shown in Figure 5.39 and Figure 5.40.

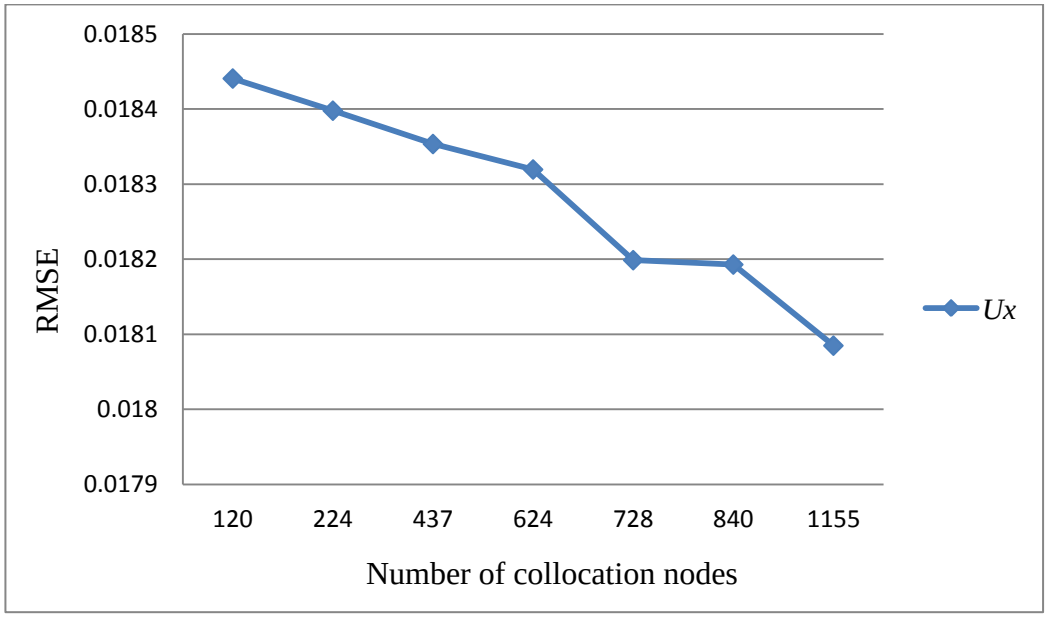

Figure 5.39: RMSE of displacement in x direction as a function of the node density.

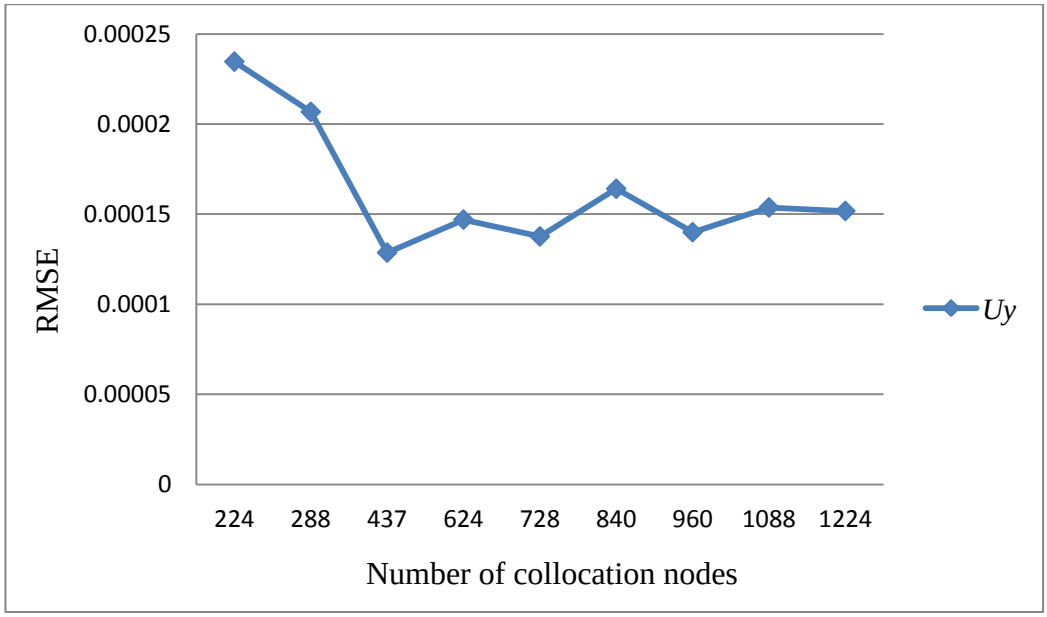

Figure 5.40: RMSE of displacement in y direction as a function of the node density.

5.2.5 Bending of a beam by a uniform load

In this problem an elastic cantilever beam with dimensions 40 m $\times$ 4 m is considered, obeying plane strain material definition. Uniform pressure is applied from the top when the central points on the left and right sides are fixed as shown in Figure 5.41, where $E = 10^7$ Pa, $\nu = 0.3$ and $P = 5000$ Pa. Boundary conditions are given below

$$\bar{\tau}_x = 0 \text{ Pa},\ \bar{\tau}_y = P \text{ Pa} \qquad \mathbf{p} \in \Gamma^{\mathrm{T}},$$

$$\begin{aligned} &\bar{u}_x = 0 \text{ m}, \bar{u}_y = 0 \text{ m} \\ &\bar{\tau}_x = 0 \text{ Pa},\ \bar{\tau}_y = 0 \text{ m} \end{aligned} \qquad \begin{cases} \mathbf{p} \in \Gamma^{\mathrm{L}} \wedge \mathbf{p} \in (-L/2, 0) \\ \mathbf{p} \in \Gamma^{\mathrm{L}} \wedge \mathbf{p} \notin (-L/2, 0) \end{cases},$$

$$\begin{aligned} &\bar{u}_x = 0 \text{ m}, \bar{u}_y = 0 \text{ m} \\ &\bar{\tau}_x = 0 \text{ Pa},\ \bar{\tau}_y = 0 \text{ m} \end{aligned} \qquad \begin{cases} \mathbf{p} \in \Gamma^{\mathrm{R}} \wedge \mathbf{p} \in (L/2, 0) \\ \mathbf{p} \in \Gamma^{\mathrm{R}} \wedge \mathbf{p} \notin (L/2, 0) \end{cases},$$

$$\bar{\tau}_x = 0 \text{ Pa},\ \bar{\tau}_y = 0 \text{ Pa} \qquad \mathbf{p} \in \Gamma^{\mathrm{B}}.$$

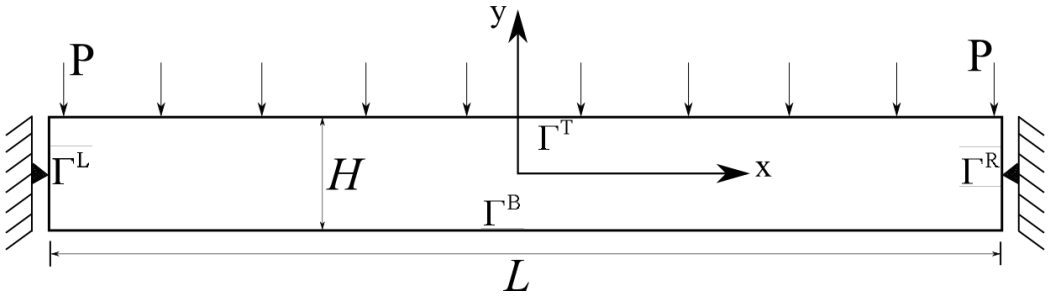

Figure 5.41: Scheme of bending of a lever by a uniform load.

Analytical solution is given by [Timoshenko and Goodier, 1951] as

$$u_x = \left(\frac{P}{2EI}\right)\left[\begin{array}{l} p_y\left(L^2 p_x - \frac{p_x^3}{3}\right) + p_x\left(2\frac{p_y^3}{3} - 2H^2\frac{p_y}{5}\right) \\ +\nu p_x\left(\frac{p_y^3}{3} - H^2 p_y + 2\frac{H^3}{3}\right) \end{array}\right], \tag{5.7}$$

$$u_y = -\left(\frac{P}{2EI}\right)\left[\begin{array}{l}\frac{p_y^4}{12} - H^2\frac{p_y^2}{2} - 2H^3\frac{p_y}{3} + \nu\left(\left(L^2 - p_x^2\right)\frac{p_y}{2} + \frac{p_y^4}{6} - H^2\frac{p_y^2}{5}\right) \\ +L^2\frac{p_x^2}{2} - \frac{p_x^4}{12} - H^2\frac{p_x^2}{5} + \left(1+\frac{\nu}{2}\right)H^2 p_x^2 \end{array}\right] \cdot \qquad (5.8)$$
$$+\frac{5}{24}\frac{PL^3}{EI}\left[1+\frac{12H^2}{5L^2}\left(\frac{4}{5}+\frac{\nu}{2}\right)\right]$$

The LRBFCM solution of the case of bending of a beam by uniform load, together with the adjacent analytical solution is shown in Figure 5.42 below. The displacement vectors are plotted in Figure 5.43.

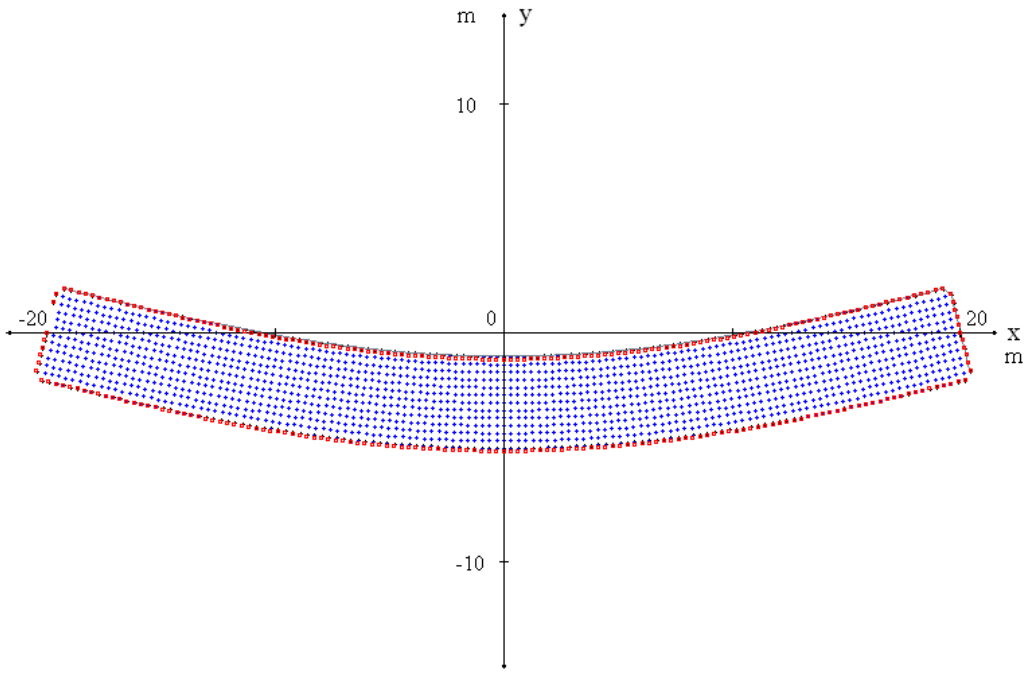

Figure 5.42: Deformation results where the blue points are calculated by LRBFCM and the red squares represent the analytical solution at the boundary. 815 collocation nodes are used.

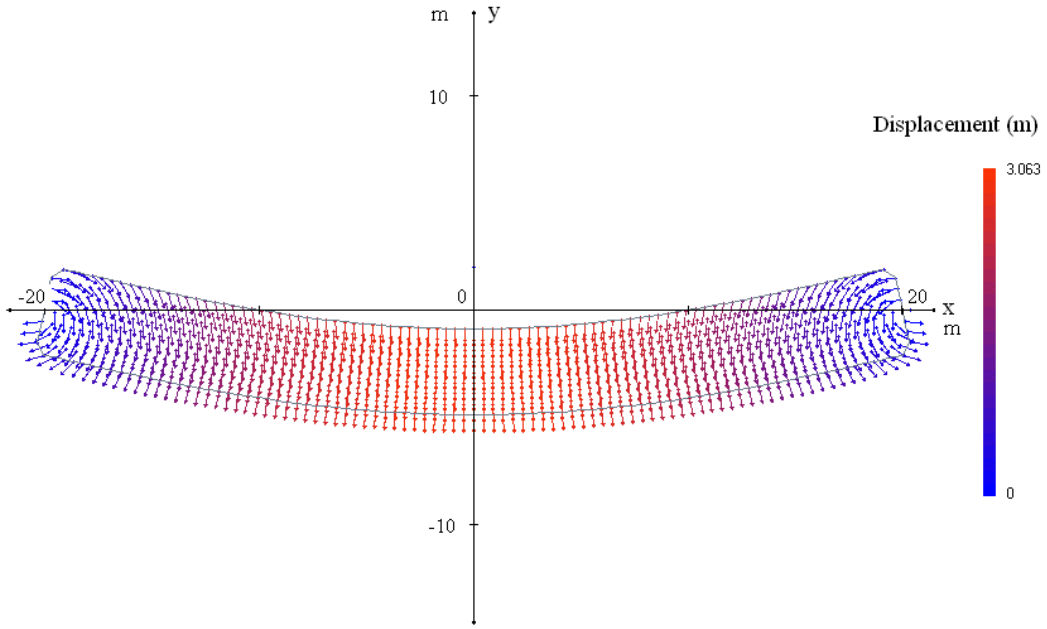

Figure 5.43: Displacement field of a cantilever beam under uniform pressure. 815 collocation nodes are used.

The RMSE of the displacements calculated by LRBFCM are expressed in Figure 5.44 with increasing number of the nodes.

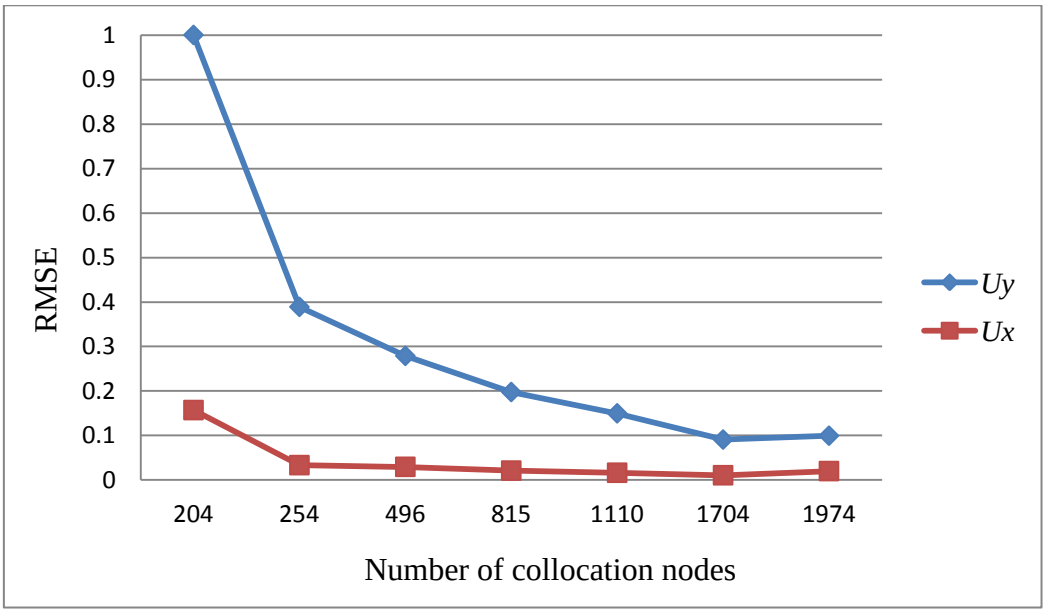

Figure 5.44: RMSE of displacements as a function of the node density.

5.2.6 Testing of ideal plastic deformation

The following flat rolling example is done for a slightly compressible ideal plastic material, where the effective stress-effective strain relation is given as $\bar{\sigma} = 589\bar{\varepsilon}^{0.214}$ MPa**.** Only the top right quarter of the material with size 80 mm × 95 mm is considered. The plane strain problem definition can be seen in Figure 5.45. No friction is assumed between the roll and the material, therefore the right side is expected to get perfectly horizontal line after the deformation. Two types of reduction are applied which are 1mm and 4 mm. the LRBFCM results are compared with FEM solution.

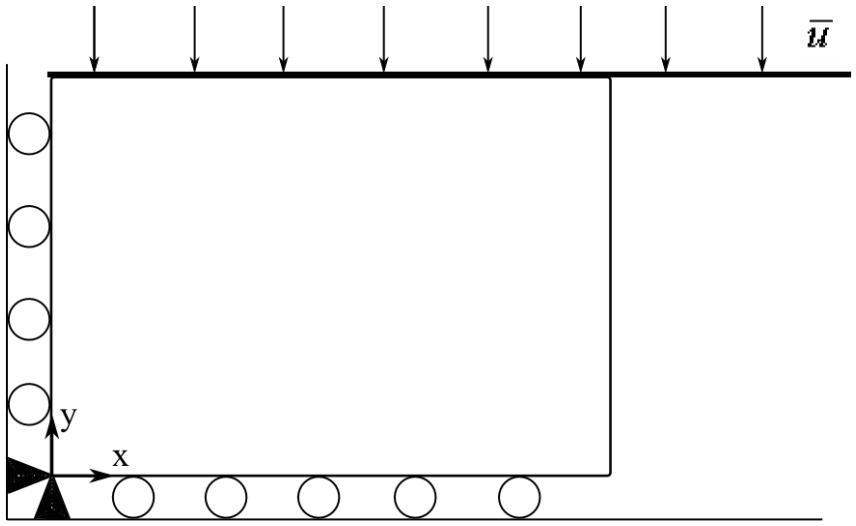

Figure 5.45: An example of compression with prescribed displacement and sticking boundary condition as in the flat rolling.

The comparisons of the displacement fields for 1 mm reduction can be seen in Figure 5.46 and for 4 mm in Figure 5.47. The displacement vectors calculated by LRBFCM are plotted in Figure 5.48 and Figure 5.49. In the calculations, governing equations in Table 2.3 are used where $g = 0.001$. 99 nodes are used in LRBFCM solutions and 80 elements are used in FEM solutions.

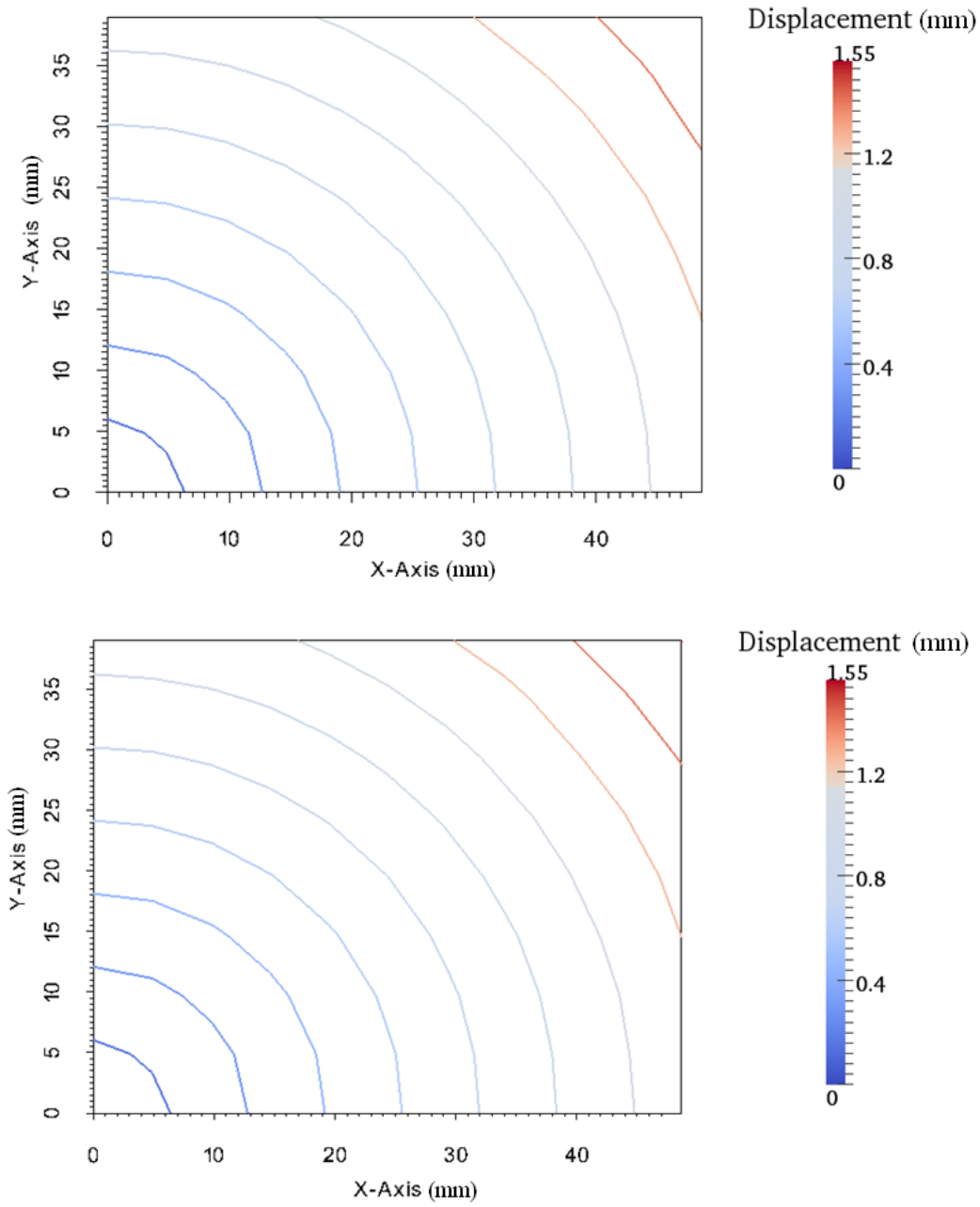

Figure 5.46: Contour graph of displacement field when 1 mm reduction is applied from the top with no friction. The material model used here is $\bar{\sigma} = 589\bar{\varepsilon}^{0.214}$ MPa. The figure on the top is calculated by LRBFCM and on the bottom is calculated by FEM.

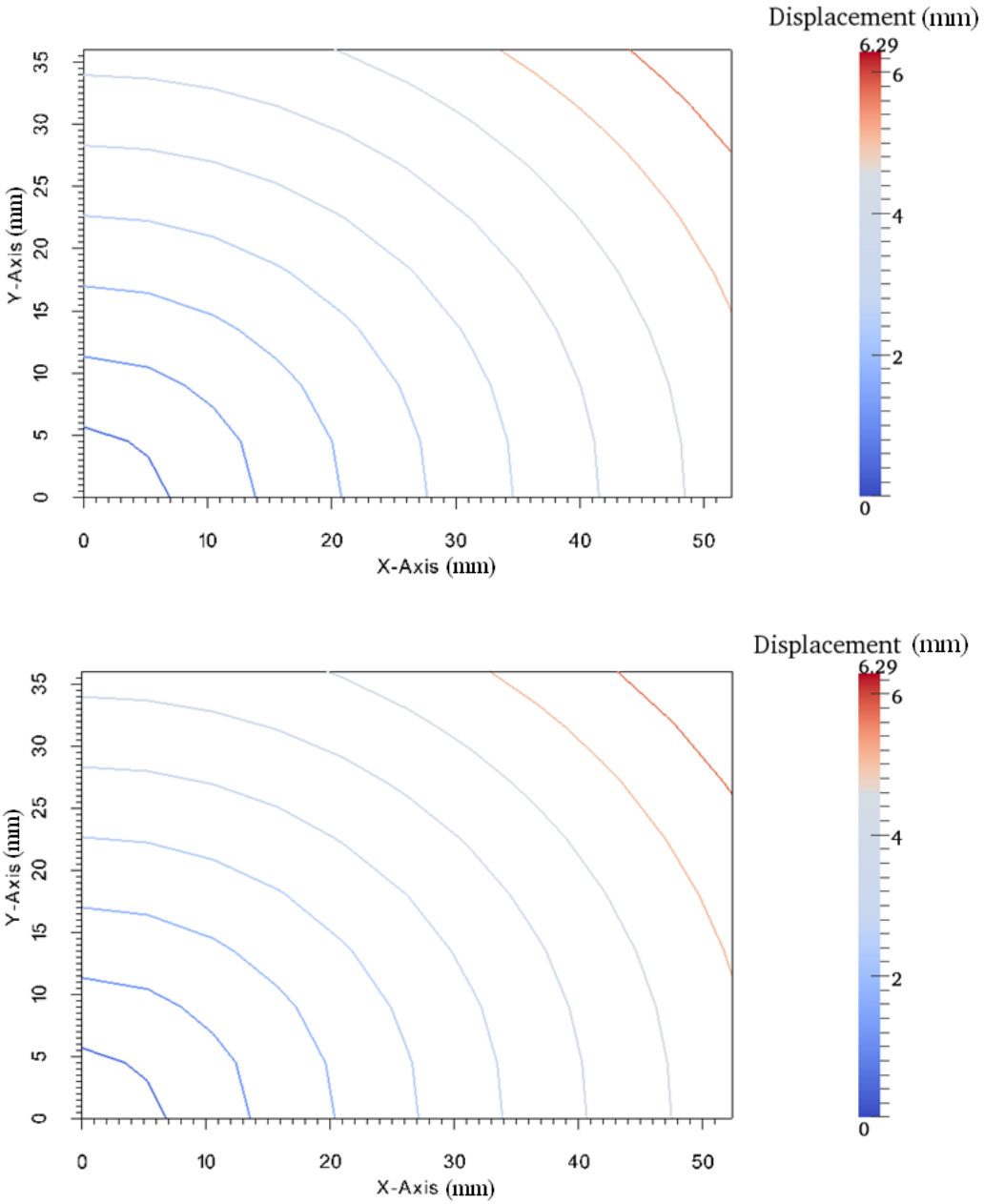

Figure 5.47: Contour graph of displacement fields when 10 % reduction is applied as described in flat rolling example Figure 5.41. The material model used here is $\bar{\sigma} = 589\bar{\varepsilon}^{0.214}$ MPa. Figure on top is calculated by LRBFCM and on the bottom is calculated by FEM.

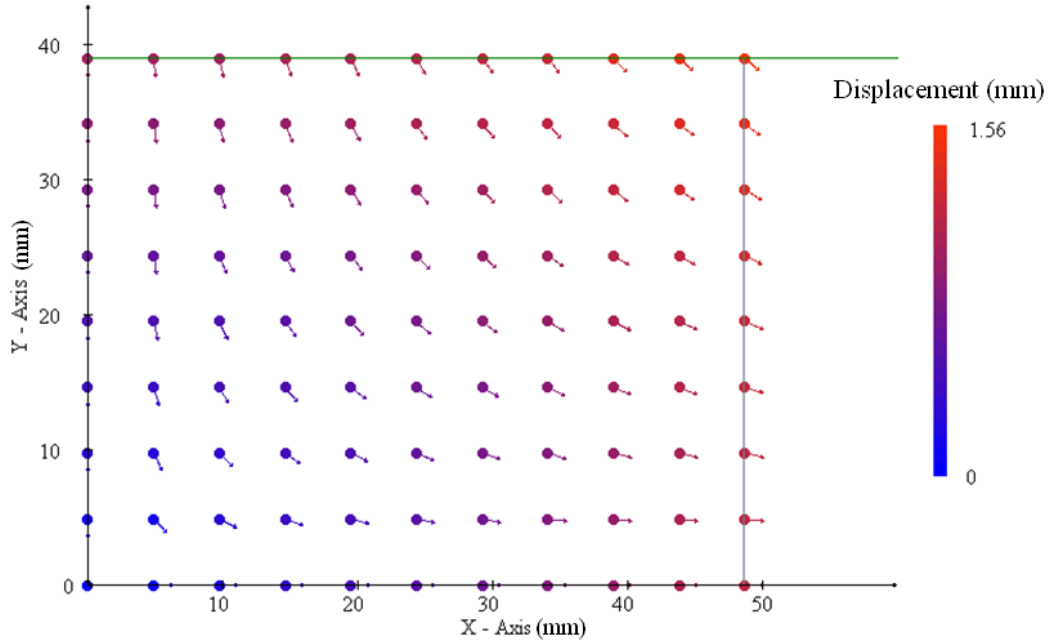

Figure 5.48: Displacement vectors calculated by LRBFCM at 1 mm compression from top as in Figure 5.42.

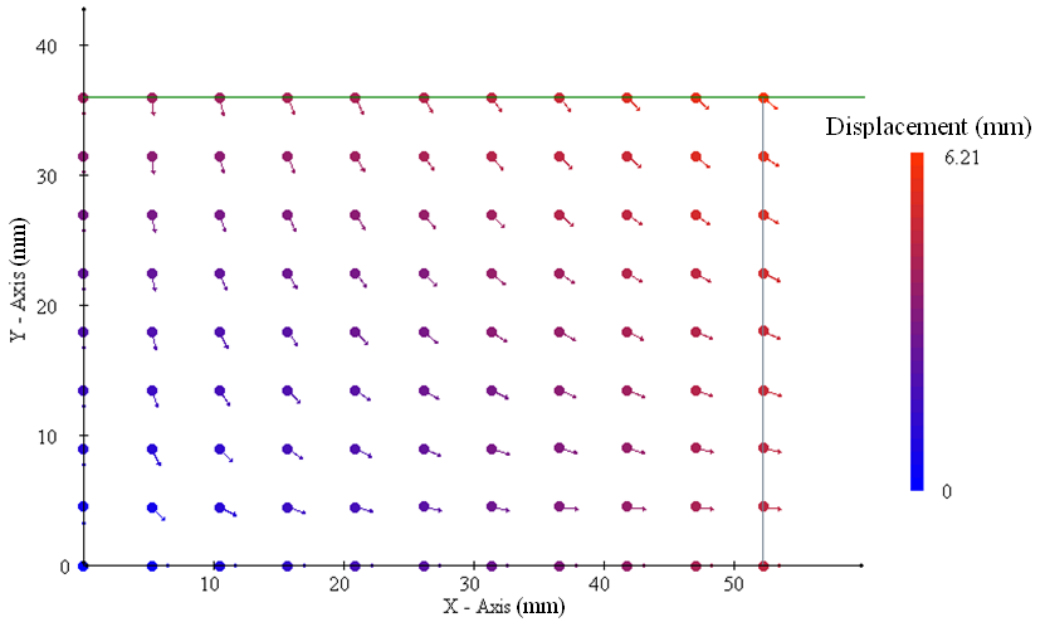

Figure 5.49: Displacement vectors calculated by LRBFCM at 10 % reduction as in Figure 5.43.

In this chapter many test cases have been performed to check the accuracy of the LRBFCM, separately for the thermal and the mechanical models. The results of simulations are individually tested and compared with FEM or analytical solutions. In every test case, there was no problem of stability issues, and a very good agreement between the reference solutions has been achieved. These test cases show that LRBFCM is capable to be further tested for large and continuous deformation problems, as shown in the next chapter.

6 Testing of the Hot Rolling Model

Several mechanical tests, specific for checking of the deformation as occurs in hot rolling are performed in chapter 6. They include flat and shape rolling examples considering elastic material properties. Two types of rolling stands; flat and oval are considered. Only the mechanical model is used in the simulations, and since there is no analytical solution for such a complicated deformation shape, the results are compared with FEM in terms of displacement and strain fields.

6.1 Flat rolling example

The geometry of material to be rolled is a rectangle with dimensions $95\ \text{mm} \times 80$ mm. For simplicity, as elaborated in chapter 3, only the top right quarter is considered. The simulation is done in 5 steps and each step has prescribed displacement of the top roll, which is 1 mm downwards. Overall the total reduction is 12.5 %. The plane strain problem is considered and the elastic material properties are $E = 10^8$ Pa and $\nu = 0.3$. The problem definition is shown in Figure 6.1.

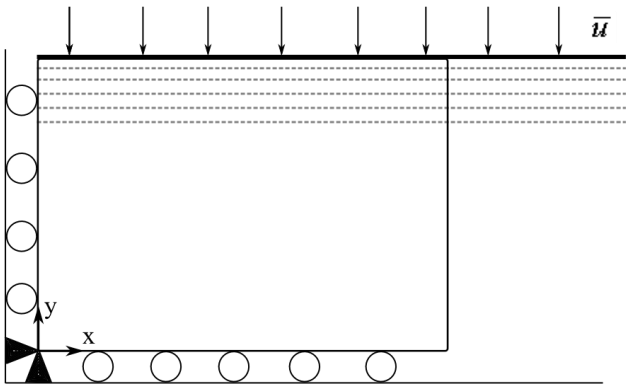

Figure 6.1: Scheme of flat rolling simulation with considered symmetric right upper corner. Sticking boundary condition is applied with 5 mm reduction with 1mm/s reduction speed in 5 steps.

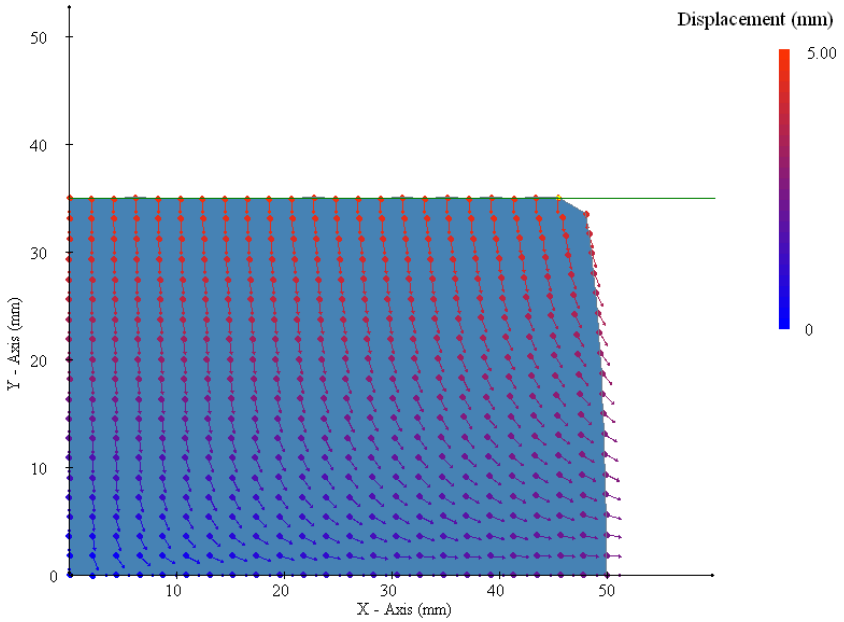

Figure 6.2: Testing of flat rolling example with displacement field calculated by LRBFCM. 479 collocation nodes are used.

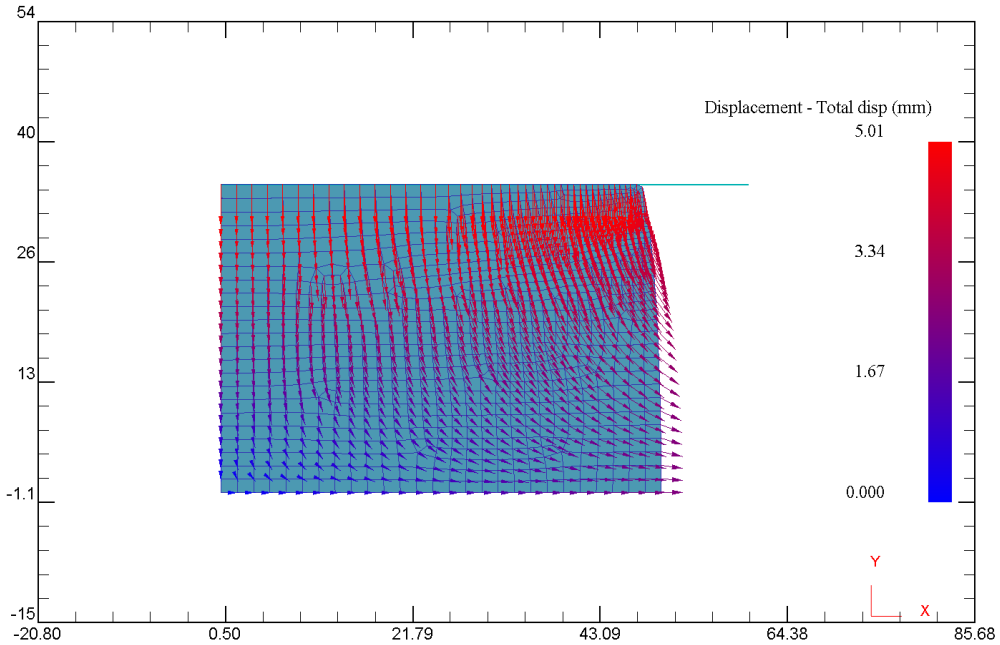

Figure 6.3: Testing of flat rolling example with displacement field calculated by FEM. 1015 elements are used.

The displacement vectors for the flat rolling case, calculated by LRBFCM, after the fifth deformation step, are shown in Figure 6.2 and by FEM in Figure 6.3. Comparison of the displacement fields is shown in Figure 6.4 and comparison of the calculated strain vector components $\varepsilon_{xx}, \varepsilon_{yy}, \varepsilon_{xy}$ are separately shown in Figures 6.5, Figure 6.6 and Figure 6.7. 479 collocation nodes are used in LRBFCM. In this test, governing equations in Table 2.1 are used.

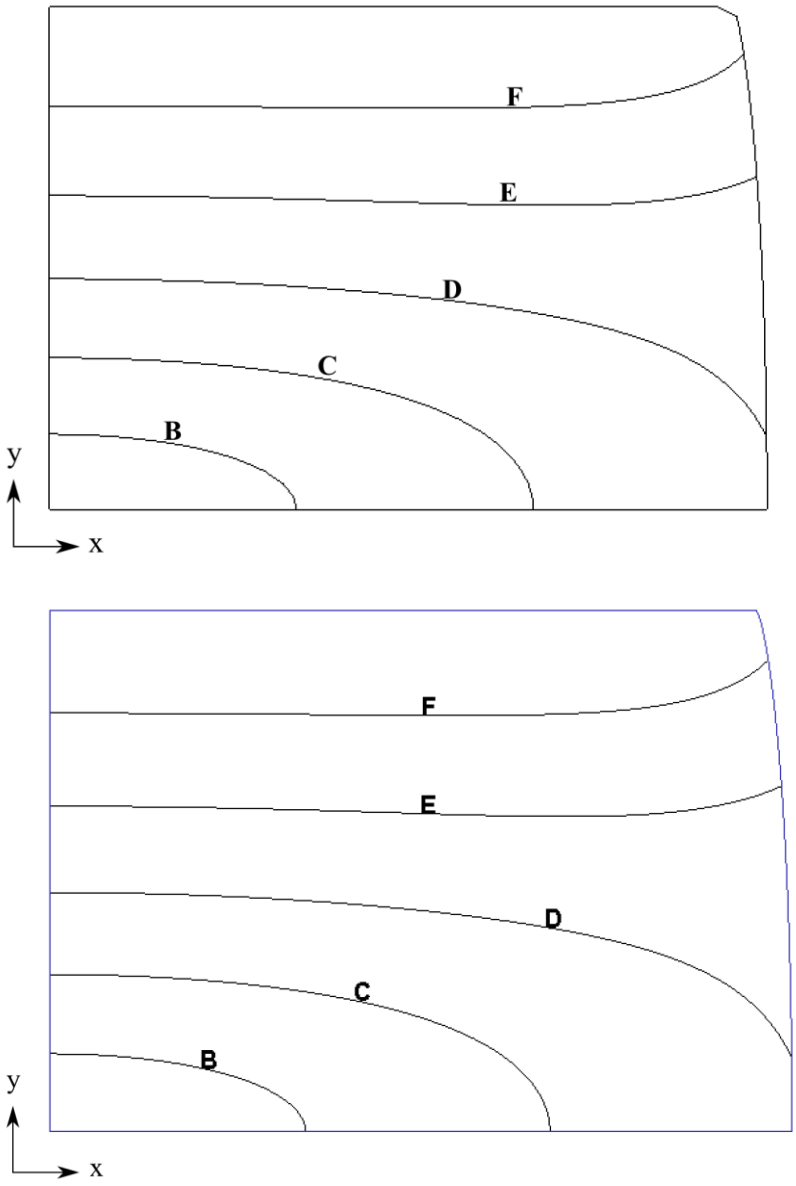

Figure 6.4: Testing of the mechanical model. Displacement field calculated by LRBFCM (on top) and FEM (at bottom). Lines represent B = 0.833 mm, C = 1.67 mm, D = 2.50 mm, E = 3.33 mm, F = 4.17 mm.

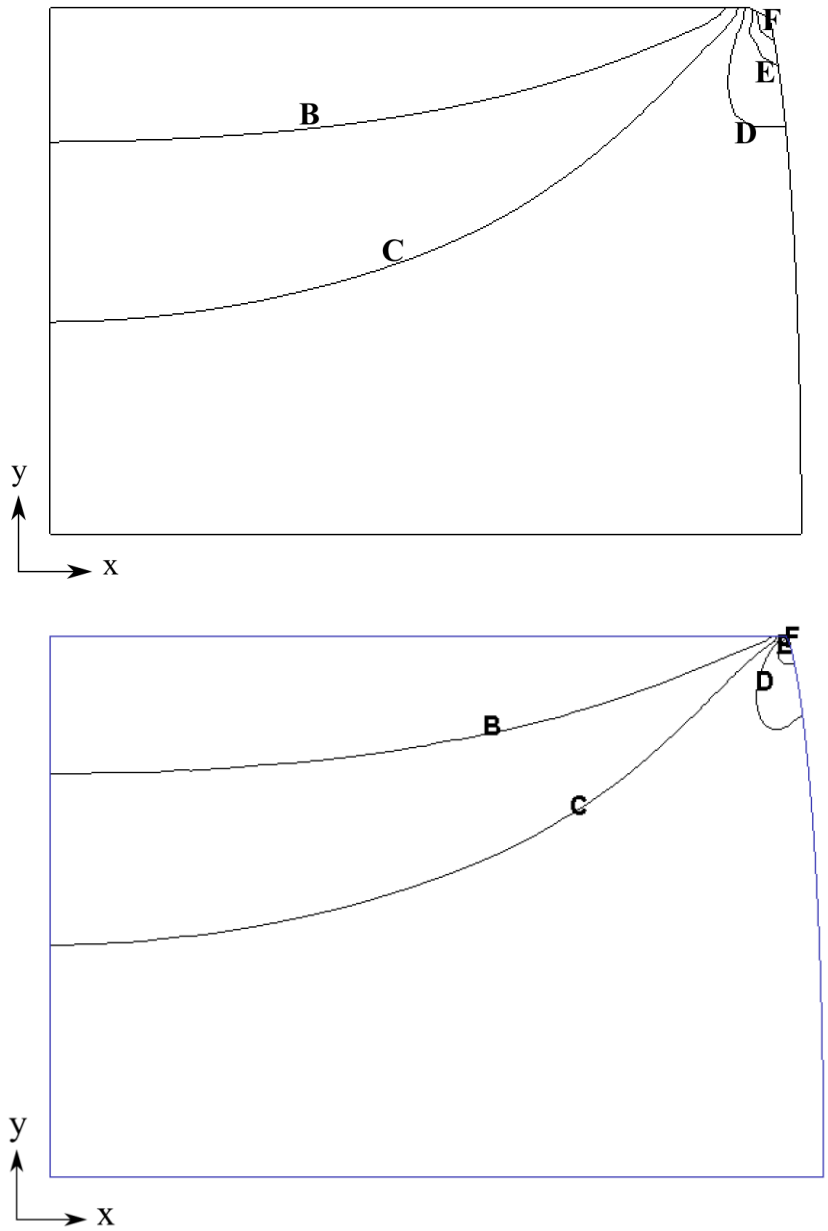

Figure 6.5: Testing of the mechanical model. ε_{xx} field calculated by LRBFCM (on top) and FEM (at bottom). Lines represent B = 0.022, C = 0.44, D = 0.066, E = 0.087, F = 0.111.

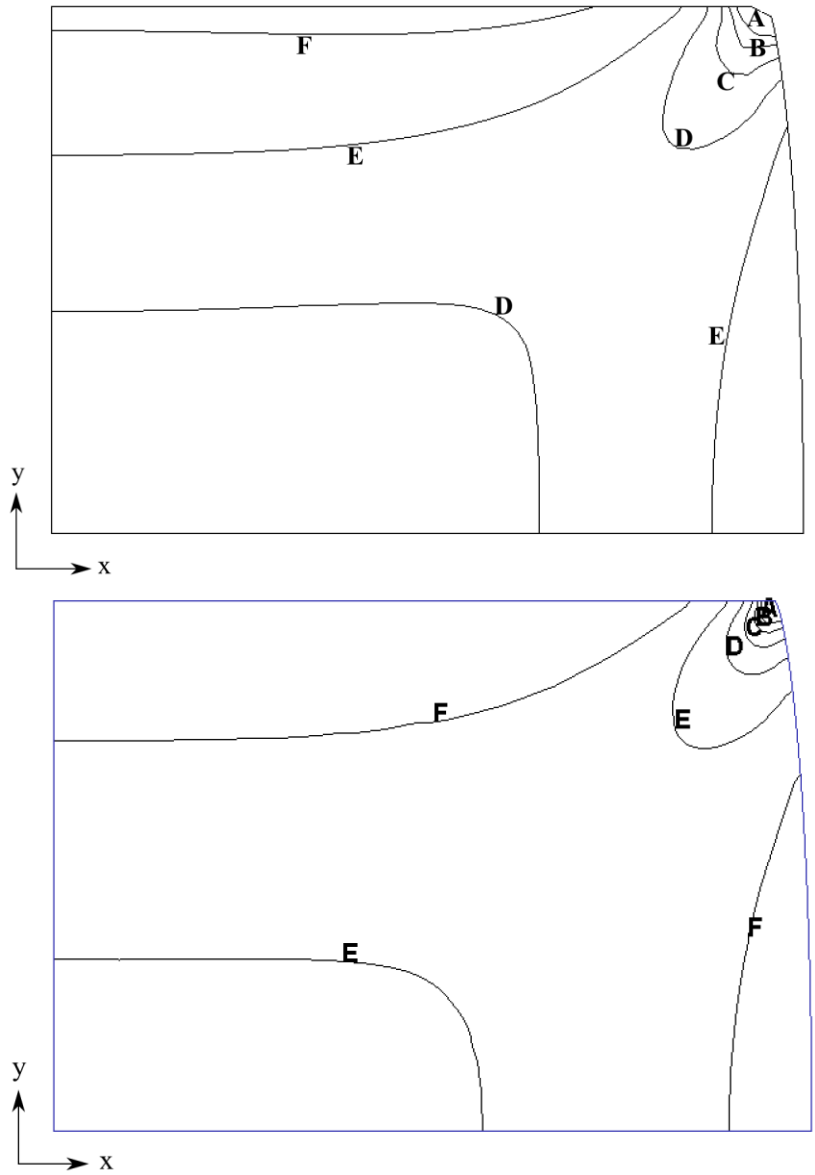

Figure 6.6: Testing of the mechanical model. ε_{yy} field calculated by LRBFCM (on top) and FEM (at bottom). Lines represent A = -0.200, B = -0.183, C = -0.167, D = -0.150, E = -0.133 and F = -0.117.

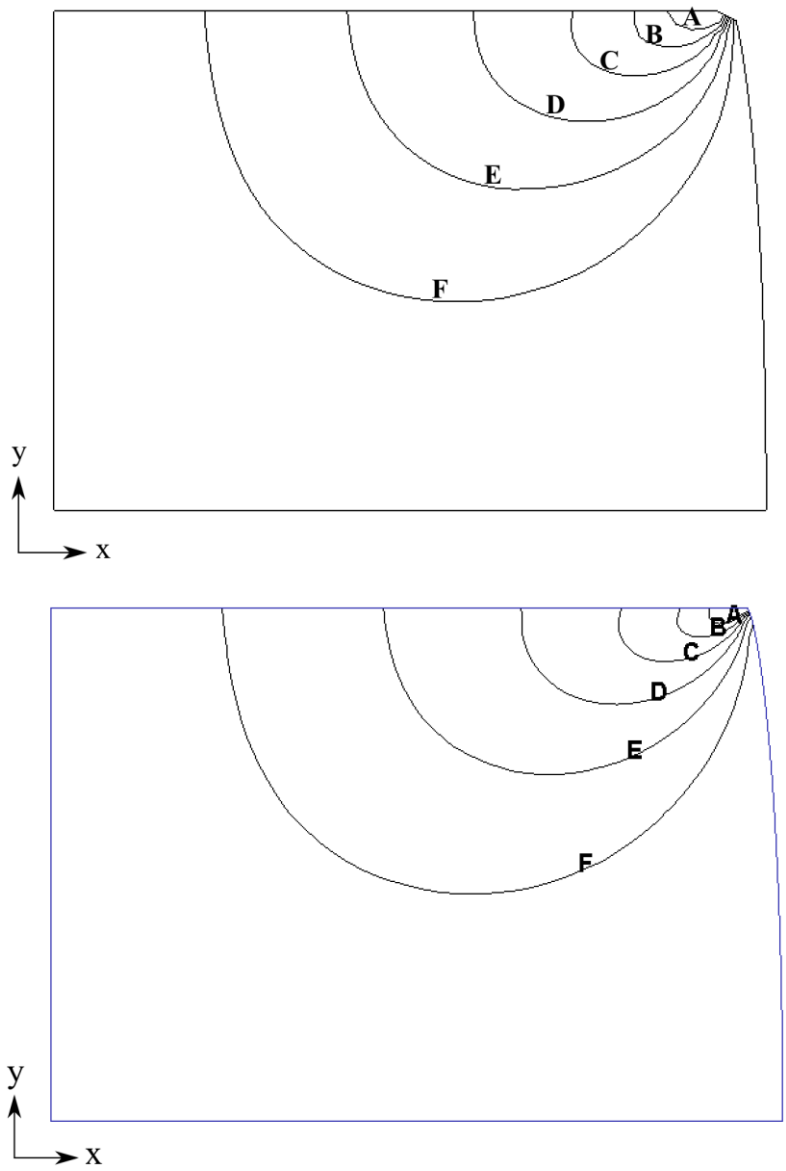

Figure 6.7: Testing of the mechanical model. ε_{xy} field calculated by LRBFCM (on top) and FEM (at bottom). Lines represent A = -0.150, B = -0.125, C = -0.100, D = -0.075, E = -0.050 and F = -0.025.

The flat rolling with sticking boundary conditions example is compared with FEM for the same material with different temperatures as in the Figure 6.8. The comparison is made in terms of width expansion over the *x* axis. The initial width is 47.5 mm and its increase in each deformation step is calculated. As expected, at high temperatures, the expansion is larger.

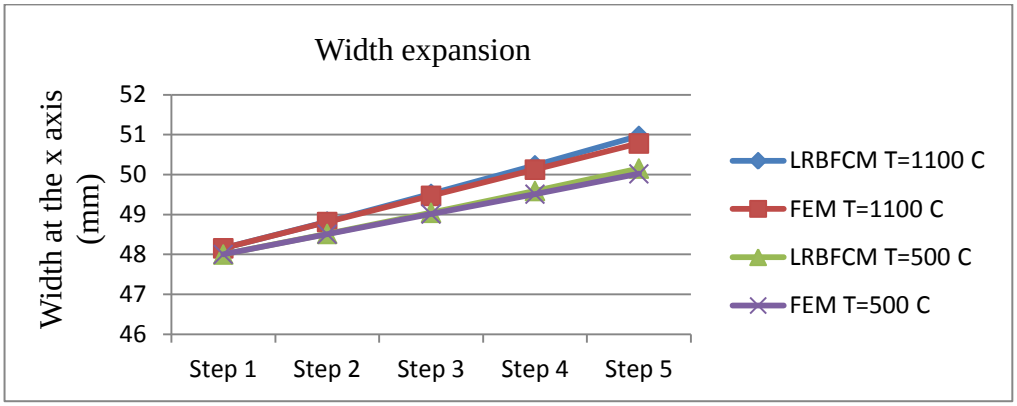

Figure 6.8: Comparison of width expansion during flat rolling with LRBFCM and FEM at two different temperatures when E (1100 °C) = 100.404 GPa and υ (500 °C) = 0.3535 and E (500 °C) = 172.963 GPa, υ (500 °C) = 0.30427. 12.5% total reduction is applied in 5 steps and 479 collocation nodes are used in LRBFCM and 1015 elements are used in FEM.

6.2 Shape rolling example

In this example same material properties are used as in the previous flat rolling example. Initial size of the slice is 47.5 mm × 40 mm. This is an elastic plane strain problem with sticking boundary conditions. An oval groove with a radius of 85 mm and width of 122 mm is used. The prescribed displacement of the oval groove is 1.7 mm downwards until the groove height is reduced to 34.5 mm. This is achieved in 11 steps. The definition of the problem is shown below in Figure 6.9.

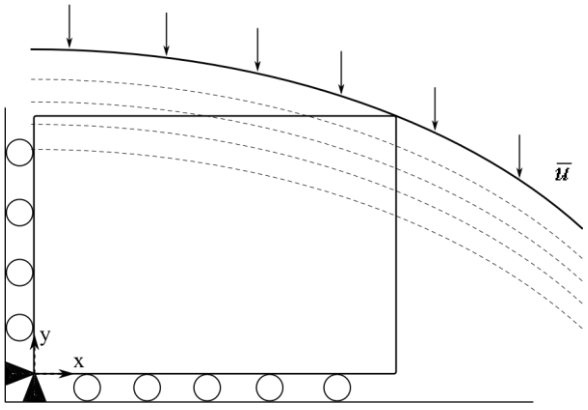

Figure 6.9: An example of oval rolling when a quarter of a 95 mm × 80 mm slice is analyzed through an oval groove with a radius of 85 mm.

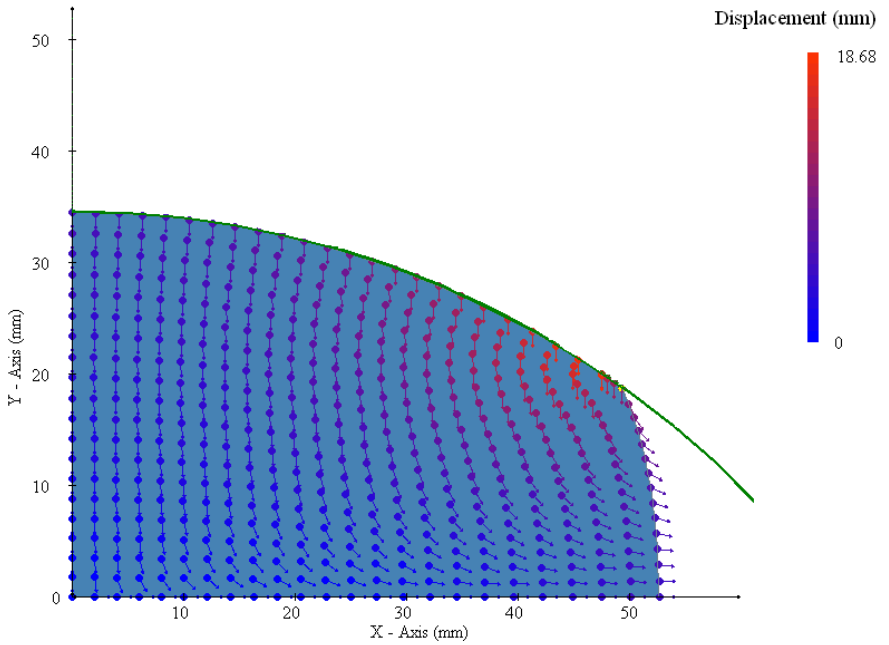

Figure 6.10: Displacement vectors calculated with LRBFCM at the exit of the rolling stand with oval groove. 525 collocation nodes are used.

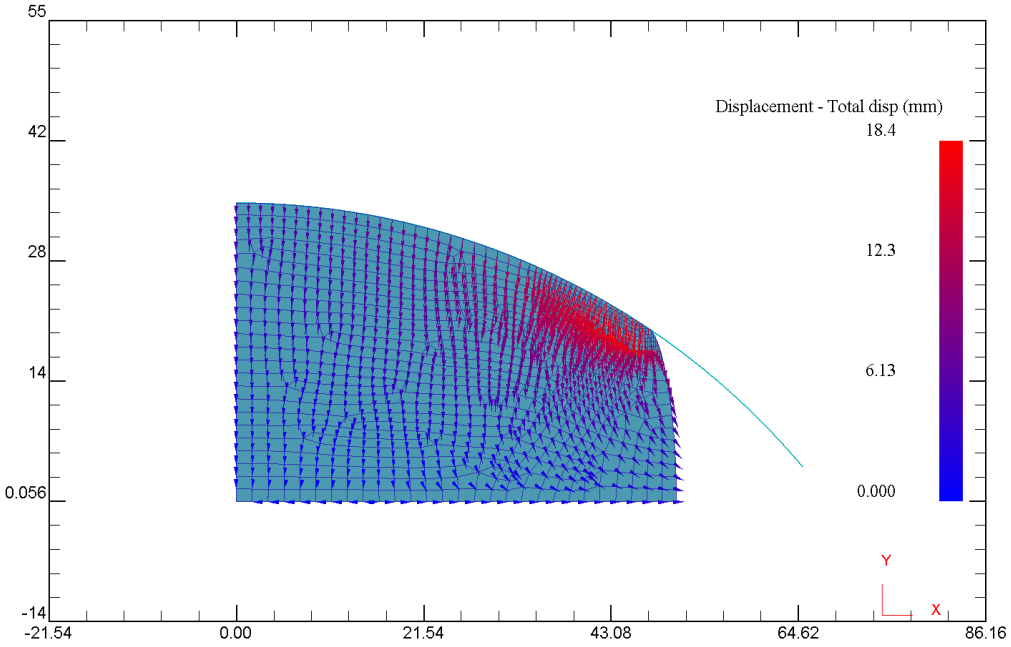

Figure 6.11: Displacement vectors calculated with FEM at the exit of the rolling stand with oval groove. 1013 finite elements are used.

The displacement vectors for the shape rolling case after the 11th deformation step are calculated by LRBFCM in Figure 6.10 and by FEM in Figure 6.11. Comparison of the total displacement fields is shown in Figure 6.12 and Figure 6.13. In this test governing equations in Table 2.1 are used.

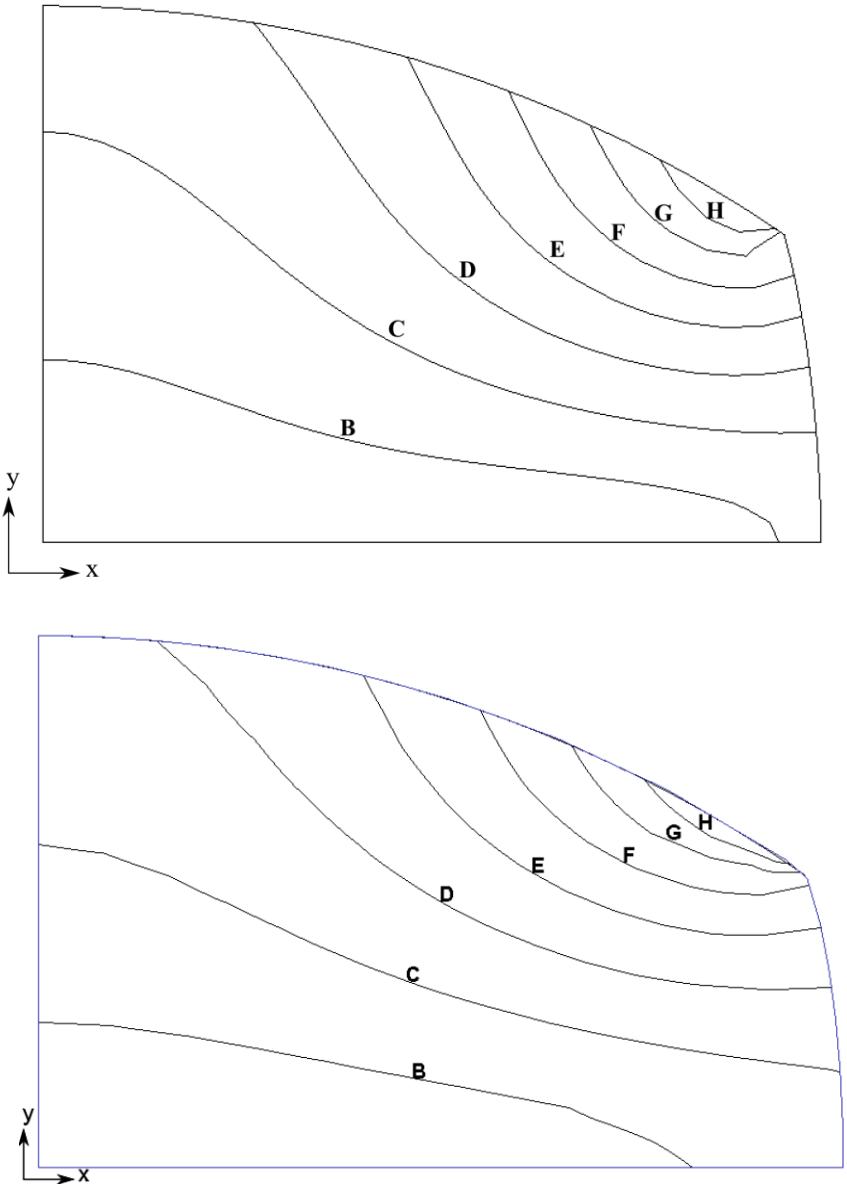

Figure 6.12: Comparison of displacement fields of the shape rolling example. The contour graph on top is calculated with LRBFCM and bottom with FEM.

The lines represent the values of B = 2.2 mm, C = 4.41 mm, D = 6.61 mm, E = 8.82 mm, F = 11.0 mm, G = 13.2 mm and H = 15.4 mm.

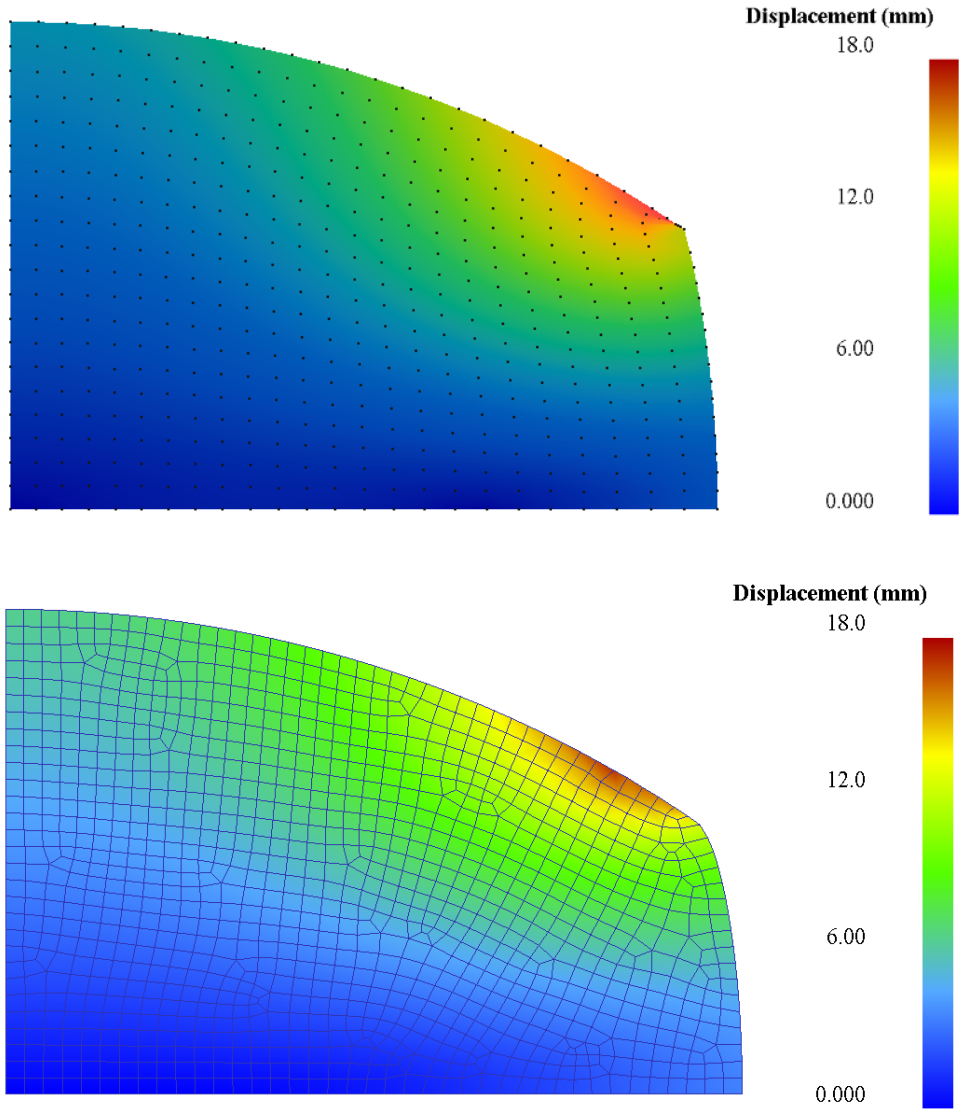

Figure 6.13: Displacement fields are calculated by LRBFCM (on top) and FEM (at bottom).

The strain vector components $\varepsilon_{xx}, \varepsilon_{yy}, \varepsilon_{xy}$ are calculated by LRBFCM and compared with FEM individually. For each component first a contour, than a shaded graph is drawn. These results are shown in next 6 figures (Figure 6.14,

Figure 6.15, Figure 6.16, Figure 6.17, Figure 6.18, Figure 6.19). 525 collocation nodes are used in LRBFCM results and 1013 elements are used in FEM.

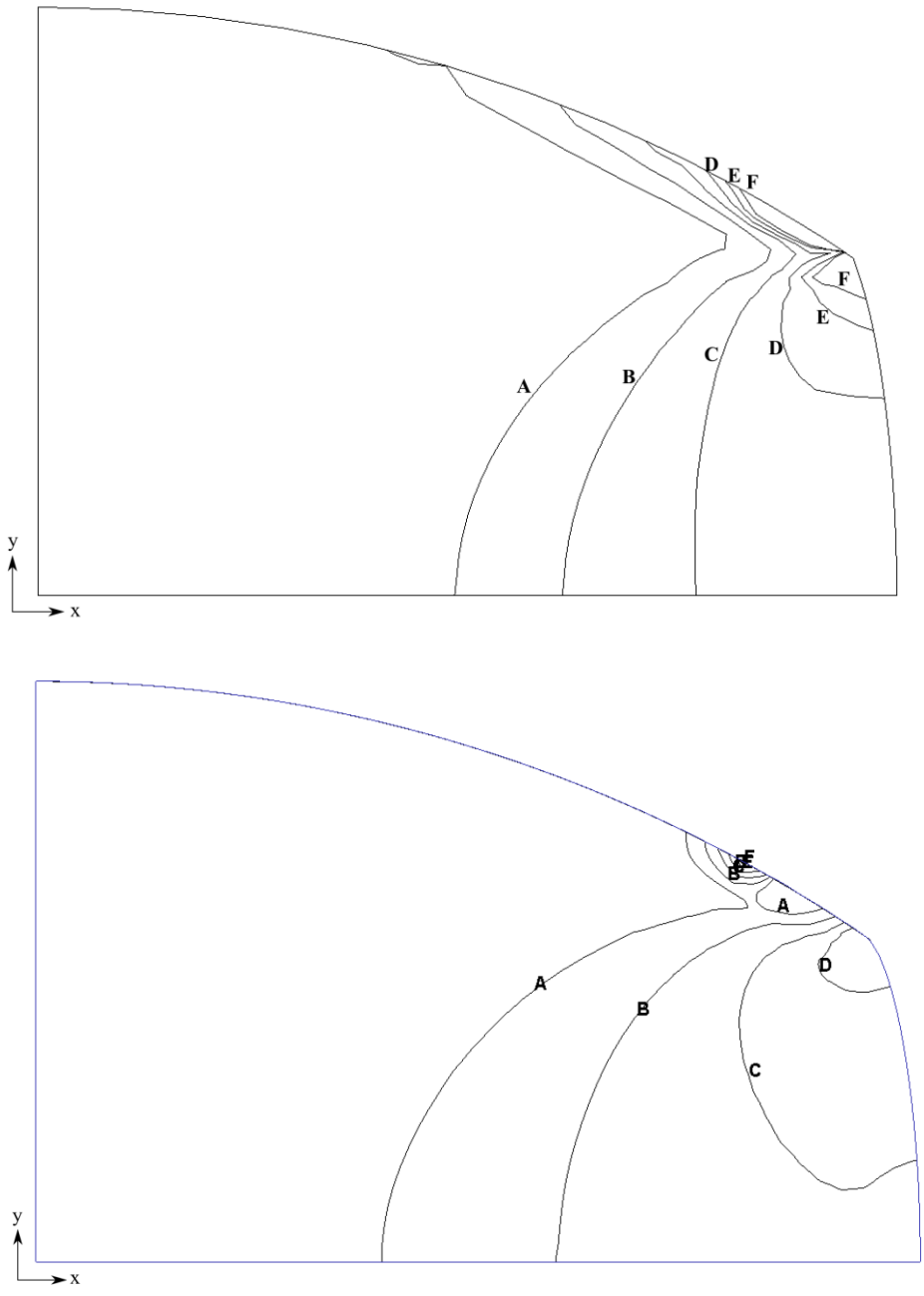

Figure 6.14: Contour graphs of ε_{xx}, results of LRBFCM (on top) and FEM (at bottom). The lines represent A = 0.05, B = 0.1, C = 0.15, D = 0.2, E = 0.25, F = 0.3.

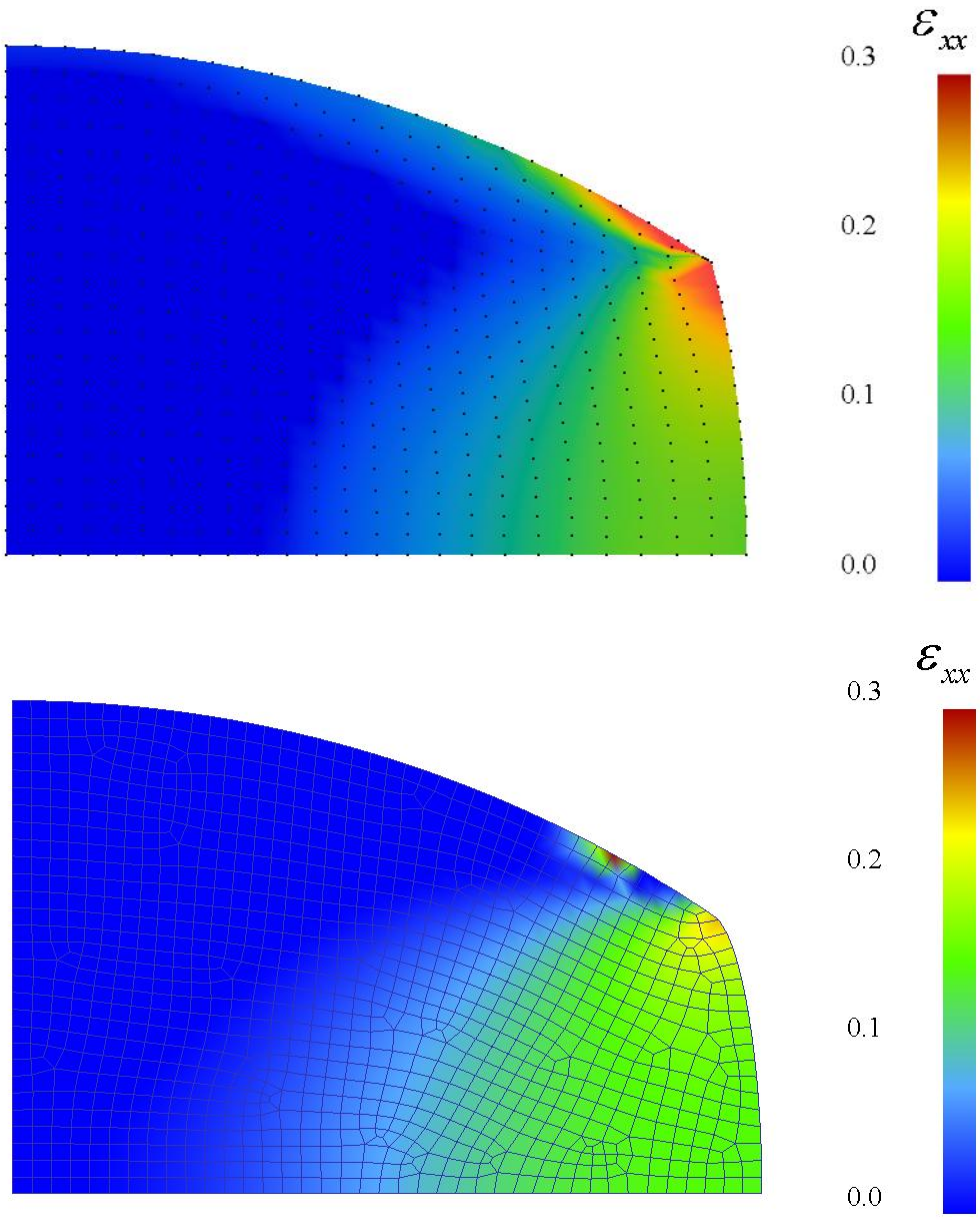

Figure 6.15: ε_{xx} fields are calculated by LRBFCM (on top) and FEM (at bottom).

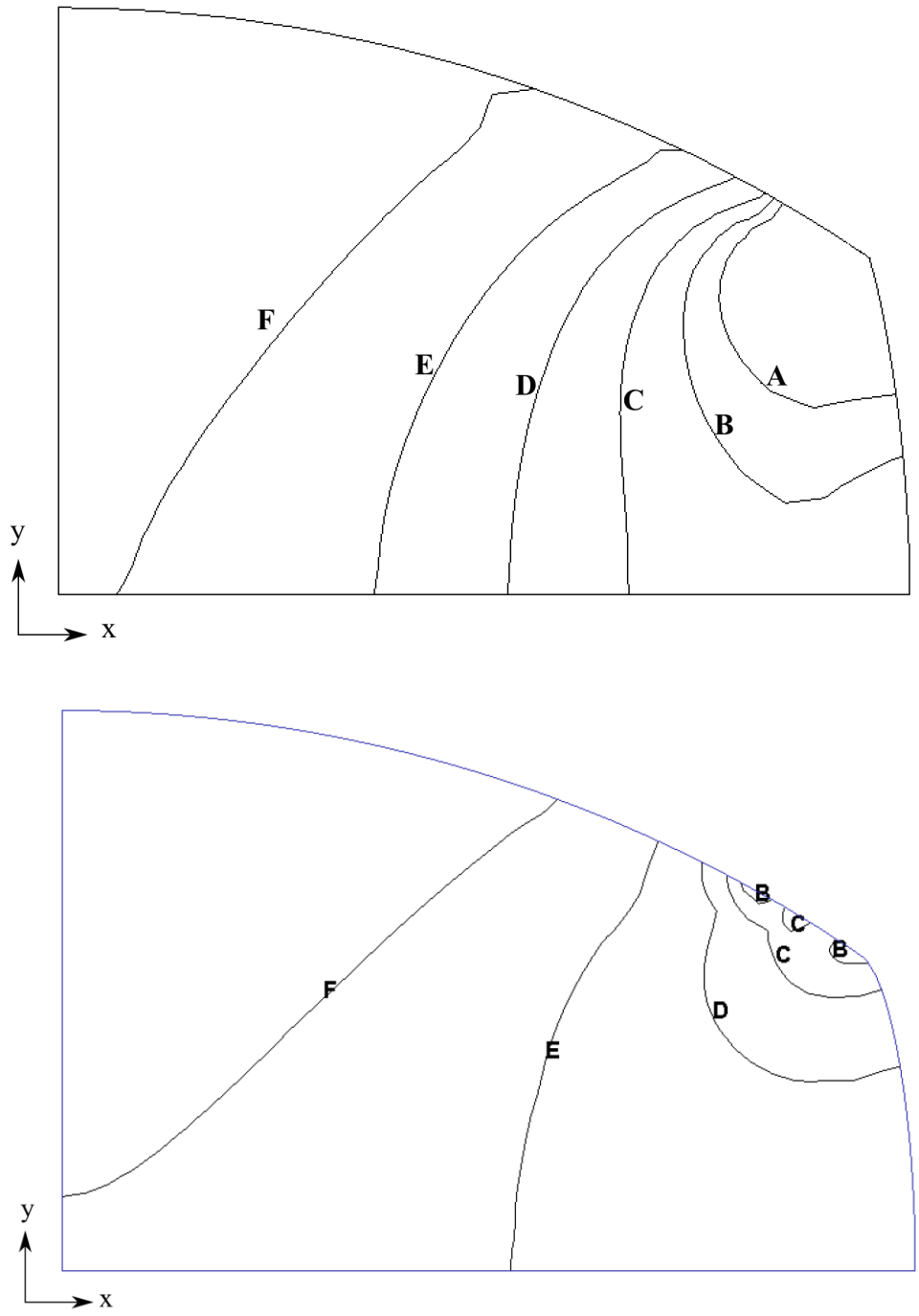

Figure 6.16: Contour graphs of ε_{yy}, results of LRBFCM (on top) and FEM (at bottom). The lines represent A = -0.7, B = -0.6, C = -0.5, D = -0.4, E = -0.3, F = -0.2.

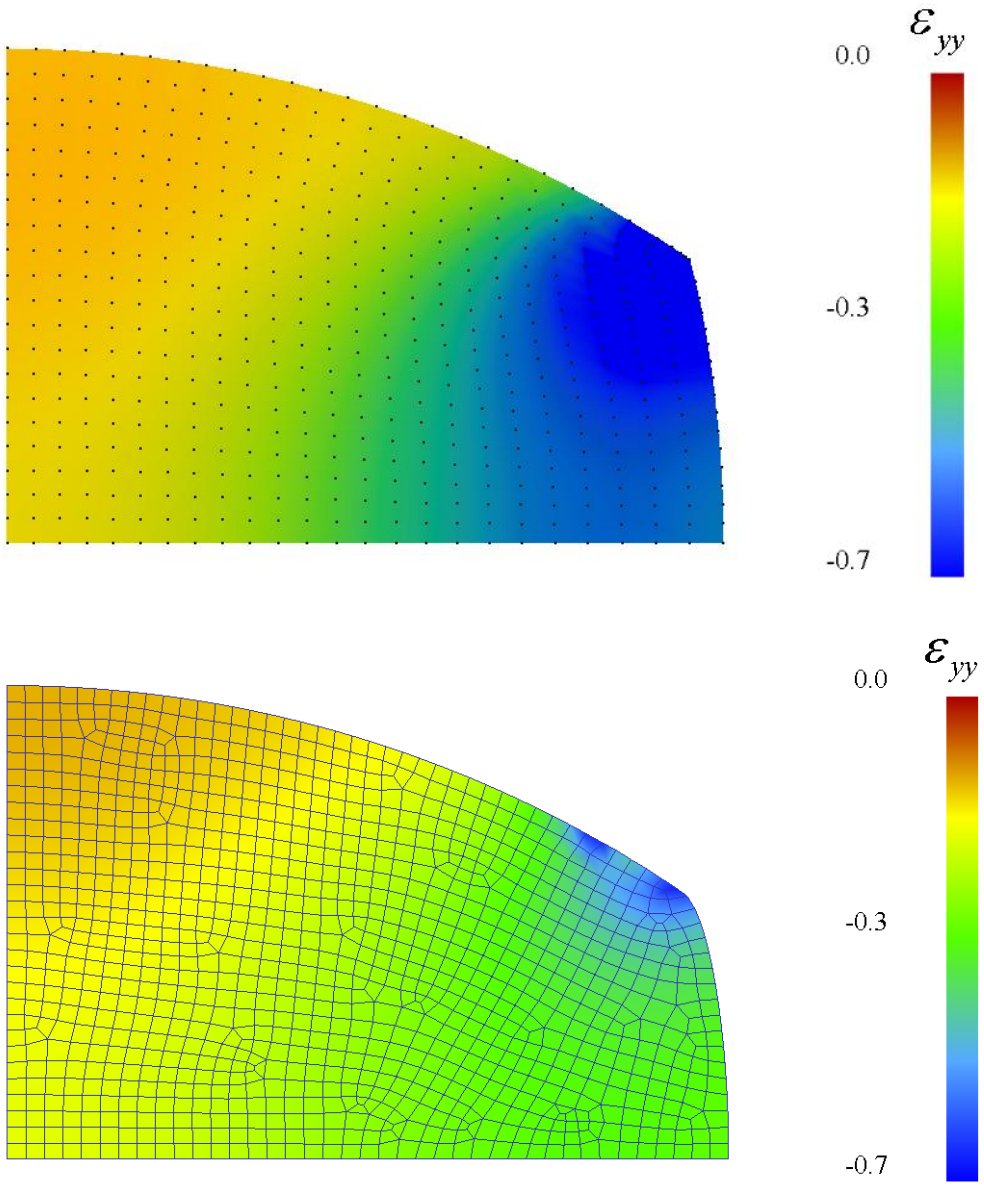

Figure 6.17: ε_{yy} fields are calculated by LRBFCM (on top) and FEM (at bottom).

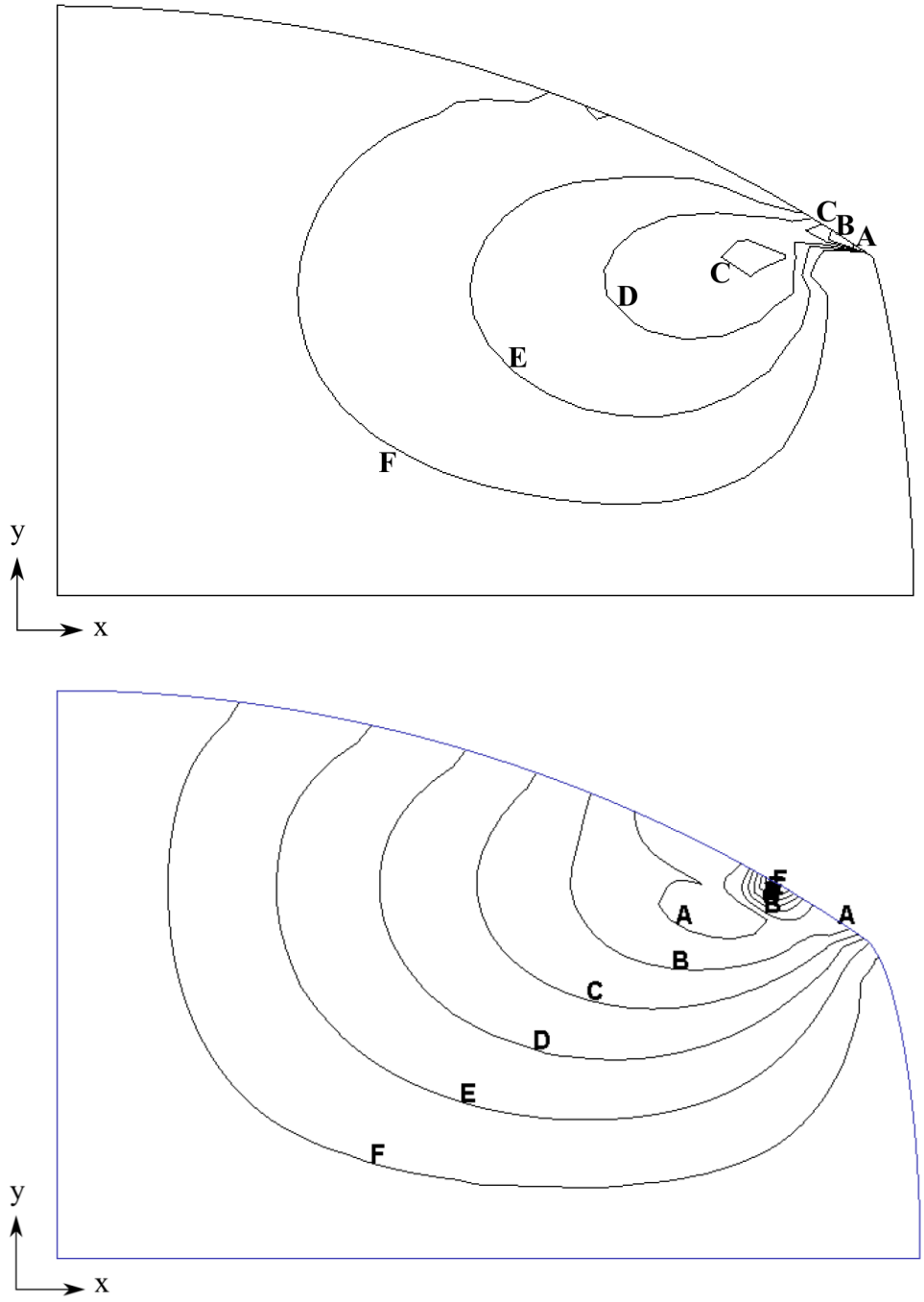

Figure 6.18: Contour graphs of ε_{xy}, results of LRBFCM (on top) and FEM (at bottom). The lines represent A = -0.4, B = -0.333, C = -0.267, D = -0.2, E = -0.133, F = -0.067.

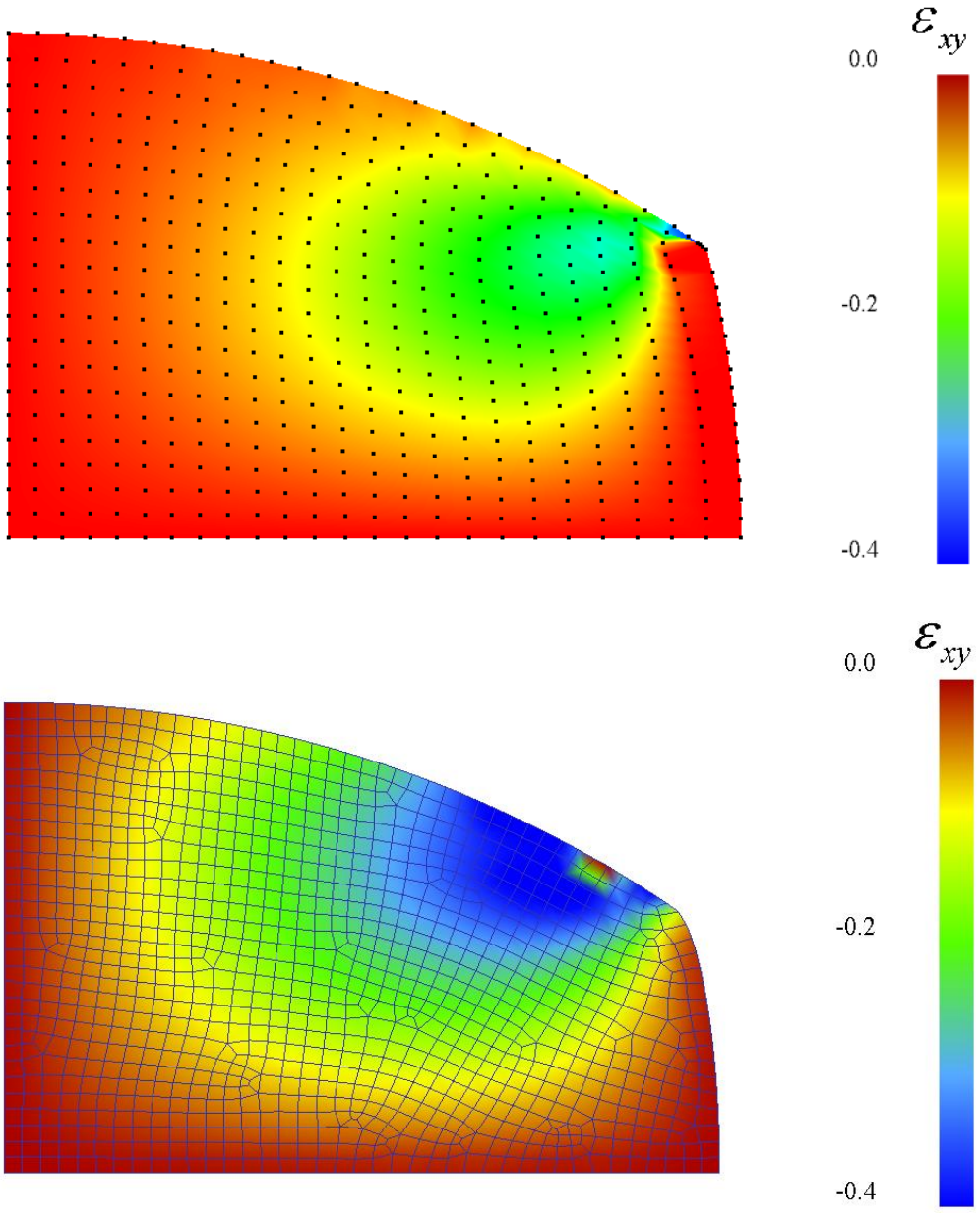

Figure 6.19: ε_{xy} fields are calculated by LRBFCM (on top) and FEM (at bottom).

The results of oval rolling simulation in previous figures are based on constant elastic material properties. However, if the temperature value is changed during the same test case, such as in the Table 6.1, then the thermal effect to the mechanical model can be seen. A comparison is made between LRBFCM and FEM solution for different temperature values. As expected, the width expansion is larger as the temperature increases. The material properties are taken for 16MnCrS5 steel for different temperature values and oval rolling test with 11 deformation steps is redone for each temperature value.

Temperature °C	**With at the exit (mm) by LRBFCM**	**With at the exit (mm) by FEM**
1200	52.99	52.66
1100	52.69	52.42
1000	52.41	52.19
900	52.14	51.96
800	51.86	51.74
700	50.80	50.88
600	50.67	50.76
500	50.53	50.65

Table 6.1: Shape rolling simulation is done by LRBFCM and the elastic material properties are previously obtained by each corresponding temperature for 16MnCrS5 steel. The width at the *x* axis after the deformation, is measured and compared with different temperature values.

The deformations, calculated by LRBFCM and FEM in this chapter, are relatively large with respect to the examples in the previous chapter. These solutions are calculated in many discrete steps and cumulative results are shown at the end. Therefore, the compared results could not anymore achieve almost perfect match. Nevertheless, a reasonably good agreement has been found. The displacement fields are again very similar and pattern of the contour lines of the strain vector components are also similar with FEM. The flat rolling results have better match than the oval rolling example since oval rolling creates remarkable

shape changes. The best agreements between LRBFCM and FEM are seen in displacement fields, as expected. The strain results require additional discretization process by using the calculated displacements, therefore there is a further process to calculate strain result when the displacement results are calculated. Even though, the displacement results are very similar, the strain results might slightly differ. It is important to note that both of the solvers rely on completely different solution procedure and commercial codes have a lot of optimization process involved, which could not be expected from our laboratory type LRBFCM solver. Therefore, it has been expected that during the detailed analysis of the cases in this chapter, it is logical that the solutions might differ.

Observation of the computing times of the examples in this chapter indcates that the computational time of FEM code is much less than LRBFCM, even though the number of collocation nodes in LRBFCM code is much smalled than the number of nodes in FEM code. It can be concluded that when there is a continuous deformation analysed in discrete steps, such as in this chapter, FEM code is well optimized and gives results much faster. The observed time difference between the codes increases against the number of deformation steps. This might also be attributed to the laboratory and commercial character of the coeds compared.

It can be concluded from the test cases shown, that LRBFCM is a straightforward and stable enough solution procedure to solve large deformation problems. Moreover, a complete rolling analysis can be done by LRBFCM as demonstrated in the next Chapter 7.

7 Sensitivity Studies of the Hot Shape Rolling

In Chapter 7, a simulation of a realistic rolling mill schedule, as appears in Štore-Steel rolling mill, manufactured by Siderimpes, is given. The rolling schedule consists of 5 rolling stands in a row, and each rolling stand has a specific groove geometry. The simulation is demonstrated for rolling of a rectangular billet into a circular rod. Results of displacement, temperature, strain and stress components are shown at the exit of each rolling stand. Several simulations are run with different operating parameters, thermal and mechanical properties and their influence on the results is elaborated.

7.1 Simulation of hot shape rolling of steel

In the simulation, an elastic plane strain material response is considered with temperature depended Young's modulus and Poisson's ratio. The material properties are obtained from JmatPro database from which a suitable table is written for every 10 °C up to 1250 °C for 16MnCrS5 steel. Each computational node's material properties are updated for corresponding temperature, and linear interpolation is used in between the values from the table. The thermo-mechanical solution is therefore coupled, however elastic. It is assumed that none of the energy due to deformation is absorbed by the material except the deformation turning into heat. Therefore, there is no elastic recovery. The geometrical definitions of the grooves and rolling stands are given in Table 7.1. In this simulation of rolling governing equations in Table 2.1 are used.

Rolling Stand	Groove Type	Groove Radius (mm)	Roll Radius (mm)	Roll Gap (mm)	Groove Height (mm)	Groove Width (mm)	z Position (mm)
1	OVAL (H)	85	450	17	26	122.4	0
2	OVAL (H)	85	450	5	26	122.4	3000
3	ROUND(V)	40	450	14	33	78.5	5600
4	OVAL (H)	55	450	2.6	25	92.2	9200
5	F.ROUND(V)	30.4	450	4	28.4	62	12200

Table 7.1: Predefined groove dimensions used in the simulation.

The rolling schedule consists of varying orientation namely horizontal or vertical. The configuration can be seen in Figure 7.1 below.

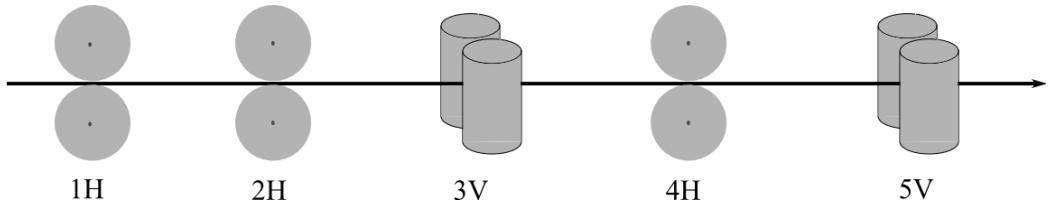

Figure 7.1: Rolling schedule consists of 5 rolling stands with vertical (V) and horizontal (H) orientation.

All the parameters of the rolling mill used in the rolling simulation are given in Table 7.2. Initial slice is positioned 500 mm away from the centre of the first rolling stand and simulation is continued for 13.000 mm. The results are shown for a slice at the exit of each rolling stand and for each rolling stand displacement vector, contour graph of displacement, shaded and contour graphs of temperature, contour graphs of strain vector components $\varepsilon_{xx}, \varepsilon_{yy}, \varepsilon_{xy}$ and shaded graphs of stress vector components $\sigma_{xx}, \sigma_{yy}, \sigma_{xy}$ are shown.

Heat transfer coefficient to air	h_{air}	20	W/m^2K
Heat transfer coefficient to roll	h_{roll}	10000	W/m^2K
Thermal conductivity of steel	k	29	W/mK
Specific heat of steel	c_p	630	J/kgK
Initial rolling temperature	T_{fur}	1100	°C
Initial rolling speed	v_{entry}	0.76	m/s
Ambient temperature	T_{air}	25	°C
Roll temperature	T_{roll}	500	°C
Taylor-Quinney parameter	η	0.001	-
Young's modulus	$E(1250\ ^0\text{C})$ - $E(30\ ^0\text{C})$	85.229 – 210.67	GPa
Poisson's ratio	$\nu(1250\ ^0\text{C})$ - $\nu(30\ ^0\text{C})$	0.36203 – 0.28728	-

Table 7.2: Input parameters for hot shape rolling simulation.

7.2 Thermo-mechanical simulation after the first rolling stand

The displacement vectors at the exit of the first rolling stand are shown in Figure 7.2. The green lines represent 26 groove lines which have contacted the slice. Initially 525 nodes are uniformly distributed on the domain and boundary. Except Figure 7.2 all the results from the first rolling stand are calculated with LRBFCM with 525 collocation nodes. The results in terms of displacement vectors in this chapter are shown with less number of collocation nodes than used in the calculation to explicitly demonstrate the vectors.

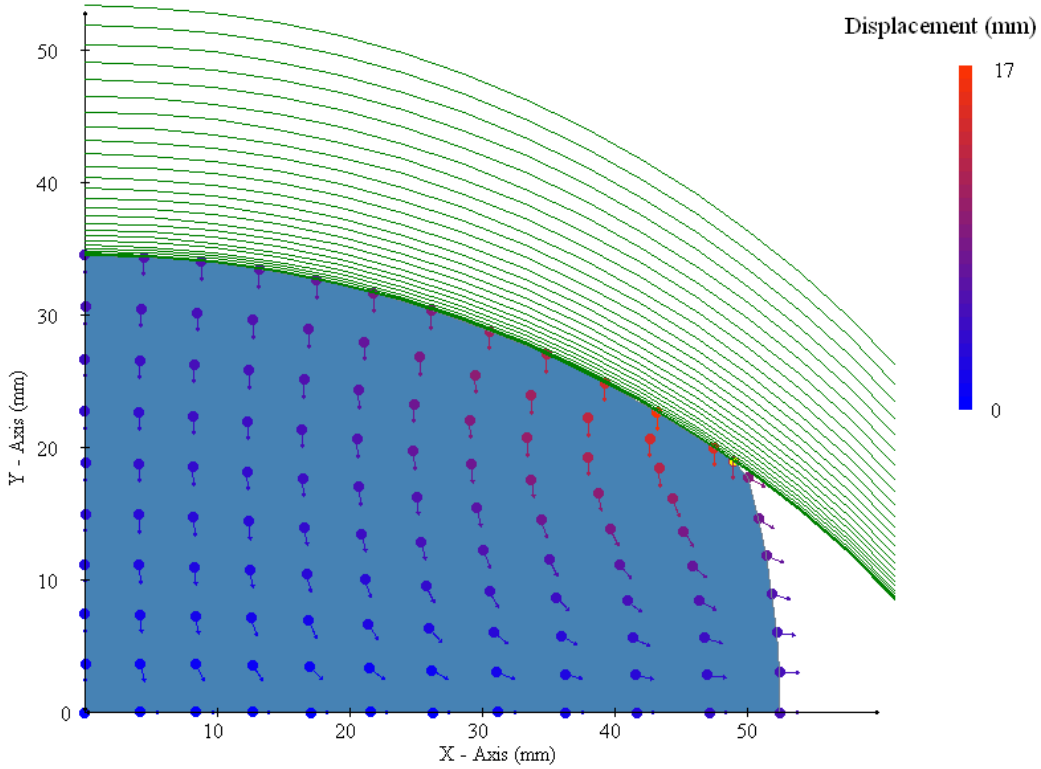

Figure 7.2: Displacement vectors at the exit of the first rolling stand. 26 groove lines represent necessary deformation steps as a consequence of the process with 121 collocation nodes.

Shaded and contour graphs of temperature field at the exit of the first rolling stand can be seen in Figure 7.3 and Figure 7.4 below. The highest temperature drop is at the top-right corner where the roll contact starts.

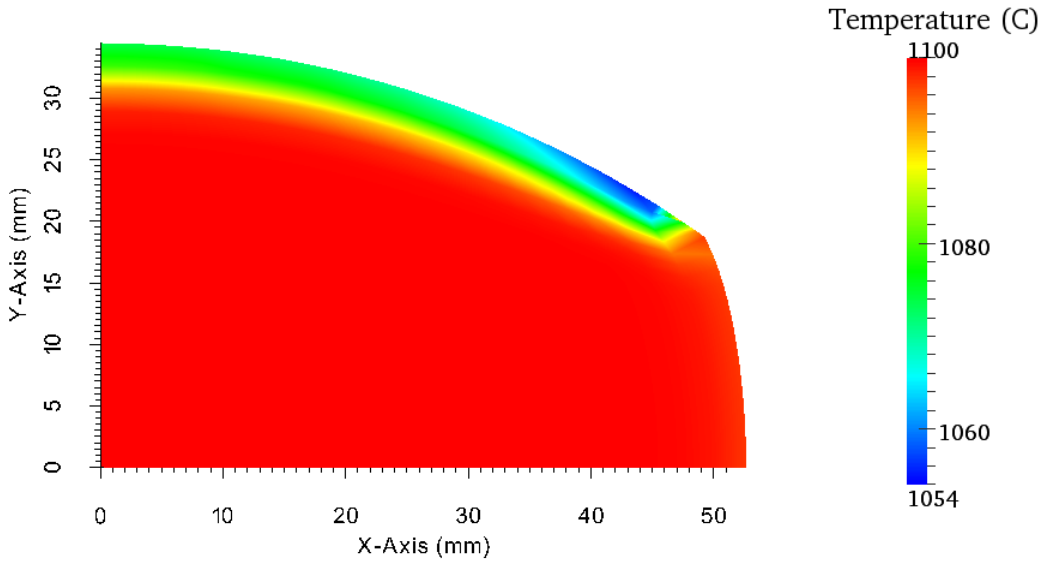

Figure 7.3: Temperature field at the exit of the first rolling stand.

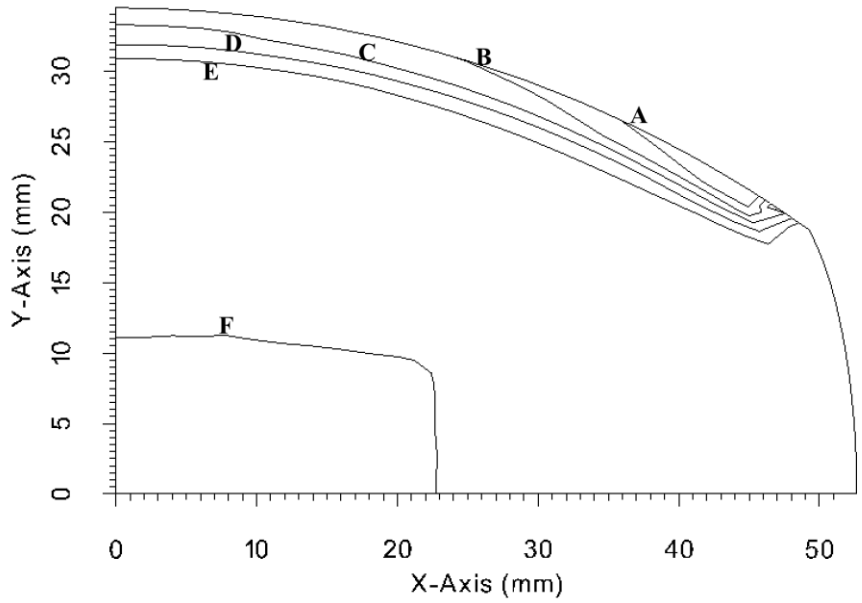

Figure 7.4: Temperature field at the exit of the first rolling stand. The lines represent A = 1060.04 °C, B = 1068.03 °C, C = 1076.02 °C, D = 1084.02 °C, E = 1092.01 °C and F = 1100.00 °C.

Contour lines of the displacement field are shown in Figure 7.5. As expected, the largest displacement is at the initial top-right corner where the first contact occurs.

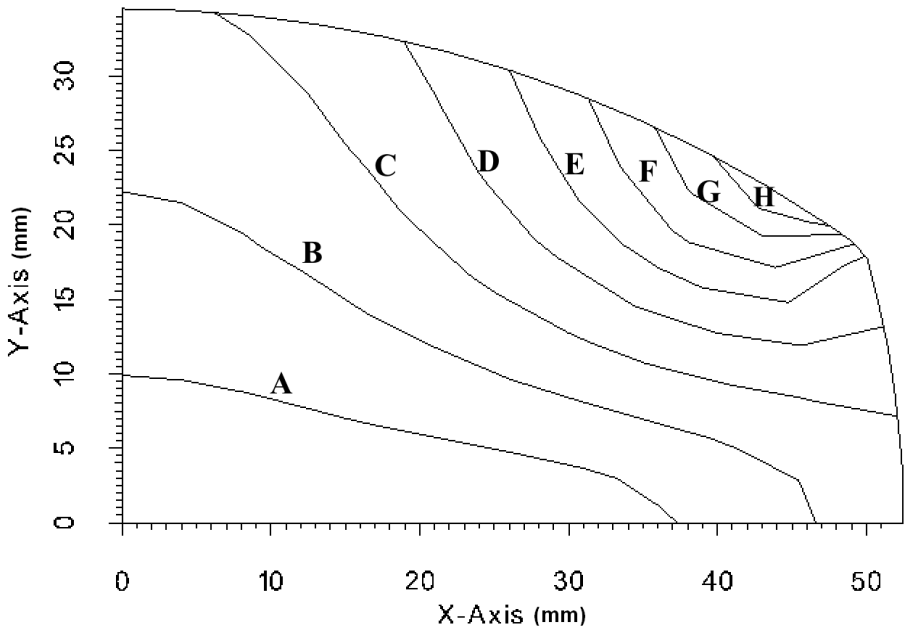

Figure 7.5: Displacement field at the exit of the first rolling stand. The lines represent A = 1.92 mm, B = 3.84 mm, C = 5.77 mm, D = 7.69 mm, E = 9.62 mm, F = 11.54 mm, G = 13.47 mm and H = 15.39 mm.

Contour lines of the components of the strain vector fields $\varepsilon_{xx}, \varepsilon_{yy}, \varepsilon_{xy}$ are shown in Figures 7.6, 7.7 and 7.8 below. As expected, the highest values are again around the first contacted region. In ε_{xx}, the lines are elongated over the boundary which has contact with the roll, however in ε_{yy} the lines are elongated over the boundary which is free to move. The highest and lowest values of ε_{xy} are symmetrically positioned right next to the last contact point, as expected for the shear strain.

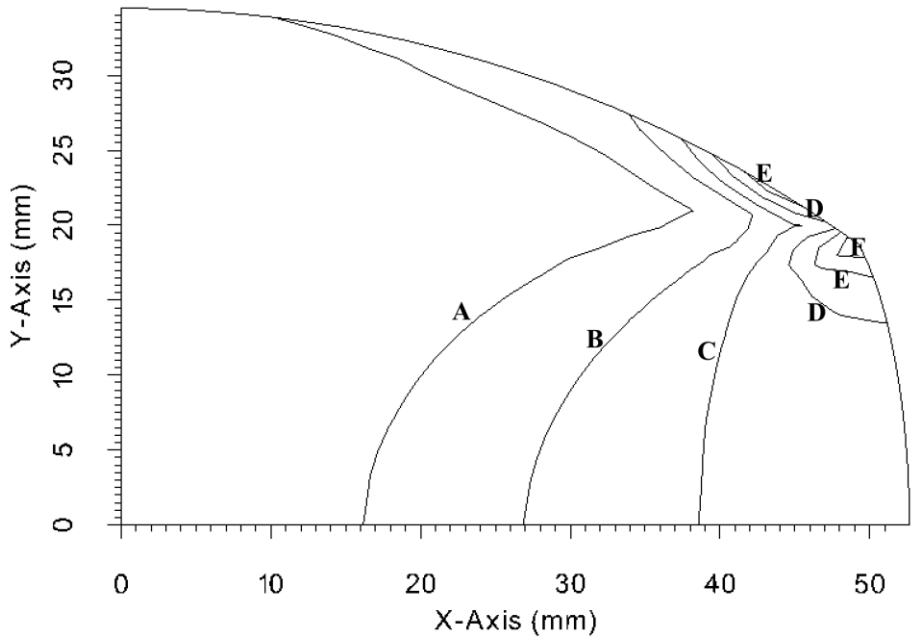

Figure 7.6: ε_{xx} field at the exit of the first rolling stand. The lines represent A = 0.023, B = 0.109, C = 0.196, D = 0.282, E = 0.369 and F = 0.456.

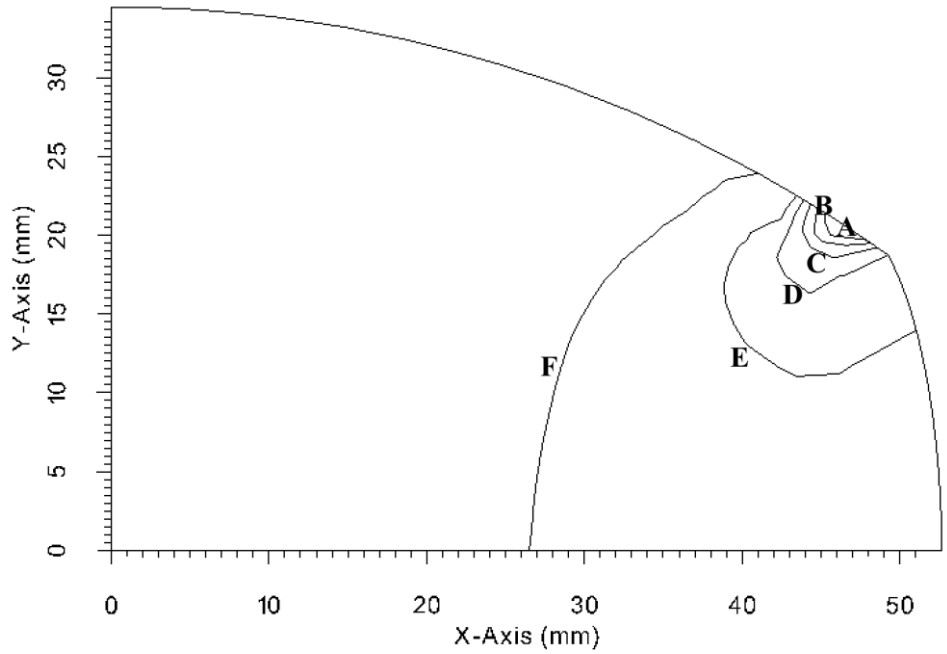

Figure 7.7: ε_{yy} field at the exit of the first rolling stand. The lines represent A = -1.84, B = -1.56, C = -1.27, D = -0.98, E = -0.70 and F = -0.41.

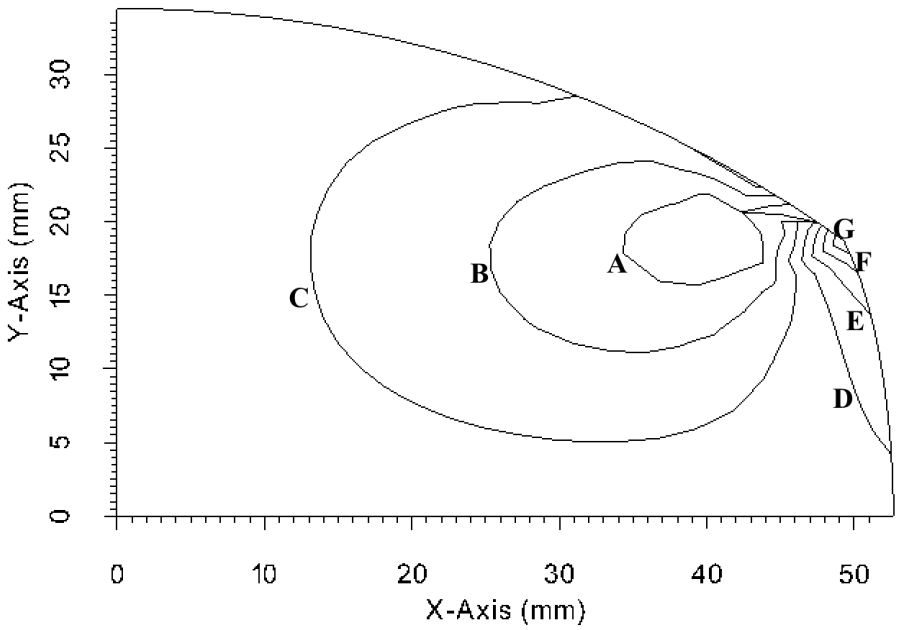

Figure 7.8: ε_{xy} field at the exit of the first rolling stand. The lines represent A = -0.269, B = -0.171, C = -0.075, D = 0.022, E = 0.119, F = 0.216 and G = 0.312.

Contour lines of the components of the stress vector fields $\sigma_{xx}, \sigma_{yy}, \sigma_{xy}$ are given in Figures 7.9, 7.10 and 7.11 below. In Figure 7.9 and Figure 7.10, the stress fields are somehow similar where the lowest region is concentrated around the first contacted region and highest values are over the contacted boundary. Shear stress has the highest and lowest values symmetrically around the last contact point and values in between are distributed circularly inside the domain.

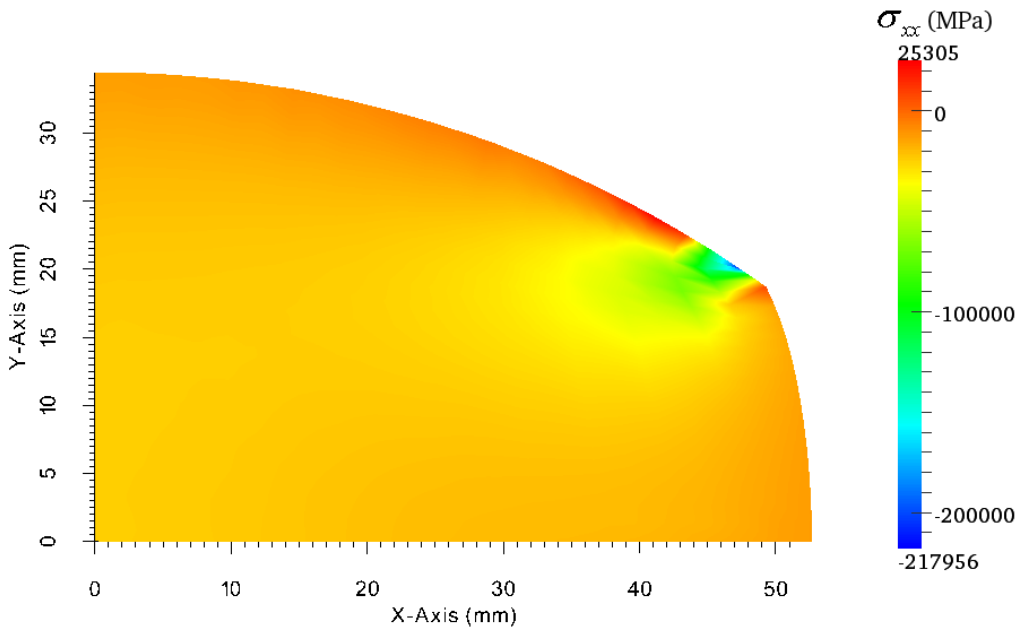

Figure 7.9: σ_{xx} field at the exit of the first rolling stand.

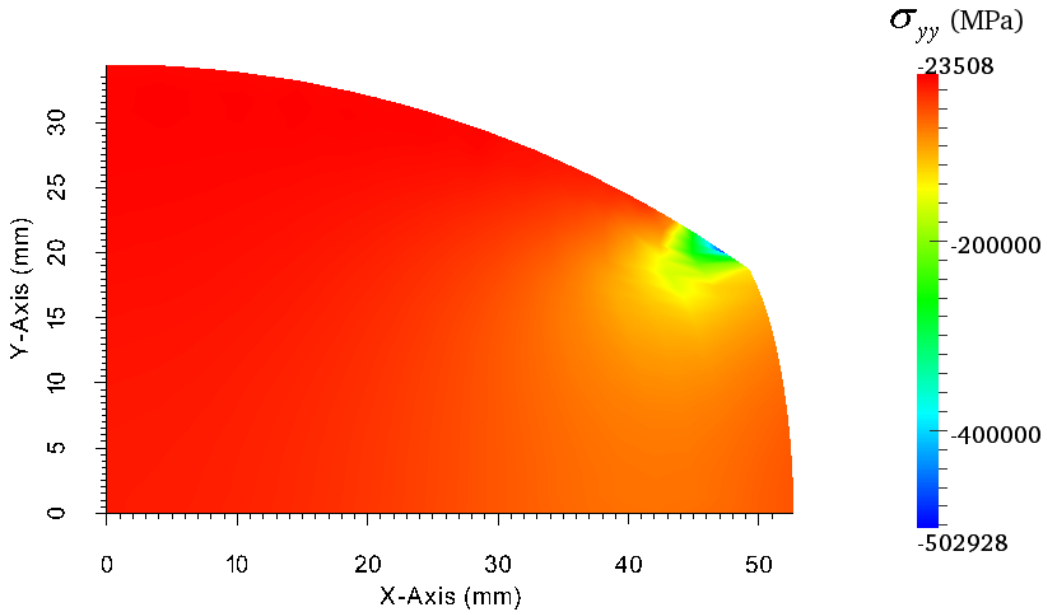

Figure 7.10: σ_{yy} field at the exit of the first rolling stand.

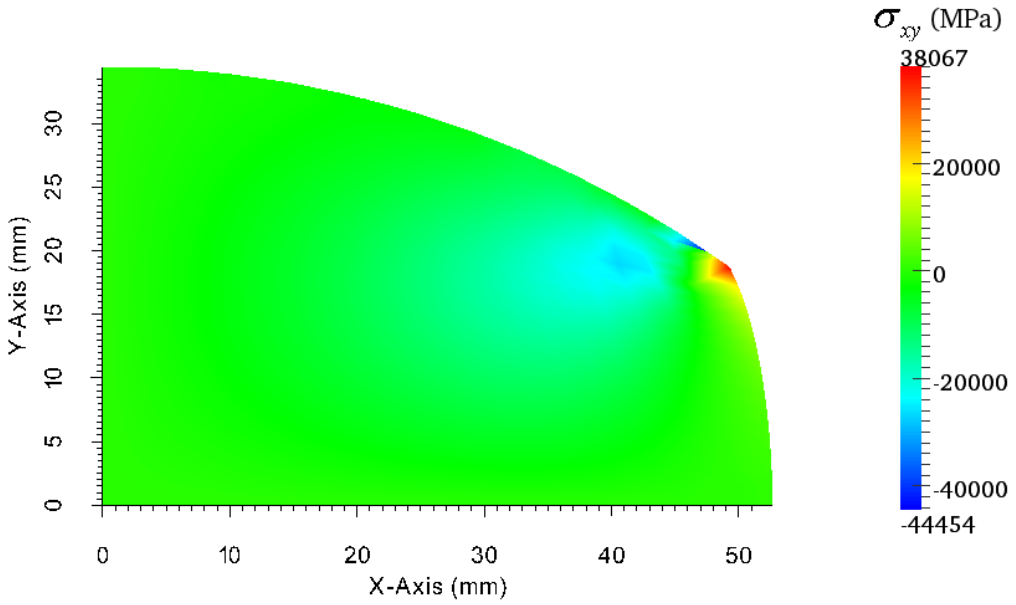

Figure 7.11: σ_{xy} field at the exit of the first rolling stand.

7.3 Thermo-mechanical simulation after the second rolling stand

The displacement vectors at the exit of the second rolling stand are shown in Figure 7.12. The dark blue lines represent the 16 groove lines which have contacted the slice. In between first and second rolling stand, ENG is applied and the total number of collocation nodes becomes 435. Except Figure 7.12 all the results from the second rolling stand are calculated with 435 collocation nodes.

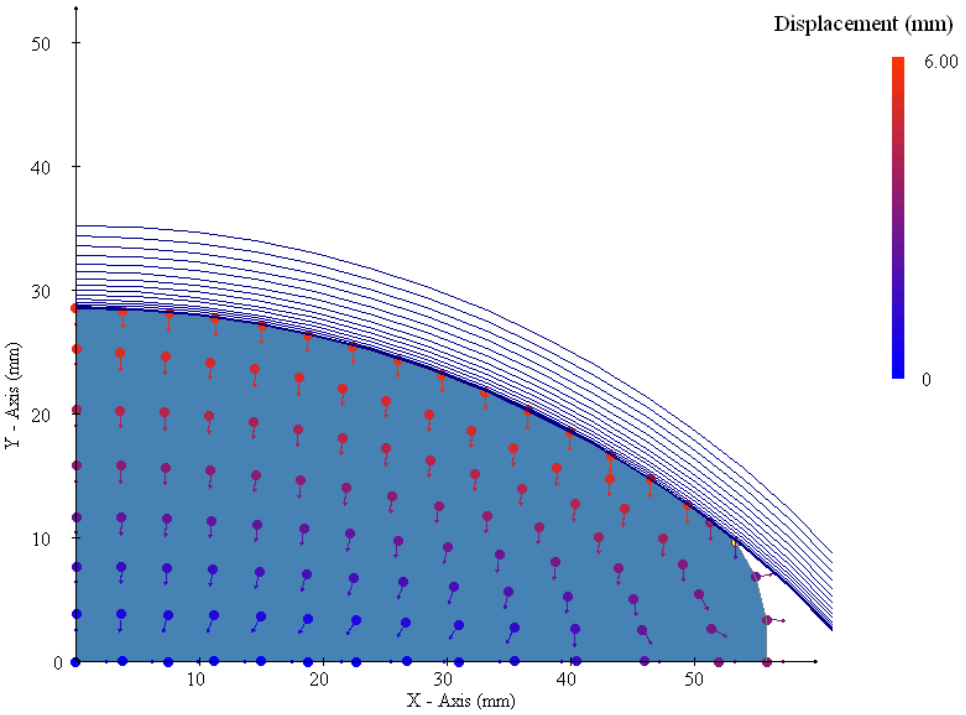

Figure 7.12: Displacement vectors at the exit of the second rolling stand with 112 collocation nodes. 16 groove lines represent necessary deformation steps as a consequence of the process.

Shaded and contour graphs of the temperature field at the exit of the second rolling stand can be seen in Figure 7.13 and Figure 7.14 below. The highest temperature decrease is still around the first contacted region during the first rolling stand. The temperature drop is relatively uniform over the contacted region because the groove geometry of the second rolling stand is the same as the first one however the roll gap is smaller. Therefore, the contacted region at the exit of the first rolling stand is the same as the contact at the beginning of the second rolling stand. In Figure 7.15 contour lines of displacement are shown. Contour lines of the components of the strain vector fields $\varepsilon_{xx}, \varepsilon_{yy}, \varepsilon_{xy}$ are given in Figures 7.15, 7.16 and 7.17 below. The highest value for ε_{xx} is around the last contact node. For the ε_{yy} and ε_{xy} values the highest values in magnitude are around the first contacted region during the first rolling stand.

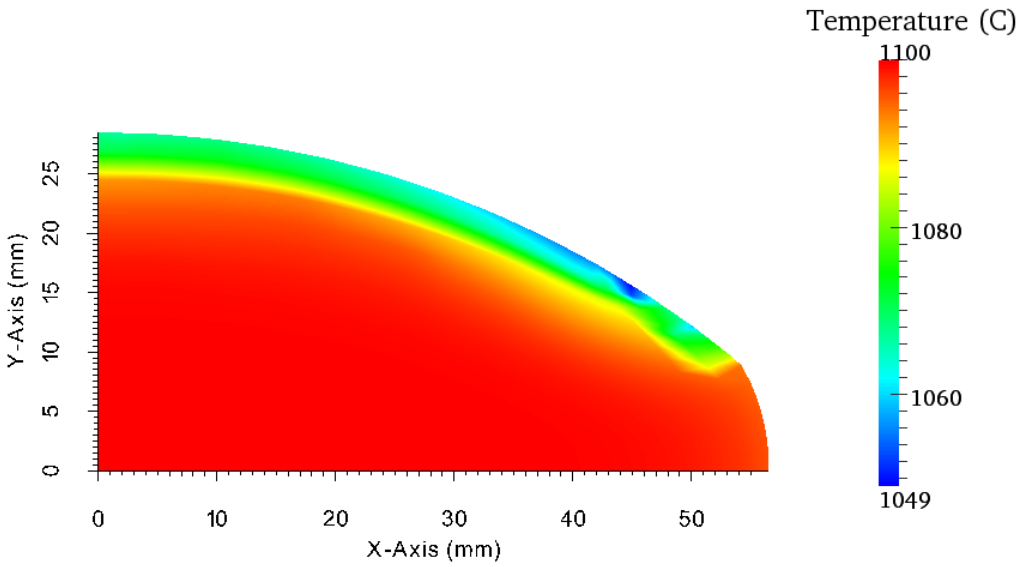

Figure 7.13: Temperature field at the exit of the second rolling stand.

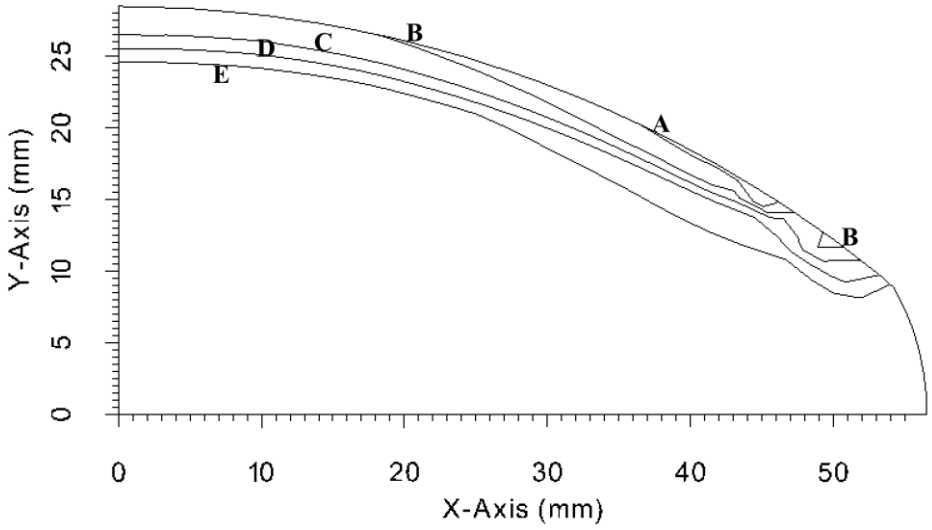

Figure 7.14: Temperature field at the exit of the second rolling stand. The lines represent A = 1057.55 °C, B = 1066.04 °C, C = 1074.53 °C, D = 1083.02 °C and E = 1091.51 °C.

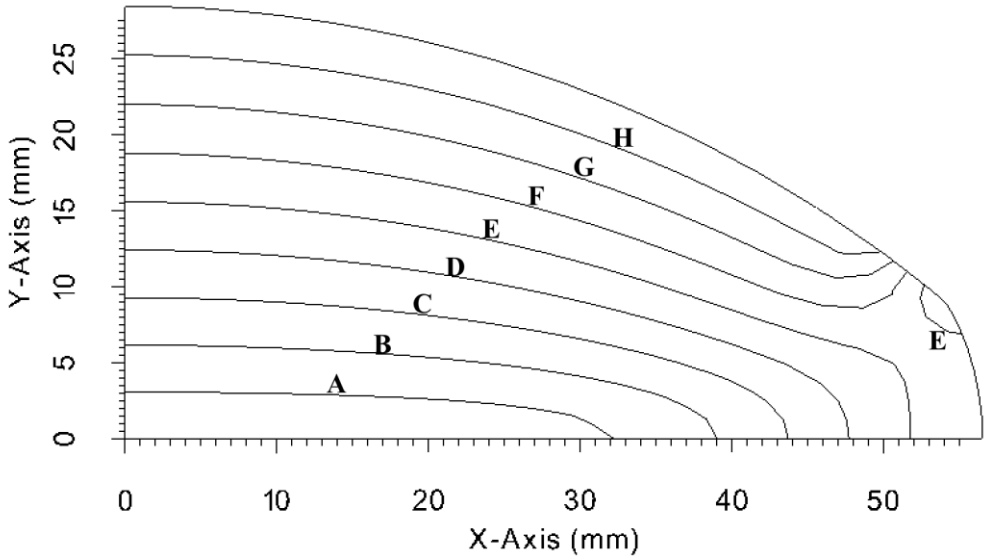

Figure 7.15: Displacement field at the exit of the second rolling stand. The lines represent A = 0.67 mm, B = 1.33 mm, C = 2.00 mm, D = 2.67 mm, E = 3.33 mm, F = 4.00 mm, G = 4.67 mm and H = 5.33 mm.

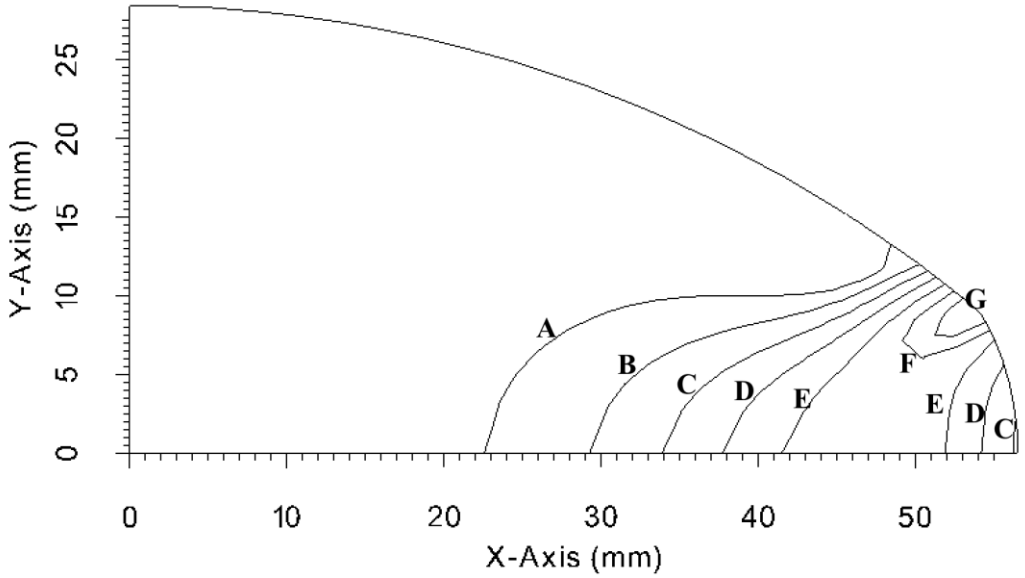

Figure 7.16: ε_{xx} field at the exit of the second rolling stand. The lines represent A = 0.030, B = 0.059, C = 0.088, D = 0.117, E = 0.146, F = 0.175, and G = 0.204.

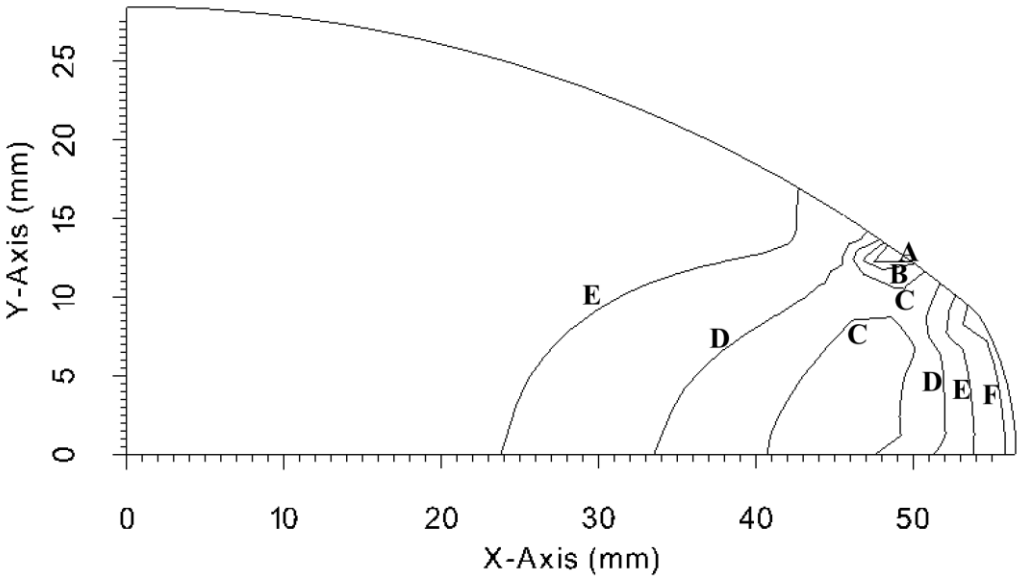

Figure 7.17: ε_{yy} field at the exit of the second rolling stand. The lines represent A = -0.564, B = -0.490, C = -0.416, D = -0.342, E = -0.268 and F = -0.194.

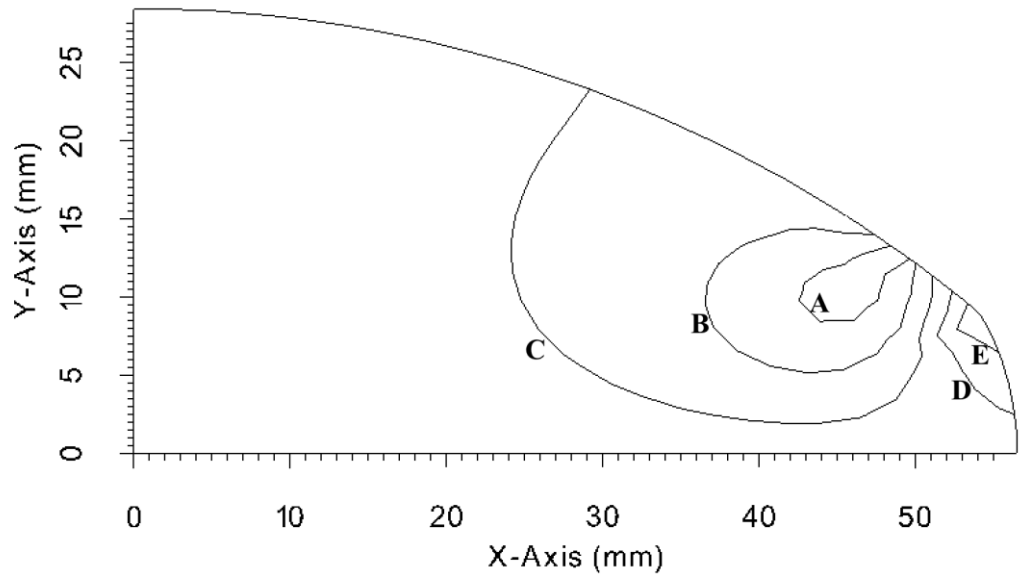

Figure 7.18: ε_{xy} field at the exit of the second rolling stand. The lines represent A = -0.148, B = -0.091, C = -0.034, D = 0.023 and E = 0.080.

Shaded graphs of stress vector components $\sigma_{xx}, \sigma_{yy}, \sigma_{xy}$ are shown in Figure 7.19, Figure 7.20 and Figure 7.20 respectively calculated at the exit of the second rolling stand.

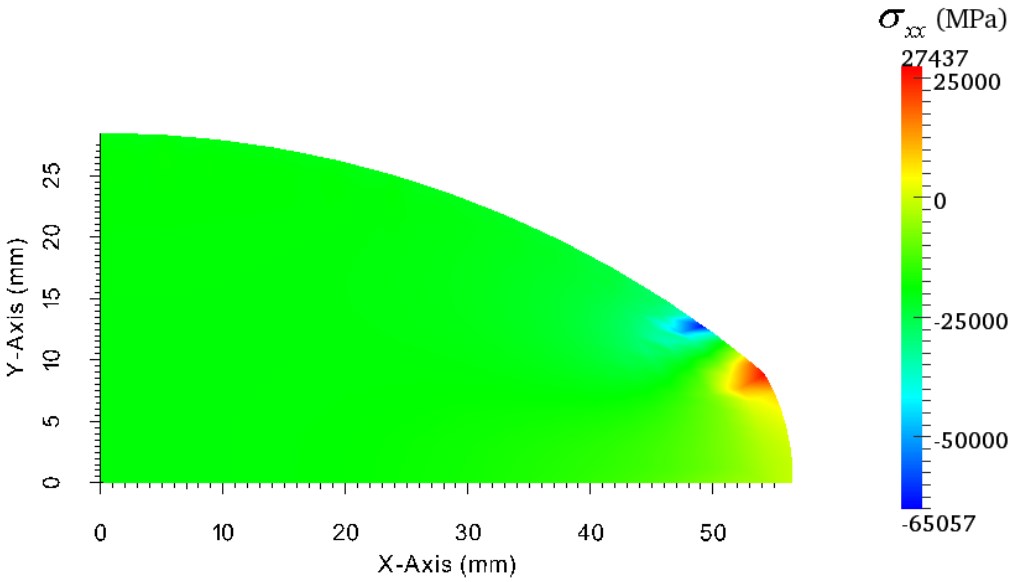

Figure 7.19: σ_{xx} field at the exit of the second rolling stand.

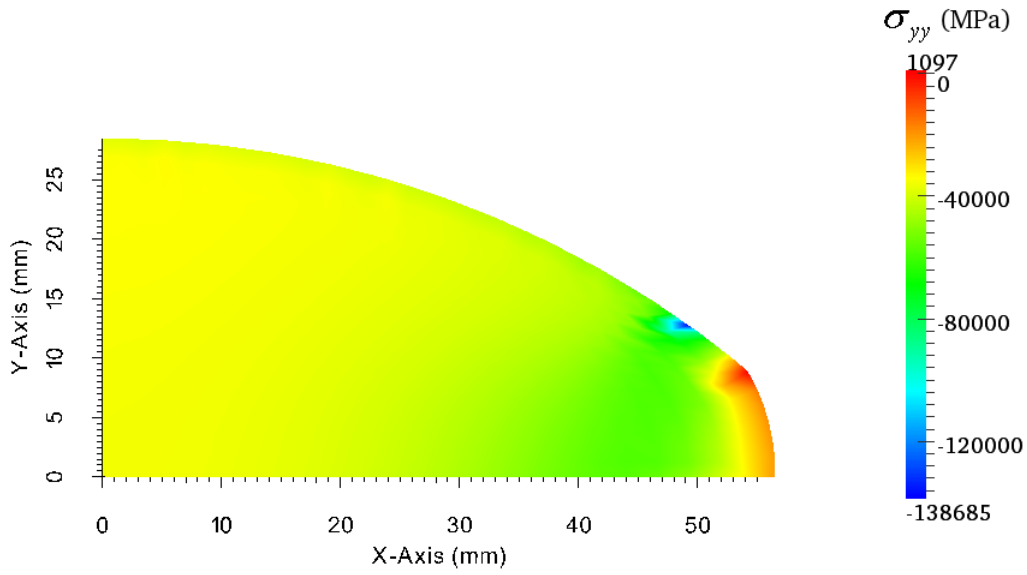

Figure 7.20: σ_{yy} field at the exit of the second rolling stand.

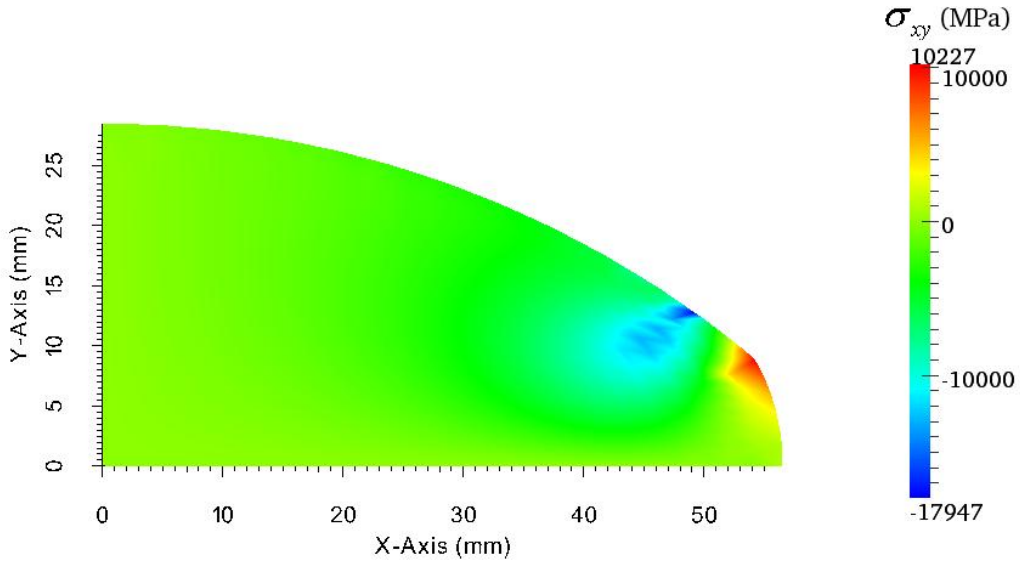

Figure 7.21: σ_{xy} field at the exit of the second rolling stand.

7.4 Thermo-mechanical simulation after the third rolling stand

The displacement vectors at the exit of the third rolling stand are shown below in Figure 7. The violet lines represent 25 groove lines which have contacted the slice. Third rolling stand is the first vertical rolling stand in the rolling schedule. Except Figure 7.22, all the results from the third rolling stand are calculated with 435 nodes. Temperature field at the exit from the third rolling stand are shown in Figure 7.23 and Figure 7.24 in shaded and contour graphs. The highest temperature drop is at the contacted boundary however the contact starts from the bottom and increases towards the top. The additional temperature drop at the top part of the contact is still due to the first contact during the first rolling stand. Also the highest displacement is at the bottom of the contact which can be seen in contour graph of the displacement in Figure 7.25.

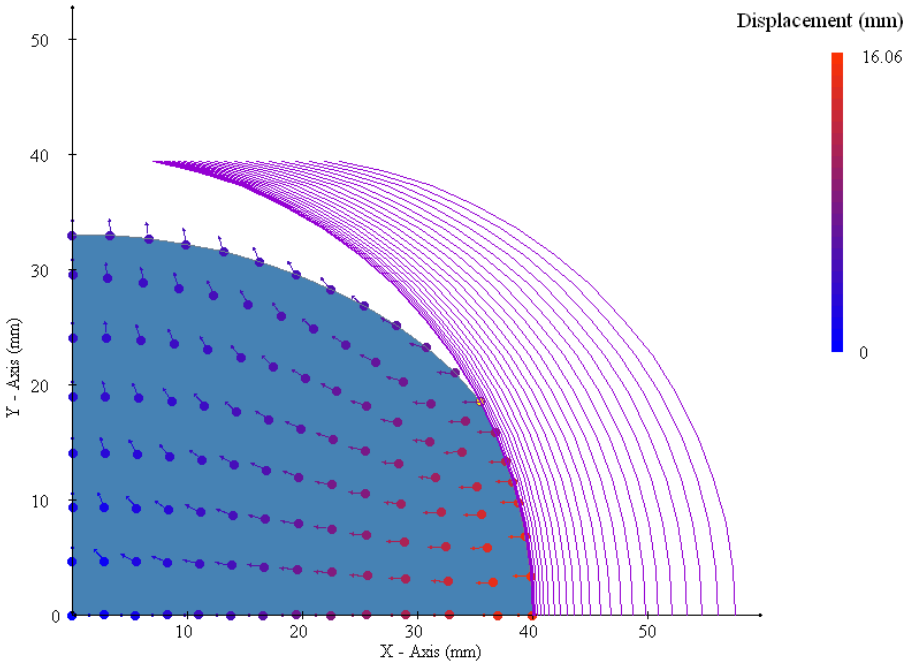

Figure 7.22: Displacement vectors at the exit of the third rolling stand. 25 groove lines represent necessary deformation steps as a consequence of the process.

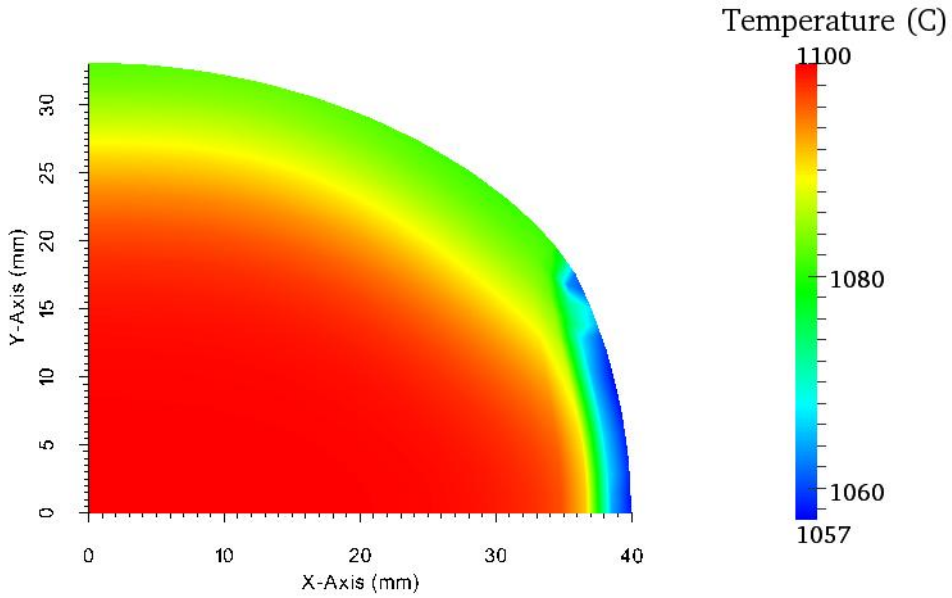

Figure 7.23: Temperature field at the exit of the third rolling stand.

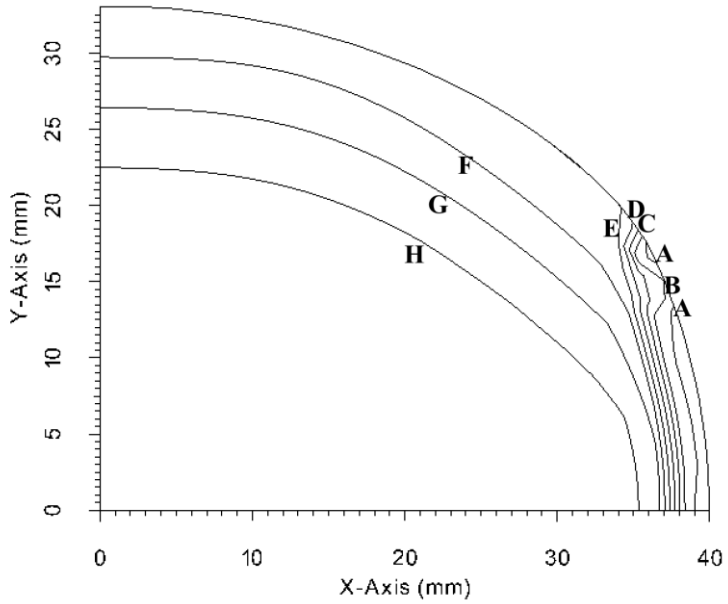

Figure 7.24: Temperature field at the exit of the third rolling stand. The lines represent A = 1061.90 °C, B = 1066.66 °C, C = 1071.42 °C, D = 1076.18 °C, E = 1080.94 °C, F = 1085.70 °C, G = 1990.47 °C and H = 1095.23 °C.

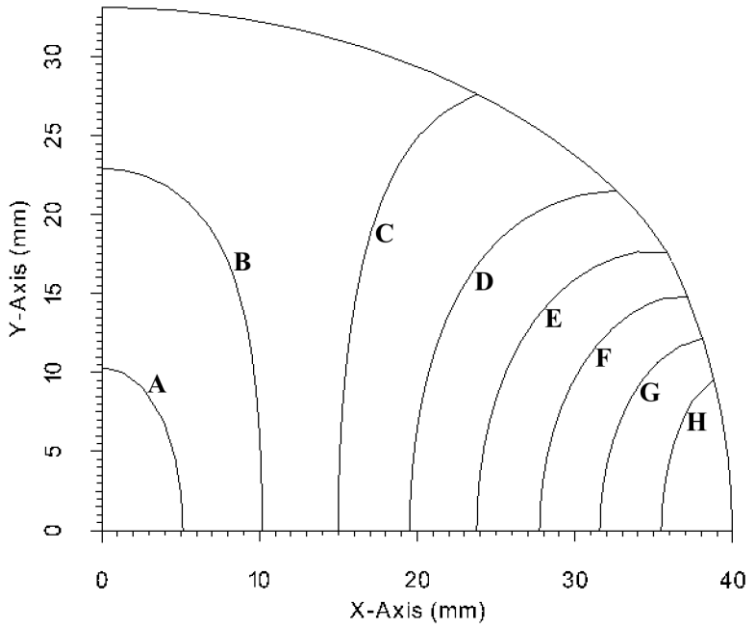

Figure 7.25: Displacement field at the exit of the third rolling stand. The lines represent A = 1.84 mm, B = 3.68 mm, C = 5.52 mm, D = 7.36 mm, E = 9.21 mm, F = 11.05 mm, G = 12.89 mm and H = 14.73 mm.

Contour lines of components of the strain vector fields $\varepsilon_{xx}, \varepsilon_{yy}, \varepsilon_{xy}$ at the exit of the third rolling stand are given in Figures 7.26, 7.27 and 7.28 below. ε_{xx} field gets negative values and ε_{yy} field gets positive values since the compression by the groove is in $-x$ direction. Contour lines of the components of the stress vector fields $\sigma_{xx}, \sigma_{yy}, \sigma_{xy}$ at the exit of the third rolling stand are given in Figures 7.29, 7.30 and 7.31. Highest stress values in magnitude are seen around the contact region for σ_{xx} and σ_{yy} fields. However highest values of shear stress and strain occurs around the last contact node.

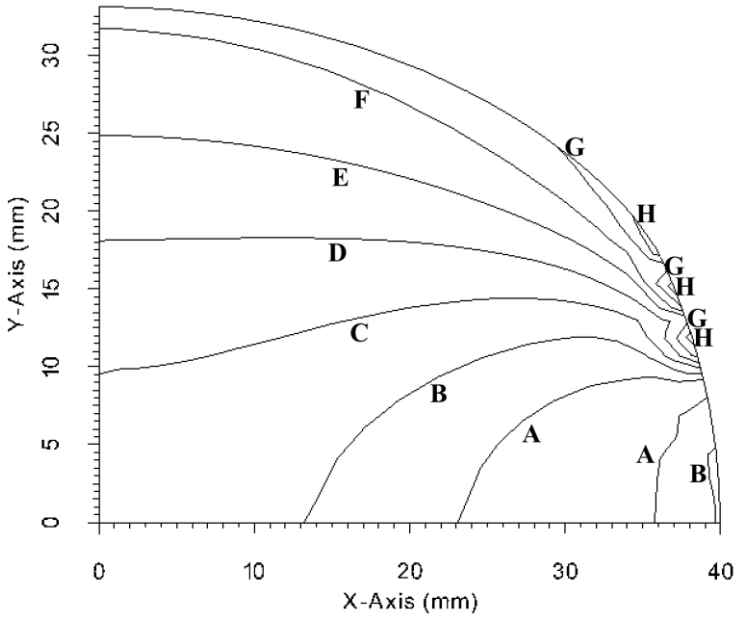

Figure 7.26: ε_{xx} field at the exit of the third rolling stand. The lines represent A = -0.447, B = -0.388, C = -0.329, D = -0.270, E = -0.211, F = -0.153, G = -0.094 and H = -0.035.

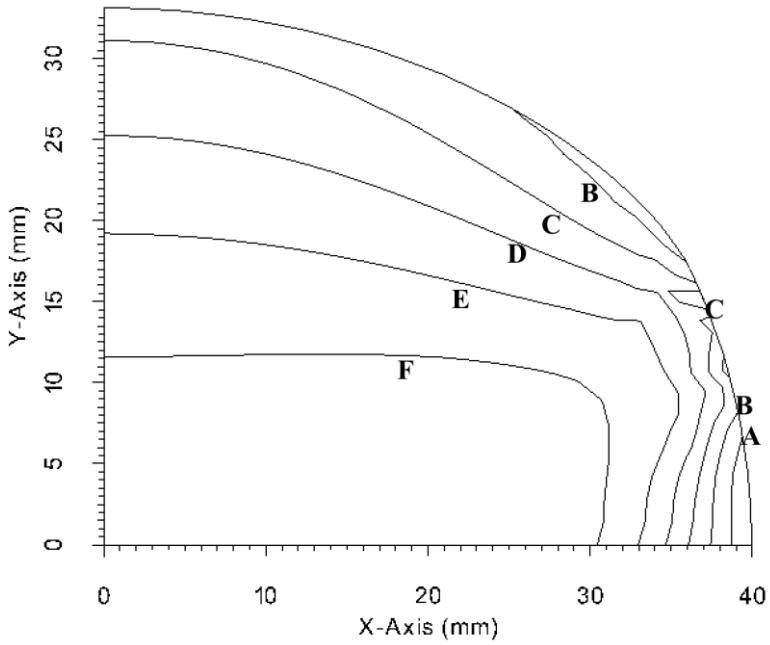

Figure 7.27: ε_{yy} field at the exit of the third rolling stand. The lines represent A = 0.021, B = 0.050, C = 0.078, D = 0.107 E = 0.136 and F = 0.165.

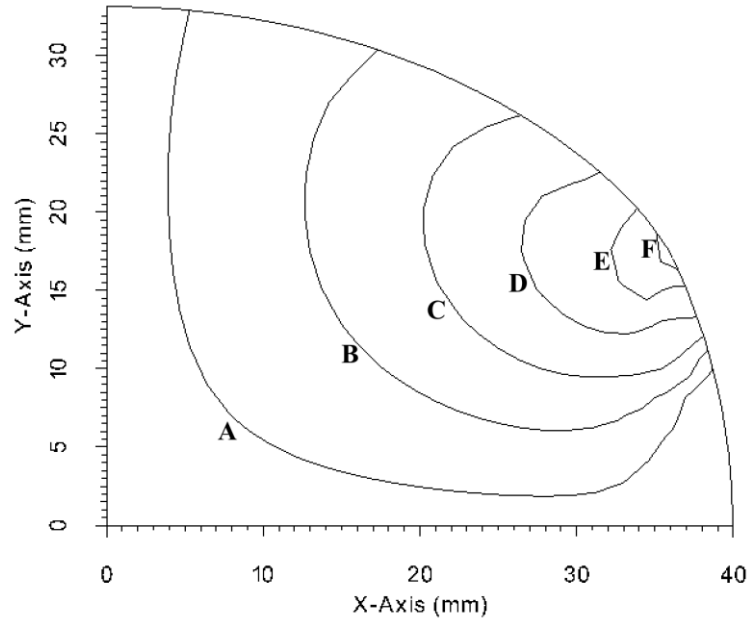

Figure 7.28: ε_{xy} field at the exit of the third rolling stand. The lines represent A = 0.017, B = 0.059, C = 0.100, D = 0.142, E = 0.183 and F = 0.225.

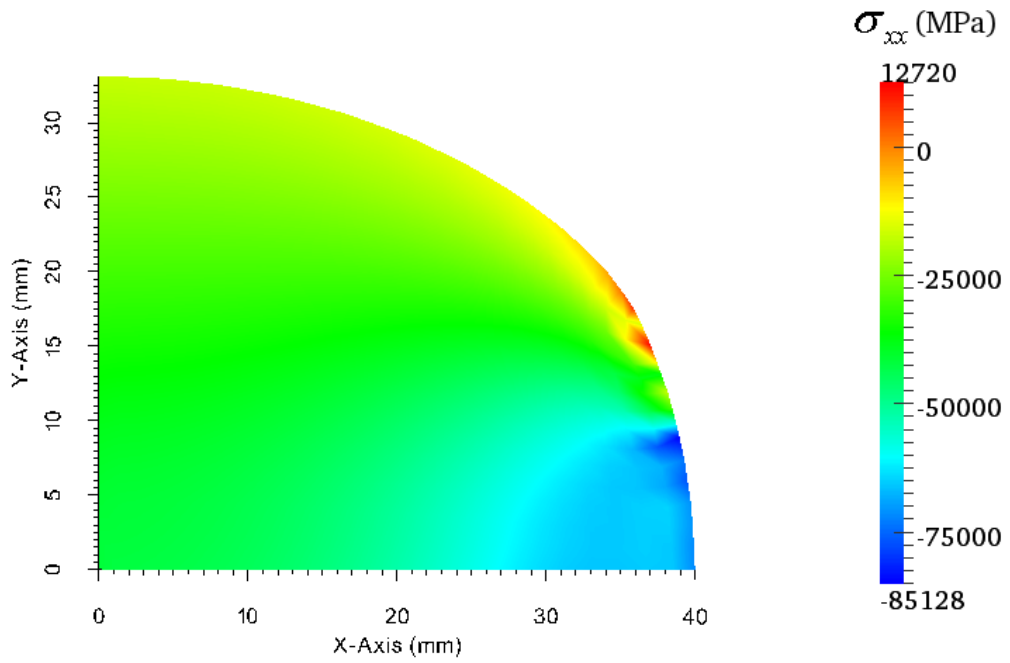

Figure 7.29: σ_{xx} field at the exit of the third rolling stand.

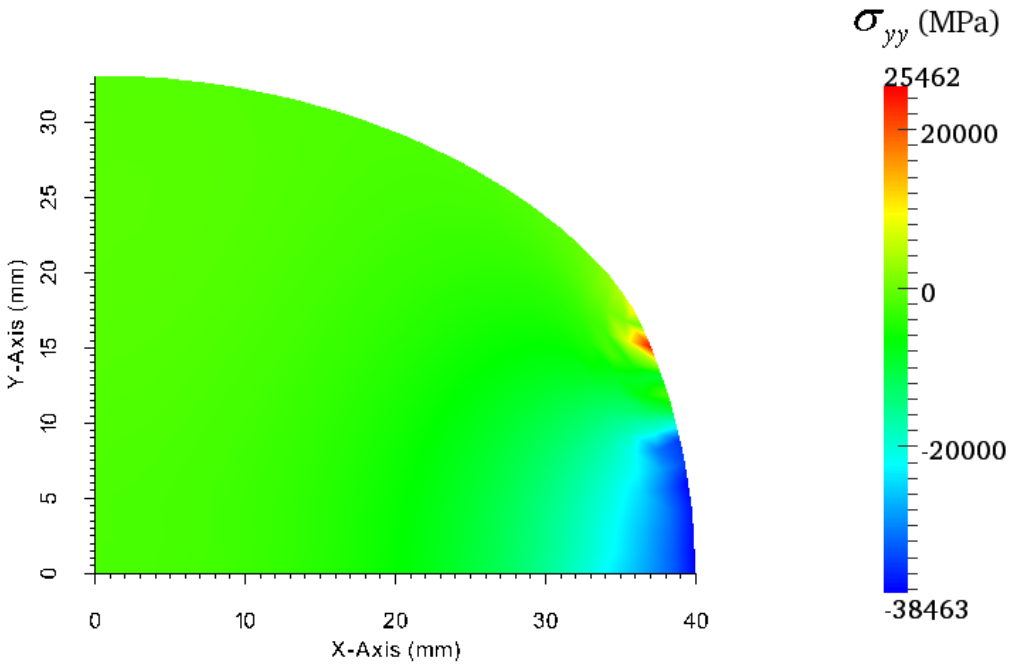

Figure 7.30: σ_{yy} field at the exit of the third rolling stand.

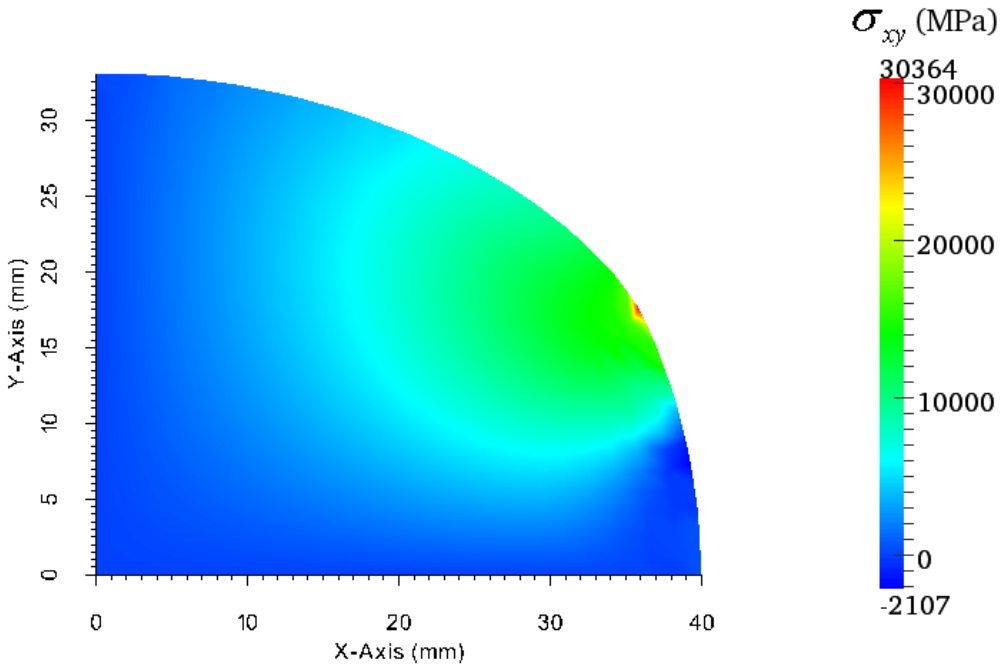

Figure 7.31: σ_{xy} field at the exit of the third rolling stand.

7.5 Thermo-mechanical simulation after the fourth rolling stand

The displacement vectors at the exit of the fourth rolling stand are shown in Figure 7.32. The red lines represent the 17 groove lines which have contacted the slice. Fourth rolling stand is again a horizontal rolling stand. Except Figure 7.32, all the results from the fourth rolling stand are calculated with 435 collocation nodes. Temperature field at the exit from the fourth rolling stand can be seen in shaded and contour graphs in Figures 7.33 and 7.34 respectively. Again the highest temperature drop is across the contacted region and additional cooling around the first contacted region during the first rolling stand can still be seen. The displacement field in contour graph at the exit of the fourth rolling stand can be seen in Figure 7.35. The highest displacement is on the left side of the contact where the contact starts.

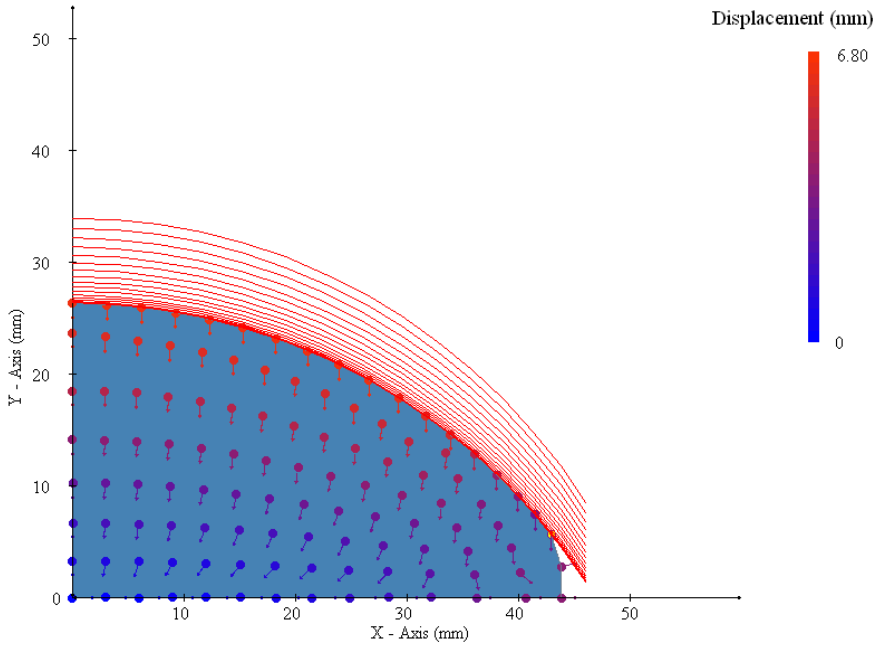

Figure 7.32: Displacement vectors at the exit of the fourth rolling stand with 112 collocation nodes. 17 groove lines represent necessary deformation steps as a consequence of the process.

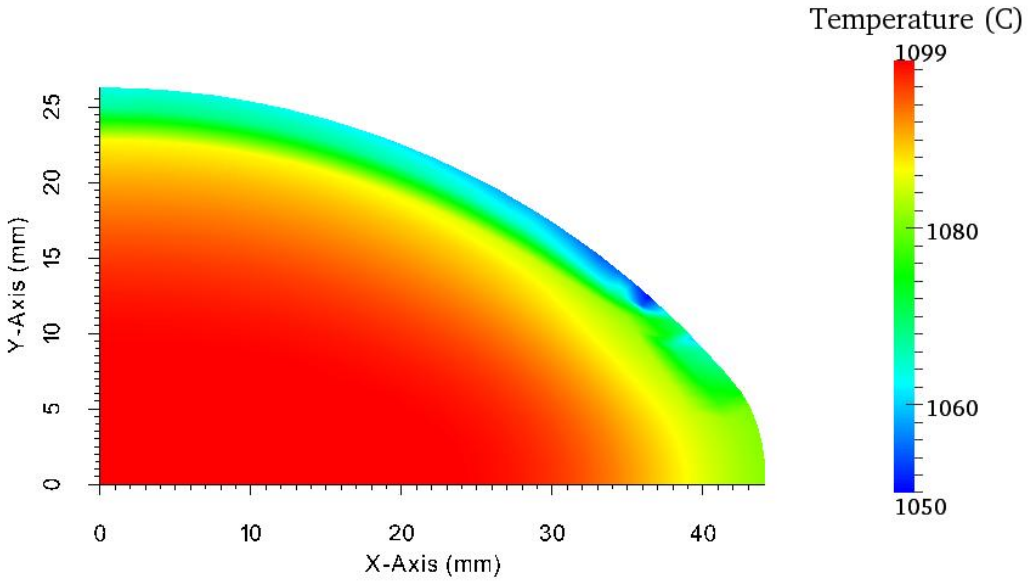

Figure 7.33: Temperature field at the exit of the fourth rolling stand.

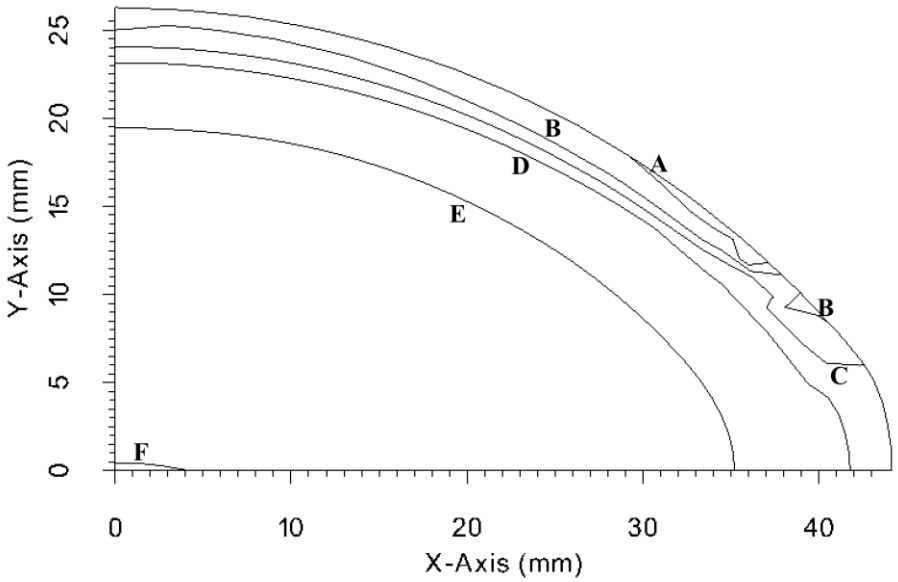

Figure 7.34: Temperature field at the exit of the fourth rolling stand. The lines represent A = 1058.24 °C, B = 1066.58 °C, C = 1074.91 °C, D = 1083.25 °C, E = 1091.58 °C and F = 1099.92 °C.

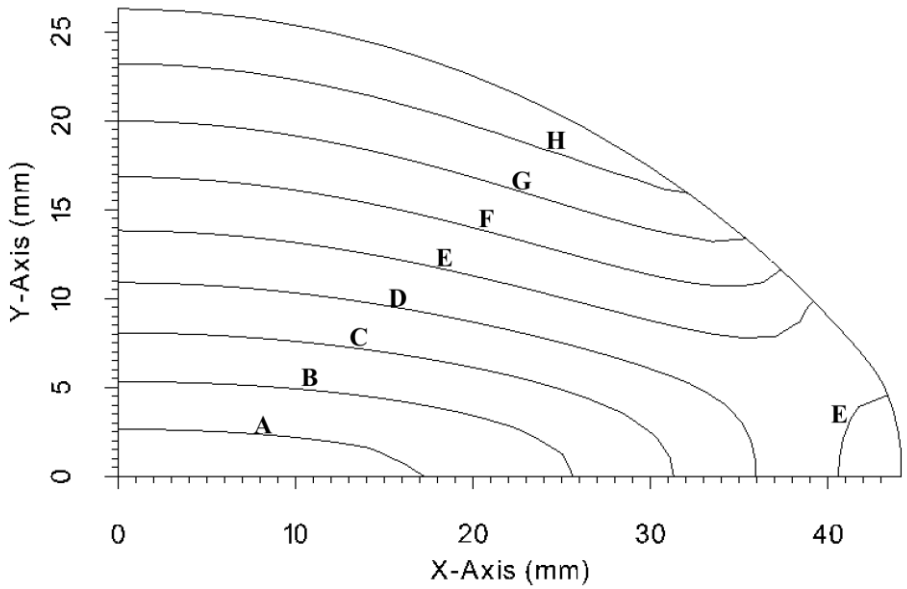

Figure 7.35: Displacement field at the exit of the fourth rolling stand. The lines represent A = 0.77 mm, B = 1.53 mm, C = 2.29 mm, D = 3.06 mm, E = 3.83 mm, F = 4.59 mm, G = 5.36 mm and H = 6.12 mm.

The components of the strain vector $\varepsilon_{xx}, \varepsilon_{yy}, \varepsilon_{xy}$ are shown in contour graphs at the exit of the fourth rolling stand in Figures 7.36, 7.37 and 7.38 respectively. Since the compression of the groove is in $-y$ direction ε_{xx} field gets positive and ε_{yy} field gets negative values. Moreover, the components of the stress vector $\sigma_{xx}, \sigma_{yy}, \sigma_{xy}$ are shown in shaded graphs at the exit of the fourth rolling stand in Figures 7.39, 7.40 and 7.41 respectively. Highest values for σ_{xx} and σ_{yy} occur across the non contacted region. For the shear strain and shear stress, highest values are again near the last contact node.

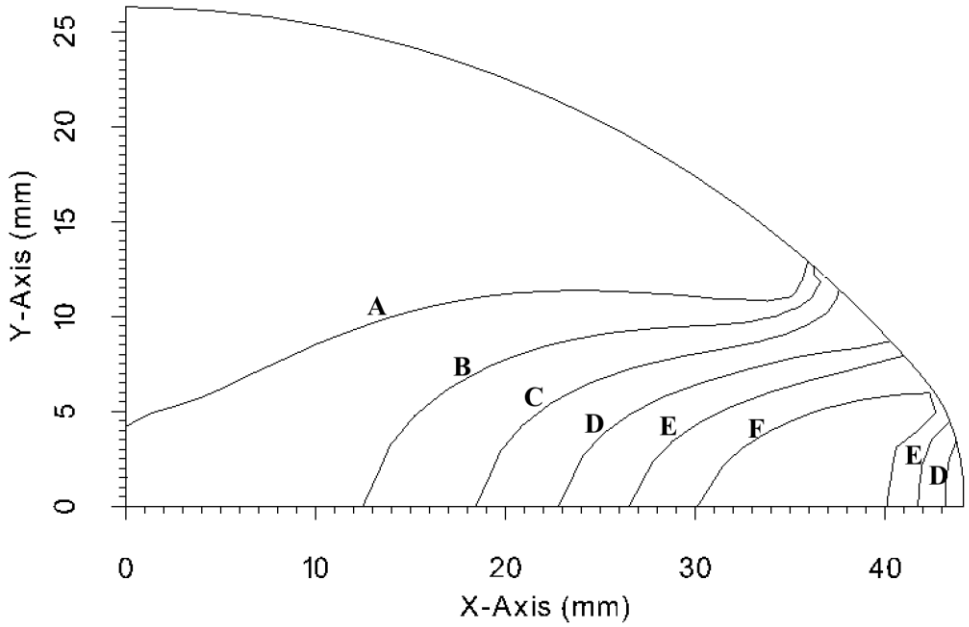

Figure 7.36: ε_{xx} field at the exit of the fourth rolling stand. The lines represent A = 0.028, B = 0.052, C = 0.076, D = 0.101, E = 0.124 and F = 0.148.

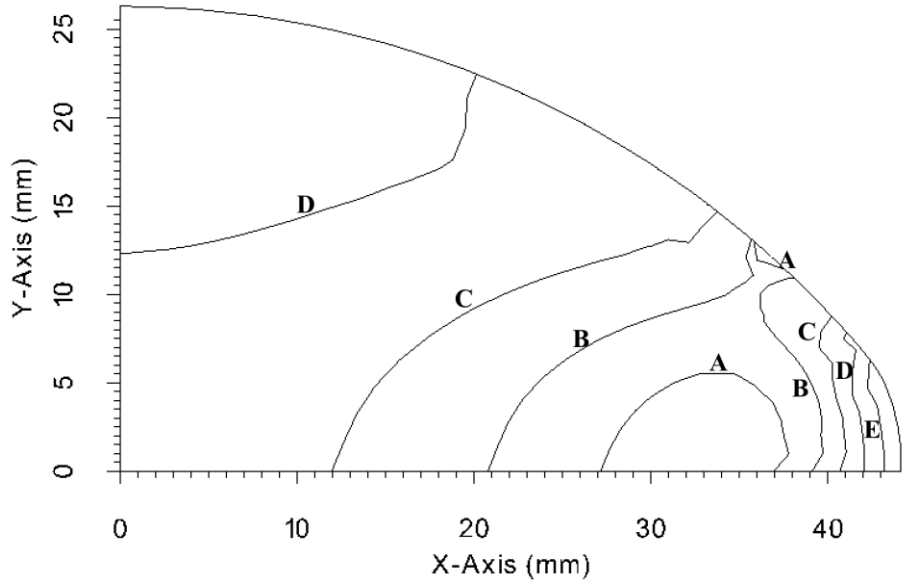

Figure 7.37: ε_{yy} field at the exit of the fourth rolling stand. The lines represent A = -0.423, B = -0.369, C = -0.315, D = -0.262 and E = -0.208.

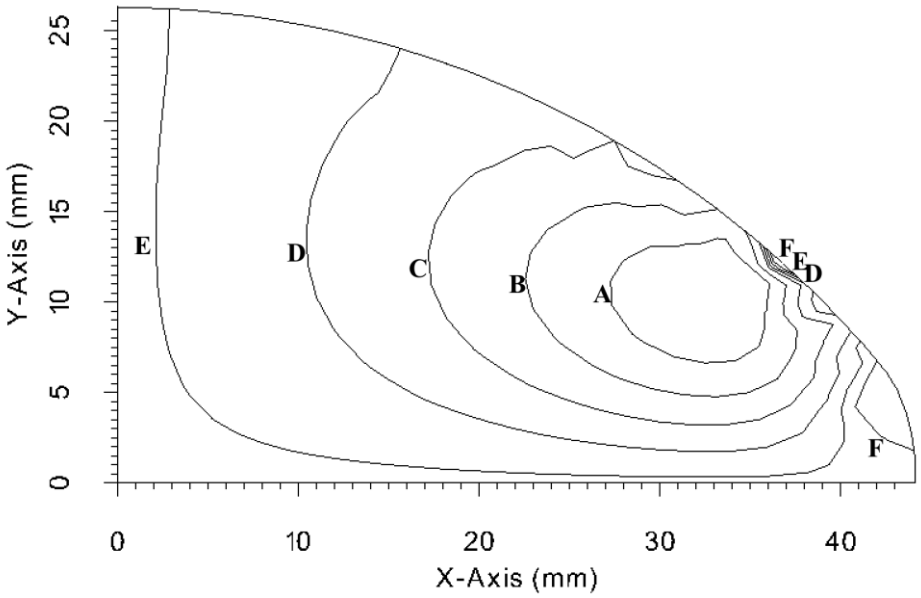

Figure 7.38: ε_{xy} field at the exit of the fourth rolling stand. The lines represent A = -0.100, B = -0.067, C = -0.034, D = -0.002, E = 0.030 and F = 0.063.

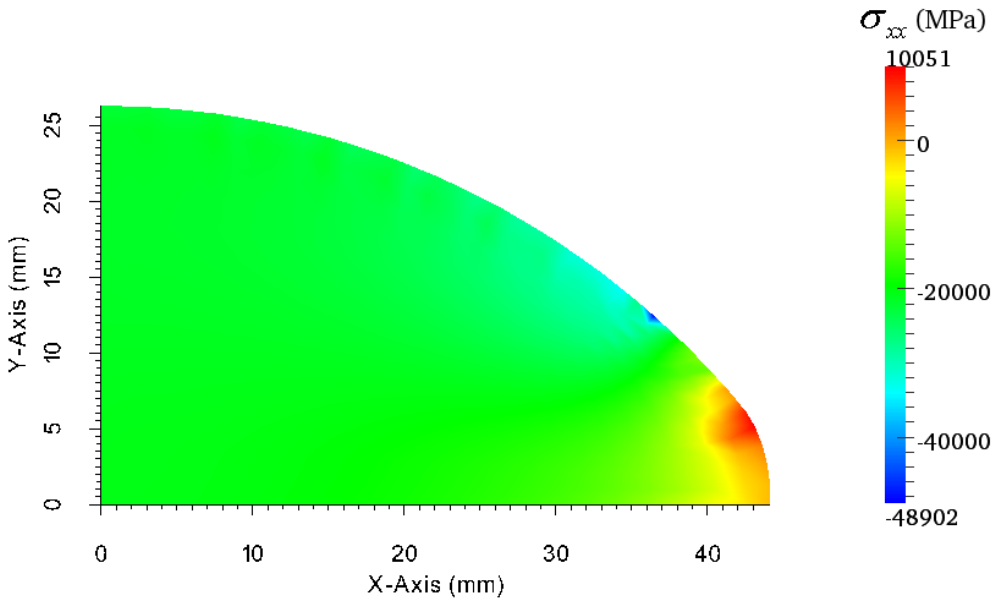

Figure 7.39: σ_{xx} field at the exit of the fourth rolling stand.

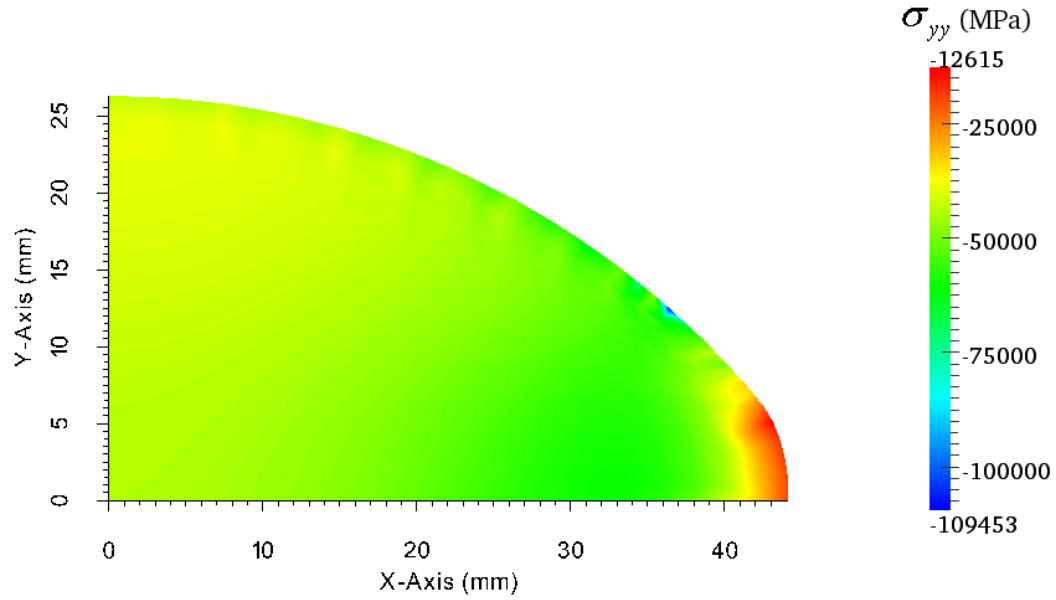

Figure 7.40: σ_{yy} field at the exit of the fourth rolling stand.

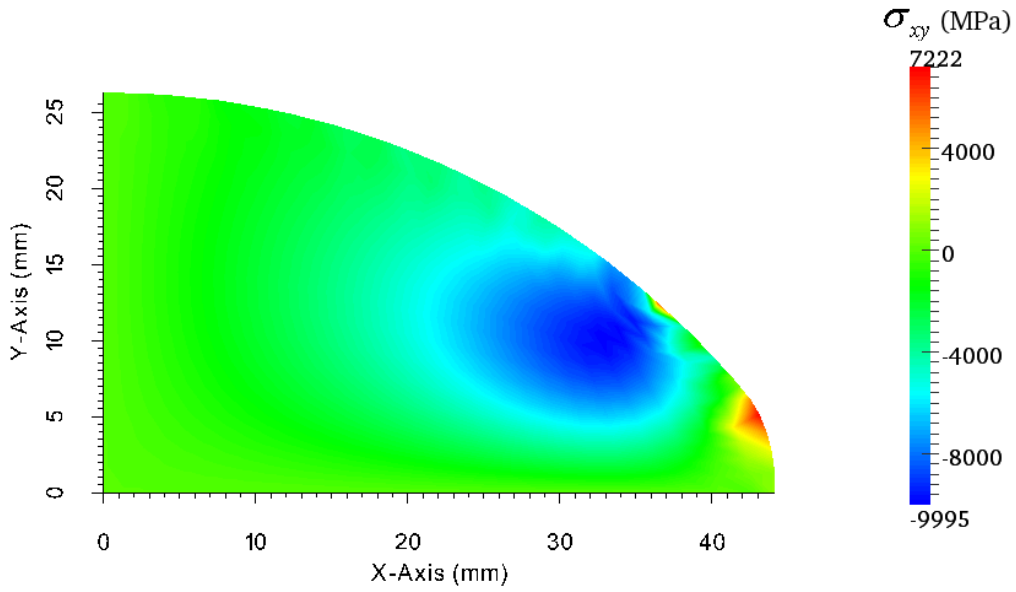

Figure 7.41: σ_{xy} field at the exit of the fourth rolling stand.

7.6 Thermo-mechanical simulation after the fifth rolling stand

The displacement vectors at the exit of the fifth rolling stand are shown in Figure 7.42. The brown lines represent the 23 groove lines which have contacted the slice. Fifth rolling stand is the second vertical rolling stand in the rolling schedule and also the finishing one. Except Figure 7.42, all the results from the fifth rolling stand are calculated with 435 collocation nodes. Temperature field at the exit from the fifth rolling stand can be seen in shaded and contour graphs in Figures 7.43 and 7.44 respectively. The temperature drop is across the contacted region and additional cooling around the first contacted region during the first rolling stand can still be seen. The displacement field in contour graph at the exit of the fifth rolling stand can be seen in Figure 7.45. The highest displacement is bottom of the contact where the contact starts.

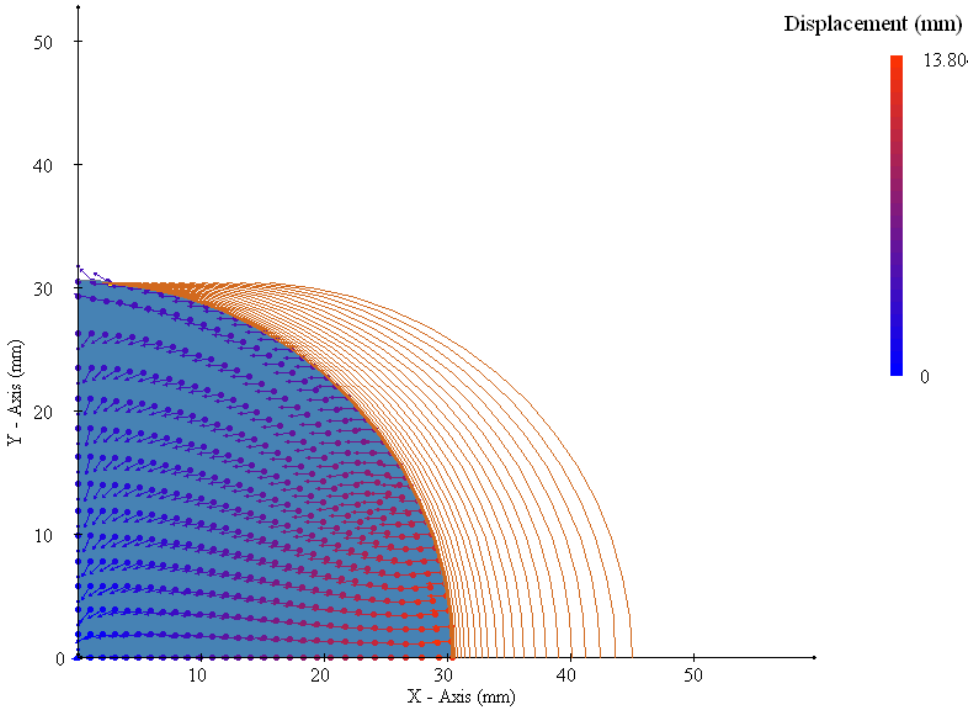

Figure 7.42: Displacement vectors at the exit of the fifth rolling stand. 23 groove lines represent necessary deformation steps as a consequence of the process.

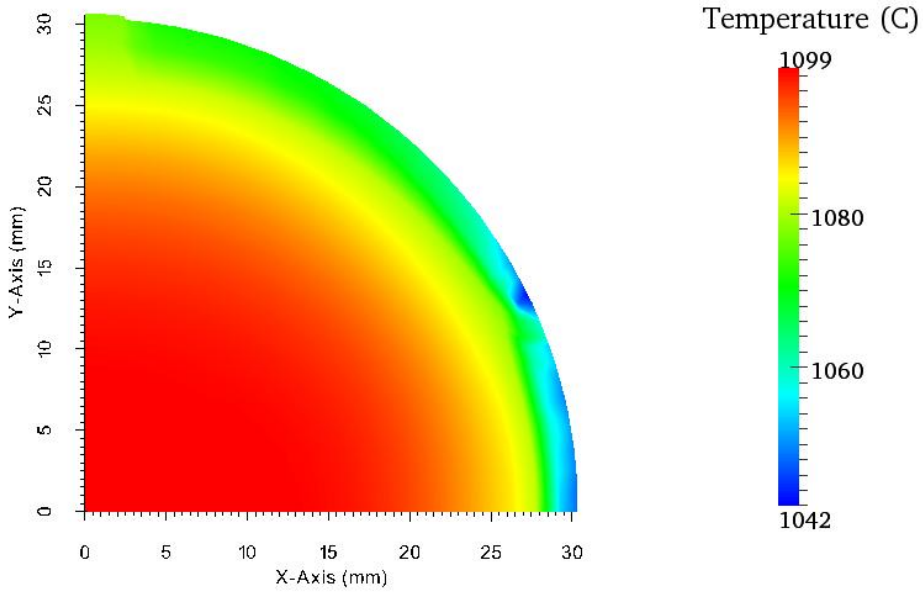

Figure 7.43: Temperature field at the exit of the fifth rolling stand.

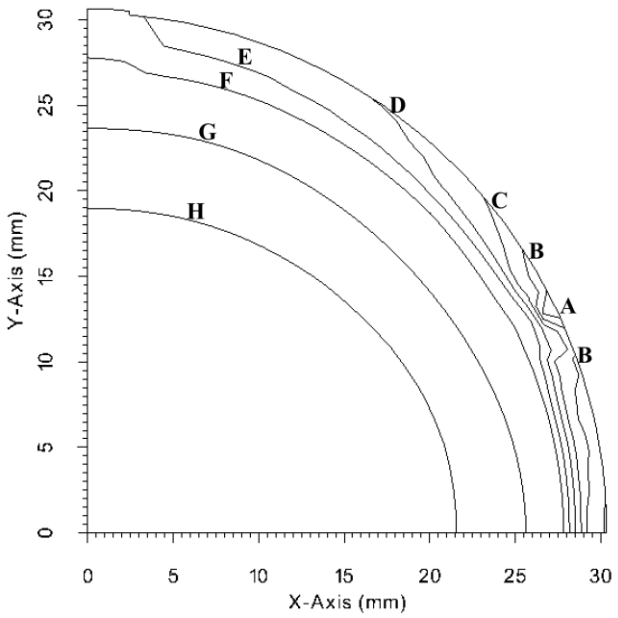

Figure 7.44: Temperature field at the exit of the fifth rolling stand. The lines represent A = 1048.63 °C, B = 1055.02 °C, C = 1061.40 °C, D = 1067.78 °C, E = 1074.17 °C, F = 1080.56 °C and G = 1086.94 °C and H = 1093.32 °C.

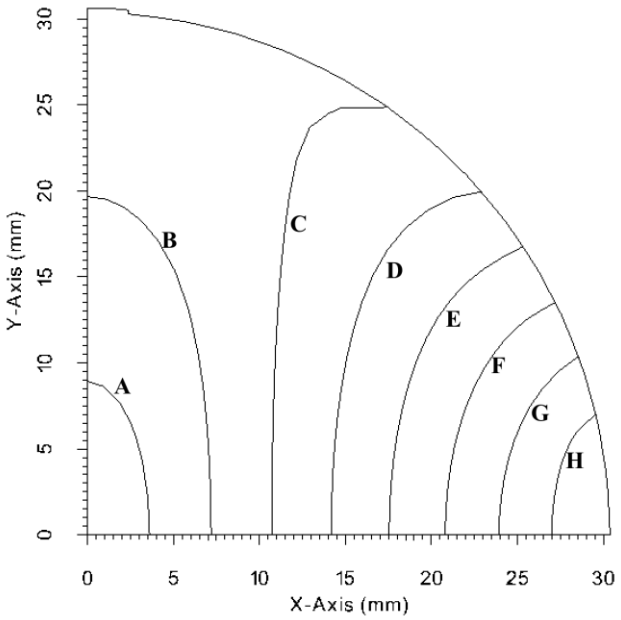

Figure 7.45: Displacement field at the exit of the fifth rolling stand. The lines represent A = 1.53 mm, B = 3.07 mm, C = 4.60 mm, D = 6.13 mm, E = 7.67 mm, F = 9.20 mm, G = 10.74 mm and H = 12.27 mm.

The components of the strain vector $\varepsilon_{xx}, \varepsilon_{yy}, \varepsilon_{xy}$ fields are shown in contour graphs at the exit of the fifth rolling stand in Figures 7.46, 7.47 and 7.48 respectively. Since the compression of the groove is in $-x$ direction ε_{xx} field gets negative and ε_{yy} field gets positive values. Since this rolling stand is the last or finishing rolling stand, almost all the boundary, except the symmetry lines, gets contact with the roll. There is a very small region over the boundary on the top which has no contact and is free to deform, therefore over that region different behaviour of strain and stress fields is observed comparing to rest of the slice. Moreover, the components of the stress vector $\sigma_{xx}, \sigma_{yy}, \sigma_{xy}$ fields are shown in shaded graphs at the exit of the fifth rolling stand in Figures 7.49, 7.50 and 7.51 respectively. Highest values for σ_{xx} and σ_{yy} occur across the non contacted region. For the shear strain and shear stress highest value in magnitude again occurs near the last contact node.

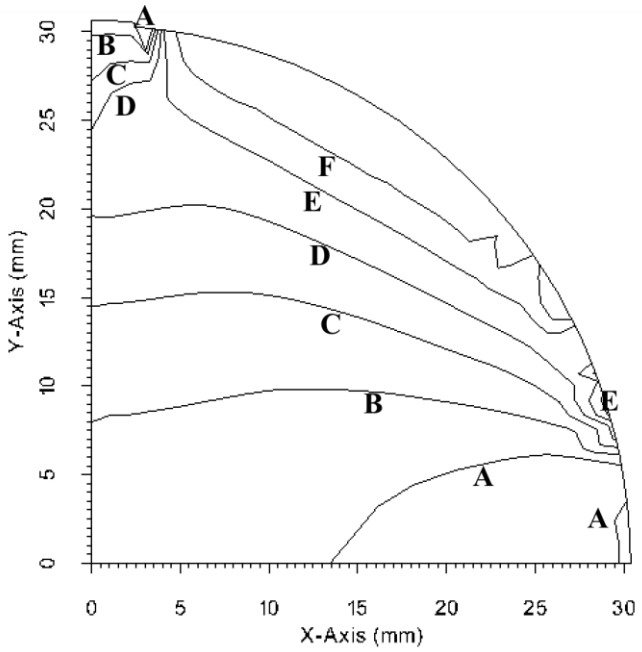

Figure 7.46: ε_{xx} field at the exit of the fifth rolling stand. The lines represent A = -0.45, B = -0.40, C = -0.35, D = -0.30, E = -0.25 and F = -0.20.

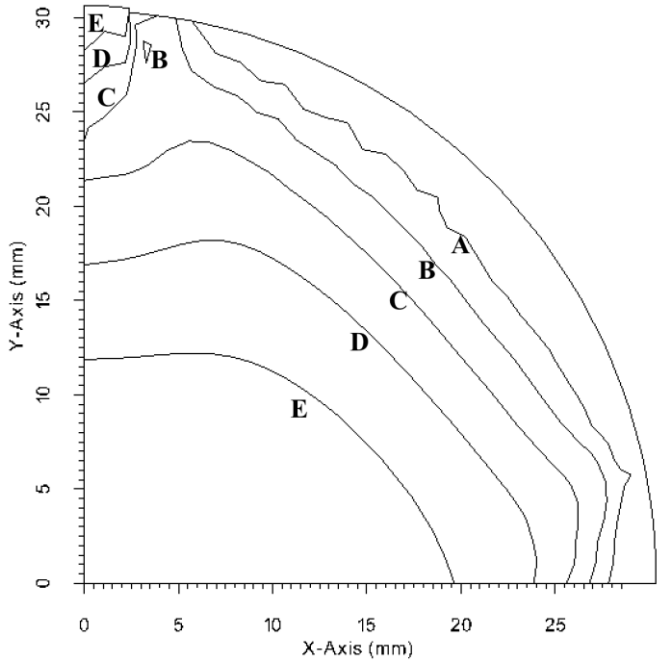

Figure 7.47: ε_{yy} field at the exit of the fifth rolling stand. The lines represent A = 0.060, B = 0.084, C = 0.107, D = 0.130 and E = 0.154.

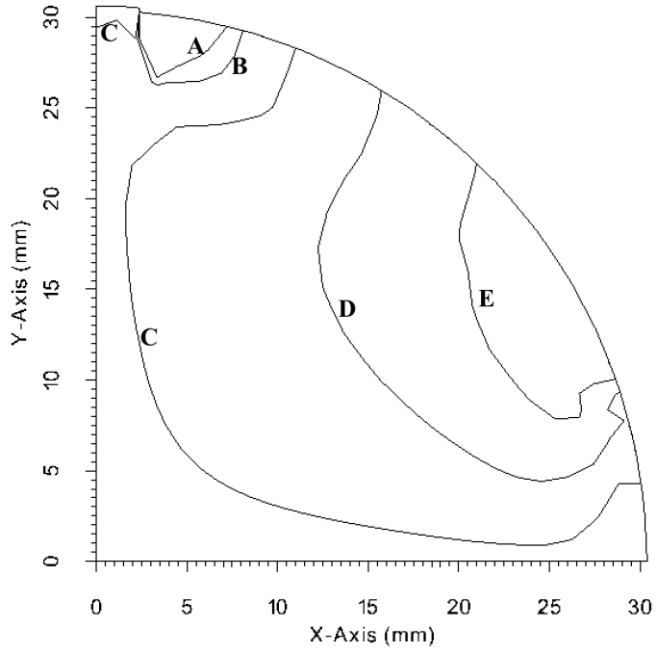

Figure 7.48: ε_{xy} field at the exit of the fifth rolling stand. The lines represent A = -0.065, B = -0.028, C = 0.009, D = 0.047 and E = 0.084.

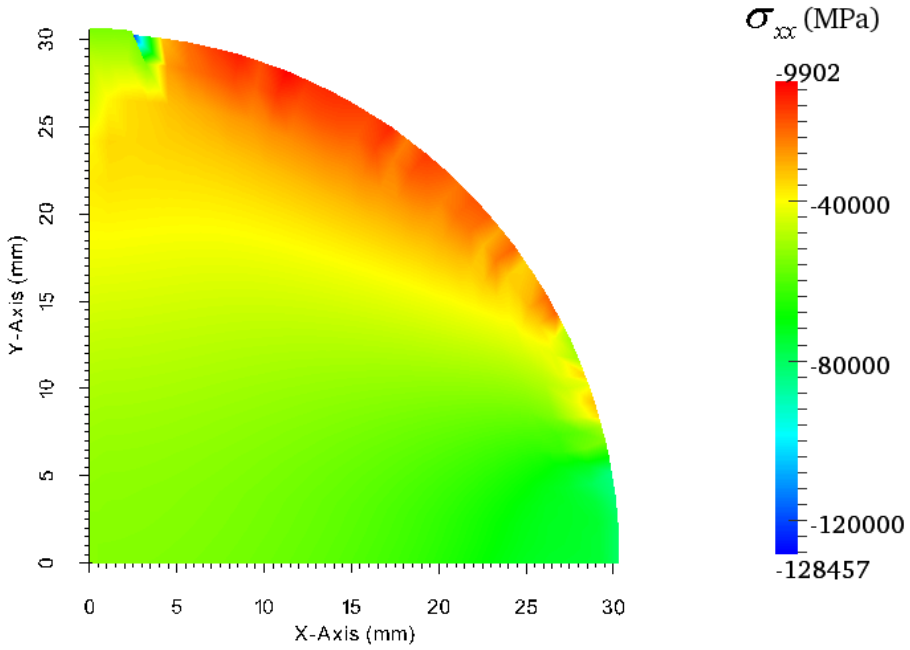

Figure 7.49: σ_{xx} field at the exit of the fifth rolling stand.

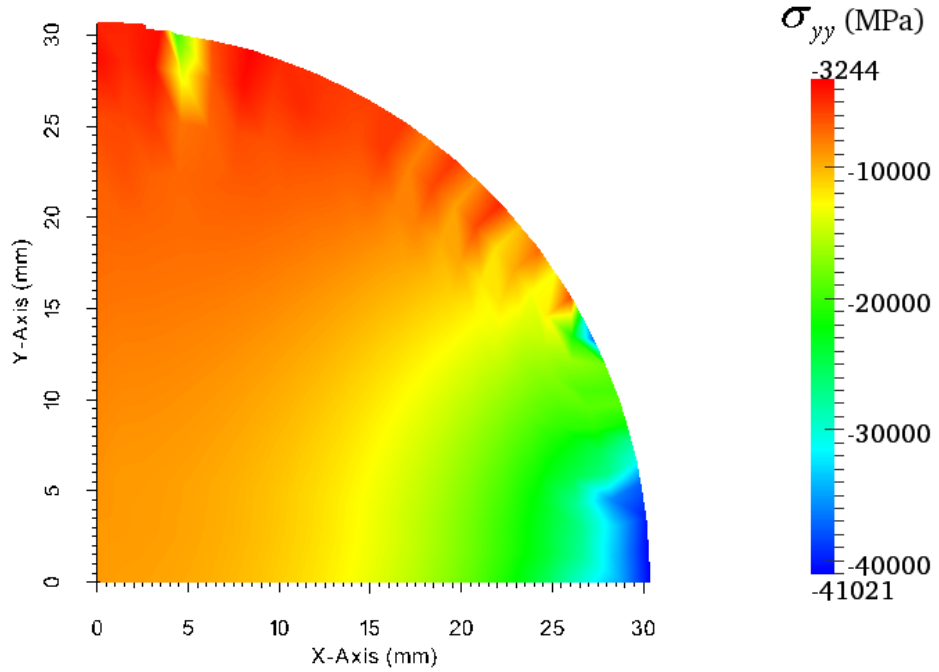

Figure 7.50: σ_{yy} field at the exit of the fifth rolling stand.

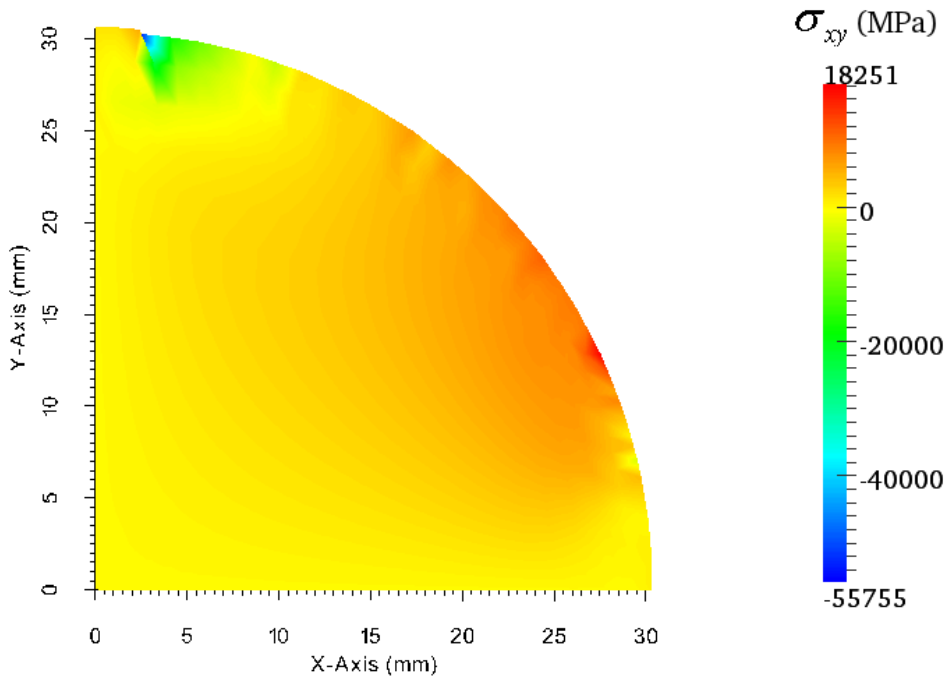

Figure 7.51: σ_{xy} field at the exit of the fifth rolling stand.

At the end of the fifth rolling stand, as expected, a quarter of a cross section of a round bar is achieved. The length on x axis is 30.4 mm and on y axis is 30.6 mm. Overall, the results in this chapter confirm that the configuration of the rolling schedule applied here is capable of producing a round bar with 60 mm diameter. It is important to note that the steel is still very hot even after the rolling and there will be further cooling and shrink until it reaches the room temperature.

7.7 Sensitivity tests of the simulation

In this simulation of rolling 1455 slices are considered over 13 m rolling schedule length and it takes 10.56 s time for the initial slice to come to the end. The previous numerical results of a rolling simulation in this chapter are calculated by LRBFCM and shown for 5 slices which are at the exit of each rolling stand. Up to now, the results were based on one slice at a time. However, in order to have a better understanding of the rolling process, some results could be shown for every slice positions such as average temperature and slice velocity. Moreover, sensitivity studies can be made with increasing or

decreasing some parameters to see their influence. In Figure 7.52, average temperature values of a each slice at different positions are plotted with nominal conditions as in Table 7.2. When the roll temperature is increased to 600 °C from 500 °C the heat loss is reduced and the average temperature is increased. If the heat transfer coefficient between the roll and the slice is increased to 15.000 W/m^2K from 10.000 W/m^2K the heat loss is increased and average temperature is decreased.

Velocity of the slice depends on the geometry of the slice and is plotted in Figure 7.53 for nominal conditions. Slice geometry is calculated through mechanical model which is coupled with thermal so if the temperature values are changed the deformation would differ. In Figure 7.53 the slice velocities are shown. When the slice temperature is kept at 1100 °C, no significant difference is observed comparing to the nominal conditions because during the nominal conditions, temperature drop is around 50 °C and this does not change much elastic material properties of the material therefore it still deforms very similar. However, if the temperature of the slice is kept at 500 °C, then the difference in slice velocity is more and more visible up to the third rolling stand. Due to the increase in the modulus of elasticity of the steel, the amount of the deformation is smaller and velocity of the slice is higher. When passing through the fourth and fifth rolling stands the velocity is again similar to the nominal conditions since those rolling stands have very small roll gap, especially the fifth one. This is also usually why the last rolling stands are called finishing rolling stands where the roll gap is very small and the steel is forced to have the final shape. The same effect can also be seen in Figure 7.53 where the final velocities, therefore the shapes, are almost the same at the end.

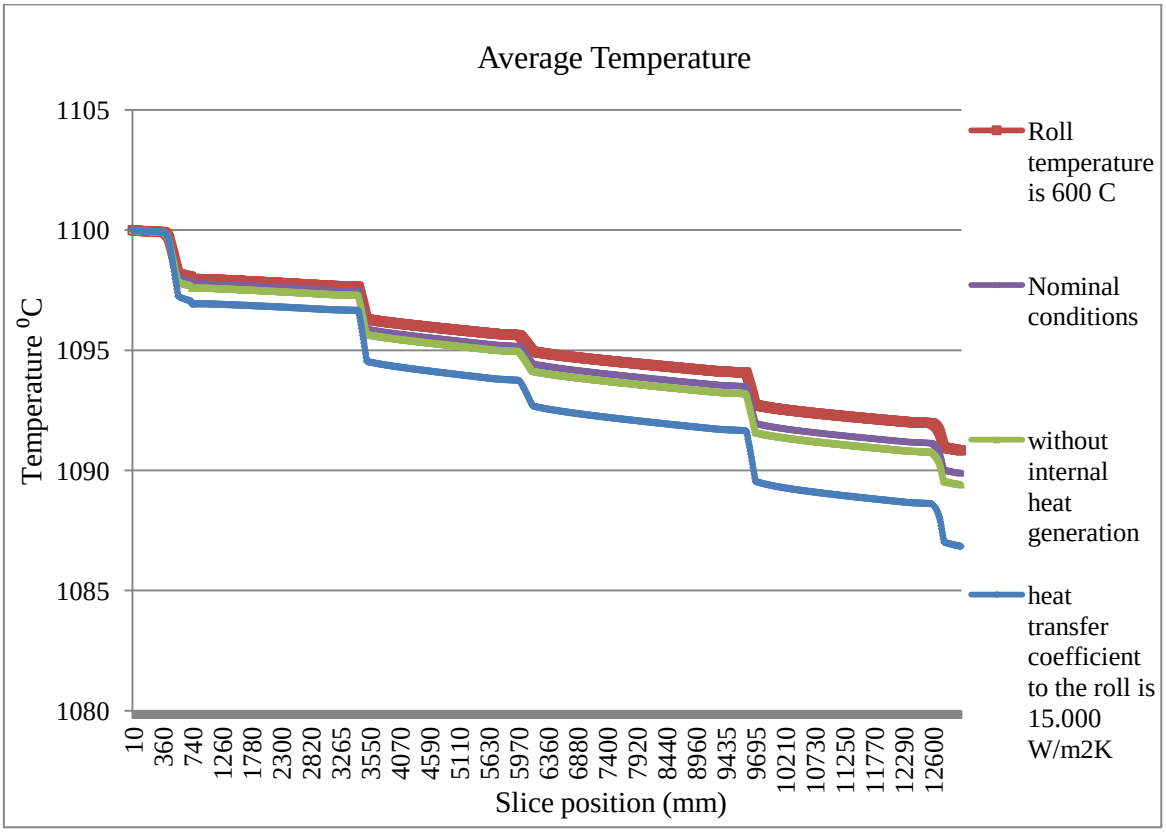

Figure 7.52: Average slice temperatures in °C versus the slice positions towards the rolling direction. Different thermal coefficients used and compared with nominal conditions.

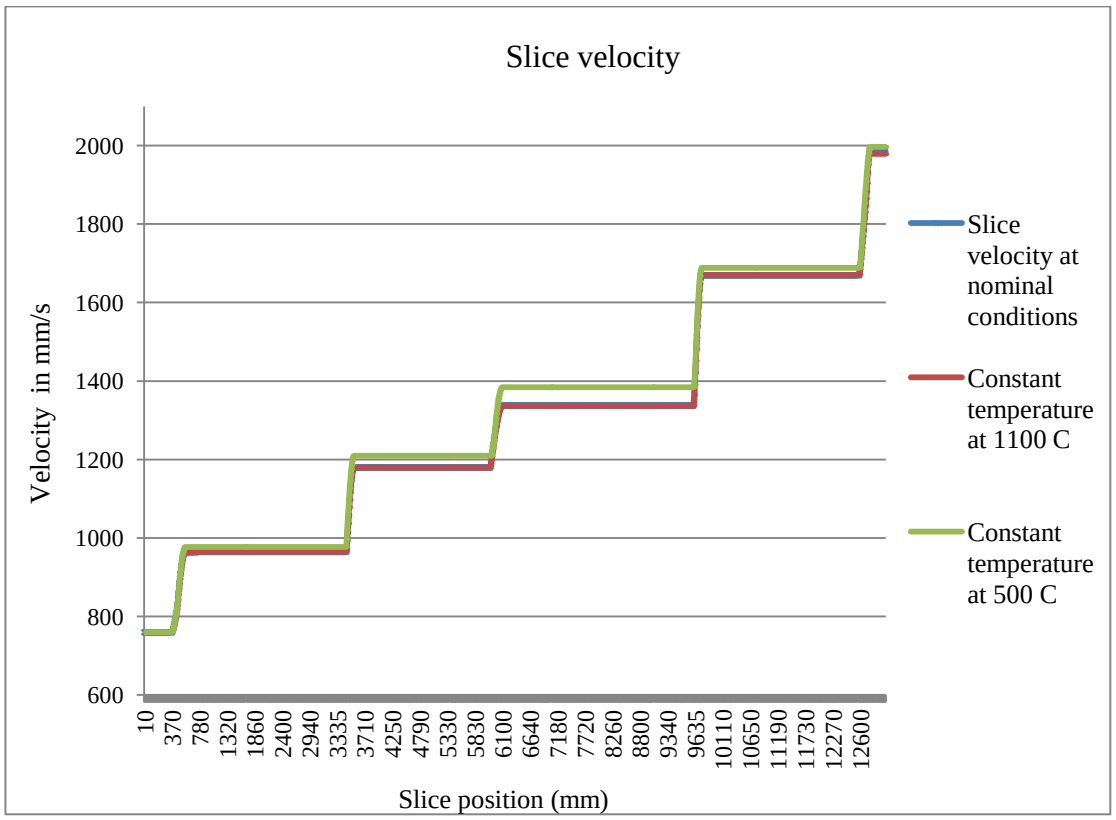

Figure 7.53: Velocity of slices versus the slice positions towards the rolling direction. Different material properties are considered and results based on constant temperature at 1100 °C and nominal conditions almost overlap.

In all the sensitivity tests for the calculation of the slice velocity, the initial slice velocity is used as defined in Table 7.2. If there would be a change in the initial speed, then the same proportional change would be observed in all the calculated velocities of the slice at different positions. Since this is a coupled thermo-mechanical problem, the influence of mechanical parameters is also observed in Figure 7.52 as a result of variation in the thermal parameters.

In this simulation, the numerical results by LRBFCM for a complete rolling schedule are given as well as the sensitivity studies at the end. Once again it is shown here that a meshless method is capable of analysing large deformation problems such as rolling.

8 Conclusion

The concluding remarks are given in chapter 8, which incorporates overview of the performed work, its originality, advantages of the approach used, contributions to science and technology, list of respective publications and suggestions for future work.

8.1 Overview

The main aim of this dissertation is the development of hot rolling process simulation that involves large deformations by a strong-form formulated local meshless solution procedure. A rolling schedule is considered in the example, which has 5 rolling stands in a sequence. During the simulation, a rectangular initial shape turns into a bar at the exit of the fifth rolling. The equations for the thermal and mechanical models are elaborated in Chapter 2 for a 3D model. The mechanical model uses balance of forces per unit volume and the thermal model uses balance of heat fluxes per unit volume. During the simulation of hot shape rolling, natural and essential boundary conditions for the mechanical model, Neumann and Robin boundary conditions for the thermal model are applied. The strong form of the governing equation of the mechanical model is rewritten for a 2D problem. The equation of the mechanical model consists of partial derivatives of stresses, however the stresses have been written in terms of displacements. This replacement is done for three different material behaviours: the linear elastic, the ideally plastic and the slightly compressible ideal plastic material behaviour. The 3D steady convective-diffusive heat transfer equation in thermal model is rewritten in a 2D transient diffusive heat transfer equation form. The thermal model requires partial derivatives of temperatures, including an additional source term, called internal heat generation rate for coupling the thermal and mechanical fields. Also the mechanical model uses temperature values from the thermal model to define the material properties, therefore both models are mutually coupled. The simulation of rolling is done by using

imaginary slices aligned with the rolling direction, when homogenous compression assumption is considered, and discussed in Chapter 3. In the plane strain problem, one slice is calculated at a time so it appears like the same slice has been travelling across the rolling stand until the end of continuous rolling. Therefore, the method is referred as a travelling slice model which makes the description of a mixed Eulerian and Lagrangian type. The slices that represent current crossection of the rolling mill, become computational domains for calculations. The necessary geometrical properties are defined for each groove so that the discrete groove lines can be drawn when the slice is positioned under the roll. If there is a contact, first the deformation (displacements, strains and stresses) is calculated by using the temperatures values from the previous slice. Later, for the same slice, temperature values are calculated by the thermal model including the internal heat generation rate, obtained from the deformation results. In the mechanical model, the displacements in the governing equation are discretized by LRBFCM and replaced as discussed in Chapter 4. Solution is obtained through local system of equations written in a global sparse matrix. For the non-linear behaviour of the material properties, which appears in plastic models, the solution can be obtained by Newton-Raphson iteration method. For the thermal model, the solution is achieved by explicit time stepping by using time discretization. Temperature field is discretized by LRBFCM. Solution is obtained by local discretization of the governing equations.

Large deformation calculations by a local meshless solution procedure require significant amount of attention to the node arrangement. Therefore, in between certain deformation steps, node rearrangement is needed. It is done by ENG and TFI. When the nodes are repositioned, their values are obtained by interpolation from the previous arrangement and node values.

Some predefined tests cases are solved by LRBFCM in Chapter 5 and 6 before the solution procedure is applied to a complete rolling simulation to assess its capabilities. Firstly, one step deformation problems are analyzed and compared with analytical solutions or FEM solutions in Chapter 5. Later, flat and oval rolling examples are analysed and compared with FEM in Chapter 6, where the deformation is analysed in small discrete steps. After satisfactory results of the theoretical tests are achieved, the solution procedure is applied to simulation of hot shape rolling, where the whole deformation is divided into 1455 deformation steps towards the rolling direction. These discrete deformation slices at the exit of the each rolling stand are then analysed in terms of temperature,

displacements, strain and stress components in Chapter 7. The material has coupled thermo-mechanical elastic properties as given in Appendix. It is also assumed that, except for the mechanical energy turning into heat, all the deformation energy has been irreversibly absorbed by the material.

8.2 Performed work

Before applying the thermo-mechanical solution for the simulation of hot shape rolling, predefined test cases are calculated for assessment purposes.

Performed tests cases for the thermal model are:

- Convective cooling
- Internal heat generation

Performed test cases for the mechanical model are:

- Compression-tension examples with prescribed displacements
- Compression-tension examples with prescribed pressure
- Bending of a cantilever beam
- Expansion of a cylindrical tube
- Linear compression-tension
- Bending of a beam by a uniform load
- Ideal plastic deformation example
- Flat rolling example
- Oval rolling example

First 9 examples, explained in Chapter 5, are calculated in one step and excellent agreement with the reference FEM results and analytical solutions has been found. Last two examples, explained in Chapter 6, are done in a stepwise solution procedure, just like during the simulation of hot shape rolling, and again a good agreement has been found with the FEM. When satisfactory results have been achieved for the test cases, a numerical simulation of hot shape rolling has been done by using elastic material properties of 16MnCrS5 steel and realistic rolling data of continuous Siderimpes company constructed Štore Stell rolling mills to simulate a complete rolling sequence. All the results are shown in various graphs after each rolling stand in Chapter 7.

8.3 Originality

LRBFCM is for the first time used for simulating hot shape rolling of steel. Strong formulation is used in the meshless solution of the thermal and mechanical models and both of them are coupled. Overall, a complex incremental deformation system is analyzed in 3D by using 2D imaginary slices. The results are verified by comparison with a weak formulation based FEM code and exact solutions. A unique rolling schedule is used in the simulation. The shape change of the steel from a rectangular prism to a bar is achieved through large deformations during the pass of each rolling stand.

8.4 Expected advantages

Since a fully meshless procedure has been used, it does not require any kind of meshing process, which might cause problems as in FEM. The advantages of using a meshless method over FEM are: it does not depend on node positioning as much as FEM, but FEM dramatically depends on mesh quality, a FEM model is usually overly stiff, which might give less accurate stress results. Meshless method is easier to code, it provides more flexibility in engineering applications, it is more capable of calculating large deformations, it is simple to pre-process, it allows to simply relocate the nodes and it has a high precision. The numerical implementation also lets changing the complexity and the type of the material model easily. In the calculations, a strong formulation is used, so there is no need for cumbersome background cells for integration that are used in the weak formulation. However, in meshless simulations, it might be necessary to suitably rearrange the node positions to be able to continue with the simulation. In this work, an ENG algorithm is used for this purpose, and it is observed that every time it is used, there is a lot of data to be interpolated for the newly positioned node. Therefore, it is critical to decide when it is necessary to use ENG since it should be used as little as possible. Based on the experience while working on the simulation results, the application of renoding is a must in between the rolling stand with the same orientation, such as horizontal - horizontal or vertical - vertical. However a more sound mathematical determination of decision of when the renoding is needed should be derived.

The presented rolling simulation capabilities are be able to simulate a complete hot shape rolling mill. The technological advantages are as follows:

- The design changes such as different groove geometries in a rolling stand can be tested based on the simulation.
- The process parameters such as initial temperature and velocity can be set, based on the simulation.

8.5 Suggestions for future work

In this dissertation, a rolling simulation is performed on the temperature depended elastic material. However, ideal plastic material properties can also be applied to the rolling simulation. A realistic yield stress function taking strain hardening into consideration will be obtained for a specific steel grade and comparison can be done with the real results from the industry. In this way the hot shape rolling simulation might be very useful in practice. During this research, also an ideal plastic material has been implemented in the rolling simulation, but during the Newton-Raphson iteration not always convergent results have been achieved. Therefore, it couldn't be reliably used in the present stage of the development. Shear stress at the boundary with using coefficient of friction may also be applied instead of only sticking boundary conditions. So that transversal slip would be considered.

Also, further research is needed on the number of collocation nodes considered in an influence domain. In this dissertation 5, and 7 nodes are considered and an increase in the accuracy has been achieved as the number increases, when comparing with the analytical solutions in Chapter 5. The free parameter in RBF is always fixed at 32 however, a varying approach based on different equations such as on boundary and governing equations, and on different node arrangements can be applied to improve the accuracy.

An algorithm must be developed to decide automatically when the node repositioning is a necessary in between the deformation steps in order to sustain stability with optimal conditions.

There are also some additional, technologically important rolling parameters to be calculated during the simulation, such as the roll separating force, which is the average pressure over the contact area, multiplied by the area of the contact. Roll torque is another important aspect of rolling and with the angular velocity of the roll, roll power can be calculated. By using angular velocity of the roll, the exact position of neutral point can be determined over the contact. At the neutral

point, the roll's surface velocity is the same as the velocity of the material being rolled towards the rolling direction. Speed of the rolls can also be verified through the simulation.

Macro scale simulations, developed for rolling in the present work will also be in the future coupled with the microstructure deformation models as in [Liu, 2014], in order to have a multiscale analysis of the deformation and an overview on evolution of the microstructure during rolling.

8.6 Publications

The following articles and contributions at international conferences have been published as a consequence of the present dissertation.

HANOGLU, Umut, ISLAM, Siraj, ŠARLER, Božidar. Numerical solution of hot shape rolling of steel. *Materials and Technology*, ISSN 1580-2949, 2011, vol. 45, pp. 545-547. [COBISS.SI ID 2120955].

HANOGLU, Umut, ISLAM, Siraj, ŠARLER, Božidar. Thermo-mechanical analysis of hot shape rolling of steel by a meshless method. *Procedia Engineering*, ISSN 1877-7058, 2011, vol. 10, pp. 3173-3178. [COBISS.SI ID 1958907].

HANOGLU, Umut, ŠARLER, Božidar. Simulation of hot shape rolling of steel in continuous rolling mill by a local radial basis function collocation method. *Computer Modeling in Engineering and Sciences*, 2015 (in review).

HANOGLU, Umut, ŠARLER, Božidar. Local radial basis function collocation method for solving thermo-mechanics of hot shape rolling of steel. In: *Proceedings of the 5th International conference on Computational Methods for Coupled Problems in Science and Engineering*, IDELSON, Sergio (ed.), PAPADRAKAKIS Manolis (ed.), SCHEFLER Bernhard (ed.). 17-19 June 2013, Ibiza, Spain. pp. 116-126. [COBISS.SI ID 2770171].

HANOGLU, Umut, ŠARLER, Božidar. Simulation of hot shape rolling by a meshless method. In: *Book of Abstracts: Proceedings of the 6th European Congress on Computational Methods in Applied Sciences and Engineering (ECCOMAS 2012)*, 10-14 September 2012, Vienna, Austria. Vienna: Vienna University of Technology, 2012, pp. 331. [COBISS.SI ID 2649339].

HANOGLU, Umut, ŠARLER, Božidar. Thermo-mechanical analysis of hot shape rolling of steel by a meshless method. In: *11th International Conference on Mechanical Behaviour of Materials (ICM 11)*, 5-9 June 2011, Lake Como, Italy. GUAGLIANO mario (ed.), VERGANI Laura (ed.), 2012 pp. 81 [COBISS.SI ID1959163].

HANOGLU, Umut, ŠARLER, Božidar. Solution of hot shape rolling by the local radial basis function collocation method. In: *Advances in Computational & Experimental Engineering and Sciences : proceedings of ICCES '10*, 28 March – 1 April 2010, Las Vegas, USA. PEPPER, Darrell W. (ed.), ATLURI, Satya N. (ed.), 2010. pp. 703. [COBISS.SI ID 1616891].

HANOGLU, Umut, ISLAM, Siraj, ŠARLER, Božidar. Solution of hot shape rolling by the local radial basis function collocation method. *11th International Conference on Boundary Element Techiques*, 12-14 July 2010, Berlin, Germany. ZHANG Chuanzeng (ed.), ALIABADI M. H. Ferri (ed.), SCHANZ Martin (ed.). 2010, pp. 406-411. [COBISS.SI ID 1541115].

HANOGLU, Umut, ISLAM, Siraj, ŠARLER, Božidar. Solution of hot shape rolling of steel. In: *18th Conference on Materials and Technology*, 15-17 November 2010, Potorož, Slovenia. JENKO, Monika (Ed.), et al. *Program and book of abstracts*. Ljubljana: Institute of Metals and Technology, 2010, pp. 46. [COBISS.SI ID 1761787].

Appendix

Temperature (°C)	Young's modulus (GPa)	Poisson's ratio	Temperature (°C)	Young's modulus (GPa)	Poisson's ratio
1250	85.22943	0.36203	630	156.26	0.30882
1240	86.25066	0.36146	620	157.6183	0.30847
1230	87.27053	0.3609	610	158.9659	0.30812
1220	88.28902	0.36033	600	160.3023	0.30777
1210	89.30615	0.35976	590	161.6272	0.30742
1200	90.32191	0.35919	580	162.9405	0.30707
1190	91.3363	0.35862	570	164.2386	0.30672
1180	92.34934	0.35805	560	165.5244	0.30637
1170	93.36101	0.35748	550	166.7976	0.30602
1160	94.37132	0.35691	540	168.0579	0.30567
1150	95.38027	0.35634	530	169.3049	0.30532
1140	96.38786	0.35577	520	170.5384	0.30497
1130	97.39409	0.3552	510	171.7581	0.30462
1120	98.39897	0.35463	500	172.9635	0.30427
1100	99.40249	0.35407	490	174.1544	0.30392
1090	100.4047	0.3535	480	175.3305	0.30357
1080	101.4055	0.35293	470	176.4915	0.30322
1070	102.4049	0.35236	460	177.646	0.30286
1060	103.403	0.35179	450	178.8045	0.30248
1050	104.3998	0.35122	440	179.9462	0.3021
1040	105.3952	0.35065	430	181.0711	0.30172
1030	106.3893	0.35008	420	182.1786	0.30134
1020	107.382	0.34951	410	183.2687	0.30096
1010	108.3733	0.34894	400	184.3409	0.30058
1000	109.3633	0.34837	390	185.395	0.3002
990	110.352	0.3478	380	186.4308	0.29983
980	111.3393	0.34723	370	187.448	0.29945
970	112.3252	0.34666	360	188.4465	0.29908
960	113.3098	0.34609	350	189.4259	0.2987
950	114.2931	0.34553	340	190.3867	0.29833
940	115.275	0.34496	330	191.3322	0.29797
930	116.2555	0.34439	320	192.258	0.29761
920	117.2347	0.34382	310	193.1638	0.29724
920	118.2126	0.34325	300	194.0477	0.29688
910	119.1891	0.34268	290	194.9135	0.29652
900	120.1642	0.34211	280	195.7589	0.29616

890	121.138	0.34154	270	196.584	0.2958
880	122.1105	0.34097	260	197.3885	0.29545
870	123.0816	0.3404	250	198.1534	0.29509
860	124.0642	0.33983	240	198.9169	0.29473
850	125.0506	0.33926	230	199.6654	0.29437
840	126.0342	0.33868	220	200.392	0.29402
830	127.0152	0.33811	210	201.0972	0.29366
820	127.9937	0.33754	200	201.7815	0.2933
810	128.9845	0.3369	190	202.4451	0.29295
800	129.9864	0.33618	180	203.0883	0.29259
790	130.9835	0.33547	170	203.7114	0.29224
780	131.9758	0.33477	160	204.3148	0.29188
770	132.9637	0.33408	150	204.8988	0.29153
760	133.9472	0.33339	140	205.4639	0.29117
750	134.9266	0.3327	130	206.0106	0.29082
740	136.0903	0.33146	120	206.5397	0.29046
730	139.6362	0.32166	110	207.0517	0.29011
720	143.037	0.31358	100	207.5477	0.28975
710	145.048	0.31163	90	208.0285	0.2894
700	146.4786	0.31128	80	208.4952	0.28905
690	147.9026	0.31092	70	208.9492	0.28869
680	149.3186	0.31057	60	209.3919	0.28834
670	150.7258	0.31022	50	209.825	0.28799
660	152.1239	0.30987	40	210.2504	0.28763
650	153.5124	0.30952	30	210.6704	0.28728
640	154.8913	0.30917	-	-	-

Table A.1: Elastic material properties for 16MnCrS5 steel for corresponding temperature values used in hot shape rolling simulation.

Bibliography

Atluri, S. N. (2004). *The Meshless Method (MLPG) for Domain & BIE Discretizations.* Tech Science Press, Encino.

Atluri, S. N. and Shen, S. (2002). *The Meshless Method.* Tech Science Press, Encino.

Avitsur, B. (1968). *Metal Forming: Process and Analysis,* McGraw-Hill, New York.

Batra, R. C. and Zhang, G. M. (2007). SSPH basis functions for meshless methods, and comparison of solutions with strong and weak formulations, *Computational Mechanics,* 41:527-545.

Beese, J. G. (1980). Nomograms for predicting the spread of hot rolled slabs. *AISE Yearly Proceedings,* 360-363.

Belinski, R. A. (1999). *An Analysis, Design, and Improvement Methodology for Shape Rolling Processes and Procedure for the Compensation of Dies.* PhD Thesis, Ohio University, Department of Mechanical Engineering.

Buhmann, M. (2003). *Radial Basis Functions - Theory and Implementations.* Cambridge University Press, Cambridge.

Chen, Y., Lee, J. and Eskandarian, A. (2006). *Meshfree Methods in Solid Mechanics*. Springer Verlag, Berlin.

Chen, J. S., Roque, C., Pan, C. and Button, S. T. (1998). Analysis of metal forming process based on meshless method. *Journal of Materials Processing Technology,* 80:642-646.

Chen, W., Fu, Z. J. and Chen, C. S. (2013). *Recent Advances in Radial Basis Function Collocation Methods*. Springer Verlag, Berlin.

Chen, W. F. and Han, D. J. (1998). *Plasticity for Structural Engineers,* Springer-Verlag, New York.

DEFORM. (2009). Scientific Forming Technologies Corporation, Version 10.1, http://www.deform.com.

El-Kalay, A.H.E.H.A. and Sparling, L.G.M. (1968). Factors affecting friction and their effect upon load, torque and spread in hot flat rolling. *Journal of the Iron and Steel Institude*, 206:152-163.

Fasshauer, G. E. (2007). *Meshfree Approximation Methods with Matlab Interdisciplinary Mathematical Sciences – Vol. 6.* World Scientific Publishers, Singapore.

Franke, R. (1982). Scattered data interpolation: Test of some methods. *Mathematics of Computation*, 38:181-200.

Fung, Y. C. and Tong, P. (2001). *Classical and Computational Solid Mechanics*. World Scientific Publishing, Singapore.

Ginzburg, V. B. (1993). *High-Quality Steel Rolling: Theory and Practice*, M. Dekker, New York.

Glowacki, M. (1990). Thermal-mechanical model of rolling of shapes in a 4-roll grooves, *Metal Odlew*, 16:541-562.

Glowacki, M. (2005). The mathematical modelling of thermo-mechanical processing of steel during multi-pass shape rolling. *Journal of Material Processing Technology*, 168:336-343.

Glowacki, M., Dyja, H. and Lesik, L. N. (1995). Finite element simulation and experimental analysis of rolling of bimetallic rods. *Proceedings of the 5th International Conference on Numerical Methods in Industrial Forming Processes*, New York, USA, June 12-21, 915-918.

Glowacki, M., Kedzierski, Z., Kusiak, H., Madej, W. and Pietrzyk, M. (1992). Simulation of metal flow, heat transfer and structure evolution during hot rolling square-oval-square series. *Journal of Materials Processing Technology*, 34:509-516.

Guan, Y., Zhao, G., Wu, X. and Lu, P. (2007). Massive metal forming process simulation based on rigid/visco-plastic elemtn free Galerkin method. *Journal of Materials Processing Technology*, 187-188:412-416.

Gu, Y. T. and G. R. Liu (2001). A local point interpolation method for static and dynamic analysis of thin beams. *Computer Methods in Applied Mechanics and Engineering,* 190:5515-5528.

Guo, Y., Nakanishi, K. and Yokouchi, Y. (2005). A nonlinear rigid-plastic analysis for metal forming problem using the rigid-plastic point collocation method. *Advances in Engineering Software,* 36:234-242.

Guo, Y. and Nakanishi, K. (2003). A backward extrusion analysis by the rigid-plastic integralless meshless method. *Journal of Materials Processing Technology,* 140:19-24.

Hanoglu, U., Islam, S. and Šarler, B. (2011). Thermo-mechanical analysis of hot shape rolling of steel by a meshless method, *Procedia Engineering,* 10:3173-3178.

Hanoglu, U. and Šarler, B. (2013). Local radial basis function collocation method for solving thermo-mechanics of hot shape rolling of steel. *5th International conference on Computational Methods for Coupled Problems in Science and Engineering*, Ibiza, Spain, June 17-19.

Helmi, A. and Alexander, J. M. (1968). Geometric factors affecting spread in hot flat rolling of steel. *Journal of the Iron and Steel Institute,* 206:1110-1117.

Hitchcock, J. H. (1935). Roll neck bearings. *ASME Research Publication*.

Hsiang, S. and Lin, S. (2000). Application of 3D FEM-slab Method to Shape Rolling. *International Journal of Mechanical Sciences*, 43:1155-1177.

HSMM. (2008). Integ process group Inc., Version 6.4.0, http://www.integpg.com/hsmm/optimization_models.aspx.

Hu, W., Yao, L. G. and Hua Z. Z. (2006). Parallel Point Interpolation Method for Three-Dimensional Metal Forming Simulation, *Engineering Analysis with Boundary Elements*, 31:326-342.

Huang, G. Cruse, T. A. (1994). On the non-singular traction-BIE in elasticity. *International Journal of Numerical Methods in Engineering*. 37: 2041-2072.

Jiang, Z. Y., Tieu, A. K., Zhang, X. M. Lu, C. and Sun W. H. (2003). Finite element simulation of cold rolling of thin strip. *Journal of Materials Processing Technology*, 140:542-547.

Kee, B. B. T., Liu, G. R. and Lu, C. (2008). A least-square radial point collocation method for adaptive analysis in linear elasticity, *Engineering Analysis with Boundary Elements*, 32:440-460.

Kee, B. B. T., Liu, G. R. and Lu, C. (2007). A regularized least-square radial point collocation method (RLS-RPCM) for adaptive analysis, *Computational Mechanics*, 40:837-853.

Kee, B. B. T., Liu, G. R., Zhang, G. Y. and Lu, C. (2008). A residual based error estimator using radial basis functions, *Finite Elements in Analysis and Design*, 44:631-645.

Kleiber, M. (1998). *Handbook of Computational Solid Mechanics. Survey and Comparison of Contemporary Methods*. Springer, Berlin.

Kosec, G and Šarler, B. (2009). Convection Driven Melting of Anisotropic Metals. *International Journal of Cast Metals Research,* 22:279-282.

Kosec, G and Šarler, B. (2014). Simulation of macrosegregation with mesosegregates in binary metallic casts by a meshless method. *Engineering Analysis with Boundary Elements*, 45:36-44.

Kwon, K. C. and Youn, S. K. (2006). The least-squares meshfree method for rigid-plasticity with frictional contact. *International Journal of Solids and Structures*, 43:7450-7481.

Lai, M., Krempl, E. and Ruben, D. (2010). *Introduction to Continuum Mechanics*, Elsevier, Burlington.

Lee, C. H. and Kobayashi, S. (1973). New solutions to rigid plastic deformation problems using a matrix method. *Journal of Engineering for Industry-Transactions of the ASME*. 95:865-873.

Lenard, J. G. (2007). *Primer on Flat Rolling*, Elsevier, Amsterdam.

Lenard, J.G., Pietrzyk, M., and Cser, L. (1999). *Mathematical and Physical Simulation of the Properties of Hot Rolled Products*, Elsevier, Amsterdam.

Li, H. and Mulay, S. S. (2013). *Meshfree Methods and Their Numerical Properties*. CRC Press, Boca Raton.

Li, S. and Liu, W. K. (2004). *Meshfree Particle Methods*. Springer Verlag, Berlin.

Libersky, L. D. and Petschek, A. G. (1991). Smooth particle hydrodynamics with strength of materials. *Proceedings of The next Free Lagrange Conference*, Moran, USA, June 3-7.

Liu, G. R. (2003). *Mesh Free Methods*, CRC Press, Boca Raton.

Liu, G. R., Kee, B. B. T., Zhong, Z. H., Li, G. Y. and Han, X. (2007). Adaptive meshfree methods using local nodes and radial basis functions, *Proceedings of Enhancement and Promotion of Computational Methods in Engineering and Science*, Sanya, Hainana, China, August 21-23, 71-86.

Liu, G. R. and Gu, Y. T. (2005). *An Introduction to Meshfree Methods and Their Programming.* Springer, Dordrecht.

Liu, G. R. and Gu, Y. T. (2001a). A local radial point interpolation method (LR-PIM) for free vibration analyses of 2-D solids. *Journal of Sound and Vibration*, 246:29-46.

Liu, G. R. and Gu, Y. T. (2001c). A local point interpolation method for stress analysis of two-dimensional solids. *Structural Engineering and Mechanics*, 11(2):221-236.

Liu, G. R. and Gu, Y. T. (2001d). A point interpolation method for two dimensional solid. *International Journal for Numerical Methods in Engineering*, 50:937-951.

Liu, G. R. and Gu, Y. T. (2002). Comparisons of two meshfree local point interpolation methods for structural analyses. *Computational Mechanics*, 29:107–121.

Liu, G. R., Zhang, G. Y., Wang, Y. Y., Zhong, Z. H., Li, G. Y. and Han, X. (2007). A nodal integration technique for meshfree radial point interpolation method (NI-RPIM). *International Journal of Solids and Structures*, 44:3840-3860.

Liu, Q. G. and Šarler, B. (2014). Non-singular method of fundamental solutions for two-dimensional isotropic elasticity problems. *Computer Modeling in Engineering & Sciences.* 91:235-266.

Liu, X., Liu, G. R., Tai, K. and Lam, K. Y. (2005) Radial point interpolation collocation method for the solution of nonlinear Poisson problems. *Computational Mechanics*, 36:298-306.

Liu, W. K., Jun, S. and Zhang, Y. F. (1995). Reproducing kernel particle methods. *International Journal for Numerical Methods in Fluids*, 20:1081-1106.

Lucy, L. B. (1977). A numerical approach to the testing of the fission hypothesis, *Astronautical Jurnal*, 82:1013-1024.

Marcel, P. V. and King, L. P. (1967). Elastic-plastic analysis of two-dimensional stress systems by the finite element method, *International Journal of Mechanical Sciences*, 9:143-155.

Math.Net Iridium. (2008). Free Software Foundation Inc, http://www.mathdotnet.com.

Microsoft Visual C#. (2007). Microsoft Corporation, Visual studio 2008 version 9.0.30729.1 SP, http://msdn.microsoft.com.

McCrum, A. W. (1956). Progress report on the experimental investigation of spread, load and torque in hot flat rolling. *BISRA Report.*

Mori, K. and Osakada, K. (1984). Simulation of three-dimensional deformation in rolling by finite element method. *International Journal of Mechanical Sciences*, 26:515-525.

Mramor, K. (2014). *Modelling of continuous Casting of Steel Under the Influence of Electromagnetic Field with Meshless Method: Dissertation.* PhD thesis, University of Nova Gorica.

Mramor, K., Vertnik, R. and Šarler, B. (2014). Simulation of laminar backward facing step flow under magnetic field with explicit local radial basis function collocation method. *Engineering Analysis with Boundary Elements*, 49:37-47.

Oñate, E., Idelsohn S., Zienkiewicz O. C. and Taylor, R. L. (1996). A finite point method in computational mechanics. Applications to convective transport

and fluid flow, *International Journal for Numerical Methods in Engineering*, 39:3839-3866.

Oñate, E. Perazzo, F. and Miquel, J. (2001). A finite point method for elasticity problems, *Computers and Structures*, 79:2151-2163

Orowan, E. (1943). The calculation of roll pressure in hot and cold flat rolling, *Proceedings of the Institution of Mechanical Engineers*, 150:140-167.

Osakada, K., Nakano, J and Mori, K. (1982). Finite Element Method for rigid-plastic analysis of metal forming formulation for finite deformation. *International Journal of Mechanical Sciences*, 24:459-468.

ParaView Parallel Visualization Application. (2012). Sandia Corporation, Kitware Inc. Sandia National Laboratories, version 3.98.0 64-bit, http://www.paraview.org.

Picque, M. B. (2004). *Experimental Study and Numerical Simulation of Iron Oxide Scales Mechanical Behaviours in Hot Rolling.* PhD Thesis, Ecole des Mines de Paris.

Pozo, L. P., Perrazzo, F. and Angulo, A. (2009). A Meshlesss FPM model for solving nonlinear material problems with proportional loading based on deformation theory. *Advances in Engineering Software*, 40:1148-1154.

Press, W. H., Teukolsky, S. A., Vetterling, W. T. and Flannery, B. P. (1992). *Numerical Recipes in Fortran. The Art of Scientific Computing, Second Edition*. Cambridge University Press, Cambridge.

Proceedings of the 4th international steel rolling conference. (1987). Paris, France, June 1-3.

Proceedings of the 9th international / 4th European steel rolling conference. (2006). Paris, France, June 19-21.

Roberts, W.L. (1978). *Cold Rolling of Steel*, Marcel Dekker Inc., New York.

Roberts, W. L. (1983). *Hot Rolling of Steel*, Marcel Dekker Inc., New York.

Rusinek, A. and Klepaczko, J. R. (2009). Experiments on heat generated during plastic deformation and stored energy for TRIP steels. *Materials and Design*, 30:35-48.

Schey, J. A. (2000). *Introduction to Manufacturing Processes, 3rd Edition,* Mc-Graw-Hill, New York.

Shepard, D. (1968). A two-dimensional interpolation function for irregularly spaced data. *Proceedings of the 23rd Association for Computing Machinery (ACM) national conference*, Las Vegas, USA, August 27-29.

Shibahara, T. (1981). Edger set-up model at roughing train in hot strip mill. *Journal of the Iron and Steel Institute of Japan*, 67:2509-2515.

Sims, R. B. (1954). The calculation of the roll force and torque in hot rolling mills, *Proceedings of the Institution of Mechanical Engineering*, 168:191-200.

Synka, J., Kainz, A. (2003). A novel mixed Eulerian-Lagrangian finite-element method for steady-state hot rolling processes. *International Journal of Mechanical Sciences*, 45:2043-2060.

Šarler, B., Kosec, G., Lorbiecka, A. and Vertnik, R. (2010). A meshless approach and solution of multiscale solidification modelling, *Material Science Forum*, 649:211-216.

Šarler, B. (2006). Solution of a two-dimensional bubble shape in potential flow by the method of fundamental solutions. *Engineering Analysis with Boundary Elements*, 30:227-235.

Šarler, B. (2007). From global to local radial basis function collocation method for transport phenomena. *Advances in Meshfree Techniques*, Springer, Berlin, 278-282.

Šarler, B. and Vertnik, R. (2006). Meshfree explicit local radial basis function collocation method for diffusion problems. *Computers and Mathematics with Applications*, 51:1269-1282.

Timoshenko, S. and Goodier, J. N. (1951). *Theory of Elasticity*, McGraw-Hill, York, USA.

Thompson, J. F. and Han, D. J. (1999). *Handbook of Grid Generation*. CRC Press, Florida.

Ullah, Z. and Augarde, C. E. (2013). Finite deformation elasto-plastic modelling using an adaptive meshless method. *Computers and Structures*, 118:39-52.

Vertnik, R. (2010). *Heat and Fluid Flow simulations of the Continuous Casting of Steel by a Meshless Method: Dissertation*. PhD thesis, University of Nova Gorica.

Vertnik, R. and Šarler, B. (2009). Simulation of continuous casting of steel by a meshless technique, *International Journal of Cast Metals Research*, 22:311-313.

Vertnik, R. and Šarler, B. (2014). Solution of continuous casting of steel benchmark test by a meshless method, *Engineering Analysis with Boundary Elements*, 45:45-61.

von Mises, R. (1913). Mechanik der Festen Korper im plastisch deformablen Zustand, *Nachrichten von der Gesellschaft der Wissenschaften zu Göttingen, Mathematisch-Physikalische Klasse*, 1: 582-592.

Wang, J. G. and Liu, G. R. (2002). On the optimal shape parameters of radial basis functions used for 2-D meshless methods. *Computer Methods in Applied Mechanics and Engineering*, 191:2611-2630.

Wendland, H. (2010). *Scattered Data Approximation.* Cambridge University Press, Cambridge.

Wicon. (2004). Danieli Morgårdshammar Group, Version 2004-1, http://www.algonet.se/~wicon/.

World Steel Organization. (2014). Steel Statistical Yearbook archive, *http://www.worldsteel.org/?action=stats_search.*

Wusatowski, Z. (1955). Hot Rolling: A study of draught, spread and elongation. *Iron and Steel*, 28:49-54.

Xiong, S., Rodrigues, J. M. C. and Martins, P. A. F. (2004). Simulation of plane strain rolling through a combined element free Galerkin boundary element approach. *Journal of Materials Processing Technology*, 159:214-223.

Zhou, Z., Qin, L., Huang W. and Wang, H. (2004). Effective stress and strain in finite deformation. *Applied Mathematics and Mechanics*, 25: 595-604

Zienkiewicz, O. C. and Taylor, R. L. (2000). *The Finite Element Method, Fifth Edition, Volume 1 The Basis.* Butterworth-Heinemann, London.